Probing few and many-body physics in a planar Bose gas : Atom-dimer interactions and zero-temperature superfluid fraction

Chloé Maury

To cite this version:

Chloé Maury. Probing few and many-body physics in a planar Bose gas : Atom-dimer interactions and zero-temperature superfluid fraction. Quantum Gases [cond-mat.quant-gas]. Sorbonne Université, 2023. English. NNT : 2023SORUS061 . tel-04082245v2

HAL Id: tel-04082245
https://theses.hal.science/tel-04082245v2

Submitted on 26 Apr 2023

Laboratoire Kastler Brossel Collège de France

Thèse de doctorat de Sorbonne Université

préparée par

Chloé Maury

sous la direction de

Jérôme Beugnon et Jean Dalibard

Probing few and many-body physics in a planar Bose gas
Atom-dimer interactions and zero-temperature superfluid fraction

---

Soutenue le 20 Février 2023 devant le jury composé de

M. Olivier Dulieu	Rapporteur
M. Jean-Claude Garreau	Rapporteur
Mme. Chiara Fort	Examinatrice
M. Xavier Leyronas	Examinateur
M. Jérôme Beugnon	Directeur de thèse

et présidé par Chiara Fort.

Travail réalisé au laboratoire Kastler Brossel, au sein du Collège de France.

Abstract

Dimensionality plays an important role in physical systems. A gas of ultracold atoms confined in a two-dimensional geometry has very different thermodynamic properties from those observed in a three-dimensional gas. In this thesis, we present experiments performed on a gas of ultracold bosons trapped in two dimensions and interacting weakly with each other. First, we describe this system with a mean-field approach and present the experimental setup that allows us to study it. Then, we describe two experiments dealing with two distinct topics, both conducted in the superfluid regime at near zero temperature. We first describe the creation of dimers by microwave-induced photoassociation of atoms trapped in a flat-bottom potential. This experiment allows us to characterise the interaction potential of our atomic species, rubidium 87. We also characterise the interactions between the dimers created and the bath of free atoms. In a third part, we impose a breaking of translational invariance on our zero-temperature gas of bosons by creating a spatially modulated potential in one of the two directions of the atomic cloud. We show with two distinct measurements that the superfluid density, equal to the total density for a homogeneous gas, decreases when the translational invariance is broken. We measure the sound velocity in the direction parallel and perpendicular to the spatial modulation on the one hand, and estimate the superfluid fraction according to a definition introduced by Leggett in 1970 on the other hand. We then observe a superfluid fraction which decreases as the modulation amplitude increases.

Résumé

La dimensionnalité joue un rôle important dans les systèmes physiques. Un gaz d'atomes froids confiné dans une géométrie à deux dimensions a des propriétés thermodynamiques très différentes de celles observées dans un gaz à trois dimensions. Dans cette thèse, nous présentons des expériences réalisées sur un gaz de bosons ultra-froids confinés à deux dimensions et interagissant faiblement entre eux. Dans un premier temps, nous décrivons ce système avec une approche de champ moyen et nous présentons le dispositif expérimental qui nous permet de l'étudier. Ensuite, nous décrivons deux expériences traitant deux sujets distincts, toutes deux menées dans le régime superfluide à température quasi-nulle. Nous commençons par décrire des expériences de création de dimères par photoassociation induite par la radiation d'un champ micro-ondes sur des atomes piégés dans un potentiel à fond plat. Cette expérience nous permet de caractériser le potentiel d'interaction de notre espèce atomique, le rubidium 87. Nous caractérisons aussi l'interaction entre les dimères créés et le bain d'atomes libres. Dans une troisième partie, nous imposons une brisure d'invariance par translation à notre gaz de bosons à température nulle en créant un potentiel spatialement modulé dans une des deux directions du nuage atomique. Nous montrons par deux mesures distinctes que la densité superfluide, égale à la densité totale pour un gaz homogène, décroît lorsque l'invariance par translation est brisée. Nous mesurons la vitesse de son dans la direction parallèle et perpendiculaire à la modulation spatiale d'une part, et nous estimons la fraction superfluide d'après une définition introduite par Leggett en 1970 d'autre part. Nous observons alors une fraction superfluide qui décroît lorsque l'amplitude de modulation augmente.

Contents

Appendices

Introduction

Over the past three decades, quantum gases have become an essential platform for the study of quantum phenomena that are observable only at low energy scales. Atomic cooling techniques now make it possible to bring the temperature, and hence the energy, of dilute atomic assemblies down enough so that their de Broglie *wavelength* becomes of the order of the interatomic distance. Reaching this so-called *quantum degeneracy* with bosonic particles allowed to study Bose-Einstein condensation: a state of matter characterised by the accumulation of particles in their ground state, predicted in 1925 by Einstein for ideal Bose gases [1]. The first three-dimensional gaseous Bose-Einstein condensates were observed in 1995 with alkali atoms [2–4]. Remarkably, atoms in three-dimensional cold dilute gases experience *weak interactions* which do not prevent the emergence of a large condensate fraction. This contrasts with cold liquid helium where, despite the presence of a superfluid phase, *strong interactions* limit the condensate fraction to a few percent of the whole system, even at zero temperature [5–7].
As a macroscopic fraction of the atoms occupy the lowest energy state, Bose-Einstein condensates are well described by a single *macroscopic wave function*. Interactions in dilute gases can be described quantitatively using a *mean-field* approach, i.e. by considering their average effect. In this context, the behaviour of the macroscopic wave function is captured by a non-linear Schrödinger equation, also known as the Gross-Pitaevskii equation. The first observations of Bose-Einstein condensates led to numerous experiments to characterise their main features [8]. Among the first experiments, their wave-like properties has been experimentally proved via the observation of interferences between two condensates [9] and the existence of long-range coherence was also probed [10].
Quantum degeneracy was also reached for Fermi gases [11–13]. In this case, there is no condensation as it would violate Pauli principle but the emergence of a so-called Fermi sea, where the atoms occupy the lowest energy states.

Although dilute cold gases were initially limited to short-range and weak interactions, researchers soon found a way to overcome both those limitations. On the one hand, the production of Bose-Einstein condensates with atomic species of large magnetic moment experiencing magnetic dipole-dipole interactions, as chromium, erbium or dysprosium, has made long-range interactions available for cold atom experiments [14, 15]. Long-range interactions have also been implemented using Rydberg excitations and cavity-mediated excitations [16, 17]. On the other hand, the strength of short-range interactions can be tuned thanks to Fano-Feshbach resonances [18, 19]. These resonances exist for bosons and fermions and they allowed to eventually reach the strongly-interacting regime [20, 21], with attractive and repulsive interactions. For instance, the crossover from a Bose-Einstein condensate of weakly bound molecules to a superfluid of Cooper pairs was observed in Fermi gases by tuning the interaction strength [22, 23]. Using Fano-Feshbach resonances also allows to study quantum gases in the so-called *unitary* regime, where the s-wave interactions are described by a scattering length a larger than the interparticle distance. This regime is particularly interesting for studying few-body physics as the corresponding eigenstates show universal features. For instance, Fermi gases close to unitarity show a universal relation between the atom-atom scattering length and the atom-dimer scattering length. On the other hand, in the case of bosons, this regime is the birthplace of the Efimov effect which predicts the presence of an infinite number of three-body bound states [24]. Outside the unitary regime, few-body interactions has been mostly studied through inelastic collisions and atom-exchange reactions. The existence of a Van der Waals universality for atom-dimer interactions remains an open question that we will address later in the manuscript.

The cold atoms toolbox was also enlarged by the ability to tune the potentials that the atoms feel. For instance, advances in lasers and optics made possible the loading of ultracold atoms in optical potentials. First, the *dimensionality* of the system can be controlled by confining a three-dimensional cold gas along one, two or three directions. This experimental breakthrough allowed to study ultracold gases in one and two dimensions for which the long-range order leading to condensation at finite temperature is destroyed by thermal and quantum fluctuations. Dilute cold gases with weak interactions in two dimensions do not show long-range order but experience a superfluid phase transition of infinite order, called the Berezinskii-Kosterlitz-Thouless transition [25–27], describing the emergence of a *quasi-long-range order* below a critical temperature. Confining ultracold atoms in one dimension made possible the realisation of Tonks-Girardeau gases, for which repulsive interactions are dominant and force the bosonic atoms to mimic Fermi gases properties [28, 29].

Without even considering the reduction of the dimensionality, the ability to impose tunable potentials allows researchers to study non-trivial effects. For instance, using optical lattices allowed to impose periodic arrangement and led to the realisation of the Fermi- and Bose-Hubbard model [30] or to the observation of the superfluid-Mott insulator *quantum* phase-transition for bosons [31–34]. Finally, the introduction of spatial light modulators completed this toolbox and researchers are now able to imprint optical potentials of arbitrary shape. In particular, the emergence of *homogeneous* potentials simplified the interpretation of results in cold atomic physics, limited by non-trivial density distributions [35].

In this thesis, we present experiments performed on a weakly-interacting Bose gas trapped in two dimensions. As mentioned above, this system does not exhibit condensation at finite temperature but still a transition to a superfluid phase. This transition is said to be of infinite order as all the thermodynamic quantities and their derivatives are continuous and because it does not rely on the breaking of a symmetry. The emergence of a quasi-long-range order and a superfluid phase when the temperature decreases is made possible by the pairing of topological defects, called *vortices*, below the critical temperature whereas isolated vortices proliferate above the critical temperature. This pairing manifests itself by a change of long-range behaviour of the spatial first order correlation function from an exponential decay to an algebraic decay. The superfluid regime describes a phase where a fraction of the gas shows superfluid properties, i.e. experiences frictionless flow for instance. In Galilean two-dimensional (2D) systems, the whole cloud is superfluid at zero temperature. The increase of the temperature comes with a reduction of the *superfluid fraction*, as part of the fluid becomes normal and can dissipate energy. The superfluid fraction decreases down to the critical point but stays finite. When going beyond the critical point however, the superfluid fraction jumps suddenly to zero. While the thermal superfluid transition is now well known, there remain other effects to explore. For instance, discussions have been opened

about superfluid flows in the presence of a breaking of translation invariance, in the context of *supersolidity* [36]. This question will be the subject of the second part of the manuscript.
A direct observation of the microscopic dynamics underlying the Berezinskii-Kosterlitz-Thouless was provided by the observation of the interference pattern between two released atomic planes [37]. The authors analysed the contrast of such fringes across the transition and observed a sudden decrease that they interpreted as a jump of the superfluid density. At high temperature, they observed *dislocations* in the interference patterns which they attributed to the proliferation of unbound vortices. On the other hand, the experimental measurement of the first order correlation function decay above and below the critical point in 2D quantum systems has been challenging and remained elusive for a long time [37–44]. Recently, researchers indirectly determined the first order correlation function expected for 2D homogeneous Bose gases by performing matter-wave interferometry on two harmonically-trapped ultracold clouds [45]. Concerning the superfluid fraction, there exists no direct experimental measurement. Two remarkable indirect measurements were performed first in 2D films of liquid helium 4 with torsion pendula [46] and more recently in a 2D homogeneous weakly-interacting Bose gas through the measurement of the speed of sound [47].
Another important feature of weakly-interacting 2D Bose gas is its scale invariance, which simplifies the derivation and therefore the experimental probing of its equation of state for instance. Indeed, its equation of state, giving the phase space density $\mathcal{D}$ for example, depends on the ratio $\mu/k_\mathrm{B}T$ of its chemical potential μ and temperature T whereas the equations of state in other dimensions depend on both those parameters independently. The equation of state was studied experimentally and its scale invariance probed [48–50].
In our group, we study weakly-interacting 2D Bose gases trapped in a *flat-bottom* optical potential, i.e. we work with homogeneous atomic clouds. In addition to this homogeneous trap, we also use spatial light modulators for shaping the in-plane confinement at wish and/or for imprinting additional potentials of local perturbations [51]. When combined with a two-photon optical transition, these spatial light modulators are also used to shape the density distribution of the spin components in binary mixtures [52, 53]. Although working with rubidium 87 prevents the use of Fano-Feshbach resonances at low magnetic fields, the presence of a so-called *clock transition* in the electronic ground state and the development of a hight-precision spectroscopy allowed us to highlight non-trivial effects as the presence of magnetic dipole-dipole interactions in our 2D binary mixture [54]. This high-precision spectroscopy tool was also used to measure Tan's contact in a bi-dimensional gas [55]. Recently, we also performed photoassociation spectroscopy and few-body physics measurements, which will be detailed in the manuscript.

In this manuscript, I present the two last results we obtained. These two results head toward different aspects of the cold atoms physics and are the result of a team effort.
The first result I describe is the probing of few-body physics through microwave-induced photoassociation of the least-bound dimers of rubidium 87. This study allows to characterise the interatomic potential and the atom-dimer interactions of ultracold bosons. It also paves the way to the implementation of microwave-induced Fano-Feshbach resonances.
Coming back to many-body physics, I describe how the breaking of translational invariance affects the superfluid behaviour of a weakly-interacting 2D Bose gas at zero temperature. This work experimentally tests the prediction made by Leggett in 1970 for supersolids [36].

DETAILED CONTENT OF THIS MANUSCRIPT

General features of the two-dimensional Bose gas

Chapter 1. I describe the weakly-interacting two-dimensional Bose gas in a mean-field approach and the theoretical framework to study this system at low temperature. I also briefly introduce the work I performed during my thesis but which is not detailed in this manuscript.

Chapter 2. I introduce the experimental setup used to produce planar Bose gases of rubidium 87. I also describe the toolbox we developed to control this ultracold gas.

Microwave photoassociation of ^{87}Rb dimers and measurement of atom-dimer interactions

Chapter 3. I describe the interatomic potential and interactions at play for ultracold bosonic gases. I focus on the bound states of these potentials: I derive a simple model to study them with rubidium 87 and detail the experimental detection of the Zeeman sub-levels of the least-bound rovibrational state of rubidium 87.

Chapter 4. The experimental probing of atom-dimer interactions is detailed. We describe these cold interactions in a mean-field approach and measure the associated atom-dimer scattering length.

Zero-temperature superfluid fraction in a density-modulated 2D Bose gas

Chapter 5. I introduce the analysis performed by Leggett in 1970 on a possible superfluid behaviour in solids. I apply the same analysis for a weakly-interacting 2D Bose gas at zero temperature and experiencing the breaking of translational invariance. The resulting superfluid fraction is analytically linked to the sound velocity in such a system.

Chapter 6. I describe the experimental probing of the zero-temperature superfluid fraction with the measurement of sound velocity in a density-modulated planar Bose gases. I finally compare these results with the measurement of Leggett's integral from the density profiles of the same system.

Part I

General features of the two-dimensional Bose gas

1

Physics of the two-dimensional Bose gas

A celebrating consequence of Bose statistics is Bose-Einstein condensation and, as an introduction, we describe in Sec. 1.1 this phenomenon and its conditions of occurrence. In particular, we discuss the effect of dimensionality. In this thesis, we study a planar Bose gas brought to quantum degeneracy and experiencing weak interactions, which does not exhibit condensation at finite temperature. We derive a mean-field description of this system in Sec. 1.2. Its main properties are described in Sec. 1.3 where we demonstrate the existence of a quasi-long-range order. We detail the resulting infinite order phase transition in Sec. 1.4. This transition, from a short-range order to a quasi-long-range order, is called the Berezinskii-Kosterlitz-Thouless (BKT) transition. Finally, we write in Sec. 1.5 the equation of state of a 2D Bose gas with short-range interactions in these different regimes. The reader will find a more complete description of the 2D ultracold Bose gas characteristics in Refs [56, 57].

1.1 Introduction to Bose-Einstein condensation

Bose-Einstein condensation is a phase transition characterised by the accumulation of particles in the single-particle ground state below a certain critical temperature. It was first introduced by Einstein in 1925 for three-dimensional (3D) ideal Bose gases [1].

This result can be established by considering N non-interacting and non-relativistic bosons of mass m in a 3D box of size $L \times L \times L$ with periodic boundary conditions. The Hamiltonian consists then only in kinetic-energy contribution and writes $H = \sum \hat{\boldsymbol{p}}_i^2/2m$ with $\hat{\boldsymbol{p}}_i$ the momentum of the particle i. The single-particle eigenstates are plane waves $\Psi_{\boldsymbol{p}}(\boldsymbol{r}) = L^{-3/2}\exp(i\boldsymbol{p}\cdot\boldsymbol{r}/\hbar)$ with corresponding energies $\varepsilon_p = p^2/2m$. At thermal equilibrium, in the grand canonical ensemble, the total atom number N reads:

$$N = \sum_{\boldsymbol{p}} N_p, \qquad\qquad N_p = \frac{1}{\exp[(\varepsilon_p - \mu)/k_\mathrm{B}T] - 1}, \tag{1.1}$$

with the Boltzmann constant k_B, the temperature T and the chemical potential $\mu < 0$ ($\varepsilon_0 = 0$). Einstein's original result was derived by considering separately the atom number in the ground state N_0 and the atom number in the excited states $N_\mathrm{exc} = \sum_{p\neq 0} N_p$, such that $N = N_0 + N_\mathrm{exc}$. In the thermodynamic limit, obtained when both N and L^3 grow to infinity while keeping N/L^3 constant, the spatial density of the atoms in the excited states writes:

$$n_\mathrm{3D,exc} = \frac{1}{\lambda_\mathrm{th}^3}\mathrm{Li}_{3/2}\left(\exp(\mu/k_\mathrm{B}T)\right). \tag{1.2}$$

We introduced the thermal wavelength $\lambda_\mathrm{th} = h/\sqrt{2\pi m k_\mathrm{B}T}$ and the polylog function $\mathrm{Li}_\alpha(x) = \sum_{j=1}^{\infty} x^j/j^\alpha$. This polylog function increases monotonically with the chemical potential μ and

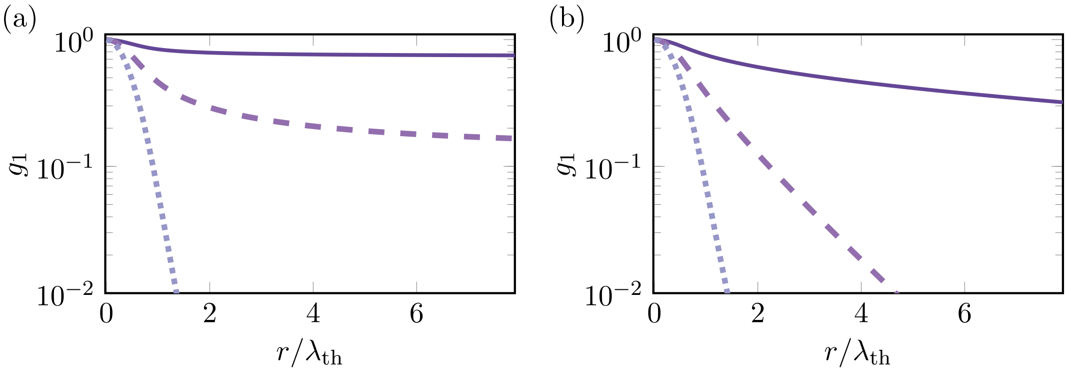

Figure 1.1: Normalised first-order correlation function $g_1(r) \equiv G_1(r)/G_1(0)$ of a 3D ideal gas (a) and a 2D ideal gas (b) for $\mathcal{D}_{\rm 3D,2D} = 0.3,\ 3,\ 10$ (dotted, dashed and solid line respectively).

is bounded to the finite value $\mathrm{Li}_{3/2}(1) = 2.612..$ when $\mu = 0$. The phase-space density (PSD) $\mathcal{D}_{\rm 3D,exc} = \lambda_{\rm th}^3 n_{\rm 3D,exc}$ saturates and we thus find Einstein's result: when the density in the excited states reaches its maximum value, the bosons accumulate in the ground state and a condensate forms.

In practice, particles in dense clouds interact and the interactions modify the eigenstates of the system, thus invalidating Einstein's criterion. A more general criterion for Bose-Einstein condensation was proposed by Penrose and Onsager in 1956 [58] for liquid helium, which applies to both interacting and non-interacting gases. This approach is based on the spectrum of the one-body density operator $\hat{\rho}_1$ and condensation occurs when its largest eigenvalue is finite in the infinite distance limit. Equivalently, we commonly evaluate this criterion with the long-distance behaviour of the one-body correlation function $G_1(\boldsymbol{r}_1, \boldsymbol{r}_2) \equiv \langle \boldsymbol{r}_1 |\, \hat{\rho}_1 | \boldsymbol{r}_2 \rangle$, also defined as the Fourier transform of the momentum distribution N_p. The condensation is then associated with a *long-range order* defined as a regime where the correlation function takes a finite value in the infinite distance limit.

The consistence between the two condensation criteria mentioned above is demonstrated by calculating the one-body correlation function of the 3D ideal gas of bosons, shown in Fig. 1.1.a and written:

$$G_1^{\rm 3D}(\boldsymbol{r}) = \frac{N_0}{L^3} + \frac{1}{\lambda_{\rm th}^3} \sum_j^{\infty} \frac{\exp(j\mu/k_{\rm B}T - \pi \boldsymbol{r}^2/2j\lambda_{\rm th}^2)}{j^{3/2}}, \tag{1.3}$$

where we assumed translation invariance and defined $\boldsymbol{r} = \boldsymbol{r}_1 - \boldsymbol{r}_2$. The second term of this last equation is the contribution of the excited states and is a sum of Gaussian functions, with different amplitudes and widths $\sqrt{j}\lambda_{\rm th}$ which increase with j. In the infinite distance limit $r \to +\infty$, this sum vanishes and we are left with the ground state contribution N_0/L^3. For large-enough densities, N_0 becomes macroscopic and the one-body correlation function tends to a finite value at infinite distances. The coherence length, i.e. the characteristic decay length of G_1, is infinite and condensation occurs.
Remarkably, the addition of weak interactions in 3D cold gases does not prevent condensation. The first direct observations of 3D gaseous Bose-Einstein condensates (BEC) were reported in 1995 [2–4].

Similarly, these condensation criteria can be evaluated in two dimensions. Dimensionality plays an important role in physical systems, in particular in the occurrence and characteristics of their phase transitions. Although condensation occurs at zero temperature for both ideal and weakly-interacting 2D gases [59], the two criteria elaborated above show that there is no condensation in ideal 2D gases at finite temperature. The PSD $\mathcal{D}_{2\mathrm{D}} = \lambda_{\mathrm{th}}^2 n_{2\mathrm{D}}$ of excited states writes in 2D:

$$\mathcal{D}_{2\mathrm{D,exc}} = -\ln(1 - \exp(\mu/k_{\mathrm{B}}T)), \tag{1.4}$$

and can take arbitrary large values when $\mu \to 0^-$. Hence, the ground state population never becomes macroscopic. On the other hand, the one-body correlation function

$$G_1^{2\mathrm{D}}(\boldsymbol{r}) = \frac{1}{\lambda_{\mathrm{th}}^2} \sum_{j=1}^{+\infty} \frac{\exp(j\mu/k_{\mathrm{B}}T - \pi \boldsymbol{r}^2/j\lambda_{\mathrm{th}}^2)}{j} \tag{1.5}$$

goes to zero in the large distance limit, as shown in Fig. 1.1. This results stands also for 2D weakly-interacting systems at finite temperature as demonstrated by the Mermin-Wagner-Hohenberg (MWH) theorem [60,61]: in dimensions lower or equal to 2, infinite systems with short-range interactions cannot undergo long-range order at finite temperature if their order parameter is continuous. Although coherence can be established for ideal and interacting gases in finite systems if the PSD is large enough, this theorem prohibits the existence of a true condensate at finite temperature. However, the presence of local interactions introduces a phase transition of a different nature associated to the emergence of a so-called *quasi-long-range order* and a *superfluid component*.

1.2 Description of a two-dimensional cold gas

We aim at studying the behaviour of weakly-interacting 2D ultracold gases. Experimentally, the 2D regime is usually realised by starting from a 3D gas whose degree of freedom in one of the three directions is frozen afterwards. In practice, there are two types of regime in 2D which are set by the vertical thickness of the cloud ℓ_z and the characteristic range of the interactions. For atoms of rubidium 87 (^{87}Rb), this range is given by the van der Waals radius[1] $R_{\mathrm{vdW}} = 82.3\, a_0$, where a_0 is the Bohr radius. The true 2D regime is reached when the particles motion is strictly reduced to the (x, y) plane, i.e. when the characteristic range of interaction, R_{vdW}, is much larger than the vertical thickness ℓ_z of the system. In this case, the scattering amplitude is energy dependent. On the opposite, a quasi-2D regime exists when $R_{\mathrm{vdW}} \ll \ell_z$, if the thermal energy and interaction energy per particle are lower than the energy difference between the ground state and the first exciting state of the vertical trapping. In this regime, the microscopic motion along the frozen direction is still possible and the collisions then conserve their 3D character.

The experiments described in this thesis are performed in the quasi-2D regime. Therefore, we first introduce interactions in a 3D Bose gas and derive its equation of motion in the case of weak interactions using a classical field formalism. Then, we transpose these equations to a 2D geometry and finally discuss their validity in the context of our experimental platform. We exclude from the discussion any consideration about the internal state.

---

[1] We use the convention:

$$R_{\mathrm{vdW}} = \frac{1}{2}\left(\frac{2m_{\mathrm{r}}C_6}{\hbar^2}\right)^{1/4} \tag{1.6}$$

where m_{r} is the reduced mass ($m_{\mathrm{r}} = \mathrm{m}/2$ here) and $C_6 = 4635\,\mathrm{a.u}$ for ^{87}Rb [62]. ($1\,\mathrm{a.u.} = 9.55 \times 10^{-80}\,\mathrm{J.m}^6$).

1.2.1 Short-range interactions

We now take into account interactions, first in a 3D dilute cloud, and we consider short-range interactions. We will assume that these interactions, between two particles at positions $\boldsymbol{r}_i$ and $\boldsymbol{r}_j$, are well described by the contact potential[2]

$$U(\boldsymbol{r}_i - \boldsymbol{r}_j) = g^{(3\mathrm{D})}\delta^{(3\mathrm{D})}(\boldsymbol{r}_i - \boldsymbol{r}_j), \tag{1.8}$$

where $g^{(3\mathrm{D})} = 4\pi\hbar^2 a/m$ is a coupling strength defined from the 3D s-wave scattering length a, obtained from the real inter-atomic potential. The use of the latter potential is possible because, for ultracold Bose gases, only low-energy collisions are relevant [63]. We enter this s-wave regime when the characteristic range of the interactions, R_{vdW}, is much smaller than the thermal wavelength λ_{th}. For temperatures of the order of 1 mK or less, the thermal wavelength is of several hundreds of nanometres. Collisions then occur between particles with zero relative angular momentum, in the s-wave channel, which is fully described by the constant a in 3D.

For ^{87}Rb atoms in the electronic ground state, the 3D interaction parameter is positive $g^{(3\mathrm{D})} > 0$ and atoms therefore undergo repulsive interactions. This is a necessary condition to form stable atomic clouds and avoid collapse.

1.2.2 Classical field formalism

We consider a gas of $N \gg 1$ identical bosons with binary interactions described by the potential $U(\boldsymbol{r}_i - \boldsymbol{r}_j)$. Particles experience a potential $V(\boldsymbol{r})$ and their Hamiltonian writes in the first quantization formalism:

$$\hat{H} = \sum_i^N \left[\frac{\hat{\boldsymbol{p}}_i^2}{2m} + V(\hat{\boldsymbol{r}}_i)\right] + \frac{1}{2}\sum_{i\neq j} U(\hat{\boldsymbol{r}}_i - \hat{\boldsymbol{r}}_j), \tag{1.9}$$

where we have introduced the position and the momentum operators $\hat{\boldsymbol{r}}$ and $\hat{\boldsymbol{p}}$. We now define $\hat{\Psi}(\boldsymbol{r})$, the operator which annihilates a particle at position $\boldsymbol{r}$, and its hermitian conjugate $\hat{\Psi}^\dagger(\boldsymbol{r})$ which creates a particle at position $\boldsymbol{r}$. We write the Hamiltonian in second quantization as follows:

$$\begin{aligned}\hat{H} = &\int \left(\frac{\hbar^2}{2m}\nabla\hat{\Psi}^\dagger(\boldsymbol{r})\cdot\nabla\hat{\Psi}(\boldsymbol{r}) + \hat{\Psi}^\dagger(\boldsymbol{r})V(\boldsymbol{r})\hat{\Psi}(\boldsymbol{r})\right)\mathrm{d}^3r \\ &+ \frac{1}{2}\int\int \hat{\Psi}^\dagger(\boldsymbol{r}_1)\hat{\Psi}^\dagger(\boldsymbol{r}_2)U(\boldsymbol{r}_1 - \boldsymbol{r}_2)\hat{\Psi}(\boldsymbol{r}_2)\hat{\Psi}(\boldsymbol{r}_1)\,\mathrm{d}^3r_1\mathrm{d}^3r_2. \end{aligned}\tag{1.10}$$

Thermal equilibrium of a N-body system is usually described by its density matrix $\hat{\rho}$. However, the presence of the pair-wise interaction term in this N-body system makes the determination of $\hat{\rho}$ too complicated.

In the following, we adopt a classical field point-of-view. This formalism is a mean-field approach and allows us to easily solve the N-body problem. It relies on two assumptions.

---

[2] The inter-atomic potential in Eq. (1.8) is actually ill-defined when acting on a wave function ψ showing a singularity at the origin and in this case we can write a pseudo-potential U_{pp} as

$$U_{\mathrm{pp}}[\psi(\boldsymbol{r})] = g^{3\mathrm{D}}\delta^{3\mathrm{D}}\,\frac{\partial}{\partial r}[r\psi(\boldsymbol{r})]\bigg|_{r=0}. \tag{1.7}$$

This pseudo-potential is the same as the contact potential when acting on regular functions.

The first one states that the atoms are considered to occupy mostly the same single-particle state described by a *macroscopic wave function* ψ. We remind that in the zero-temperature regime, both 3D and 2D weakly-interacting ultracold gases form a true condensate [59], which means that this assumption is at least true for $T = 0$. We then use the *Hartree ansatz* and write the many-body quantum state $|\Phi_N\rangle$ as a product of the single-particle wave function ψ:

$$\langle \boldsymbol{r}_1, ..., \boldsymbol{r}_N | \, \Phi_N \rangle \propto \psi(\boldsymbol{r}_1) ... \psi(\boldsymbol{r}_N), \tag{1.11}$$

where the wave function ψ is normalized as follows:

$$\int |\psi(\boldsymbol{r})|^2 \, \mathrm{d}^3 r = N. \tag{1.12}$$

The second hypothesis stipulates that one can neglect the granularity of the quantum field and we then treat ψ with classical-field equations.
Therefore, the problem simplifies to the deduction of a density of probabilities $\mathcal{P}[\psi]$ which best reproduces the density matrix $\hat{\rho}$, i.e.:

$$\langle \hat{A} \rangle = \mathrm{Tr}[\hat{A}\hat{\rho}] = \int \mathcal{P}[\psi] A[\psi] \, \mathrm{d}[\psi], \tag{1.13}$$

for a class of "reasonable" observables $\hat{A}$. Applying this formalism to Eq. (1.10), we describe the thermal equilibrium of the 3D ultracold gas with contact interactions thanks to the energy functional

$$E[\psi] = \int \left(\frac{\hbar^2}{2m} |\nabla \psi(\boldsymbol{r})|^2 + V(\boldsymbol{r}) |\psi(\boldsymbol{r})|^2 + \frac{g^{(3\mathrm{D})}}{2} |\psi(\boldsymbol{r})|^4 \right) \mathrm{d}^3 \boldsymbol{r}. \tag{1.14}$$

Experimentally, we obtain a 2D geometry by imposing to the particles a tight confinement along one of the three directions, here the vertical one, and the motion of the atoms along the vertical axis z is then frozen. We assume that the particles lie in the ground state of the vertical confinement. Assuming also that the energy difference between the ground state and the first excited state of the vertical confinement is larger than the thermal energy $k_\mathrm{B} T$ and the interaction energy per particle E_i/N, we use the ansatz:

$$\psi(\boldsymbol{r}) = \phi(x, y) \chi_0(z), \tag{1.15}$$

where χ_0 is the single-particle ground state wave function along the frozen direction z, while ϕ is the in-plane single-particle wave function. The condition of normalisation Eq. (1.12) then writes:

$$\int |\phi(\boldsymbol{r})|^2 \, \mathrm{d}^2 r = N, \qquad \int |\chi_0(z)|^2 \, \mathrm{d}z = 1, \tag{1.16}$$

and the in-plane density writes $n(\boldsymbol{r}) = |\phi(\boldsymbol{r})|^2$. We obtain an energy functional describing the motion in the (x, y) plane (up to a constant):

$$E[\phi] = \int \left(\frac{\hbar^2}{2m} |\nabla \phi(\boldsymbol{r})|^2 + V(\boldsymbol{r}) |\phi(\boldsymbol{r})|^2 + \frac{g^{(2\mathrm{D})}}{2} |\phi(\boldsymbol{r})|^4 \right) \mathrm{d}^2 \boldsymbol{r}, \tag{1.17}$$

with the introduction of the parameter

$$g^{(2\mathrm{D})} = g^{(3\mathrm{D})} \int |\chi_0(z)|^4 \, \mathrm{d}z, \tag{1.18}$$

which describes the interactions strength in 2D. The three terms of Eq. (1.17) describe respectively the kinetic energy E_k, the potential energy E_p and the interaction energy E_i in the 2D case.

Note that we transposed here a mean-field description of 3D collisions to a 2D system, and it is not straight-forward to conclude that the 2D interaction parameter is energy-independent when considering the 2D problem.

1.2.3 Quasi-two-dimensional regime in our experimental platform

In our experimental platform, the vertical confinement is ensured by a harmonic potential $V(z) = m\omega_z^2 z^2/2$ of frequency $\omega_z/2\pi$ and the ground state of the system is Gaussian in the vertical direction:

$$\chi_0(z) = \frac{1}{(\pi\ell_z^2)^{1/4}} \exp\left(-z^2/2\ell_z^2\right). \tag{1.19}$$

The vertical thickness of the cloud is then written $\ell_z = \sqrt{\hbar/m\omega_z}$ and, with our typical trapping frequencies, reaches a few hundreds of nanometres $\ell_z \sim 180$ nm.

As mentioned earlier, the experiments are then performed in the quasi-2D regime $\ell_z \gg R_\mathrm{vdW}$. The analysis of binary interactions in this regime has been performed by Petrov et al. [64,65] and the authors find the following two-dimensional coupling strength:

$$g^{(\mathrm{2D})} = \frac{\hbar^2}{m}\sqrt{8\pi}\frac{1}{\ell_z/a - \ln(\pi q^2\ell_z^2)/\sqrt{2\pi}}, \tag{1.20}$$

with $q^2 = 2m\mu/\hbar^2$. The energy dependence persists, hence the coupling strength depends on the density of the condensate. However, we perform our experiments with rubidium 87, for which the 3D scattering length is close to the range of the interaction potential $a \sim R_\mathrm{vdW}$. We study then a configuration with $\ell_z \gg a$ and therefore the logarithm term has a negligible contribution. The coupling simplifies to the constant

$$g^{(\mathrm{2D})} = \frac{\hbar^2}{m}\frac{\sqrt{8\pi}a}{\ell_z}, \tag{1.21}$$

which corresponds to the result expected from Eq. (1.18) using Eq. (1.19). Remarkably, the interactions in the quasi-2D regime can thus be described by a dimensionless parameter defined as $\tilde{g} = mg^{(2D)}/\hbar^2 = \sqrt{8\pi}a/\ell_z$.

Finally, we work in the weak interaction regime, defined by $\tilde{g} \ll 1$ [56], and the interactions remain repulsive $\tilde{g} > 0$. The possible occupation of the excited states of the harmonic potential has been studied in Ref. [66], and it has been shown that this can lead to a reduction of $\tilde{g}$ by a few percent only within our experimental parameters ($a\ell_z n \ll 1$).

Work performed during my thesis and not detailed in this manuscript

Although the contact interactions are dominant in our system, we observed more exotic interactions such as magnetic dipole-dipole interactions (MDDI) [54]. These interactions are commonly studied with atom species with large magnetic moment in the ground state. While we work with alkali atoms, for which the magnetic moment is of the order of $\lesssim 1$ Bohr magneton μ_B, we demonstrated the non-negligible presence of MDDI in a *mixture* of two magnetic-field insensitive states. We used a high resolution Ramsey interferometric method on the so-called *clock-transition* between these two states and interpreted the effect of MDDI as a modification of the inter-species scattering length.

From now on, we drop the notation (2D) and all quantities are assumed to be 2D except for the 3D s-wave scattering length a.

1.2.4 Description at zero temperature for uniform gases

We dedicate this section to the specific case of 2D weakly-interacting Bose gases at zero temperature, at equilibrium in the dilute regime. Under these conditions, the ground state is a true condensate and the Hartree ansatz Eq. (1.11) is known to be valid. We minimize the energy functional Eq. (1.17) after introducing the chemical potential $\mu = \partial E/\partial N$, a Lagrangian multiplier, to satisfy the condition of normalisation of the macroscopic wave function ϕ Eq. (1.16). We obtain the stationary *Gross-Pitaevskii equation* (GPE), also known as the *nonlinear Schrödinger equation* (NLSE):

$$-\frac{\hbar^2}{2m}\nabla^2\phi + V(\boldsymbol{r})\phi + \frac{\hbar^2}{m}\tilde{g}|\phi|^2\phi = \mu\phi. \tag{1.22}$$

This equation, valid for $T = 0$, also gives an appropriate description of the system at low temperature in the degenerate regime, when the PSD is large enough $\mathcal{D} \gg 1$.

We focus our interest on uniform gases which are the subject of this thesis. In practice, we confine the atoms in a potential $V(\boldsymbol{r})$ constant and equal to zero over the size of the sample and with sharp edges.

Ground state At equilibrium, the ground state of the system is the solution of Eq. (1.22) with the minimum energy. We study the bulk of a uniform 2D gas at zero temperature and, as $E_\mathrm{i} \gg E_\mathrm{k}$, we neglect the kinetic part of the GPE. This approximation defines the *Thomas-Fermi regime* and leads to:

$$\frac{\hbar^2}{m}\tilde{g}|\phi|^2 = \mu. \tag{1.23}$$

Therefore, in this regime, the in-plane density $n = |\phi|^2$ is uniform. Naturally, this regime is only valid in the bulk, and the kinetic energy cannot be neglected at the edges. The density $|\phi|^2$ then varies smoothly from n to zero over a distance ξ called the *healing length*:

$$\xi = \frac{1}{\sqrt{2\tilde{g}n}}, \tag{1.24}$$

which results from the balance between the kinetic and interaction energies. This distance therefore gives the characteristic length scale of the interactions.

Excitation spectrum In uniform systems, the elementary excitations are deduced from Bogoliubov analysis [67]. This approach is purely phononic and does not take into account other excitations such as vortices for example. The excitation modes are defined by real frequencies ω_k in the context of repulsive interactions and are associated with plane waves of wave vector $\boldsymbol{k}$ of norm k. The energy spectrum

$$\hbar\omega_k = \frac{\hbar^2}{2m}\sqrt{k^2(k^2 + 4\tilde{g}n)} \tag{1.25}$$

describes two distinct regimes separated by a characteristic wave vector $k_\mathrm{c} = 1/\xi$. In the high-k limit $k \gg k_\mathrm{c}$, one enters the free-particle regime, whereas for $k \ll k_\mathrm{c}$ the relation of

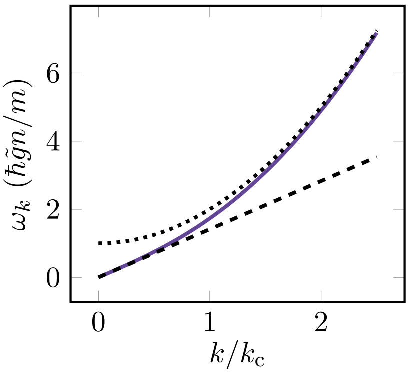

Figure 1.2: Bogoliubov excitation spectrum (solid purple line), with the phononic regime ($k \ll k_\mathrm{c}$) and its linear relation $\omega_k = c_\mathrm{B}k$ (dashed black line) and the free-particle regime ($k \gg k_\mathrm{c}$) described by a quadratic relation of dispersion (dotted black line). The momentum is expressed in units of k_c.

dispersion Eq. (1.25) is linear $\omega_k \sim c_\mathrm{B}k$ and phonons propagate with the so-called *Bogoliubov speed of sound*:

$$c_\mathrm{B} = \frac{\hbar}{m}\sqrt{\tilde{g}n}. \tag{1.26}$$

The excitations spectrum is represented in Fig. 1.2 and the sound modes have been observed experimentally in 2D [47, 68, 69].

In our experimental platform, described in the next chapter, the healing length is $\xi \sim 0.2\,\mu\mathrm{m}$ for the largest density achievable and the corresponding Bogoliubov speed of sound is $c_\mathrm{B} \sim 3\,\mathrm{mm/s}$.

1.3 Some properties

Although the 2D weakly-interacting gas does not exhibit condensation, we will now see that its symmetry properties make it an interesting system.

1.3.1 Scale invariance

Symmetries in physical systems generally constrain their behaviour and are exploited to simplify many problems. Remarkably, the 2D homogeneous system with short-range interactions, when described by a classical field theory, presents an interesting feature when it undergoes a dilatation of length by a factor $\lambda > 0$.

Indeed, the action $\mathcal{S}[\phi]$ associated with the GPE (with $V(\boldsymbol{r}) = 0$) is kept invariant for a transformation in which the length ℓ, the time t and the wave function ϕ are rescaled as follows:

$$\begin{aligned} \ell \to \quad & \ell' = \ell/\lambda, \\ t \to \quad & t' = t/\lambda^2, \\ \phi(\boldsymbol{r}) \to \quad & \phi'(\boldsymbol{r}', t') = \lambda\phi(\boldsymbol{r}, t). \end{aligned} \tag{1.27}$$

This property is due to the adimensionality of the interaction parameter $\tilde{g}$: the interaction energy E_i does not introduce any new length scale. Therefore, the interaction energy E_i and the kinetic energy E_k scale in the same way under Eq. (1.27) and they are transformed as $E \to \lambda^2 E$. As the energy functional is only rescaled by a constant factor, the laws governing the system are unchanged. This property, known as *scale invariance*, has important consequences and we can demonstrate that the equation of state of the system depends on the single parameter[3] $\mu/k_\mathrm{B}T$ [57]. The study of GPE solutions also highlights the scale invariance of the 2D ultracold gas. Indeed, using the transformation Eq. (1.27), we can deduce a new solution ϕ' of the GPE Eq. (1.22) from a previously known ϕ.

Scale invariance and its dynamical consequence in 2D harmonic potentials have been discussed earlier in the team for breathers [70]. Another situation where scale invariance plays a crucial role is in the context of localised stationary solutions of the GPE. In the presence of repulsive interactions and without confinement, there do not exist such solutions, so-called *solitary* solutions. In the case of attractive interactions, such stationary solitary solutions exist, even if they are weakly unstable. Among them, the so-called *Townes soliton* is a real nodeless localised stationary solution of zero-energy. Remarkably, the scale invariance property of the 2D system implies that there is no size condition to form a Townes soliton. Indeed, the only conditions yielding these solitons are to have the right shape for the wave function ϕ and a fixed atom number $N_\mathrm{T} = 5.85/\tilde{g}$. Townes solitons were observed in quasi-2D samples of caesium atoms with attractive interactions by Chen & Hung [71, 72]. The authors confirmed that Townes solitons arise from samples of any size and observed the expected scaling of N_T with $\tilde{g}$.

Work performed during my thesis and not detailed in this manuscript

During my thesis and simultaneously with the work by Chen & Hung, we studied the physics of mixtures of two *non-miscible* species, $|1\rangle$ and $|2\rangle$, with repulsive intra- and inter-species interactions. In particular, we considered a *minority* component $|2\rangle$ of density n_2 immersed in a *majority* component $|1\rangle$ of density n_1. We showed that in the limit of weak depletions, i.e. when $n_2 \ll n_1$, the system is well described by a *one-component* GPE with effective attractive interactions, due to the non-miscibility of the two species. This platform is then adapted to the study of solitary waves. In order to observe Townes solitons, the minority component must have the right atom number $N = N_\mathrm{T}$ and the right profile. We have deterministically imprinted Townes solitons [52] in our *two-component* 2D ultracold sample. We confirmed the scale invariance of such solutions of the GPE with the observation of Townes solitons of various sizes. Thanks to the presence of tunable magnetic dipole-dipole interactions in our mixture (see Sec. 1.2.3), we also confirmed the scaling of the Townes atom number N_T with the effective interaction parameter.

Recently, we also carried out a numerical study of the two-component system [53]. We confirmed the presence of localised and stationary states for any atom number N larger than the Townes atom number N_T. As the atom number N increases, we leave the weak depletion regime $N/N_T \lesssim 1.05$. For small but finite depletions $1.05 < N/N_T < 1.5$, the additional length scale induced by the presence of the bath $|1\rangle$ is no longer negligible. This introduces a weak non-local correction to the GPE which breaks scale invariance. However, it stabilises the system and we numerically find stationary solutions with Townes-like profiles. By further increasing the atom number $N/N_T \gtrsim 1.5$, the one-component GPE is no longer suitable. We use then two coupled GPEs while we enter the spin-domain regime. Together with this phase diagram, we studied the excitation spectrum of the stationary solutions when $N > N_\mathrm{T}$. In particular, we have shown the absence of localised excitation modes in the region $1.45 \lesssim N/N_\mathrm{T} \lesssim 3.5$, called a

---

[3] In one and three dimension, the equation of state depends on the chemical potential μ and the temperature T separately.

self-evaporation region.
The reader can find a complete description of this work in Ref. [73].

1.3.2 Quasi-long-range order

We emphasised in the introduction to 2D systems that condensation does not occur at finite temperature for non-interacting and interacting 2D gases. However, the presence of repulsive weak interactions restores the notion of order in the system. We now describe some properties of the system at low temperature that lead to the definition of a quasi-long-range order.

Reduction of the density fluctuations When the temperature of an interacting system is sufficiently low (or equivalently when the PSD is large enough), the interaction energy E_{i} becomes dominant. This leads to a reduction of the density fluctuations which come with an energy cost. Indeed, the interaction energy in our system is calculated from Eq. (1.17) and is written:

$$E_{\mathrm{i}} = \frac{\hbar^2 L^2}{2m} \tilde{g} \langle n^2(\boldsymbol{r}) \rangle. \tag{1.28}$$

The energy cost is then directly proportional to the density fluctuations which we usually characterise by the (normalised) second-order correlation function

$$g_2(\boldsymbol{r}_1, \boldsymbol{r}_2) \equiv \frac{1}{n^2} \langle n(\boldsymbol{r}_1) n(\boldsymbol{r}_2) \rangle. \tag{1.29}$$

This function, also called the density-density correlation function, evaluates the probability to find a particle at a position $\boldsymbol{r}_1$ knowing that a second particle has been detected at a position $\boldsymbol{r}_2$ and depends on the distance $r = |\boldsymbol{r}_1 - \boldsymbol{r}_2|$. The quantity $g_2(0)$ then represents the probability to find two particles at the same position. For ideal Bose gases, $g_2(0) = 2$ and this reflects a tendency towards atoms bunching ($g_2(0) > 1$) whereas for thermal Fermi gases $g_2(0) = 0$, which indicates a tendency towards atoms anti-bunching ($g_2(0) < 1$).
When the density fluctuations are totally suppressed, one finds $g_2(0) = 1$. In this configuration, the only degree of freedom left for the classical field ϕ is its phase θ. This regime is called the *quasi-condensate* regime or *pre-superfluid* regime [64, 74, 75] and has been observed experimentally in non-uniform systems [38, 49, 76]. We stress that the definition of the quasi-condensate includes the suppression of density fluctuations only and that there is no extended phase coherence in the system, as observed in Ref. [38].

Work performed during my thesis and not detailed in this manuscript

In practice, $g_2(0)$ is ill-defined for 2D interacting gases and the correct observable to study the probability to find two particles close to each other is Tan's contact $C \equiv \partial E / \partial a$. Indeed, $g_2(r)$ is expected to diverge in the short distance limit. Initially defined by Tan in 2008 for strongly-interacting Fermi gases [77–79], the two-body contact has been measured recently, in our group, in a uniform 2D weakly-interacting Bose gas across the superfluid transition [55]. We measured the change of internal energy for a small modification of the scattering length using Ramsey spectroscopy. Our results are in good agreement with the theoretical predictions in the limiting case of deeply degenerate and normal gases and recent calculations performed by A. Rançon & N. Dupuis [80].

First-order correlation function The emergence of phase ordering in interacting gases is studied through the infinite distance behaviour of the first-order correlation function following Penrose and Onsager criterion. We therefore need to calculate G_1 in the quasi-condensate regime. In the low-temperature phase, we can apply the same Bogoliubov treatment as used for the zero temperature case in Sec. 1.2.4. Indeed, only long-wavelength phase perturbations are significant [56] and this approach was justified by Castin & Mora for quasi-condensates in 2D in Refs. [81, 82]. The macroscopic wave function is written $\phi = \sqrt{n}\exp(i\theta)$ with a fixed density n and a fluctuating phase θ. The normalised first-order correlation function $g_1(r) = G_1(r)/G_1(0)$ yields within this formalism:

$$g_1(r) \approx \exp[-\langle\theta(\boldsymbol{r}_2) - \theta(\boldsymbol{r}_1)\rangle^2]. \tag{1.30}$$

The computation of the phase variations (performed introducing a UV cut-off at λ_{th} in the population of the excitation modes) shows that the decay of g_1 in the quasi-condensate regime is different than the exponential decay expected in the thermal regime. Indeed, g_1 decays algebraically:

$$g_1(r) \approx \left(\frac{\lambda_{\text{th}}}{r}\right)^{\alpha}, \qquad \alpha = \frac{1}{\mathcal{D}_{\text{s}}}, \tag{1.31}$$

and the exponent α depends on the non-zero superfluid PSD $\mathcal{D}_{\text{s}}$ of the system. It still vanishes for infinite distances which is consistent with MWH theorem, but this slow decay of the correlations defines a quasi-long-range order and is represented in Fig. 1.3. For large $\mathcal{D}$, phase coherence is established over a macroscopic distance. This has great consequences for finite-size systems for which the correlation function can have a finite value over the whole sample.

1.4 Berezenskii-Kosterlitz-Thouless phase transition

The 2D Bose gas with short-range interactions does not exhibit Bose-Einstein condensation. However, we have shown that a notion of order is restored below a critical temperature T_{c}, including the appearance of a quasi-condensate and a quasi-long-range order. In the following, we give a phenomenological description of superfluidity and describe the mechanism allowing the 2D Bose gas to evolve from a normal fluid at low PSD to a superfluid at high PSD. This phase transition is studied with the Berezenskii-Kosterlitz-Thouless mechanism derived in 1972 [25, 26, 83], originally for the two-dimensional XY spin model.

Superfluidity In a very simplified way, superfluidity is often described as an absence of viscosity. First interpreted as a property of helium at low temperature in 1938 by Kapitza [5] and Allen & Misener [6] simultaneously, it was introduced after the measurement of the flow of liquid helium II through capillarities. In 1941, Landau gave a first explanation of this phenomenon by showing that a fluid can move at a velocity v without friction against static walls if its elementary excitation spectrum $\varepsilon(p)$ satisfies the criterion $v < \min_{p\to 0}\varepsilon(p)/p$, p being the fluid momentum [84].

In practice, superfluidity relies on subtle definitions and one has to go beyond Landau criterion. Some established properties of superfluidity are given here, but the reader will find a more complete description of this phenomenon in Refs. [85–87]. Let us mention two fundamental properties that characterise a superfluid state [88, 89]. These properties are deduced from thought experiments which consist in describing how the state of a fluid in a cylindrical or toric container varies as a function of its rotating velocity around the central axis. First, if we place a classical fluid in such a container rotating with an angular frequency Ω, it will acquire a velocity $\boldsymbol{v}(\boldsymbol{r}) = \boldsymbol{\Omega} \times \boldsymbol{r}$ through viscous force between the walls and the atoms. In contrast, if we consider a superfluid, a non negligible fraction of the fluid must stay at rest in the Galilean frame of the laboratory, at least under a critical frequency $\Omega < \Omega_\mathrm{c}$. This criterion imposes a certain *stiffness* of the superfluid state. This phenomenon is associated to a reduction of the moment of inertia compared to the classical fluid and has been observed for the first time with liquid helium [90]. Second, if the container rotates with an angular frequency $\Omega > \Omega_\mathrm{c}$ such that the superfluid is now in rotation, and the rotation of the container is stopped, the motion of the superfluid will continue for a long time. In this sense, the superfluid state is metastable: while its energy would be minimised if it were static, it continues to rotate. For ultracold atomic gases, the flow can last for several tens of seconds. In contrast, a normal fluid set in motion in a static container will stop in a few seconds due to the roughness of the walls.

The *two-fluid* model gives a useful framework to characterise the properties of a superfluid. It consists in describing the quantum gas or fluid as a superposition of two components: a superfluid component of density n_s and velocity $\boldsymbol{v}_\mathrm{s}$ which does not carry entropy, and a normal component of density n_n and velocity $\boldsymbol{v}_\mathrm{n}$. We emphasise that the *superfluid fraction* n_s/n is not necessarily equal to the *condensed fraction* in systems exhibiting condensation. In the quasi-condensate regime, the macroscopic wave function is written $\phi = \sqrt{n}\exp(\mathrm{i}\theta)$ and the superfluid velocity is defined as $\boldsymbol{v}_\mathrm{s} = \hbar\boldsymbol{\nabla}\theta/m$. This definition shows that the superfluid component rotational $\boldsymbol{\nabla} \times \boldsymbol{v}_\mathrm{s}(\boldsymbol{r})$ is zero except where $\theta(\boldsymbol{r})$ is singular. On the other hand, if the fluid is placed in a container of rigid walls or trapped in a time-independent potential, the normal velocity is zero when the container is at rest and equal to $\boldsymbol{v}_\mathrm{n} = \boldsymbol{\Omega} \times \boldsymbol{r}$ when the container has an angular velocity Ω, i.e. $\boldsymbol{\nabla} \times \boldsymbol{v}_\mathrm{n} = \boldsymbol{\Omega}$ [85].

We briefly describe two equivalent formalisms to quantitatively study superfluid states, which are demonstrated in Refs. [8, 85]. Superfluidity can be established by applying a momentum constraint on the Hamiltonian, which corresponds to work in the moving frame. In this context, only the normal component of density n_n reacts to the perturbation. This method is equivalent, within a gauge transformation, to impose a so-called *twisted boundary condition* (TBC) in one direction of space for finding the eigenstates ϕ of the systems. For instance, in a 2D system of size $L \times L$ we would impose:

$$\phi(x+L, y) = \exp(\mathrm{i}\Theta)\phi(x,y), \qquad \phi(x, y+L) = \phi(x,y), \qquad \Theta \ll 1. \tag{1.32}$$

Let us consider the fraction of atoms n_s/n remaining motionless in a container in rotation with an angular frequency $\Omega < \Omega_\mathrm{c}$. As mentioned above, this stiffness is associated with a reduction of the moment of inertia in comparison with a normal fluid, which can be evaluated via a free energy cost $\Delta\mathcal{F} = \mathcal{F}(\Omega) - \mathcal{F}(0)$, for having a part of the fluid that stays at rest. Considering TBC, we can show that this energy cost is related to the superfluid fraction by $\Delta\mathcal{F}(\Theta) = \hbar^2\Theta^2 n_\mathrm{s}/2m$ [85].

Destruction of the phase ordering Phase ordering is limited by the presence of *topological defects* which are vortices. A vortex defines a zero in the wave function ϕ around which the phase rolls in an integer multiple of 2π, called the topological charge q of the vortex. The density $n(\boldsymbol{r})$ is then depleted over a distance given by the healing length ξ and the phase field $\theta(\boldsymbol{r})$ undergoes a strong change over short distances. Therefore, we understand that the presence of many vortices makes impossible the presence of a phase order.

The BKT phase transition in 2D relies on the fact that, under a critical temperature T_c, the creation of isolated vortices is not favourable and they survive in the system only by forming pairs of vortices with opposite charges q, called vortex-anti-vortex pairs. These pairs

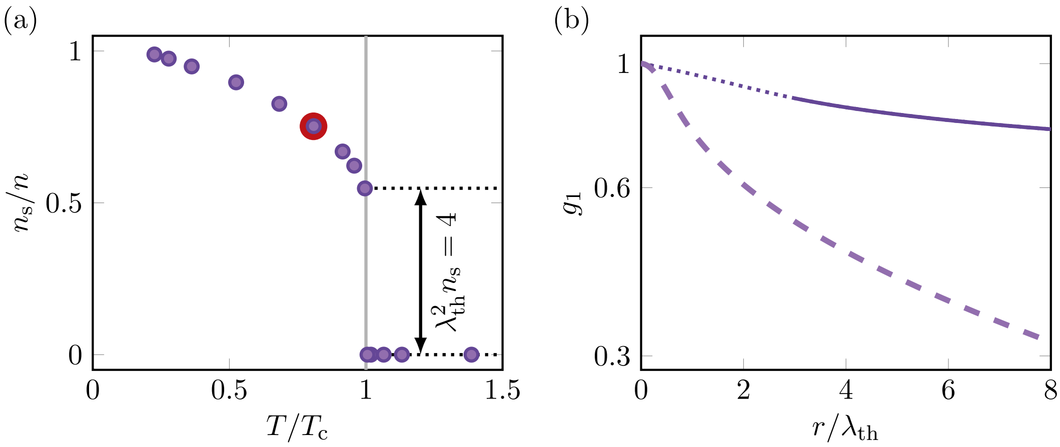

Figure 1.3: (a) Superfluid fraction n_s/n computed from the Monte Carlo simulations of Prokof'ev & Svistunov [91] with $\tilde{g} = 0.15$. (b) Normalised first-order correlation function for an ideal 2D Bose gas (dashed line) and a weakly-interacting 2D Bose gas (solid line) with $\mathcal{D} = 10$. For the interacting gas with $\tilde{g} = 0.15$ and according to the Monte Carlo simulations, $\mathcal{D} = 10$ corresponds to a superfluid fraction of $n_s/n = 0.77$. We indicate with a red point in (a) the system shown in (b). We used a total density $n = 100\,\mu\text{m}^{-2}$, fixing $T = 350\,\text{nK}$, and the decay of g_1 at large distances is computed using Eq. (1.31). The extrapolation to short distances (dotted line) is not physical but reminds $g_1(0) = 1$.

do not affect the coherence and the thermodynamic properties are essentially determined by phonon modes. Above T_c, isolated vortices of random charges proliferate and prevent any long-distance phase coherence from occurring, making this transition a *topological transition*.

A superfluid transition Across this transition, and going to low temperatures, a *superfluid fraction* $n_s \leq n$ appears. This superfluid fraction is not easy to determine and was computed by Prokof'ev, Ruebenacker & Svistunov using Monte-Carlo simulations [91, 92]. We have reproduced n_s from their results in figure Fig. 1.3. They also characterised the critical point of this transition and found the critical PSD $\mathcal{D}_c$ and the critical chemical potential μ_c using the definitions of Fisher et al. [93]:

$$\mathcal{D}_c = \ln\left(\frac{\xi_{\mathcal{D}}}{\tilde{g}}\right), \tag{1.33}$$

$$\mu_c = \frac{\tilde{g}}{\pi} \ln\left(\frac{\xi_{\mu}}{\tilde{g}}\right), \tag{1.34}$$

where the constants $\xi_{\mathcal{D}} = 380(3)$ and $\xi_\mu = 13.2(4)$ are calculated numerically. The transition is continuous for all the thermodynamic quantities but the superfluid PSD $\mathcal{D}_s = \lambda_{th}^2 n_s$, which undergoes a jump from zero to $\mathcal{D}_s = 4$ at the critical point. This superfluid PSD sets the exponent of the algebraic decay of the correlation function g_1 in Eq. (1.31) and it therefore lies between 0 and 1/4.

The quasi-long-range order was observed in cold atoms for the first time by Hadzibabic et al. in 2006 [37], whereas the superfluid fraction was recently measured via the measurement of the speed of sound modes in a homogeneous 2D sample [47]. In 2015, Fletcher et al. studied the critical point of the BKT transition in a harmonically trapped 2D Bose gas as a function of the interaction strength $\tilde{g}$ [94]. They found this critical point to be in good

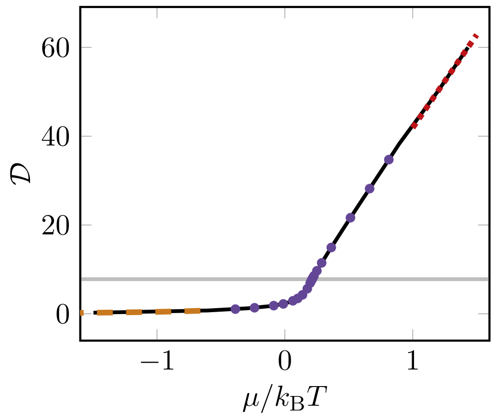

Figure 1.4: Equation of state of the weakly-interacting 2D Bose gas. We obtain a numerical EoS (solid black line) by interpolating the points from the Hartree-Fock limit (dashed orange line) together with the Monte Carlo simulations of Prokof'ev & Svistunov (purple points) and the Thomas-Fermi regime (dotted red line). The computation is performed with an interaction parameter $\tilde{g} = 0.15$ and the critical PSD $\mathcal{D}_\mathrm{c} = 7.3$ is represented by the solid grey line.

agreement with the classical field predictions and showed that it converges to the BEC critical point in the limit of vanishing interactions. As explained above, the first-order correlation function is an interesting observable to attest the presence of quasi-coherence. The recent work of Sunami et al. [45] reports a measurement of g_1 in an 2D homogeneous gas. They performed wave-matter interferometry and confirmed the expected change in the decay of g_1 at the critical point. A similar but unpublished study was performed in our group in 2019 and reported in Ref. [43].

1.5 Equation of state

All the thermodynamic quantities of a system can be calculated from its equation of state (EoS). There exists no analytical form of the EoS of the 2D Bose gas, however, thanks to its scale invariance property, the thermodynamic variables and thus the EoS depends only on the quantity $\mu/k_\mathrm{B}T$:

$$\mathcal{D} = \mathcal{D}\left(\frac{\mu}{k_\mathrm{B}T}\right). \tag{1.35}$$

We study independently the two limiting cases of very degenerate gases $\mathcal{D} \gg 1$ and thermal clouds $\mathcal{D} \ll 1$.

Thomas-Fermi regime We have already presented this regime in Sec. 1.2.4. Deeply degenerate gases ($\mathcal{D} \gg 1$) are well described by the GPE Eq. (1.22). We neglect the effect of kinetic energy and the EoS reads:

$$\mathcal{D} = \frac{2\pi}{\tilde{g}} \frac{\mu}{k_\mathrm{B}T}. \tag{1.36}$$

Hartee-Fock regime The *Hartree-Fock regime* describes clouds far from degeneracy $\mathcal{D} \ll 1$. Under these conditions, the interactions in and between the condensed and thermal part of the cloud are taken into account. For weakly-interacting gases, the EoS is then given by the ideal gas Eq. (1.4), where we add to the chemical potential a mean field correction $\mu \to \mu - 2\hbar^2 \tilde{g} n/m$ (the minus sign stands for the repulsive interactions):

$$\mathcal{D} = -\ln\left[1 - \exp\left(\frac{\mu}{k_{\mathrm{B}}T}\right)\exp\left(-\frac{\tilde{g}\mathcal{D}}{\pi}\right)\right]. \tag{1.37}$$

Furthermore, the EoS was measured and the results of Prokof'ev & Svistunov were confirmed for quasi-condensates [48, 49]. In practice, we use their data together with the two limiting cases described above to determine a numerical form of the total EoS:

$$\mathcal{D} = \mathcal{D}\left(\frac{\mu}{k_{\mathrm{B}}T}\right), \tag{1.38}$$

which is represented in Fig. 1.4 with the Monte-Carlo results.

1.6 Conclusion

We have introduced the theoretical framework to describe 2D Bose gases with short-range and weak interactions. These interactions are treated with a contact potential and the derivation of the energy functional of the system is achieved in the classical formalism. We have presented some interesting properties of this system, such as the presence of scale invariance and the emergence of quasi-long-range order for deeply degenerate gases. Indeed, the 2D weakly-interacting gas presents a phase transition from a superfluid state at very low temperature to a normal gas at higher temperatures. The intermediate regime, called *fluctuation regime*, shows a reduction of density fluctuations and the emergence of a quasi-condensate together with a superfluid fraction below a critical temperature. We have also described the mechanism behind this superfluid transition, called the Berezinskii-Korterlitz-Thouless transition.

2

Preparation of an ultracold Bose gas in a planar geometry

The experimental platform on which the results presented in this thesis were collected was built almost 10 years ago with the aim of studying the properties of Bose gases in two dimensions with homogeneous density profiles. The construction was already completed before I joined the team. Therefore, in this chapter, I describe the physical system under study in Sec. 2.1 and refer to the section Sec. 2.2 for details about the experimental techniques. A full account of the construction can be found in Refs. [95, 96] and subsequent updates in Refs. [43, 97].

2.1 Overview

As an introduction, we summarize in this section the main features of our system which will be more detailed in the following sections.

Optical cooling and trapping requires lasers with a specific wavelength addressing the electronic transitions of the chosen atomic species. Because of their simple electronic structure, Alkali atoms are popular for ultracold gases experiments. Among them, rubidium 87 (^{87}Rb) is one of the most common to prepare and study Bose-Einstein condensates.

After following a traditional cooling scheme (see Sec. 2.2.2 for more details), 1.5×10^5 cold atoms are trapped in a 2D flat-bottom potential. They lie in a vertical harmonic trap $V(z) = m\omega_z^2 z^2/2$ of angular frequency $\omega_z = 2\pi \cdot 3.6(1)\,\mathrm{kHz}$ created with an optical accordion of wavelength 532 nm (calibration detailed in Sec. 2.2.4). The atoms occupy the lowest energy level and their vertical density profile is a Gaussian of thickness $\ell_z = 181(2)\,\mathrm{nm}$. We ensure that the quasi-2D regime is reached by setting $\hbar\omega_z$ higher than both the thermal energy $k_\mathrm{B}T$ and the interaction energy per particle E_i/N. The 2D trap is closed by an in-plane confinement made of light hard-walls provided by a blue-detuned laser beam of wavelength 532 nm sent to a digital micro-mirrors device (DMD). A more complete description of this 2D box potential, so-called *green box*, is given in Sec. 2.2.3. The DMD is mounted in direct imaging so that the binary pattern on the mirrors is imaged onto the atoms and we are able to imprint grey-levels pattern on the atoms following a simple process detailed in Sec. 2.2.5. The 2D density profile of the sample is then tunable and we can imprint arbitrary continuous profiles or perturbations on our atomic sample. We can also tune the 2D density n from $100\,\mu\mathrm{m}^{-2}$ to $5\,\mu\mathrm{m}^{-2}$: we partially transfer the atoms in a different level and blast them with a resonant light pulse.

The temperature of the cloud is set by the tunable height of the green box light walls from $\sim 150\,\mathrm{nK}$ to $\lesssim 20\,\mathrm{nK}$ and is measured in situ (see Sec. 2.2.7). Therefore, we have access to a large range of PSD $\mathcal{D}$ by simultaneously changing the temperature T and the critical temperature $T_c \propto n$ and we can study the characteristics of the sample across the BKT phase transition.

Three pairs of coils along x, y and z are used to generate magnetic fields of any direction and amplitude up to $\sim$ 10 G. Usually, a vertical magnetic field of a few Gauss (with fluctuations of $\sim$ 1 mG) is applied and defines the quantization axis.

Our experiments are carried out in the two hyperfine levels $f = 1$ and $f = 2$ of the ^{87}Rb electronic ground state $^2S_{1/2}$. They are separated by ~ 6.834 GHz and, in the presence of an external magnetic field, they split into three and five Zeeman sub-levels of angular momentum projection $m_f = -1, 0, 1$ and $m_f = -2, -1, 0, 1, 2$ respectively. The electronic states of interest are fully described in Sec. 2.2.1.

The atomic sample can be prepared in any of the eight Zeeman states or in a superposition of these states thanks to successive microwave (mw) induced one-photon coherent transfers between the two hyperfine levels. The manipulation of the internal state is described in Sec.2.2.6. Among the eight sub-levels, two are magnetic insensitive at first order: $|f = 1, m_f = 0\rangle$ and $|f = 2, m_f = 0\rangle$, which facilitates their use. The so-called clock transition between these two states is used, for example, to perform Ramsey spectroscopy with a resolution of 1 Hz. Otherwise, we work mainly in the hyperfine level $f = 1$ to benefit from its long lifetime $\tau \sim 10$ s compared to the $f = 2$ lifetime $\tau \sim 100$ ms. Therefore, the preferred configuration is to work with atoms in $|f = 1, m_f = 0\rangle$ to combine long lifetime and magnetic field insensitivity. In this case, the 2D interaction parameter is written $\tilde{g}_{11} = \sqrt{8\pi} a_{11}/\ell_z = 0.150(2)$ with $a_{11} = 100.9(1)\, a_0$ the 3D scattering length from [98]. Finally, we image the cloud in situ with absorption imaging with 1 µm resolution, described in Sec. 2.2.8, and record density distributions as shown in Fig. 2.1.

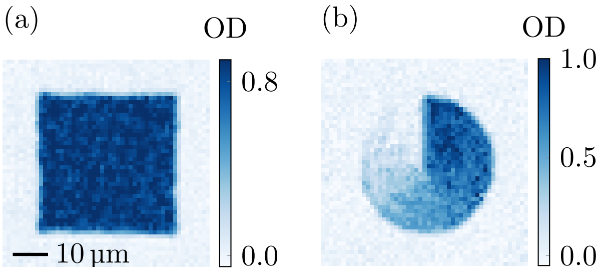

Figure 2.1: Two-dimensional density profiles realised in our experiment. (a) The typical homogeneous profile in a 40 µm × 40 µm square. (b) An example of arbitrary density profile: azimutal density gradient imprinted on the atoms using the grey-level feedback loop. The optical depth (OD) is defined in Sec. 2.2.8.

2.2 Experimental methods and calibrations

2.2.1 ^{87}Rb electronic structure

As an Alkali, ^{87}Rb has only one electron occupying its valence layer, so its electronic spin $s = 1/2$. Its nuclear properties are characterised by a nuclear spin $i = 3/2$. The ^{87}Rb electronic ground state is then $^2S_{1/2}$ and its first excited state separates into two fine levels $^2P_{1/2}$ and $^2P_{3/2}$ [99]. The electronic transitions to these fine levels are labelled D1 ($^2S_{1/2} \rightarrow {}^2P_{1/2}$) and D2 ($^2S_{1/2} \rightarrow {}^2P_{3/2}$) and their wavelengths are $\lambda_1 = 795$ nm and $\lambda_2 = 780$ nm respectively. The excited level $^2P_{3/2}$ is used for cooling schemes and splits into four hyperfine

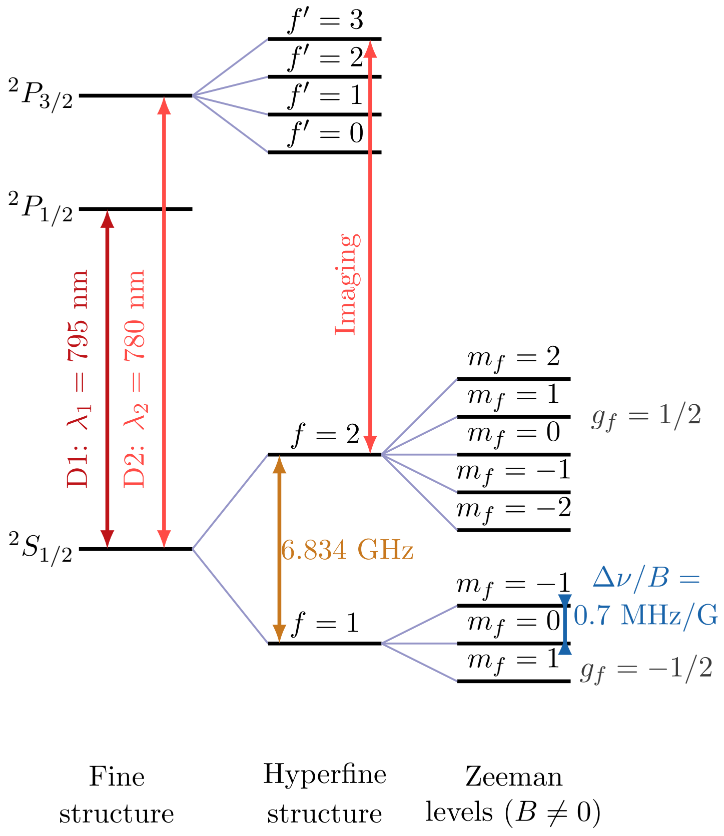

Figure 2.2: Electronic structure of ^{87}Rb atoms. The fine and hyperfine structure and first order Zeeman splitting are detailed for levels of interest only.

levels $f' = 0, 1, 2, 3$. Moreover, all the interesting physics is performed in the $^2S_{1/2}$ two hyperfine levels $f = 1$ and $f = 2$, separated by $E_{\text{hfs}} \sim 6.834\,\text{GHz}$. In the presence of a magnetic field, these hyperfine levels experience Zeeman splitting and separate into three and five sub-levels of angular momentum projections $m_f = -1, 0, 1$ and $m_f = -2, -1, 0, 1, 2$ respectively. These energy shifts with the magnetic field can be determined by the Breit-Rabi formula and read as follows:

$$\Delta E_{f,m_f} = E(f, m_f, B \neq 0) - E(f, 0, 0) = \mu_B g_i m_f B + \frac{E_{\text{hfs}}}{2}\left(\pm\sqrt{1 + \frac{4m_f\xi}{2i+1} + \xi^2} \mp \sqrt{1+\xi^2}\right) \tag{2.1}$$

where the signs are assigned to $f = 2$ and $f = 1$ respectively. E_{hfs} is the hyperfine structure energy splitting, μ_B the Bohr magneton, g_i and g_j the Landé factors of $\boldsymbol{i}$ and $\boldsymbol{j} = \boldsymbol{s} + \boldsymbol{l}$ respectively, and ξ stands for $\xi = \mu_B(g_j - g_i)B/E_{\text{hfs}}$. For low magnetic fields, one gets the linear Zeeman shift $\Delta E_{f,m_f} = g_f m_f \mu_B B$, where $g_f = \pm 1/2$ is the Landé factor associated with hyperfine levels and represented in Fig. 2.2. The ^{87}Rb electronic structure is shown in a summary diagram Fig. 2.2 where only the relevant levels are indicated.

2.2.2 Preparation of a 3D ultracold cloud

Before transferring the atoms into a 2D box, we follow a classical cooling scheme, summarised in Fig. 2.3, to obtain a 3D degenerate cloud.

We start by cooling 5×10^9 atoms to $250\,\mu\text{K}$ in a 3D magneto-optical trap (MOT) loaded in

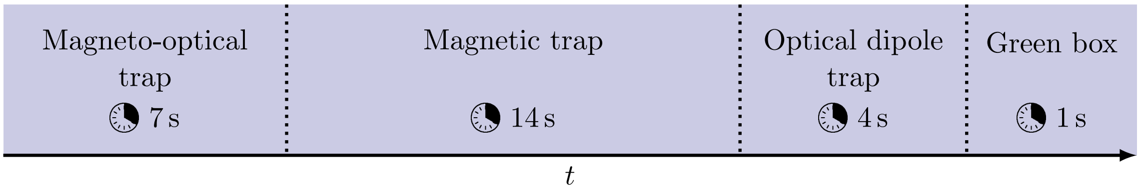

Figure 2.3: Experimental sequence to prepare a 2D homogeneous ultracold atomic sample.

a glass cell under vacuum. We proceed by switching on a magnetic trap. We perform an RF-evaporative cooling and obtain 2.2×10^7 atoms at $\sim 20\,\mu\mathrm{K}$. This step facilitates the transfer of the atoms into an optical dipole trap (ODT) where we perform a second evaporative cooling and obtain a degenerate 3D cloud of 5×10^5 atoms with a temperature of $\sim 80\,\mathrm{nK}$. Passing through this ODT serves mainly to load a large atom number in a cloud of small Thomas-Fermi radius to facilitate the transfer into the green box. The following paragraphs detail the individual cooling steps. Each tool and device presented is remotely controlled by the Cicero Generation computer software which handles all the experimental steps sequentially.

^{87}Rb vapour The experimental sequence starts with an oven heating rubidium rock pieces in a vacuum system with a pressure of 10^{-7} mbar. A commercial 2D magneto-optical trap (MOT) cools down the formed vapour in a glass cell. A D2-line resonant light beam, labelled P in Fig. 2.4.a, pushes only the ^{87}Rb atoms in a glass tube, along the x axis, towards a second glass cell located 30 cm away. All subsequent steps are carried out in the last glass cell.

3D magneto-optical trap We proceed by loading 5×10^9 atoms into a 3D MOT. The quadrupolar magnetic field is provided by anti-Helmholtz coils (MC1 and MC2 in Fig. 2.4.b) in the horizontal plane along the y axis, near the cell. The magnetic gradient is at maximum 22 G/cm. In the mean time, three pairs of counter-propagating light beams light up: one along the horizontal y axis and two in a xz plane with an angle of 60° with respect to the vertical axis (see M1, M2 and M3 in Fig. 2.4). They are all slightly red-detuned from the D2-line to produce a viscous force on the atoms and trap them at the centre of the MOT. The MOT is on during 7 s and cools the atoms to $250\,\mu\mathrm{K}$. After that, the atoms are optically pumped in the hyperfine level $f = 1$.

Magnetic trap We pursue by switching on a quadrupolar magnetic field, with a maximum gradient of 240 G/cm, generated by two water-cooled anti-Helmholtz coils in the vertical direction. This creates a magnetic trap for atoms in $|f = 1, m_f = -1\rangle$ only, so that we load $\sim 1/3$ of the total atom number. We increase the collision rate by compressing the trap and then perform an evaporating cooling using a radio-frequency (RF) ramp of final value 2.5 MHz. The atoms with the largest energy are transferred to the untrapped states and are eventually lost while the remaining atoms thermalise. The RF ramp lasts 12 s and we obtain at the end 2.2×10^7 atoms at $\sim 20\,\mu\mathrm{K}$.

Optical crossed beams trap Near the end of the RF evaporation, an optical trap is loaded. Two beams with an angle of 120° are turned on in the horizontal plane and cross a few micrometres below the magnetic-trap centre. They are red-detuned from the D2-line to a 1064 nm wavelength to attract the atoms in the intensity maxima. Each arm has a power of 3 W, a horizontal waist of $90\,\mu\mathrm{m}$ and a vertical waist of $30\,\mu\mathrm{m}$. The magnetic trap is decompressed by decreasing the magnetic gradient, and the atoms are transferred into this optical dipole trap. A small magnetic gradient is maintained to compensate gravity. Thereafter, we perform an optical evaporation by slowly decreasing the light beam powers for 3 s. We obtain a degenerate 3D cloud of 5×10^5 atoms with a temperature of $\sim 80\,\mathrm{nK}$.

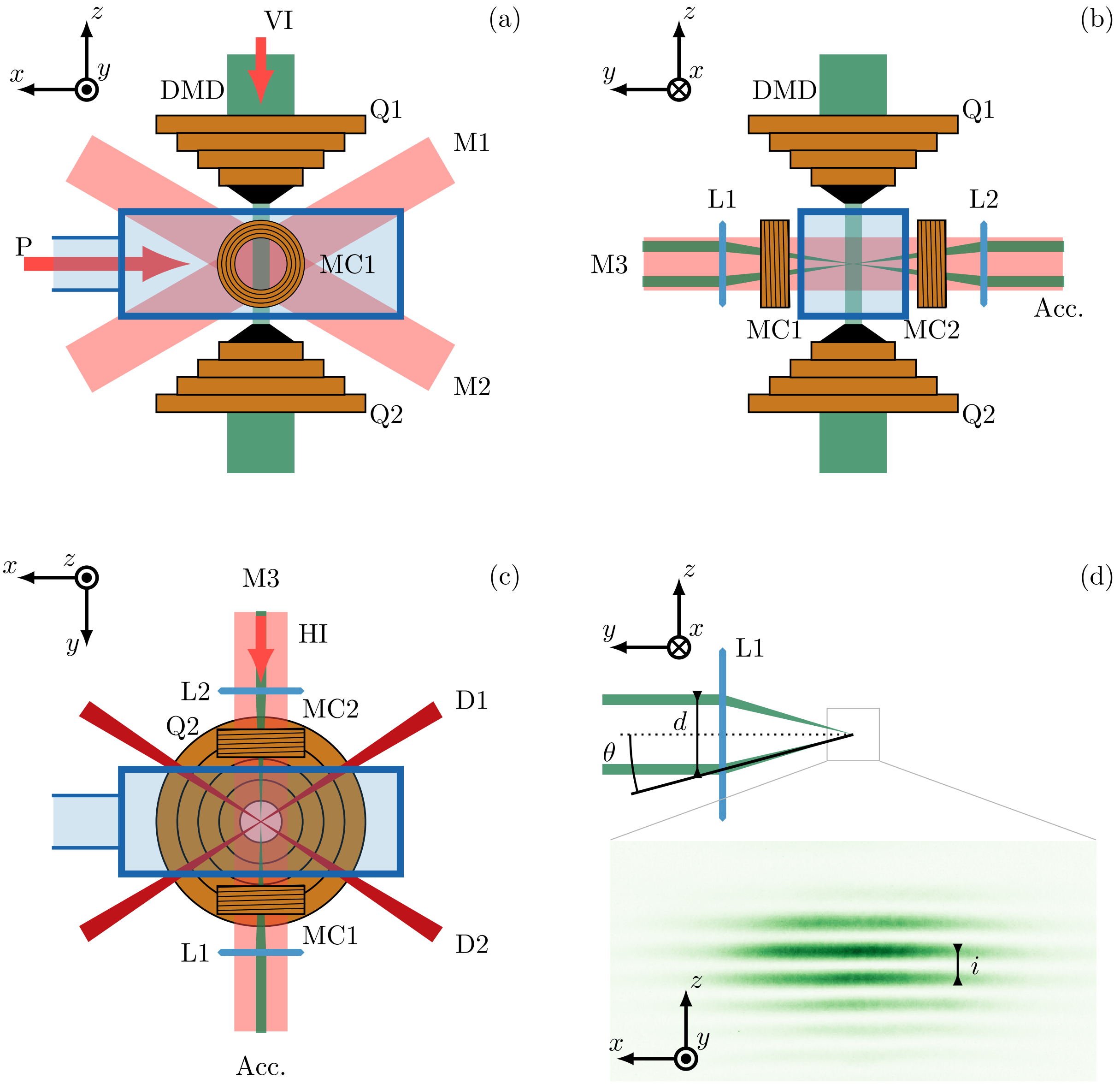

Figure 2.4: Experimental setup from the side view (a), the front view (b) and the top view (c). The ^{87}Rb atoms are pushed to the cell with a light beam (P) resonant with the D2 line. They are loaded in a MOT created by one pair of coils (MC1/2) and three pairs of beams (M1/2/3). The two quadrupole coils (Q1/2) produce the next magnetic trap. We then switch on two dipolar trap beams (D1/2) before ramping up the green box. The in-plane confinement is ensured by a vertical beam reflected by a DMD and an optical microscope. The atoms are vertically trapped in an optical accordion (Acc.) formed by two parallel beams separated by a distance d going through an aspheric lens (L1), interfering on the atoms with an angle θ as shown in (d), and finally passing through a second lens (L2) to image them. The atomic cloud is imaged either on the vertical axis (VI) or on the horizontal axis (HI).

2.2.3 Transfer to a 2D flat-bottom optical box

Following the proposal of [100], the atoms are transferred from the red dipole trap to the central node of a blue-detuned vertical optical lattice [43, 101] of initial fringe spacing $i = 12\,\mu\text{m}$. This lattice, called the accordion, is produced from two beams of wavelength 532 nm interfering on the atoms with a variable angle θ. We vary the fringe spacing by tuning the angle θ thanks to a translation stage setting the distance d between the beams before the lens as shown in Fig. 2.4.d. A feedback loop controls the phase of the interference pattern so that the central node does not move from shot-to-shot.

Meanwhile, we raise light-walls to confine the atoms in the horizontal plane. These are made using a DMD shined with a repulsive light beam of wavelength 532 nm. The DMD (Texas Instrument model DLP7000), mounted in direct imaging, is a 1024 × 768 array of squared mirrors with sides of 13.7 µm. The mirrors can be individually set to two positions: (1) the light is reflected to the atoms, (0) the light is deflected in another direction. When reflected to the atoms, the light passes through a microscope objective of numerical aperture 0.4 and the effective[1] side of the mirrors is of 0.2 µm on the atomic plane. Therefore, we imprint any binary image on the DMD mirrors and the in-plane confinement takes a tunable shape.

To reach the 2D regime, the atomic vertical degree of freedom must be frozen. To this end, we adiabatically reduce the fringe spacing i to $2\,\mu\text{m}$. Because the light is blue-detuned, it repels the atoms and compresses the 3D cloud into a planar Bose gas. Finally, we produce a quasi-2D uniform Bose gas.

2.2.4 Measurement of the cloud vertical thickness

As we introduced earlier in Sec. 1.2.3, the atoms are trapped in a single node of a vertical blue-detuned optical lattice approximated by a harmonic potential $V(z) = \frac{1}{2}m\omega_z^2 z^2$ of frequency $\omega_z/2\pi$. They occupy the lowest energy level, thus their profile is Gaussian in the vertical direction z and its vertical thickness writes $\ell_z = \sqrt{\hbar/m\omega_z}$. The precise knowledge of the angular frequency ω_z allows us to estimate the dimensionless 2D interaction parameter ($\tilde{g} \propto a/\ell_z$) and to verify that the quasi-2D regime is reached. Indeed, $\hbar\omega_z$ must be higher than both the thermal energy $k_\text{B}T$ and the interaction energy per particle E_i/N.We perform parametric heating to characterize the frequency trap $\omega_z/2\pi$. After evaporation in the green box potential and thermalisation of the cloud, we modulate the accordion beams power around their mean value. We fix the amplitude of the modulation to be low and vary its frequency $\omega_\text{m}/2\pi$. We observe the maximal atom loss for a power modulation frequency twice larger than the trap frequency $\omega_\text{m} = 2\omega_z$ as shown in Fig. 2.5.

In our typical configuration, we work with an accordion frequency of $\omega_z/2\pi = 3.6(1)$ kHz which corresponds to a vertical thickness $\ell_z = 180(2)$ nm and the atoms are in the hyperfine level $f = 1$ in which they experience long lifetimes. Therefore, using the 3D scattering length $a_{11} = 100.9(1)\ a_0$ from [98], we get a weakly interacting 2D Bose gas of interaction parameter $\tilde{g}_{11} = \sqrt{8\pi}a_{11}/\ell_z = 0.149$. Our typical uncertainty on the interaction parameter is $\Delta\tilde{g} = 0.002$.

2.2.5 Shaping the density profile

The atoms are confined in the horizontal plane in between light hard-walls produced with a DMD. We use a similar DMD, shined with a light beam of wavelength 532 nm, to imprint

---

[1] The light passes through a telescope composed of a lens and the microscope objective so the pattern on the DMD is imaged onto the atoms with a magnification of $\sim 1/70$.

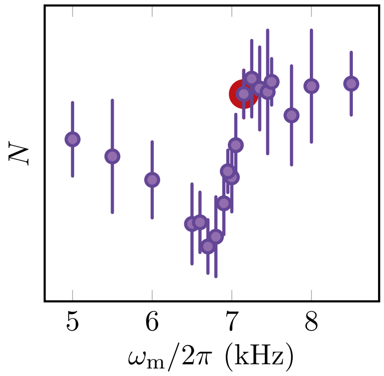

Figure 2.5: Atom losses induced by the parametric heating. We modulate the power of the accordion beams with an amplitude of modulation of a few percent of their final value with a frequency $\omega_\mathrm{m}/2\pi$ during 400 ms and measure the atom number N remaining in the trap. We observe an asymmetric signal due to the anharmonicity of the vertical trapping potential. Indeed, atoms with higher kinetic energy need less energy to be ejected of the trap and can fall off even for $\omega_\mathrm{m} \lesssim 2\omega_z$. Therefore, we determine the accordion frequency by taking the frequency on the hard-side right edge, shown with the red disk background: $\omega_\mathrm{m} = 2\pi \cdot 7.2\,\mathrm{kHz}$.

additional potentials on the cloud without changing the height of the green box potential. Furthermore, as the effective mirrors size onto the atoms (0.2 µm) is smaller than the optical resolution ($\sim$ 1 µm), we generate optical potentials of controllable intensity. Indeed, we discretise the DMD surface in *macro-cells* of several adjacent mirrors and set the effective size of these macro-cells smaller than the optical resolution. The density of pixels (0) and (1) on a given macro-cell is averaged to grey levels of light intensity over the sample. Therefore, we convert any continuous profile into a binary image with a dithering algorithm following the *error diffusion method* [102] and imprint it on the atoms.

Work performed during my thesis and not detailed in this manuscript

We recently developed a feedback loop to control the imprinting of these grey level patterns accurately [51,97]. We work in the Thomas-Fermi regime, where the chemical potential reads $\mu = gn$ (see Eq. (1.36)). In a sample of global chemical potential μ_0, we apply an optical potential $V(x,y)$ of spatial scale much larger than the healing length ξ. This perturbation locally modifies the chemical potential to $\mu(x,y)$. We can then apply the local density approximation (LDA) and the density profile reads:

$$n(x,y) = \frac{1}{g}\left(\mu_0 - V(x,y)\right). \tag{2.2}$$

Thus, the figure of merit of the feedback loop is computed from the density profile.

An initial binary profile `binary_0`, which can be either a blank image or an initial guess based on the target density profile `target`, is defined to be projected onto the atoms. The initial density profile `density_0` is then measured. The feedback loop (shown in Fig. 2.6) starts with the computation of the local error `error_0 = density_0 - target` which we filter with a Gaussian to remove high frequency noise. This error is converted into a binary image via the error diffusion algorithm and reshaped to the DMD dimensions in an array called `binary_error_0`. The next binary image (here `binary_1`) to be printed on the atoms is then calculated

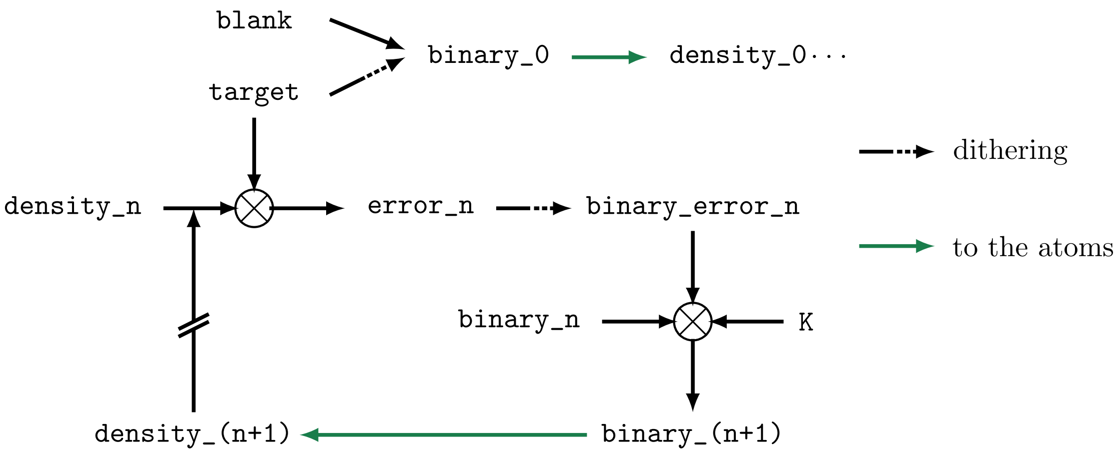

Figure 2.6: Diagram of the grey levels iterative loop. The first row represents the initialisation while the second row describes a loop. Dithering time steps are represented with half-dashed arrows and green arrows mean imprinting the image on the atoms via the DMD.

with the recursive step: `binary_(n+1) = binary_n + K*binary_error_n`, where `K` is a spacial-dependent gain taking into account the Gaussian envelope of the beam intensity and whose amplitude is adjusted by hand. One projects back `binary_(n+1)` onto the atoms, measures `density_(n+1)` and computes `error_(n+1)`. If the target accuracy is not reached one goes on and computes `binary_error_(n+1)` and `binary_(n+2)` etc...

Usually, we set the number of averaged images to 10 to measure the density profiles `density_n` to get rid of the optical shot noise and we observe that the global error decreases for the first 10-15 steps of the loop.

2.2.6 Manipulation of the internal state

We perform the interesting physics in the eight Zeeman sub-levels of the two hyperfine levels $f = 1$ and $f = 2$ of the ^{87}Rb electronic ground state. We mostly work in the $f = 1$ level, composed of three Zeeman sub-levels of angular momentum $m_f = -1, 0, 1$ in order to take advantage of its long lifetime $\tau \sim 10$ s. Usually, we choose to work in the magnetic-insensitive state $|f = 1, m_f = 0\rangle$. However, the cloud is prepared in the state $|f = 1, m = -1\rangle$ and we must therefore coherently transfer the atoms within the hyperfine level $f = 1$. Furthermore, the ability to manipulate the internal state allows us to create superpositions of states and to study mixtures [52, 73, 97].

Coherent coupling A coherent field induces Rabi oscillations between two states $|1\rangle$ and $|2\rangle$ separated in energy when close to the resonance of the transition $|1\rangle \leftrightarrow |2\rangle$. Shining a coherent field of frequency ν detuned from the resonance frequency ν_0 by $\delta = 2\pi(\nu - \nu_0)$ for a time t transfers the atoms initially in the state $|1\rangle$ into a superposition of states: $c_1|1\rangle + c_2|2\rangle$. The populations $p_1 = |c_1|^2$ and $p_2 = |c_2|^2$ of the states $|1\rangle$ and $|2\rangle$ read:

$$p_2 = \frac{\Omega_0^2}{\Omega_0^2 + \delta^2} \sin^2\left(\sqrt{\Omega_0^2 + \delta^2}\,\frac{t}{2}\right), \qquad p_1 = 1 - p_2, \tag{2.3}$$

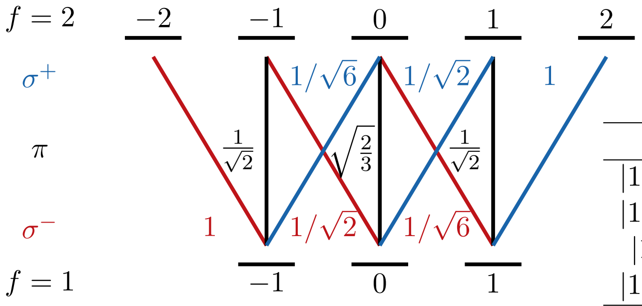

Figure 2.7: Clebsch-Gordan coefficients for the magnetic dipole transitions of polarization σ^+ ($\Delta m_f = +1$), π ($\Delta m_f = 0$) and σ^- ($\Delta m_f = -1$).

Transition	Ω_0 [kHz]	mw chain
$\lvert 1,-1\rangle \rightarrow \lvert 2,0\rangle$	9.5	RS1
$\lvert 1,0\rangle \rightarrow \lvert 2,-1\rangle$	8	RS2
$\lvert 1,0\rangle \rightarrow \lvert 2,0\rangle$	38.5	RS2
$\lvert 1,0\rangle \rightarrow \lvert 2,+1\rangle$	16.5	RS1

Table 2.1: Microwave coupling strengths for the most commonly used transitions associated to its mw chain in the presence of a vertical magnetic field.

where Ω_0 is the frequency describing the coupling strength between the two states and induced by the microwave pulse. At resonance ($\delta = 0$), a full transfer is achieved after a so-called π-pulse when $t = \pi/\Omega_0$.

Microwave transfers The two hyperfine levels of the electronic ground state of the ^{87}Rb, $f = 1$ and $f = 2$, are separated by ~ 6.834 GHz. Therefore, a microwave (mw) of appropriate frequency provides a one-photon coherent transfer from a state in one hyperfine level to a state in the other hyperfine level while respecting $\Delta m_f = 0, \pm 1$. Furthermore, when external magnetic fields of 0 to 10 G are applied, the Zeeman sub-levels of the same hyperfine level separate by a few MHz and a one-photon RF transition can be used to transfer the atoms. However, RF transitions are less convenient[2] so transfers between two states of the same hyperfine level are performed by doing successive mw pulses. These mw have wavelengths of a few centimetres, which means that the whole cloud is reached homogeneously, and they do not induce momentum transfer.

Two mw antennas are installed on the experimental setup, close to the glass cell. The first one is placed in the horizontal plane on the x axis. The second one is a one-loop antenna of diameter ~ 1 cm located in the horizontal plane on a diagonal axis. They are connected to different mw chains which have been modified during my thesis and are now composed of a synthesizer (both Rohde and Schwarz SMB100AV) followed by an amplification system. We place a mw switch (PMC SW1AD-15) before each amplification system to control the mw pulses duration and a circulator (Aerotek H13-1FFF) after the amplification systems to protect it from reflections on the antenna. The signal of the first mw chain (labelled RS1) is amplified by a pre-amplifier (Mini-Circuit ZJL-7G+) and a 10 W amplifier (Khune KU PA 700) before radiating to the atoms. The second chain (RS2) benefits of a greater amplification thanks to a water-cooled 50 W amplifier (RF Lambda RFLUPA05G08GA). The amplitudes of the respective fields are ~ 10 mG and ~ 30 mG and their tomography is detailed in appendix A. Both mw chains are remotely controlled by GPIB connections and their frequencies are stabilised by a common 10 MHz reference oscillator.

---

[2] The RF antenna present on our setup provides lower coupling strengths (< 5 kHz) than mw. Furthermore, to recover a two-level atom picture one has to generate external magnetic fields large enough so that the Zeeman second-order effect is no longer negligible. Originally, adiabatic transfers were performed [96] but proved to be less stable and practical than mw pulses.

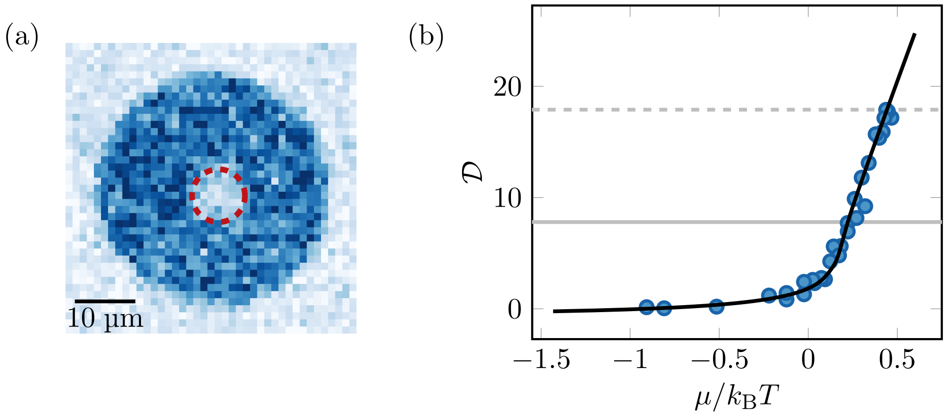

Figure 2.8: Temperature calibration using the equation of state. (a) Example of CCD image we use for thermometry. A flat potential is additionally imprinted at the centre of the cloud and its height is varied. We measure the density n in the depleted area, circled in red, as a function of this height V and the density n_0 of the non-perturbed part, outside the circle. (b) We rescale both n and V (blue points) to match a numerical form of the equation of state (solid black line) and find in this example $T = 83.5\,\mathrm{nK}$. The bulk density $n_0 = 43\,\mu\mathrm{m}^{-2}$ gives the bulk PSD (dashed grey line) $\mathcal{D} = 17.9$ while the critical PSD (solid grey line) is $\mathcal{D}_\mathrm{c} = 7.8$.

Coupling strengths and stability In the usual configuration, a vertical magnetic field is applied to the atoms. On the other hand, the experiment is surrounded by fluctuating magnetic fields mostly due to the Parisian metro. These fluctuations must be corrected to ensure the stability of magnetic-field sensitive transitions and therefore we use a compensation loop. The magnetic field of the external environment is measured in a separate room. This magnetic field is then converted into a current that is sent through a coil generating a compensation magnetic field. Finally, we obtain a peak-to-peak variation of ~ 1 mG of the vertical magnetic field on the atoms which corresponds to fluctuations of magnetic-sensitive transition frequencies $\lesssim 1\,\mathrm{kHz}$ at first-order.
The mw coupling strengths provided by both mw chains are large enough ($\gtrsim 5\,\mathrm{kHz}$) to prevent atom number fluctuations and are written in Tab. 1.1 for the usual transitions, the others can be easily found using the Clebsch-Gordan coefficients in Fig. 2.7.

Microwave spectroscopy These mw induced transfers represent a powerful spectroscopic tool. In particular, we perform Ramsey spectroscopy with a resolution of 1 Hz on the magnetic-field insensitive transition $|f = 1, m_f = 0\rangle \leftrightarrow |f = 2, m_f = 0\rangle$. The large coupling strength provided by the RS2 mw chain also allowed us to carry out single-photon mw photoassociation to create weakly-bound ^{87}Rb dimers in their electronic ground state, which will be the subject of Part II.

2.2.7 Temperature and PSD of the sample

The temperature of the cloud is set by the height of the light hard-walls of the in-plane confinement in the green box. We therefore perform optical evaporative cooling to tune the temperature from $\sim 150\,\mathrm{nK}$ to $\lesssim 20\,\mathrm{nK}$. A wide range of PSD $\mathcal{D}$ is also available by simultaneously changing the temperature T and the critical temperature $T_\mathrm{c} \propto n$.
We measure the temperature of the sample from in-situ images using a numerical form of the

2D Bose gas equation of state described in Sec. 1.5:

$$\mathcal{D} = \mathcal{D}\left(\frac{\mu}{k_{\mathrm{B}}T}\right). \tag{2.4}$$

Following the method of [103], we imprint on the sample a flat disk-shaped repulsive potential of height V and small diameter compared to the size of the cloud (see Sec. 2.2.5). In the local density approximation, the local depletion of the cloud $\propto V$ is adjusted by varying the light power on the dedicated DMD and does not affect the height of the in-plane confinement potential. We vary V and measure the density n in the depleted region. We fit the parameters (μ, T) to rescale the data and match the equation of state Eq. (2.4) and an example is shown in Fig. 2.8. Measuring the density n_0 in the unperturbed region gives the critical temperature T_{c} and we access the PSD $\mathcal{D} = \mathcal{D}_{\mathrm{c}}T_{\mathrm{c}}/T$.

2.2.8 Imaging system

Absorption imaging We perform absorption imaging by sending a light pulse of intensity I and wavelength λ onto the sample, addressing the closed transition $f = 2 \to f' = 3$ shown in Fig. 2.2. Atoms initially in a $|f = 2\rangle$ state scatter light in all directions, while the cameras collect the photons in the forward direction only. Thus, the region occupied by the atoms leaves a shadow on the image. We work in the low saturation regime: the pulse intensity I is lower than the saturation intensity $I_{\mathrm{sat}} = \hbar\omega_L^3\Gamma/12\pi c^2$ (we fix $I/I_{\mathrm{sat}} < 0.2$), with $\omega_L/2\pi$ the laser frequency, Γ the linewidth of the transition and c the speed of light in vacuum.

Imaging axes and resolution We image the atoms on three axes and two of them are in the horizontal plane. The former is mainly used to image the side of the 2D cloud or clouds in time of flight (ToF) while the latter is used as a control camera and does not operate for the science presented in this thesis. In practice, most images are taken along the vertical axis with a low noise CCD camera (Princeton Instruments, Pixis 1024 BR Excelon) with a magnification of 11 and a pixel size of 1.15 µm on the atoms. The light beam passes through the microscope of numerical aperture 0.4 so that our optical resolution is $\sim 1\,\mu$m.

Two-dimensional density profile The vertical imaging provides in-situ images of the 2D density profile $n(x, y) = \int n_{3\mathrm{D}}(x, y, z)\,\mathrm{d}z$ from the 3D atomic density $n_{3\mathrm{D}}$. Theoretically, in the low saturation regime, the light intensity collected on cameras in the presence of atoms $I_{\mathrm{c,a}}$ follows a Beer-Lambert law:

$$I_{\mathrm{c,a}} = I \exp\left(-\int \sigma_{\mathrm{light}} n_{3\mathrm{D}}(x, y, z)\,\mathrm{d}z\right) + I_{\mathrm{bgd}}. \tag{2.5}$$

This equation contains σ_{light} the light-scattering cross section and I_{bgd} a residual background intensity. In a two-level model, the light-scattering cross-section is given by $\sigma_{\mathrm{light}} = \sigma_0 = 3\lambda^2/2\pi$. However in the case of ^{87}Rb, one must take into account the complex structure of the addressed transition. This is done simply pondering the light-scattering cross section by the average of the Clebsh-Gordan coefficient for π-transitions $\epsilon = 7/15$: $\sigma_{\mathrm{light}} = \epsilon\sigma_0$. In the absence of atoms, the collected intensity writes:

$$I_{\mathrm{c},0} = I + I_{\mathrm{bgd}}. \tag{2.6}$$

One defines the optical depth OD as:

$$\mathrm{OD} = \int \sigma_{\mathrm{light}} n_{3\mathrm{D}}(x, y, z)\,\mathrm{d}z = -\log\left(\frac{I_{\mathrm{c,a}} - I_{\mathrm{bgd}}}{I_{\mathrm{c},0} - I_{\mathrm{bgd}}}\right). \tag{2.7}$$

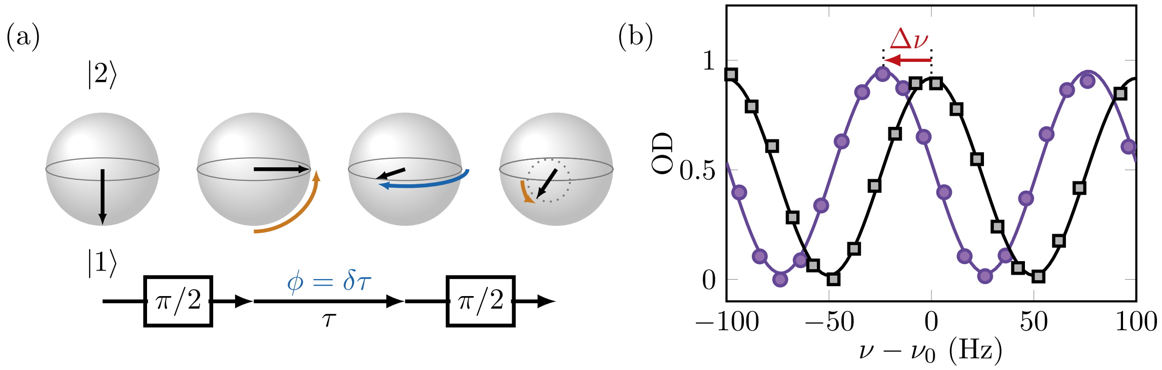

Figure 2.9: Ramsey spectroscopy. (a) Sequence diagram in the Bloch sphere representation. (b) Ramsey oscillations of the population in $|2\rangle$ centred on ν_0 for a non-interacting atomic cloud (black squares) and shifted by $\Delta\nu$ for our weakly interacting gas (violet circles). Figure reproduced from [73].

Therefore, by taking two images: one with and one without atoms, we access the density $n(x,y)$:

$$n(x,y)=\int n_{3\mathrm{D}}(x,y,z)\,\mathrm{d}z=\frac{1}{\sigma_{\text{light}}}\mathrm{OD}. \tag{2.8}$$

This Beer-Lambert law is a single-atom model and cannot apply for dense clouds. Indeed, when the condition $n\lambda_{\text{th}}^2 \ll 1$ is not fulfilled, the light pulse can excite collective modes and the OD is not linear with the density n anymore. Therefore, we work in the linear regime, imposing $\mathrm{OD} \lesssim 1.5$. Moreover, in practice, the experimental environment affects the imaging and the last relation must be multiplied by a correction factor. The calibration of this correction factor is performed with a Ramsey spectroscopy described in Sec. 2.2.9.

Most of the experiments are conducted in $f = 1$ although this hyperfine level is not resonant with the imaging beam. Therefore, we perform a partial coherent transfer to $f = 2$ (detailed in Sec. 2.2.6) just before the imaging process.

2.2.9 Calibration of the density with Ramsey spectroscopy

The 2D density of the sample is a tunable quantity that we measure via in-situ absorption imaging described in Sec. 2.2.8. In practice, this imaging process is affected by the experimental environment, such as surrounding magnetic fields, which modifies the simple relation Eq. (2.8). A correction factor is embedded in the light cross-scattering section σ_{light} which we calibrate with Ramsey spectroscopy on the hyperfine clock-transition $|f=1,m_f=0\rangle \rightarrow |f=2,m_f=0\rangle$ labelled here $|1\rangle \rightarrow |2\rangle$.

Indeed, the atoms experience in the two states involved, $|1\rangle$ and $|2\rangle$, repulsive interactions characterised by dimensionless parameters $\tilde{g}_{11}$ and $\tilde{g}_{22}$ and inter-species repulsive interactions of associated strength $\tilde{g}_{12}$. As demonstrated in the supplemental material of [55], the presence of interactions results in an additional phase shift $\Delta\nu$ in the Ramsey signal.

In a zero-temperature picture, this mean-field shift $\Delta\nu$ is given by the difference of chemical potential $h\Delta\nu=\mu_2-\mu_1$ where the chemical potentials (μ_1,μ_2) read:

$$\mu_1=\frac{\hbar^2}{m}\frac{n}{2}\left(\tilde{g}_{11}+\tilde{g}_{12}\right), \tag{2.9}$$

$$\mu_2=\frac{\hbar^2}{m}\frac{n}{2}\left(\tilde{g}_{22}+\tilde{g}_{12}\right), \tag{2.10}$$

where n is the initial density[3]. The mean-field shift is therefore written:

$$\Delta\nu = \frac{\hbar}{4\pi m}\Delta\tilde{g}\,n, \qquad \Delta\tilde{g} = \tilde{g}_{22} - \tilde{g}_{11}. \tag{2.11}$$

The Ramsey spectroscopy consists of two mw pulses separated by a duration $\tau = 10$ ms addressing the hyperfine transition with a Bohr frequency $\simeq \nu_0$ and a coupling strength Ω. The duration t of both pulses is set to $t = 2\Omega/\pi \simeq 25\,\mu\text{s}$ so that an atom initially in $|1\rangle$ experiences a $\frac{\pi}{2}$-pulse. We scan the coherent field frequency ν and measure the population in $|2\rangle$ right after the second pulse. The sequence of mw pulses is displayed in Bloch representation in figure Fig. 2.9.a.

We first look at a sample of non-interacting atoms: we perform a Ramsey sequence after a time-of-flight long enough (2 ms) to suppress the interactions. The atoms, initially in the state $|1\rangle$, find themselves in a superposition of state $(c_1|1\rangle + c_2|2\rangle)^{\otimes N}$ after the first mw induced $\frac{\pi}{2}$-pulse. During the free-evolution, the two populations get dephased with a total rate $\delta = 2\pi(\nu - \nu_0)$ so that, after the second pulse, the population in $|2\rangle$ oscillates with δ and is maximal for $\delta = 0$. From this measurement, we determined ν_0.

Afterwards, we perform a similar Ramsey sequence on the atoms trapped in the green box, in order to measure the shift of resonance $\Delta\nu$ induced by the interactions. Both measurements are presented in Fig. 2.9.b.

The density n is then determined from Eq. (2.11) and compared to the optical depth of the same initial sample to calibrate σ_{light} with Eq. (2.8).

The high precision of this calibration relies on the high-resolution of the spectroscopy (1 Hz) and on the precise knowledge of $\tilde{g} \propto a/\ell_z$. Indeed, the vertical thickness of the cloud is measured with a precision of a few nanometres. On the other hand, the a_{ij} are obviously independent of the fluctuations of the experimental parameters and relatively well known [98]. We estimate that their values are known with an accuracy $< 1\,a_0$.

2.3 Conclusion

In this chapter, we presented the atomic system and the different techniques we use to control it. Following a standard cooling scheme we obtain a 3D degenerate cloud that we transfer afterwards into a 2D optical trap. We shape the density profile of the atoms at will using DMDs and grey-levels intensity. We also manipulate their internal state using mw. Our mw system is a powerful spectroscopic tool and we use Ramsey spectroscopy with a resolution of 1 Hz to calibrate the cloud density, which we vary from $100\,\mu\text{m}^{-2}$ to $5\,\mu\text{m}^{-2}$. The temperature of the atoms can be adjusted from $\sim 150\,\text{nK}$ to $\sim 20\,\text{nK}$. Therefore, we control the phase space density over a wide range and study the properties of the atoms across the BKT phase transition.

---

[3] The equations Eq. (2.9) and Eq. (2.10) actually depend on the densities n_1 and n_2 in $|1\rangle$ and $|2\rangle$ after we perform a first mw pulse on the transition $|1\rangle \rightarrow |2\rangle$. However we perform this calibration imposing $n_1 = n_2 = n/2$ by using $\pi/2$-pulses.

Part II

Microwave photoassociation of pairs of ^{87}Rb atoms and measurement of atom-dimer interactions

3

^{87}Rb least-bound dimers

Interactions between particles in cold atom physics were briefly introduced in Chapter 1. In particular, we discussed their importance in 2D cold systems, in which they allow for the rising of a quasi-long-range order.

In this chapter, we describe the interaction potential and its eigenstates in the context of ultracold collisions. In particular, we will discuss the importance of bound states - describing dimers - for the characterisation of interaction potentials and the control of interactions in cold atomic samples. In a second part, we describe the spectroscopy by microwave-induced photoassociation that we performed on the least-bound dimer of ^{87}Rb during my thesis.

3.1 Binary interactions and dimers

This section is dedicated to the description of interactions in a dilute ultracold gas of neutral atoms, where the three-body interactions are then negligible. We consider binary interactions only and neglect magnetic dipole-dipole interactions. The interaction potential describes first the scattering properties of two atoms. In the low-energy regime, the relevant scattering process occurs in the s-wave, which is characterized by a single parameter: the scattering length a. As mentioned in Chapter 1, this length defines, in this regime, the strength of the interactions. Furthermore, there exist bound states of the interaction potential, which describe dimers and are the focus of this chapter and the next one. Here, we emphasis the importance of such bound states to characterise the interaction potential and introduce the universal relation linking the energy of the least-bound states to the scattering length a. Finally, we discuss some scattering resonances, in particular the ones known as Feshbach resonances, as examples of experimental use of weakly bound dimers.

3.1.1 The interaction potential

We consider the interaction potential between two identical atoms in their electronic ground state. Working with ultracold gases considerably simplifies the study of collisions under the action of this potential. For temperatures $\lesssim 1\,\mu\text{K}$, the thermal wavelength λ_{th} ($\gtrsim 100\,\text{nm}$) of the atoms is large compared to the typical size of a dimer ($\lesssim 1\,\text{nm}$). The ultracold atoms are delocalised and this leads to a *smoothing* of the interaction potential, i.e. the latter is not distinguished in detail as its range and spatial variation scale are much lower than λ_{th}. In these conditions, we will show that the interaction potential is described by only a few numbers, as already outlined in Sec. 1.2.1. We first focus in the long-distance behaviour of the interaction potential, which will be shown to be the important part to describe the least-bound dimers, and then describe the short-distance potential, also called here *core potential*.

Long-distance behaviour: van der Waals interactions We consider two atoms whose centres of mass are separated by a distance r. We focus here on the large-distance regime, where r is larger than the typical size of the electronic clouds of the atoms (a few angströms) so that they do not overlap. In this configuration, there is no position in space for which the electronic wave functions of the two atoms are both non-zero and non-negligible. Therefore, there is no possible exchange of electrons between the atoms. We write then the interaction potential as the electromagnetic interaction between the two separated atoms A and B, treated with a multipolar expansion. The first and dominant term is the dipole-dipole interaction

$$U_{\text{dip}} = \frac{1}{4\pi\varepsilon_0 r^3}\left[\boldsymbol{d}_A \cdot \boldsymbol{d}_B - 3(\boldsymbol{u}\cdot\boldsymbol{d}_A)(\boldsymbol{u}\cdot\boldsymbol{d}_B)\right], \tag{3.1}$$

where ε_0 is the vacuum permittivity, $\boldsymbol{u}$ the unitary vector connecting the atoms and $\boldsymbol{d}_A$ (resp. $\boldsymbol{d}_B$) is the dipole operator associated with the atom A (resp. B). The dipole operator $\boldsymbol{d}_X$ reads

$$\boldsymbol{d}_X = \sum_j q(\boldsymbol{r}_j - \boldsymbol{r}_X) \tag{3.2}$$

where we sum the contributions of all the electrons j, at position $\boldsymbol{r}_j$ and with elementary charge q, of an atom $X = \{A, B\}$ whose centre of mass is at $\boldsymbol{r}_X$.

Let us consider the Hamiltonian $\hat{H}_0$ of the isolated atoms A and B individually. We note its eigenstates $|\psi_n\rangle$ and the corresponding energies E_n, with $E_0 < E_{n>0}$. We study the potential U_{dip} as a perturbation of $\hat{H}_0$. At first order, because the mean electric dipole for an isolated atom in its ground state is always zero, there is no displacement of E_0 and everything happens like the two atoms do not "see" each other. At second order, the displacement in energy $\Delta E_0^{(2)}$ writes:

$$\Delta E_0^{(2)} = -\sum_n \frac{|\langle\psi_0|\, U_{\text{dip}}|\psi_n\rangle|^2}{E_n - E_0}. \tag{3.3}$$

This second order displacement is the only dominant term and, because it is negative, lowers the ground state energy E_0. The energy $\propto U_{\text{dip}}^2$ varies then as $1/r^6$ and is written

$$V(r) = -\frac{C_6}{r^6}. \tag{3.4}$$

This formulation was proposed in 1930 by London [104] and describes the so-called Van der Waals interactions. The positive coefficient C_6 depends on the atomic species considered and can be numerically calculated through the computation of the wave functions of the atomic states and the estimation of the matrix element of the dipole operator. Mitroy et al. [62] estimated this coefficient for most of the alkali-metals, together with the coefficients C_8 and C_{10} corresponding to the contributions of the next terms in the multipolar expansion of the electromagnetic interaction, which write $-C_{2n}/r^{2n}$.

The van der Waals interactions are associated with a characteristic range, R_{vdW}, over which they have a non-negligible effect. For a given wave packet, the potential energy is significantly larger than the kinetic energy induced by the localisation for distances $r \lesssim R_{\text{vdW}}$ where

$$R_{\text{vdW}} = \frac{1}{2}\left(\frac{2m_{\text{r}}C_6}{\hbar^2}\right)^{1/4}, \tag{3.5}$$

with m_{r} the reduced mass ($m_{\text{r}} = m/2$ for homonuclear atoms). This characteristic range is associated with an energy scale $E_{\text{vdW}} = \hbar^2/(2m_{\text{r}}R_{\text{vdW}}^2)$.

Core potential When the distance between the atoms becomes shorter, their electronic clouds overlap. We first discuss the form of the expected potential $V(r)$ phenomenologically. At long distances, which we already discussed, the potential is expected to be attractive $V'(r) < 0$ and must tend to zero for $r \to +\infty$. At smaller distances, the potential decreases to a minimum value at a distance r_{min}. Beyond this value, the electronic clouds repel each other and the potential increases, becomes repulsive $V'(r) > 0$ and tends to a large value while $r \to 0$.
The determination of this potential was first achieved with the simplest atom: hydrogen (H). Indeed, considering two H atoms, it becomes a four-body problem with one proton and one electron per atom. As we will discuss later, the problem is easily reduced to a two-body problem under simple assumptions.
We give an outline of the resolution for H atoms. As we now look at the internal degrees of freedom of the atoms, we define here the quantities that will be useful to us. We consider the interactions between two neutral atoms of hydrogen in their electronic ground state. The problem involves then two protons, labelled A and B, at positions $\boldsymbol{r}_A$ and $\boldsymbol{r}_B$ and two electrons, labelled 1 and 2, at positions $\boldsymbol{r}_1$ and $\boldsymbol{r}_2$. As we treat alkali atoms in their electronic ground states, the orbital angular momentum of their electron is zero $\ell_1 = \ell_2 = 0$ and so is the orbital angular momentum of the electronic pair $L = 0$. The electronic spins of the electrons 1 and 2 are written respectively $\hat{\boldsymbol{s}}_1$ and $\hat{\boldsymbol{s}}_2$, and we define the total electronic spin of the atomic pair as $\hat{\boldsymbol{S}} = \hat{\boldsymbol{s}}_1 + \hat{\boldsymbol{s}}_2$. Similar definitions apply to the nuclear spins of the nuclei A and B, $\hat{\boldsymbol{i}}_A$ and $\hat{\boldsymbol{i}}_B$ and the total nuclear spin $\hat{\boldsymbol{I}} = \hat{\boldsymbol{i}}_A + \hat{\boldsymbol{i}}_B$.

The so-called *Born-Oppenheimer approximation*, which relies on the large difference between the proton mass m_{p} and the electron mass $m_{\text{e}} \sim m_{\text{p}}/1800$, enables the reduction of this four-body problem to a two-body problem. Indeed, electrons being much lighter, they evolve in shorter characteristic times than protons. The electronic observables adjust almost instantaneously to the slower evolution of the nucleus. Therefore, we first assume that the nuclei are fixed and look for the eigenstates of the electrons in the Coulombian field created by the nuclei. Once we know their energy, we use it as an effective potential energy $V(|\boldsymbol{r}_A - \boldsymbol{r}_B|)$ for the nucleus Hamiltonian written as

$$\hat{H} = \frac{\hat{p}_A^2}{2m_{\text{p}}} + \frac{\hat{p}_B^2}{2m_{\text{p}}} + \hat{V}(|\boldsymbol{r}_A - \boldsymbol{r}_B|), \tag{3.6}$$

where the two first terms are the kinetic energies of the nuclei A and B of momentum $\hat{\boldsymbol{p}}_A$ and $\hat{\boldsymbol{p}}_B$.

After having decomposed the problem in an electronic and nuclear part, one must study the electronic Hamiltonian

$$\hat{H}_{\text{e}} = \frac{\hat{p}_1^2}{2m_{\text{e}}} + \frac{\hat{p}_2^2}{2m_{\text{e}}} + \hat{V}_{\text{C}} + 2E_{\text{i}}. \tag{3.7}$$

The first two terms are the kinetic energies of the electrons 1 and 2 of momentum $\hat{\boldsymbol{p}}_1$ and $\hat{\boldsymbol{p}}_2$ while $\hat{V}_{\text{C}}$ is the Coulombian potential. The last term is a constant with $E_{\text{i}} = 13.6\,\text{eV}$ being the H ionisation energy, here to set the zero in energy when the atoms are at an infinite distance, in their ground state. A good approximation for the electronic energy levels is obtained following the Heitler-London method [105] which relies on the following variational argument: as the distance between the nuclei $r_{AB} = |\boldsymbol{r}_A - \boldsymbol{r}_B|$ becomes infinite, the ground state of $\hat{H}_{\text{e}}$ consists in two degenerate states with a possible eigenbasis given by:

$$\Psi_{\text{I}}(\boldsymbol{r}_1, \boldsymbol{r}_2) = \phi_A(\boldsymbol{r}_1)\phi_B(\boldsymbol{r}_2) \qquad\qquad \Psi_{\text{II}}(\boldsymbol{r}_1, \boldsymbol{r}_2) = \phi_A(\boldsymbol{r}_2)\phi_B(\boldsymbol{r}_1). \tag{3.8}$$

The single-particle wave function ϕ_A (resp. ϕ_B) describes one electron in the ground state $1s$ localised around the nucleus A (resp. B), and the electrons 1 and 2 can be localised around the nucleus A or B. The calculations of the energies at each distance r_{AB} can then be summarised as follows: one looks for linear combinations $\Psi = \alpha\Psi_{\mathrm{I}} + \beta\Psi_{\mathrm{II}}$ which give extrema of the average energy. This procedure reveals two solutions: a symmetric and an antisymmetric combinations $\Psi_{\mathrm{I}} \pm \Psi_{\mathrm{II}}$. These extremal energies can be written in a form of an effective potential $V_{\mathrm{eff},\pm}$ for the motion of the nuclei. This effective potential writes as two contributions: a "direct" energy and "exchange" energy term. The direct energy corresponds to the matrix element of $\hat{H}_{\mathrm{e}}$ where each electron stays around its original proton, and the exchange energy corresponds to matrix elements where the atoms exchange their electrons. This last contribution is null when the electronic clouds do not overlap.

Electrons are indistinguishable fermionic particles of spin $s = 1/2$. Given a quantization axis, the electrons have two possible spin states: $|\uparrow\rangle \equiv |m_s = 1/2\rangle$ and $|\downarrow\rangle \equiv |m_s = -1/2\rangle$, where m_s is the projection of $\hat{\boldsymbol{s}}$ on the quantization axis. The Pauli principle stipulates that the state of the electrons must be antisymmetric by exchange. Therefore, the spin state must have a symmetry opposite to the orbital part one. For the symmetric potential $V_{\mathrm{eff},+}$ one finds the so-called *singlet* ($S = 0$) spin state $(|\uparrow,\downarrow\rangle - |\downarrow,\uparrow\rangle)/\sqrt{2}$ while the potential $V_{\mathrm{eff},-}$ is associated with *triplet* ($S = 1$) spin states: $|\uparrow,\uparrow\rangle$, $|\downarrow,\downarrow\rangle$, $(|\uparrow,\downarrow\rangle + |\downarrow,\uparrow\rangle)/\sqrt{2}$.
Numerical calculations show that $V_{\mathrm{eff},\pm}$ tend to zero in the infinite distance limit while they diverge for $r_{AB} \to 0$. The potential $V_{\mathrm{eff},-}$ is a decreasing function of r_{AB}, always positive and higher than $V_{\mathrm{eff},+} < V_{\mathrm{eff},-}$. The other one, $V_{\mathrm{eff},+}$ presents a negative minimum at a finite distance r_{min}. They define, with their respective spin states, an *anti-bonding* orbital and a *bonding* orbital respectively.
We emphasize that here we restricted the single-particle test functions ϕ to wave functions associated with $1s$ states. This first approximation excludes van der Waals interactions. Indeed, we calculated earlier the energy displacement induced by such interactions within perturbation theory, and one can also compute the first-order state vector. Considering H atoms in their electronic ground state $1s$, one can show that the perturbed state at first order implies p-states. As we did not include p-states in the test functions, the van der Waals interactions are not described by the potential $V_{\mathrm{eff},\pm}$. Opening the basis of test functions ϕ, allowing for p-states for instance, leads to a more accurate model. The van der Waals interactions can then be taken into account and their presence restores the attractiveness of the anti-bonding orbital, which now presents a minimal value (under the dissociation limit), even if it is still less deep than the bonding orbital. This last one is also made deeper by the van der Waals interactions.

In this discussion, we let apart the spin dimension of the nucleus. However, nuclei have usually a non-zero magnetic moment which interact with the magnetic moment of the electron. The coupling between the electron and nucleus spin angular momentum is called hyperfine coupling and splits the ground state into hyperfine levels, described by their total angular momentum $f = |i - s|, ..., |i + s|$. Moreover, as electrons, nuclei are indistinguishable particles. Therefore, their spin must be taken into account in the symmetries of the problem to satisfy Pauli principle. In practice, it is easier to consider the total angular momentum f to attribute spins states to their orbital part $V_{\mathrm{eff},\pm}$. When f is an integer, the wave function of the atomic pair must be symmetric by exchange, otherwise it must be anti-symmetric by exchange. Note that, *a priori*, the different channels $\{f_j; f_{j'}\}$ are coupled, as the hyperfine Hamiltonian does not commute with the Hamiltonian giving the orbitals.

3.1.2 Scattering states and bound states

In the previous section, we described the interaction potential $V(r)$ between two particles separated by a distance r. This potential goes from repulsive to attractive with increasing r and presents a minimum value for a distance r_{min}. Its long-distance tail is dominated by van der Waals interactions. We also presented a method to calculate the core potential, which brings out the presence of two potential energies: a singlet potential and a triplet potential. Thanks to this knowledge, one can solve the two-body Hamiltonian Eq. (3.6). The eigenstates with energies larger than $V(+\infty)$ are called the *stationary scattering states* and describe collisions between the two particles. These states can be calculated with the so-called scattering theory which is extensively treated in quantum physics textbooks [106]. For an isotropic potential, binary collisions can be described by a scattering amplitude $f(k)$ decomposed into contributions of independent scattering channels with well-defined angular momenta ℓ. Each channel is associated with a scattering amplitude $f_\ell(k)$, $\boldsymbol{k}$ being their relative wave vector, and can be treated independently. For ultracold atoms, the wavelength λ_{th} is typically a few hundred nanometres and is much larger than the potential range b. In this regime $\lambda_{\mathrm{th}} \sim 1/k \gg b$, and for polarized bosons, only the s-wave associated with $\ell = 0$ contributes and the collisions are well-described at first order by one parameter: the scattering length

$$a = -\lim_{k\to 0} f_0(k). \tag{3.9}$$

The scattering length can be determined thanks to the scattering state at the dissociation limit ($E = 0$), whose wave function asymptotic behaviour writes $\propto 1/r - 1/a$. Its value can be positive, negative, equal to zero or even infinite.

Since the low-energy properties of the interaction potential are characterised by a only, we can simplify the binary collision model by replacing the real potential by a much simpler regularised contact-potential as written in Sec. 1.2.1 in the 3D case:

$$\hat{V}_{\mathrm{pp}}[\psi(\boldsymbol{r})] = g\delta(\boldsymbol{r})\frac{\partial}{\partial r}[r\psi(\boldsymbol{r})], \qquad g = \frac{2\pi\hbar^2}{m_{\mathrm{r}}}a. \tag{3.10}$$

This potential yields the same scattering length a and the same isotropic scattering amplitude $f(k)$ at first order.

Let us now turn to the eigenstates with energies lower than $V(+\infty)$. These are *bound states* of the dimer and are the centre of this chapter. Their energies are related to the scattering properties: it can be demonstrated that the scattering amplitude $f(k)$ diverges when evaluated for an energy equal to the energy of a bound state [63]. The energies of the bound states can then be calculated by looking at the poles of $f(k)$. At first order and for s-waves only, one finds one bound state of energy

$$E = -\frac{\hbar^2}{2m_{\mathrm{r}}a^2}, \tag{3.11}$$

when the scattering length is positive $a > 0$ and no bound states for negative values of the scattering length $a < 0$. By construction, the pseudo-potential Eq. (3.10) gives the same result. In practice, the atomic species used in cold atoms platforms have many bound states. However, Eq. (3.11) gives a good approximation of the position of the least-bound state, for any potential, when it is close to the dissociation limit. Moreover, the scattering length a diverges when a new bound state is very close to the dissociation limit or appears, i.e. if we modify the potential parameters (depth or position $r_{\min}$) until the total number of bound states is increased by one.

From a chemical point-of-view, dimers are formed thanks to the covalent bond, which only exists when there are exchange interactions at play, and thus when the electronic clouds overlap. This covalent bound is prohibited for noble gases or alkaline-earth metals whose valence layer is complete. However, the van der Waals potential enables the formation of stable weakly bound dimers and, for instance, the dimer He_2 was indirectly observed in 1994 [107]. These weakly bound states have interesting properties and, as we will see later, they are of great experimental interest, both from a spectroscopic point-of-view and for controlling interactions in cold atomic gases. Considering a realistic potential, the least-bound states are essentially localised in the range where the van der Waals interactions are dominant. In 1970, LeRoy and Bernstein [108] used a semi-classical approach [109] to show that, as long as the potential has a van der Waals tail, it is not necessary to know the repulsive short-range potential to find the energies of the least-bound states. The calculation of the bound states wave functions in the real potential show that these wave functions are "phase locked" for $r \lesssim R_{\mathrm{vdW}}$, i.e. they oscillate with the same spatial phase Φ. The short-range potential effect is only to fix this spatial phase. Therefore, as long as Φ is known and/or measured, the potential can be described by a van der Waals potential with any core potential. The position of the potential minimum $r_{\min}$ can be adjusted to set the phase Φ on the wave functions. The energies of the least-bound states in such a potential are universal and write:

$$E_j \approx -28.65(j_d - j)^3 E_{\mathrm{vdW}}, \qquad\qquad j_d \propto \Phi, \tag{3.12}$$

where j is an integer and indicates the j-th bound state with $j < j_d$ and $E_{j-1} < E_j$.

The wave function of the state at the dissociation limit $E = V(+\infty)$ appears to undergo the same spatial phase locking than the wave functions of the least-bound states. As a consequence, the scattering length a, given by the asymptotic wave function at the dissociation limit, depends also on the spatial phase Φ of the wave functions, for any potential with a van der Waals tail [110]. More precisely, a depends on Φ and on R_{vdW} which defines the *most probable* value of a: $\bar{a} \sim 0.956\, R_{\mathrm{vdW}}$[1]. Therefore, knowing Φ allows us to calculate the scattering length and the bound states energies. In other words, once we know one element of the ensemble:

$$\{a, E_{j_{\max}}, E_{j_{\max-1}}, ...\}, \tag{3.13}$$

one can deduce the others. For instance, measuring the position of a single bound state is sufficient to have a good approximation of the scattering length and the position of the other least-bound states.

3.1.3 Dimers and spectroscopy of the bound states

Molecular physics is a field of research in its own right for which methods to create and observe molecules have been developed. Because of their complex internal structure, it is difficult to prepare and trap ultracold molecules. We first highlight some examples of such preparations. For instance, ultracold molecules can be prepared in magnetic traps thanks to laser ablation of solids before being cooled by elastic collisions with a cold atomic gas [111]. This method apply for paramagnetic molecules[2] only. Another method to trap cold molecules

---

[1] The scattering length a writes indeed $a = \bar{a}\,[1 - \tan(\Phi - \pi/8)]$. The evolution of $a/\bar{a}$ with respect with Φ shows that $a \sim \bar{a}$ for most values of Φ, making $\bar{a}$ the most probable value of a.

[2] Molecules are paramagnetic when they possess unpaired electrons. When an external magnetic field is applied, the paramagnetic molecules are aligned with the magnetic field.

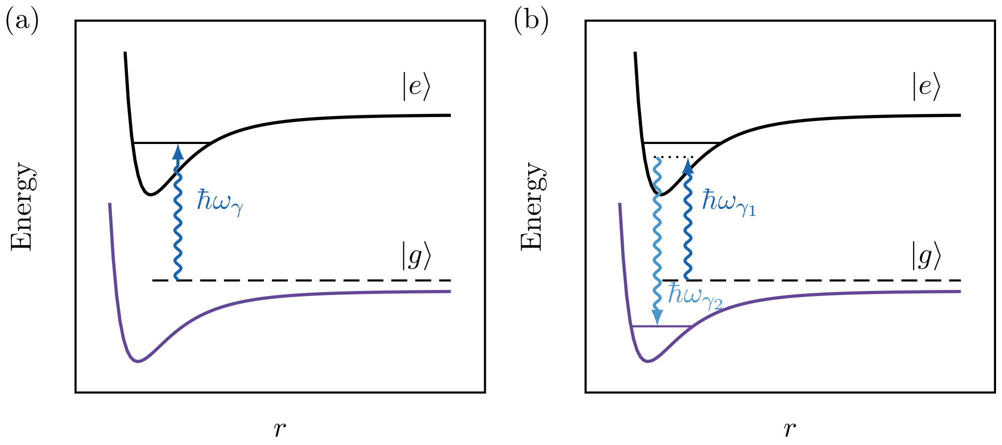

Figure 3.1: (a) Optical one-colour photoassociation of two atoms in their electronic ground state $|g\rangle$ to a dimer in an electronic excited state $|e\rangle$. (b) Two-colour photoassociation creating dimer in the electronic ground bound state.

is to use their electric dipole moment properties. Starting with a molecular beam (prepared in a closed valve and cooled in contact with a cold buffer-gas), the molecules are decelerated with a quasi-static inhomogeneous electric field and then trapped in a electrostatic trap [112]. The trapped molecules can be observed with fluorescence imaging (using a transition to an excited molecular state) or after being ionised.

Dimers can also be formed from cold atom physics platforms. Taking advantage of the technical progresses made on the atomic cooling schemes, cold molecules have been formed by *photoassociation* of pairs of ultracold atoms [113–116], first introduced in this context by Thorsheim et al. [117]. The first observation of cold molecules created following this method has been reported by Fioretti et al. [118]. This process associates two free atoms A and B with a photon whose energy $\hbar\omega_\gamma$ is equal to the energy difference between the collisional channel of A and B and a specific rovibrational state of the excited molecule AB, as shown in Fig. 3.1.a. It can be summarised as:

$$A + B + \hbar\omega_\gamma = AB. \tag{3.14}$$

Photoassociation has a particular interest in ultracold atoms platforms as the kinetic energy of the atoms is negligible. The kinetic energy spread is suppressed and we therefore observe narrow lines, which ensures a larger precision on the measurement of bound states energy. Moreover, the creation of the dimer results from low-temperature collisions, which are mostly limited to s-waves for bosonic systems. Photoassociation produces then molecules in low rotational levels. Finally, photoassociation allows to create shallow dimers for which the atoms remains at large interatomic distances. As the electronic clouds of the two atoms do not overlap, the behaviour of these so-called *long-range* molecules are expected to be well-determined by the properties of the atoms which constitute it [115]. From an experimental point of view, we define two domains for photoassociation: the optical domain for which the corresponding photoassociations imply optical transitions, and the radio-frequency (rf) and microwave (mw) domain for which photoassociation is performed on transitions whose frequencies are of the order of the megahertz and gigahertz respectively.
First photoassociations were performed in the optical domain, to create, from two atoms in their electronic ground state $|g\rangle$, dimers in an electronic excited state $|e\rangle$, as shown in Fig. 3.1.a. Optical photoassociation benefits from the large coupling strengths accessible,

however, the dimers formed in electronic excited state have short lifetimes. They can spontaneously decay to an electronic ground bound state or the two atoms can separate and acquire a large kinetic energy. Sample of long-lived cold molecules can be produced by waiting for the electronically excited molecules to spontaneously decay to an electronic ground bound states. However, it is difficult to target a given final state. Two-colour photoassociation appears then to be a useful tool to target rovibrational bound states of energy below the collisional channel energy threshold, allowing for the pairing of two atoms in their electronic ground state. In this case, two laser pulses of angular frequencies ω_{γ_1} and $\omega_{\gamma_2} > \omega_{\gamma_1}$ are sent onto the atomic pair, see Fig. 3.1.b. The first one couples the pair to an electronic excited bound state, playing the role of an intermediate state. The frequency of the second pulse is set to couple the intermediate state to a bound state placed at an energy ε below the continuum.
In the rf and mw regime, the transitions remain in the electronic ground state and one-photon transitions can address the different hyperfine levels of the electronic ground state. Photoassociation creates then long-lived cold molecules. However, unless the rf and/or mw fields are generated directly on atom chips, the free-bound coupling strengths are smaller than the ones achievable with optical transitions.
Finally, one can create dimers in the ground state by resonantly coupling the free atomic pair and the bound state. This is achieved with the application of an external magnetic field, for magnetic moments of the spin-state channels which are different.

Photoassociation has been performed on most of the alkali atoms [119–128]. As mentioned earlier, knowing the position of the bound states just below the dissociation limit enables the study of the properties of the potential at large distance and the corresponding scattering length [129–131]. Spectroscopy measurement could confirm the van der Waals universality discussed above in Sec. 3.1.2. Indeed, the measurement of many weakly bound state energies of the same atomic species shows that they are well-predicted by Eqs. (3.12) and (3.13). More specifically, all the measured energies match this model for a single spatial phase Φ. High-resolution two-colour photoassociation performed on ytterbium isotopes also allowed to improve this model by taking into account the contributions of the other terms of the multipolar development (see Sec. 3.1.1) [132].

3.1.4 Fano-Feshbach resonances: using weakly bound states to control interactions in ultracold gases

We have already mentioned the scattering resonances for which the scattering length diverges. We have highlighted the existence of resonances at the dissociation limit. This resonance occurs if the least-bound dimer is close to the dissociation limit. For instance, caesium in zero-magnetic field is naturally in this configuration. Its triplet scattering length has been measured at $a \sim 130\,\mathrm{nm}$ and found to be 25 times the most probable value $\bar{a} \sim 5\,\mathrm{nm}$ obtained from the universal van der Waals model [133]. The presence of this resonance induces atom losses due to inelastic collisions and prevents condensation under these conditions.

We will now describe another type of scattering resonances called Fano-Feshbach resonances (FFR). They were introduced by Feshbach in 1958 [134, 135] and Fano in 1961 [136] for nuclear and atomic physics respectively. In the context of quantum gases, FFR were first mentioned for the hydrogen atom [137, 138] before their transposition to alkaline systems was proposed in the 1990s [139, 140]. They are an essential tool in the physics of ultracold gases as they allow to tune the interaction strength. Thanks to FFR, we can reach the *strongly-interacting regime* for which the scattering length is of the order of the distance between the

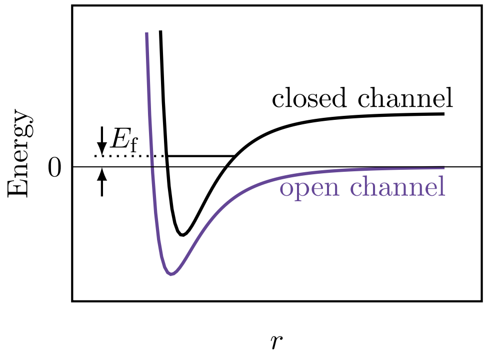

Figure 3.2: Scheme of a two channels FFR. The potential $V_1(r)$ (violet line) describes the open channel. The potential $V_2(r)$ (black line) has a bound state and represents the closed channel. The pair of atoms have initially an energy close to $V_1(+\infty) \sim 0$ here. The energy gap E_f between the bound state and the initial free state is also represented.

particles. On the other hand, they allow to reduce the interactions strength to study ideal gases. We can also reach the *unitary regime*, for which the scattering length is infinite. These resonances have been widely studied and the reader will find more complete discussions in Refs. [141, 142]. Here, we will limit ourselves to giving a phenomenological model of these resonances in order to underline the role of bound states in this process.

Fano-Feshbach resonances involve at least two channels, and we will discuss a simple model with two channels involved and represented in Fig. 3.2. We consider two cold atoms colliding with s-wave interactions. They have an initial energy close to the dissociation threshold of a potential $V_1(r)$, describing the open channel. The second channel involved is described by a potential $V_2(r)$ and is closed, i.e. the asymptotic value of its potential $V_2(+\infty)$ is much larger than the initial atoms energy $\sim V_1(+\infty)$. If the coupling between these two channels is large enough during the collision, it can modify the phase shift δ_0 associated with the open channel and thus the corresponding scattering length a. Furthermore, if the closed channel presents a bound state whose energy E_f is close to the incident energy of the atoms, dimers may be temporarily formed during the collision. The occupation of the bound state generates a rapid and considerable variation of the phase shift δ_0 and scattering length a. This variation can be scanned by tuning the energy gap between the bound state and the incident energy $E_f - V_1(+\infty)$[3]. This can be achieved by applying an external field when the two channels have different magnetic moments. It works similarly to the magneto-association we already discussed, but now one fixes the magnetic field to obtain a given value of a. In this case, a phenomenological model is commonly used to describe the variation of the scattering length which writes:

$$a = a_{\mathrm{bgd}} \left(1 - \frac{B_1}{B - B_0}\right). \tag{3.16}$$

The *background* scattering length, i.e. the scattering length far from the resonance in the open channel is written a_{bgd}. The parameters B_0 and $|B_1|$ are magnetic fields representing respectively the position of the resonance and its width. The scattering length is zero for

---

[3] In practice, the resonance does not occur when the gap $E_f - V_1(+\infty)$ is reduced to zero but for $E_f + \Delta = V_1(+\infty)$. The energy shift Δ is a shift of the closed channel induced by the coupling between the free and the bound states. In the case of magneto-association, the coupling strength depends on the atomic species involved. The relation between the energy gap and the magnetic field writes

$$E_f + \Delta = \delta\mu(B - B_0), \tag{3.15}$$

where $\delta\mu$ is the difference between the magnetic moments of the atomic pair and the bound state.

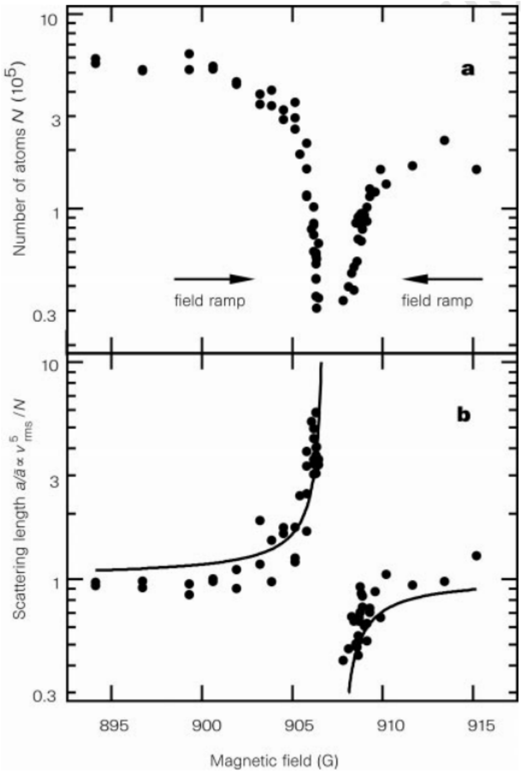

Figure 3.3: Observation of a Feshbach resonance in an ultracold atomic sample of sodium by scanning the magnetic field around 900 G. (a) Atom losses induced by the inelastic collisions. (b) Rapid variation of the normalised scattering length calculated from the interaction energy. The interaction energy is measured with a ballistic expansion of the gas. The solid line is the prediction of the simple model Eq. (3.16). Figure extracted from [18].

$B = B_0 + B_1$.
The first experimental observations of FFR were performed in 1998 by two groups, at MIT [18] and at the University of Austin [19]. We illustrate this phenomenon with the results of the MIT group, shown in Fig. 3.3. They observed a FFR in a sodium Bose-Einstein condensate at a magnetic field $\sim$ 900 G. They scanned the magnetic field around the resonance and measured the atomic losses and the interaction energy with a ballistic expansion of the gas. They deduced the scattering length from the interaction energy and showed the divergence of the latter, together with an increase of atomic losses due to inelastic collisions.

The FFR induced by magneto-association depends strongly on the atomic species since the wave functions of the incident and bound states determine the coupling strength. This limitation can be overcome by using other methods. Indeed, one can couple an atomic pair to the bound state of a closed channel with light or microwave pulses. In these cases, the coupling does not depend on the species but on the amplitude of the applied field. The energy difference $E_{\mathrm{f}} - V_1(+\infty)$ is scanned by adjusting the field frequency.
Optical FFR was first proposed by Fedichev et al. [143] and is carried out with one- or two-photon transitions [144, 145]. In the first case, it couples a pair of atoms in their electronic ground state to a closed channel where one of them is in an electronic excited state. In the second case, an electronically excited state is used as an intermediate state to couple the pair of atoms to a closed channel where the atoms are also in their electronic ground state. However, this method is limited by atom losses due to spontaneous emission in the electronic excited

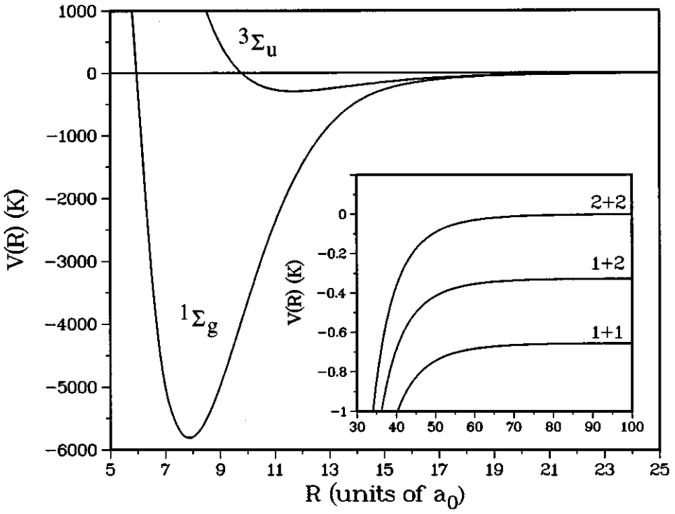

Figure 3.4: Ground states of the molecular energy potential V of the ^{87}Rb dimers with respect with the distance R between the centre of mass of the atoms. The so-called anti-bonding orbital $^{3}\Sigma_{\mathrm{u}}$ presents a negative minimum for $R \sim 11\,a_0$. The bonding orbital $^{1}\Sigma_{\mathrm{g}}$ is much deeper and presents a minimum for $R \sim 8\,a_0$. The three entry channels of the free ^{87}Rb atoms in their ground state at zero-magnetic field are represented in the inset and the two upper potentials, $\{f = 1; f = 2\}$ and $\{f = 2; f = 2\}$, converge adiabatically to the $^{3}\Sigma_{\mathrm{u}}$ potential. This figure is extracted from [149].

state. The radio-frequency- or microwave-induced FFR, proposed by [146–148], does not suffer from this problem since it does not involve electronically excited states. For this type of FFR, because the wavelength of the field is much larger than the interaction potential range, the amplitude of the scattering length modification depends on the amplitude of the field, on one hand, and on the overlap between the incident and bound states on the other [63]. To maximise the overlap, the potentials describing the channels must be significantly different. For alkali atoms, this condition is fulfilled when they have different weights on the singlet and triplet potentials and if the singlet and triplet scattering lengths are significantly different.

3.2 Production and characterization of ^{87}Rb dimers

In this manuscript, our interest is focused on ^{87}Rb -^{87}Rb dimers. As an alkaline, its valence layer has only one electron in the ground state. The core layers play a minor role in the determination of the interaction potential. The situation is then very similar to the hydrogen case that we described in the previous section Sec. 3.1.1. For ^{87}Rb, the coupling between the electronic spin angular momentum $s = 1/2$ and the nucleus spin angular momentum $i = 3/2$ leads to a splitting of the ground state into two hyperfine levels $f = 1$ and $f = 2$. The pairs can then have three different energies associated with the channels $\{f = 1; f = 1\}$, $\{f = 1; f = 2\}$ and $\{f = 2; f = 2\}$. The total angular momentum taking integer values, the wave functions of an atomic pair must be symmetric by exchange of one electron. As for the hydrogen, we find an anti-bonding and a bonding orbital associated with a triplet and a singlet electronic spin state respectively. These potentials are written in the language of molecular spectroscopy $^{3}\Sigma_{\mathrm{u}}^{+}$ and $^{1}\Sigma_{\mathrm{g}}^{+}$, expressing the properties of the electronic wave functions. The notation Σ specifies that the pair of atoms has a zero projection of the total orbital angular momentum on the diatomic axis. The indexes "g" (gerade) and "u" (ungerade) refer to the

Channel	n	Two-colour	rf
$\{f=2; f=2\}$	-1	-25.045(3)	
$\{f=1; f=2\}$	-1		-24.984(3) -26.055(5)
$\{f=1; f=1\}$	-1	-24.242(5)	
	-2	-636.0094(12)	

Table 3.1: Energies in MHz of the weakly bound state of ^{87}Rb dimers with zero orbital angular momentum, at zero-magnetic field, observed with two-colour photoassociation and rf-induced photoassociation. The values n designates the index of the rovibrational state counted from the dissociation limit. Values are extracted from [152–154] and [155] respectively.

symmetry after the inversion with respect to the center of the molecular axis and the exponent corresponds to $2S+1$. These two molecular potentials are represented in Fig. 3.4 and were characterised by Deiß et al. [150]. The so-called singlet and triplet potentials are described by a scattering length a_s and a_t respectively, as explained in Sec. 3.1.2. A numerical resolution of ^{87}Rb potentials parametrised with existing measurements of the least-bound states shows that they happen to have very close scattering lengths $a_\mathrm{s} = 90.0(2)\,a_0$, $a_\mathrm{t} = 98.99(2)\,a_0$ [151]. At large inter-atomic distance, relevant for the least-bound states, the molecular potentials do not have a well-defined singlet or triplet character. The ^{87}Rb singlet and triplet potentials shown in Fig. 3.4 are indeed mixed for $r > 20\,a_0$. They are well-described by a van der Waals potential $V(r) = -C_6/r^6$ with $C_6 = 4635\,\mathrm{a.u.}$[4] [62].

We introduced in a previous section the photoassociation as a useful spectroscopic tool and we present now the results of two research groups on the free-bound state transition spectra of the electronic ground state of ^{87}Rb. Two-color photoassociation in a ^{87}Rb Bose-Einstein condensate has been performed, for instance, in the group of Heinzen in Austin [152–154]. They measured some selected least-bound dimers of two hyperfine channels $\{f=1; f=1\}$ and $\{f=2; f=2\}$ of the electronic ground state. They observed narrow lines of width $\sim 1.5\,\mathrm{kHz}$ which confirms the interest of performing this measurement in ultracold atomic platforms. More recently, researchers in Melbourne reported the first rf-induced observation of the ^{87}Rb least-bound rovibrational state, with zero orbital angular momentum, of the hyperfine channel $\{f=1; f=2\}$ [155]. They measured two levels $24.984(3)\,\mathrm{MHz}$ and $26.055(5)\,\mathrm{MHz}$ below the continuum at zero-magnetic field. They also partially measured the Zeeman sub-levels diagram of this bound state. These measurements are reported in table 3.1 for a zero-magnetic field.

We complete these results using mw-induced photoassociation and propose a simple model to describe the hyperfine and Zeeman diagrams of a rovibrational bound state with zero orbital angular momentum.

3.2.1 Model for the energy levels of ^{87}Rb least-bound dimers

We derived a simple model to describe the hyperfine and Zeeman splitting of any $^{87}\mathrm{Rb}_2$ rovibrational state with zero orbital angular momentum as long as it is weakly bound, in a sense that its binding energy must be much smaller than the hyperfine structure of an atomic pair.

These energy diagrams have already been numerically computed using coupled-channels equa-

---

[4] Here, a.u. stands for atomic unity and writes in SI: $1\,\mathrm{a.u.} = 9.55\times10^{-80}\,\mathrm{J.m}^6$.

tions [148] and quantum defect theory [147,156,157]. The first method consists in diagonalising the total asymptotic ($r \to +\infty$) Hamiltonian in a basis of symmetric states before using the resulting wave functions to expand the collisions complex wave functions. Afterwards, the extended wave functions are inserted into the Schrödinger equation, leading to coupled-channels equations which yield energy of the bound states. The quantum defect theory is a faster method to obtain the free-bound resonances position. This methods relies on the van der Waals universality that we introduced before. The interactions are described by the van der Waals potential only. The short-range potential - for which the depths of and splitting between the singlet and triplet potentials are larger than the hyperfine splitting, Zeeman splitting and initial collision energy - is described by a simple parametrisation, imposing an appropriate boundary condition at short distances. This model relies then on three parameters: the singlet and triplet scattering lengths and the van der Waals potential range. The model proposed here is phenomenological and much simpler to compute.
We consider two atoms of ^{87}Rb, labelled 1 and 2, in their electronic ground state and characterised by their electronic and nuclear spins, $\{s_1 = 1/2, i_1 = 3/2\}$ and $\{s_2 = 1/2, i_2 = 3/2\}$. The ^{87}Rb electronic ground state, fully described in Sec. 2.2.1, splits into two hyperfine levels $f = 1$ and $f = 2$ of degeneracy $2f + 1$. We write the Hamiltonian $\hat{H}$ acting on atomic pairs and whose eigenvectors are bound state levels. As mentioned in Sec. 3.1.1, at low energy, two collision channels are involved and associated with a singlet potential $^1\Sigma_\mathrm{g}$ and a triplet potential $^3\Sigma_\mathrm{u}$. We introduce in the Hamiltonian an effective coupling between these two potentials to take into account the small difference of scattering lengths. We assume that the hyperfine channels $\{f_1; f_2\}$ are not coupled by this *singlet-triplet coupling*. Indeed, the two least-bound states are expected to be $\sim 25\,\mathrm{MHz}$ and $\sim 630\,\mathrm{MHz}$ below the continuum (see Tab. 3.1), so the binding energies are much lower than the hyperfine splitting $\sim 6.8\,\mathrm{GHz}$.

The energy diagram of an atomic pair is composed of three multiplicities according to the hyperfine levels involved. These multiplicities labelled $\mathcal{A}$, $\mathcal{B}$ and $\mathcal{C}$ are each separated by the hyperfine splitting $A_\mathrm{hfs} \sim h \cdot 6.8\,\mathrm{GHz}$. The lowest-energy multiplicity $\mathcal{A}$ describes pairs with both atoms in $f = 1$, multiplicity $\mathcal{B}$ describes pairs with an atom in each hyperfine level $\{f = 1; f = 2\}$ while the highest-energy multiplicity $\mathcal{C}$ defines pairs of two atoms in $f = 2$. When the interatomic distance decreases, these free pairs can form weakly bound dimers described by their total angular momentum $F = |f_1 - f_2|, ..., |f_1 + f_2|$. The hyperfine diagrams of the three multiplicities are shown in Fig. 3.5. Considering s-wave collisions only, one has to select states that are symmetric by exchange. Thus, only even values of F are retained in multiplicities $\mathcal{A}$ and $\mathcal{C}$, while in multiplicity $\mathcal{C}$, F can take the values 1, 2 or 3. Again, these levels are of degeneracy $2F + 1$ and, considering states symmetric by exchange only, we are left with thirty-six levels: $\{1 + 5 = 6\}$ levels in multiplicity $\mathcal{A}$, $\{3 + 5 + 7 = 15\}$ levels in $\mathcal{B}$ and $\{1 + 5 + 9 = 15\}$ levels in $\mathcal{C}$.

We write the Hamiltonian acting on pairs of free atoms as the sum of three contributions:

$$\hat{H} = \hat{H}_\mathrm{hfs} + \hat{H}_\mathrm{Z} + \hat{H}_\mathrm{st}. \tag{3.17}$$

The first term, $\hat{H}_\mathrm{hfs}$, is the hyperfine coupling between the magnetic momenta of a nucleus and its attached electron. The second one, $\hat{H}_\mathrm{Z}$, is the Zeeman term accounting for magnetic coupling with a non-zero magnetic field B, while the last term is a phenomenological coupling between the singlet and the triplet states which takes into account the small differences in their scattering length. These three terms read:

$$\hat{H}_{\text{hfs}} = \frac{A_{\text{hfs}}}{2}\left(\hat{\boldsymbol{s}}_1 \cdot \hat{\boldsymbol{i}}_1 + \hat{\boldsymbol{s}}_2 \cdot \hat{\boldsymbol{i}}_2\right), \tag{3.18}$$

$$\hat{H}_{\text{Z}} = \frac{\mu_B B}{\hbar}\left[g_S(\hat{s}_{1,z} + \hat{s}_{2,z}) + g_I(\hat{i}_{1,z} + \hat{i}_{2,z})\right], \tag{3.19}$$

$$\hat{H}_{\text{st}} = A_{\text{st}}\hat{\boldsymbol{s}}_1 \cdot \hat{\boldsymbol{s}}_2 = \frac{A_{\text{st}}}{2}\left(\hat{\boldsymbol{S}}^2 - \frac{3}{2}\right), \tag{3.20}$$

where A_{hfs} and A_{st} are the hyperfine coupling strength and the singlet-triplet coupling strength respectively. The latter, A_{st}, may *a priori* be different for each multiplicity. The singlet-triplet coupling Eq. (3.20) is treated as a perturbation within a single multiplicity as $A_{\text{st}} \ll A_{\text{hfs}}$. We write the state of the free pair of atoms 1 and 2 in the decoupled basis:

$$|\sigma_1, \iota_1; \sigma_2, \iota_2\rangle \equiv |s_1 = 1/2, \sigma_1, i_1 = 3/2, \iota_1; s_2 = 1/2, \sigma_2, i_2 = 3/2, \iota_2\rangle. \tag{3.21}$$

The projections on the quantization axis z of the electronic spin angular momentum $s = 1/2$ and the nucleic spin angular momentum $i = 3/2$ are written $\sigma = \pm 1/2$ and $\iota = \pm 1/2, \pm 3/2$. We use all the 64 atomic pairs $|f_1, m_{f_1}; f_2, m_{f_2}\rangle = |f_1, m_{f_1}\rangle \otimes |f_2, m_{f_2}\rangle$ to diagonalise the Hamiltonian $\hat{H}$ and select afterwards the thirty-six states symmetric by exchange. The hyperfine levels are given in this basis in appendix A.

Hyperfine diagram At zero-magnetic field, the Hamiltonian reads $\hat{H} = \hat{H}_{\text{hfs}} + \hat{H}_{\text{st}}$. As we already mentioned, the hyperfine term $\hat{H}_{\text{hfs}}$ gives three energy multiplicities, each separated by $A_{\text{hfs}} \sim h \cdot 6.8\,\text{GHz}$. The two terms commute with $\hat{\boldsymbol{F}}$ so F is an appropriate quantum number. The singlet-triplet coupling, treated as a perturbation within a multiplicity, leads to the following lift of degeneracy:

- in multiplicity $\mathcal{A}$: the levels $F = 0$ and $F = 2$ are respectively shifted by $-A_{\text{st}}^{(\mathcal{A})}/8$ and $A_{\text{st}}^{(\mathcal{A})}/16$.
- in multiplicity $\mathcal{B}$, one finds the levels $F = 1$ and $F = 3$ to be pure electronic spin-triplet shifted by $A_{\text{st}}^{(\mathcal{B})}/4$. The level $F = 2$ is lowered by $-A_{\text{st}}^{(\mathcal{B})}/8$.
- in multiplicity $\mathcal{C}$: the levels $F = 0$, $F = 2$ and $F = 4$ are respectively shifted by $-3A_{\text{st}}^{(\mathcal{C})}/8$, $-3A_{\text{st}}^{(\mathcal{C})}/16$ and $A_{\text{st}}^{(\mathcal{C})}/4$. The level $F = 4$ is a pure electronic spin-triplet.

We defined a singlet-triplet coupling strength A_{st} per multiplicities as they may differ from one another. Note that in our computation, we consider them equal. The energy diagram at zero magnetic field is presented in Fig. 3.5.a.

Zeeman diagam If we now apply an external magnetic field B, the levels split into $2F+1$ Zeeman sub-levels. By adding the Zeeman term Eq. (3.19) to the Hamiltonian, F is no longer an appropriate quantum number, but its projection on the quantization axis m_F remains a good quantum number to describe the sub-levels. As $\hat{H}_{\text{Z}}$ is linear in $\hat{S}_z$ and $\hat{I}_z$ it cannot couple two sub-spaces such as $\Delta F \geq 2$. Thus, in multiplicities $\mathcal{A}$ and $\mathcal{C}$ the hyperfine levels are not coupled together and consequently, the Zeeman sub-levels are linear with B. However, in the multiplicity $\mathcal{B}$ we observe a less trivial behaviour.

In all the multiplicities, we could identify at least one state whose energy is independent of the magnetic field. For the multiplicities $\mathcal{A}$ and $\mathcal{C}$, there are two and three magnetic-insensitive states, which is a direct consequence of the fact that the Zeeman coupling induces linear

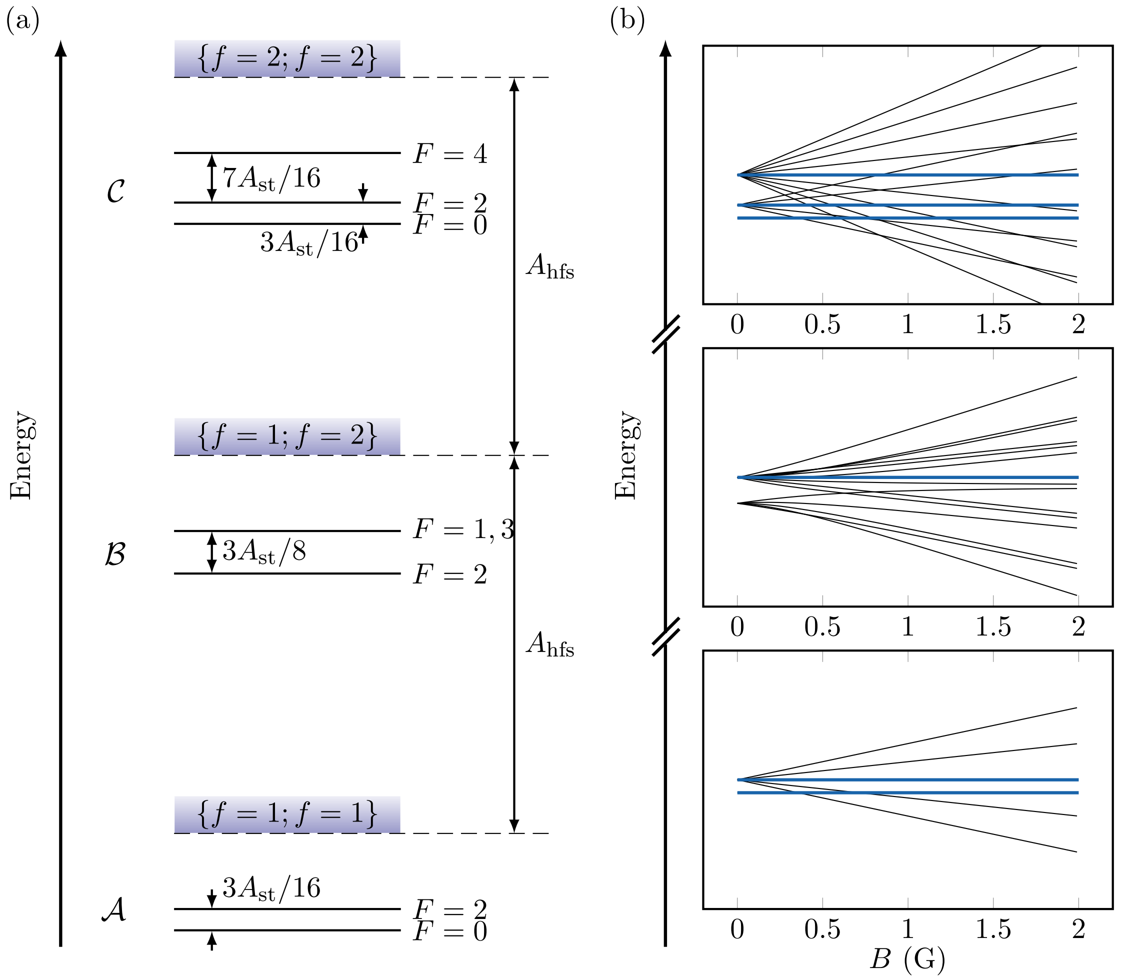

Figure 3.5: (a) Hyperfine diagram scheme. (b) Zeeman diagram of a rovibrational wealky bound state numerically calculated from the simple model Eq. (3.17). We fix the hyperfine splitting constant to $A_{\mathrm{hfs}} = h \cdot 6.834\,682\,\mathrm{GHz}$, measured on the clock transition $|f=1, m_f=0\rangle \rightarrow |f=2, m_f=0\rangle$ on our setup. The singlet-triplet coupling is set to $3A_{\mathrm{st}}/8 = h \cdot 1\,\mathrm{MHz}$ to be consistent with the splitting measured for the least-bound state of the multiplicity $\mathcal{B}$, labelled $n=-1$ in Tab. 3.1, $3A_{\mathrm{st}}/8 = h \cdot 1.074(5)\,\mathrm{MHz}$ [155]. Note that, in practice, there is no guarantee that the three multiplicities experience the same singlet-triplet coupling. Moreover, the weakly bound states that are lower in energy, $n < -1$, are expected to have larger couplings A_{st}[5]. The blue lines represent the magnetic-insensitive levels. The three frames have a same vertical scale and their height is 10 MHz.

variations with B for these multiplicities. In the last multiplicity, $\mathcal{B}$, we found one magnetic-insensitive state. This state, called $|\Psi_0\rangle$, will be of particular interest in our experimental exploration. It is a pure electronic spin-triplet and writes in the decoupled basis:

$$|\Psi_0\rangle = \frac{1}{\sqrt{2}}\big[|1/2,\,1/2;\,-1/2\,-1/2\rangle + |-1/2,\,-1/2;\,1/2\,1/2\rangle\big]. \tag{3.22}$$

Its total angular momentum F is not well-defined as it is a combination of the $F=1$ and $F=3$ levels, written in the coupled basis:

$$|\Psi_0\rangle = \sqrt{\frac{3}{5}}|F=3, m_F=0\rangle - \sqrt{\frac{2}{5}}|F=1, m_F=0\rangle. \tag{3.23}$$

In conclusion, this perturbative model suits well the case of ^{87}Rb atoms as the singlet and triplet potentials have similar scattering lengths. It provides the hyperfine and Zeeman energy diagram of a weakly bound rovibrational state with zero orbital angular momentum with two free parameters: an offset energy level E_0 and a singlet-triplet parameter A_{st}. Note that this model relies only on internal variables and says nothing about the radial part of the dimer wave functions. We assumed that an approximate characterisation of the radial part is provided by the scattering lengths associated with the atomic hyperfine channels: a_{11}, a_{12} and a_{22}.
What happens if we want to model strongly bound states? As the binding energy becomes larger, the bound state may be too deep in the potential and the assumption $A_{\mathrm{st}} \ll A_{\mathrm{hfs}}$ is no longer valid. The singlet-triplet coupling cannot be treated as a perturbation.

We present in the following sections our work on the study of weakly bound dimers. Thanks to our high-resolution mw spectroscopic tool, we photoassociate free pairs of atoms to the two least-bound states $n = -1, -2$ of the multiplicity $\mathcal{B}$. Using the internal degree of freedom of the atoms, we were able to measure the fifteen Zeeman sub-levels of the least-bound rovibrational state $n = -1$ and provide an accurate estimate of E_0 and $A_{\mathrm{st}}^{(\mathcal{B})}$ by comparing our result with the simple model we have developed above. Note that, as we work on a single multiplicity, we diagonalize the singlet-triplet coupling over the whole ensemble of states and then restrict the energies to the multiplicity $\mathcal{B}$. Moreover, this allows to take into account the Zeeman quadratic effect which couples the different multiplicities.

3.2.2 Microwave-induced photoassociation spectroscopy of the ^{87}Rb least bound dimers

The energy levels of a free pair of ^{87}Rb atoms in their electronic ground state is composed of three multiplicities, introduced in the previous section, separated by the hyperfine splitting $A_{\mathrm{hfs}} \sim 6.8\,\mathrm{GHz}$. Microwave single-photon transitions can then address lines with $\Delta m_F = 0, \pm 1$ connecting different multiplicities:

$$\left.\begin{array}{l}\{f=1; f=1\}\\ \{f=2; f=2\}\end{array}\right\} \leftrightarrow \{f=1; f=2\}. \tag{3.24}$$

In practice, the short lifetime of atoms in the hyperfine level $f = 2$, $\tau \sim 100\,\mathrm{ms}$, makes it difficult to search for bound states from free pairs other than $\{f = 1; f = 1\}$. We then mostly limit ourselves to the transitions $\{f = 1; f = 1\} \to \{f = 1; f = 2\}$ and thus to the spectroscopy of the multiplicity $\mathcal{B}$.

Microwave-induced photoassociation We write the magnetic field created by the electromagnetic wave of frequency $\nu = \omega/2\pi$:

$$\boldsymbol{B}_\omega(t) = \frac{B_\omega}{2}\boldsymbol{\varepsilon}\exp(-i\omega t) + c.c. \tag{3.25}$$

and introduce the real amplitude B_ω of the field and the complex unit vector $\boldsymbol{\varepsilon} = (\varepsilon_+, \varepsilon_-, \varepsilon_0)$ characterising the orientation of the field for a given quantization axis. This quantization

---

[5] A list of the predicted bound states of the ^{87}Rb potential has been given in Wynar thesis (page 171) [153]. Using these results we find, for $n = -1$: $A_{\mathrm{st}}^{(\mathcal{A})} = h \cdot 4.8\,\mathrm{MHz}$, for $n = -2$: $A_{\mathrm{st}}^{(\mathcal{A})} = h \cdot 42.7\,\mathrm{MHz}$, for $n = -3$: $A_{\mathrm{st}}^{(\mathcal{A})} = h \cdot 133\,\mathrm{MHz}$, for $n = -4$: $A_{\mathrm{st}}^{(\mathcal{B})} = h \cdot 165\,\mathrm{MHz}$ and for $n = -5$: $A_{\mathrm{st}}^{(\mathcal{C})} = 1102\,\mathrm{MHz}$.

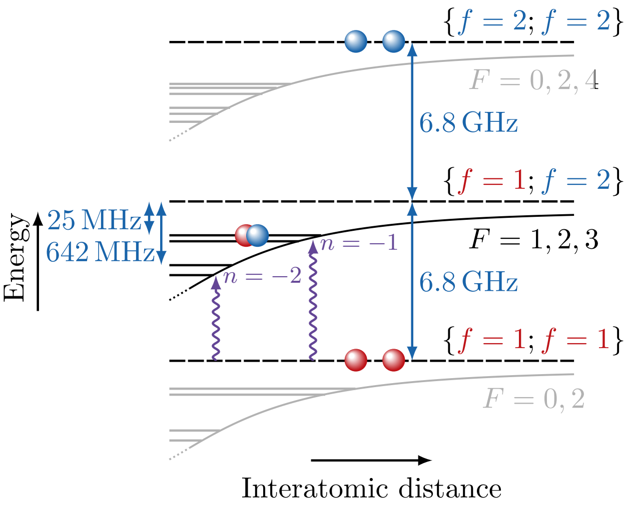

Figure 3.6: Relevant levels for atom pairs in the hyperfine sub-levels $f = 1$ and $f = 2$ of ^{87}Rb. The dissociation limits of molecular state manifolds, represented by dashed lines, are separated by $h \cdot 6.8\,\mathrm{GHz}$. The molecular potentials are represented by thick continuous lines, together with the values of the total angular momentum F of the dimers. The mw transitions (violet arrows) address the least-bound rovivrational levels $n = -1$ and $n = -2$ of the $\{f = 1; f = 2\}$ branch respectively, with zero orbital angular momentum, from the free pair level $|f = 1; f = 1\rangle$.

axis is set by the direction of the external static magnetic field B, whose amplitude and direction are tunable. For most of the experiments we performed, the static magnetic field is vertical. We use two mw chains and antennas, described in Sec. 2.2.6, to address free-bound transitions of polarisation σ^-, π and σ^+. The two antennas have different field amplitudes and orientations. We characterise the amplitude of the field for a given polarisation $\mathcal{P}$ by the quantity $B_\omega^{\mathcal{P}} = |B_\omega \varepsilon_{\mathcal{P}}|$. The amplitudes of the two antennas for the three polarisations with a vertical magnetic field are given in Tab. 3.2.

mw chain	σ^-	π	σ^+
RS1	2	8	12
RS2	8	31	4

Table 3.2: Amplitude $B_\omega^{\mathcal{P}}$ in mG of the microwave field shined by the two antennas, labelled RS1 and RS2, for the different transition polarisations $\mathcal{P}$ and a vertical external static magnetic field B, when using the 10 W (RS1) and the 50 W (RS2) amplifiers at full power.

We photoassociate two atoms in the hyperfine level $f = 1$ to the least-bound states of the multiplicity $\mathcal{B}$, as shown in Fig. 3.6. We shine a mw field on a uniform quasi-2D atomic sample of tunable surface density n_a and vertical thickness $\ell_z = 180(2)\,\mathrm{nm}$. The in-plane profile of the sample is shaped as a flat disk of radius $r = 20\,\mu\mathrm{m}$ and is shown in Fig. 3.7.a. We set the temperature to be the lowest achievable in our platform $T \lesssim 20\,\mathrm{nK}$. The initial kinetic energy of the atoms is then negligible and collisions occur in the s-wave. When the frequency of the mw field shined on the atoms is resonant with a free-bound transition, we observe atom losses due to the creation of dimers. After the mw excitation, we partially transfer the atoms into the hyperfine level $f = 2$ with a resonant mw pulse. We measure the optical density (OD) in $f = 2$ and calculate the surface density $n_\mathrm{a}(\nu)$ of the atoms in the $f = 1$ hyperfine level from this measurement. Since we create dimers from the association of two atoms, we expect the density n_a to undergo two-body losses and its evolution in time to follow:

$$\frac{\mathrm{d}n_\mathrm{a}}{\mathrm{d}t} = -\beta n_\mathrm{a}^2, \tag{3.26}$$

where β is the time-independent loss coefficient[6]. We consider durations δt of the mw excitations short-enough to induce small depletions of the atomic cloud. The excitation strength is low enough so that we do not observe coherent oscillations between the atomic and the molecular state, as was observed with Strontium atoms [159]. The photoassociation signal is thus described thanks to a Fermi golden rule. We define the depletion of the surface density $\delta n_\mathrm{a}/n_\mathrm{a} = (n_\mathrm{a}(\nu) - n_\mathrm{a})/n_\mathrm{a}$ as a more convenient observable to quantify the atomic losses, which are expected to scale as:

$$\delta n_\mathrm{a}/n_\mathrm{a} \propto -\beta n_\mathrm{a} \delta t. \tag{3.27}$$

The least-bound rovibrational state of the multiplicity $\mathcal{B}$ We now detail the spectroscopy of the least-bound rovibrational state $n = -1$ that we performed with mw-induced photoassociation, which is represented in Fig. 3.6.

By starting from an atomic sample prepared in the Zeeman sub-level $|f = 1, m_f = 0\rangle$, to benefit from its long lifetime $\tau \sim 10\,\mathrm{s}$ and its magnetic-field-insensitivity, we can address the levels of a bound state with a total angular momentum projection $m_F = 0, \pm 1$. The energy diagram of the multiplicity $\mathcal{B}$, calculated with our simple model, is shown in Fig. 3.5.b. There are nine lines out of the fifteen corresponding to these m_F, three for each value. We measured the positions of three of them, with $m_F = 0, \pm 1$, by shining a mw field during $\lesssim 1\,\mathrm{s}$. A typical signal of dimer creation by photoassociation is shown in Fig. 3.7.b. The losses are fitted with a Lorentzian function written:

$$n_\mathrm{a}(\nu) = n_\mathrm{a}\left[1 + \frac{\delta n_\mathrm{a}/n_\mathrm{a}}{1 + [2(\nu - \nu_\mathrm{m})/\Gamma]^2}\right], \tag{3.28}$$

with four free parameters: the surface density off resonance n_a, the depletion $\delta n_\mathrm{a}/n_\mathrm{a}$, the full width at the half maximum depletion Γ and the frequency ν_m for which the depletion is maximal. The dimer energy from the initial state energy is then set by $h \cdot \nu_\mathrm{m}$. We varied the static magnetic field amplitude from $\sim 0.75\,\mathrm{G}$ to $\sim 1.75\,\mathrm{G}$ and measured the Zeeman shift of the three lines, as shown in Fig. 3.7.c. We observed depletions $\delta n_\mathrm{a}/n_\mathrm{a}$ lower than $\lesssim 15\,\%$ and width lower than $\lesssim 2\,\mathrm{kHz}$. The individual data of the lines are presented in appendix A.

Among these three lines, we observed the magnetic-insensitive bound state $|\Psi_0^{(n=-1)}\rangle$ we introduced earlier in Sec. 3.2.1. As its total angular momentum projection is zero $m_F = 0$, we address this line with a transition of polarisation π, for which our microwave intensity is maximum, see Tab. 3.2. For an initial density $n_\mathrm{a} = 75\,\mu\mathrm{m}^{-2}$ of atoms in $|f = 1, m_f = 0\rangle$, a mw excitation of $115\,\mathrm{ms}$ creates a depletion of $14\,\%$ in the sample. The width of the line is always smaller than $1\,\mathrm{kHz}$ and, as there is no magnetic broadening of the line at first order, it can give an indication of the lifetime of the dimer. This specific state $|\Psi_0^{(n=-1)}\rangle$ and properties will be the centre of next chapter.

The three lines measured from $|f = 1, m_f = 0\rangle$ are sufficient to compare the model derived in Sec. 3.2.1 with our experimental measurement, as a first approximation. We fit the model to our data using a least-squares method and two free parameters: the spin-triplet energy at $B = 0$, E_0, and the singlet-triplet coupling A_st. The model matches our three lines with

---

[6] This two-atom pictures stands for many-body systems if the loss coefficient is large enough [158].

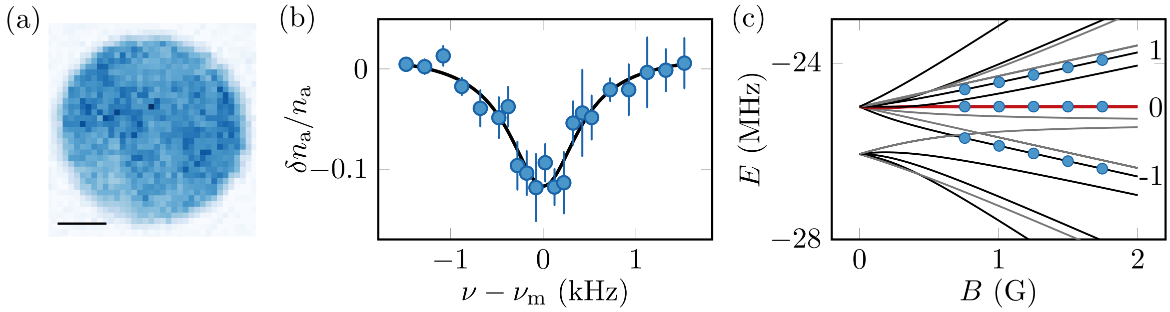

Figure 3.7: (a) Homogeneous atomic sample (bar length: 10 µm). (b) Typical microwave photoassociation signal. The atoms are initially prepared in $|1,0\rangle$ and shined by a mw field of frequency ν. The depletion, maximal at $\nu = \nu_{\mathrm{m}}$, indicates the creation of dimers. The solid line is a fit to the data, using Eq. (3.28). (c) Energy diagram of the multiplicity $\mathcal{B}$ showing the three lines measured from $|f = 1, m_f = 0\rangle$ (blue points) and the fitted model (solid lines). The corresponding total angular momentum projection is indicated on the right. The red line indicates the magnetic-insensitive state $|\Psi_0^{(n=-1)}\rangle$ and the grey lines are forbidden from $|f = 1, m_f = 0\rangle$ by the electronic selection rules.

N	1	3	4	5	9	10	11	14	15
m_F	-1	0	1	-1	0	-1	1	0	1
Ω/Ω_0	< 0.05	< 0.05	< 0.05	0.21	1	< 0.05	0.34	< 0.05	< 0.05

Table 3.3: Total angular momentum projection m_F of the nine lines allowed by the selection rules if starting from a sample in $|f = 1, m_f = 0\rangle$ and their relative coupling Ω/Ω_0 to $|f = 1, m_f = 0\rangle$ for a vertical magnetic field. We attribute to each level of the multiplicity $\mathcal{B}$ a number (N) standing for its position in the energy scale at large magnetic field ($B \sim 2\,\mathrm{G}$), N = 1 being the lowest in energy. The three coloured columns correspond to the transitions we observed. We chose the mw antenna maximising Ω/Ω_0 for each individual line. The values given in this table are computed with $B = 2\,\mathrm{G}$. In practice, Ω/Ω_0 is magnetic field dependent but changes for only a few percent over the range of magnetic field we explored.

$E_0 = h \cdot -24.985(3)\,\mathrm{MHz}$ and $A_{\mathrm{st}} = h \cdot 2.875(11)\,\mathrm{MHz}$ and is shown in Fig. 3.7.c with the experimental points. The energy of a pair of atoms in $|f = 2, m_f = 0\rangle$ at $B = 0$ defines the zero of energy and the errors are computed with a bootstrap analysis.

Once we have a first fit of the experimental values, we can determine what are the other accessible states and their energies. The diagonalisation of the Hamiltonian Eq. (3.17), in addition to giving the dimers energies, gives the angular part of their eigenstates. Using the calibration of the mw field tomography, we can compute the matrix $\hat{W}$ coupling a pair of atoms to a molecular level of the multiplicity $\mathcal{B}$. The coupling of the microwave field to the electronic degree of freedom of a pair of atoms of ^{87}Rb in the electronic ground state ($L = 0$) writes:

$$\hat{W} = \frac{\mu_B g_s}{\hbar} \hat{\boldsymbol{S}} \cdot \boldsymbol{B}_\omega(t). \tag{3.29}$$

The matrix elements $\langle \mathrm{final}|\,\hat{W}|\mathrm{initial}\rangle = \hbar\Omega$ do not give a complete information about the overlap of the states as we do not have any information on the radial part of the initial state $|\mathrm{initial}\rangle$ and final state $|\mathrm{final}\rangle$. However, their relative values can still be useful to predict the strength of the lines. The transition $|f = 1, m_f = 0; f = 1, m_f = 0\rangle \to |\Psi_0^{(n=-1)}\rangle$ has the strongest coupling Ω_0, so we define for each line a relative coupling strength Ω/Ω_0. The rela-

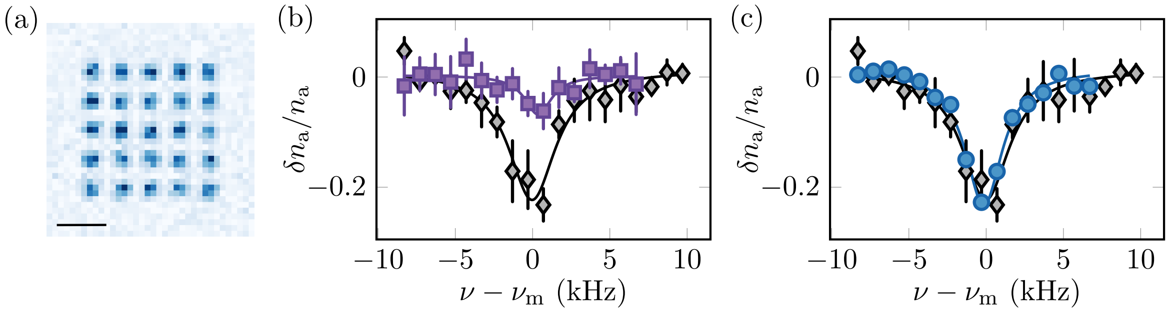

Figure 3.8: (a) Microtraps used for microwave spectroscopy with binary mixtures (bar length: 10 µm). (b) Typical photoassociation signal when the initial state is a binary mixture prepared in a homogeneous potential (violet squares) and in microtraps (black diamonds). We photoassociate a pair of atoms $|f = 1, m_f = -1; f = 1, m_f = +1\rangle$ to a dimer with $m_F = 0$. The depletions is 7 % in a uniform disk and 23 % in microtraps. The shift of the line centre comes from the difference of density in the homogeneous cloud and the microtraps, and will be explained in the next chapter. The mw excitation duration is 5 s and we image only the component $|f = 1, m_f = -1\rangle$. (c) We verify that the centre and width of the line are the same while imaging the other component $|f = 1, m_f = +1\rangle$ (blue points) in microtraps.

tive coupling elements between a pair of atoms in $|f = 1, m_f = 0\rangle$ and the nine lines allowed by the selection rules are given in Tab. 3.3. The coupling with the six unobserved lines are at least five times smaller than the coupling to the lines we measured. It therefore appears that we cannot photoassociate these dimers with the setup described above. In order to confirm this statement, we scanned the mw frequency around the predicted frequency of an allowed transition of smaller coupling. Since we do not observe the bound state, we can set a lower limit on the coupling elements enabling the observation of dimers with our experiment[7]. Once this lower limit is known, one can find which initial state in the hyperfine level $f = 1$ has the highest coupling to which dimer. In practice, we can prepare each pure state or binary mixture in the $f = 1$ manifold with a sequence of mw pulses. It is more convenient to prepare pure states as this reduces the number of mw pulses and ensures better stability. Moreover, in mixtures, the atoms have different magnetic moments so the two components can spatially separate in the presence of a residual magnetic field gradient. As the overlap of the components diminishes, the probability to photoassociate the atoms to a bound state strongly decreases. We therefore privileged pure initial states while searching for the remaining bound state levels. However, some of them can be addressed from mixtures only. In this case, we prepared the atomic sample in an array of microtraps of size $\sim$ 5 µm, to prevent phase separation. An in-situ image of such preparation is shown in Fig. 3.8, as well as a photoassociation signal from a mixture state with and without microtraps. We see clearly that the microtraps preparation allows us to observe signals with larger amplitudes as the depletion is increased from $\sim$ 5 % to $\sim$ 20 %. Indeed, the density in each microtrap is larger and the two components overlap. We also imaged both components to check that the depletion and the line centre are the same, the lines do indeed overlap and are shown in Fig. 3.8.c.

Finally, we could detect the fifteen Zeeman sub-levels of the least bound state $n = -1$ as a function of the magnetic field amplitude. The error on the resonance frequency ν_m is always $\lesssim$ 1 kHz. The simple model we derived allowed us to predict the position of these sub-levels from the measurement of a few lines. We could fit our data and adjust the prediction after

---

[7] By combining all our photoassociation measurement, it appears that our limit is given by $\Omega/\Omega_0 \sim 0.16$.

each new measurement. The tomography of our two mw fields allowed us to find the best initial state and mw antenna to photoassociate each level.

The full Zeeman diagram of the multiplicity $\mathcal{B}$ is shown in Fig. 3.9. The fit of the model to our complete data set gives the position of the triplet at $E_0 = -24.985(1)\,\mathrm{MHz}$ from the continuum of $|f = 1, m_f = 0; f = 2, m_f = 0\rangle$ at $B = 0$. The singlet-triplet coupling is $A_{\mathrm{st}} = h \cdot 2.875(5)\,\mathrm{MHz}$ so the energy splitting between the $F = 1$, 3 and $F = 2$ manifolds at $B = 0$ is $3A_{\mathrm{st}}/8 = h \cdot 1.078(2)\,\mathrm{MHz}$. These results are in good agreement with the measurement of Mordovin [155], given in Tab. 3.1. We define the distance between our experimental results and the best fitted diagram as:

$$\sigma = \sqrt{\frac{1}{N_{\mathrm{points}}} \sum_i \left(\nu_{\mathrm{m},i} - \nu_i^{(\mathrm{fit})}\right)^2}, \tag{3.30}$$

where $\nu_{\mathrm{m},i}$ is the measured resonance frequency, $\nu_i^{(\mathrm{fit})}$ the resonance frequency from the fit and N_{points} is the total number of experimental points. We obtain $\sigma = 3.7\,\mathrm{kHz}$. The distribution of distances between the measured values and the fit is shown in Fig. 3.10 for each individual value of the magnetic field and the global diagram. We give in appendix A the experimental parameters used for the measurement of each level and the experimental points together with their distance from fit.

The second-least-bound rovibrational state of multiplicity $\mathcal{B}$ We also scanned our mw frequency further below the free pair energy of $|f = 1; f = 2\rangle$ to find the second-least-bound rovibrational state, labelled $n = -2$. Similarly, we prepare the atomic sample in the hyperfine level $f = 1$ and the corresponding transition is also represented in Fig. 3.6.

The rovibrational state $n = -2$ with zero orbital angular momentum of the multiplicity $\mathcal{A}$ was observed by Wynar & Freeland et al. [152] and its position is reported in Tab. 3.1. As the scattering length in the hyperfine levels $f = 1$ and $f = 2$ are very close $\sim 100\,a_0$, the position of this bound state in $\mathcal{A}$ gave us a good approximation of the position of the similar bound state in $\mathcal{B}$.

We were able to measure one Zeeman sub-level of the $n = -2$ bound state. We prepared a uniform cloud of atoms in the state $|f = 1, m_f = 0\rangle$ and photoassociated atom pairs to the magnetic-insensitive level $|\Psi_0^{(n=-2)}\rangle$. We used the mw chain RS2, which has the largest field intensity for π-transitions, and whose amplifier has a large bandwidth. We observed atom losses, signature of the photoassociation, $-642.219(1)\,\mathrm{MHz}$ below the continuum of $|f = 1; f = 2\rangle$. The overlap between the bound and free states is much smaller than for the $n = -1$ rovibrational state: the duration of the mw excitation was set to $t = 10\,\mathrm{s}$ to observe a depletion in the atomic sample of $\delta n_{\mathrm{a}}/n_{\mathrm{a}} \sim 15\,\%$. The amplifier power was set to 0.76 times its maximum and this duration is the longest it can stand without undergoing thermal problems. As already mentioned, the coupling strength Ω_0 indicates that this line is the strongest for our setup. Taking into account the line broadening due to the difference of magnetic moment of the free and bound states, we concluded that it was impossible with our experiment to measure the other Zeeman sub-levels. However, as we were able to observe the magnetic-insensitive one, which has a narrow linewidth, we can compare its properties to the $n = -1$ magnetic-insensitive level. This will be presented in the next chapter.

Comparison to universal models In the first section of this chapter, we discussed the universality of the bound states energy. The ^{87}Rb least-bound state is not close enough to the dissociation threshold (i.e. the scattering length is not large enough) for the universal relation Eq. (3.11):

$$E = -\frac{\hbar^2}{2m_{\mathrm{r}}a^2} \tag{3.31}$$

to give a good approximation of its energy. Indeed, the latter expression predicts the least-bound state to have an energy of $\sim -h \cdot 4\,\mathrm{MHz}$, where we measured $\sim -h \cdot 25\,\mathrm{MHz}$. We also described the van der Waals universality: if the interatomic potential has many bound states and is well-described by a van der Waals potential at large-distance, then the least-bound states energies are given by Eq. (3.12):

$$E_j \approx -28.65(j_d - j)^3 E_{\mathrm{vdW}}. \tag{3.32}$$

The integer j indicates the j-th bound state with $E_{j-1} < E_j$. In practice, j_d is not an integer but its integer part, $\mathrm{E}[\,j_d\,]$, gives the total number of bound states. Using these notations, the energies of the two least-bound states $n = -1$ and $n = -2$ correspond to $j = \mathrm{E}[\,j_d\,]$ and $j = \mathrm{E}[\,j_d\,] - 1$ respectively and they write:

$$E_{(n)} = -28.65\left[j_d - \mathrm{E}[\,j_d\,] - (n+1)\right]^3 E_{\mathrm{vdW}}. \tag{3.33}$$

Using the value of $C_6 = 4635\,\mathrm{a.u.}$ and the energies of the two least-bound states $E_{(n=-1)} = h \cdot 24.985\,\mathrm{MHz}$ and $E_{(n=-2)} = h \cdot 642.219\,\mathrm{MHz}$, we find:

$$E_{(n=-1)} \quad \longrightarrow \quad j_d - \mathrm{E}[\,j_d\,] = 0.522, \tag{3.34}$$

$$E_{(n=-2)} \quad \longrightarrow \quad j_d - \mathrm{E}[\,j_d\,] = 0.540. \tag{3.35}$$

The two values of $j_d - \mathrm{E}[\,j_d\,]$ are close but not equal. This mismatch is explained by the fact that the van der Waals model relies only on the first term of the multipolar expansion of the electromagnetic interactions between the two atoms, as mentioned in Sec. 3.1.1. The discrepancy between the two values should vanish by taking into account the effect of the other terms of the expansion. If we take the average value $j_d - \mathrm{E}[\,j_d\,] \approx 0.531$, we find two energies distant by $\sim 1\,\mathrm{MHz}$ and $\sim 11\,\mathrm{MHz}$ from the energies $E_{(n=-1)}$ and $E_{(n=-2)}$ respectively.

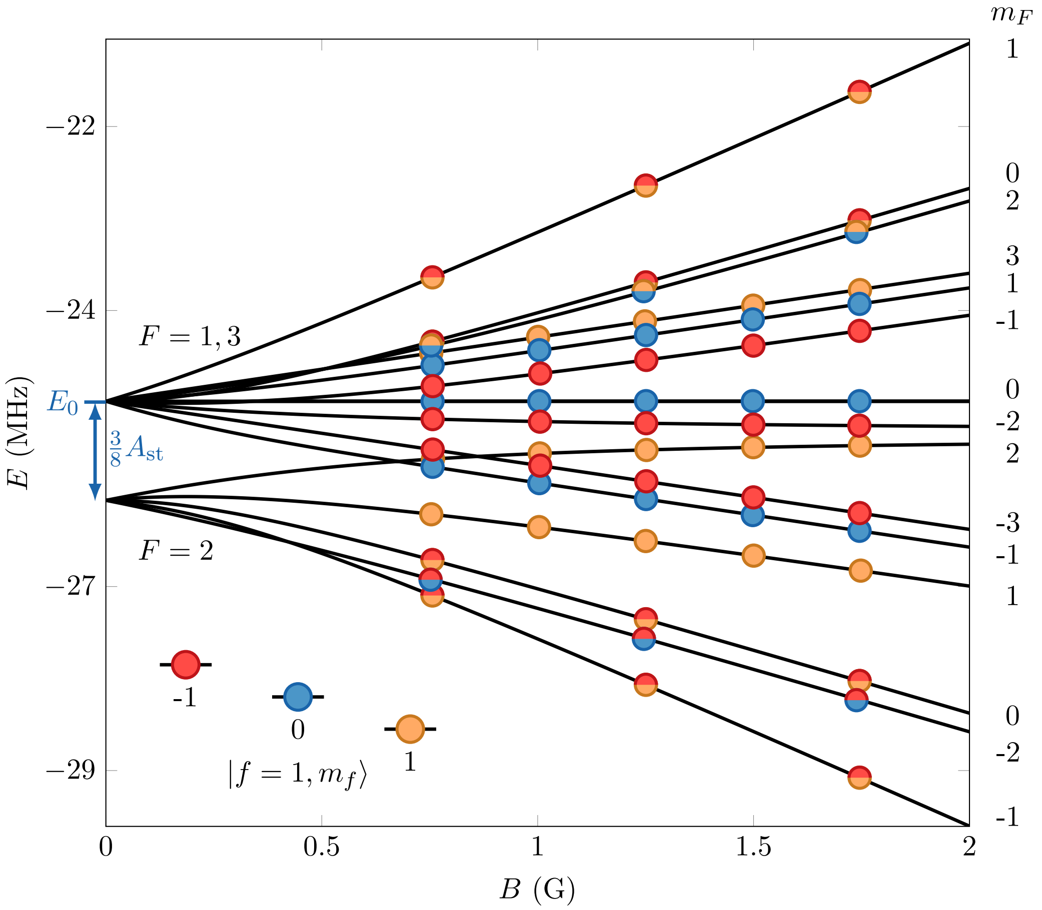

Figure 3.9: Zeeman diagram of the least bound state of the ^{87}Rb $\{f = 1; f = 2\}$ manifold. The different color of the experimental points represent the initial atomic state from which photoassociation is performed. It could be either a pure sample of atoms in $|f = 1, m_f = 0, \pm 1\rangle$ (monochrome points) or a binary mixture of two of these hyperfine states (bi-chrome points). The value of the projection of the total angular momentum m_F is shown on the right of each level. Solid lines are a fit with the phenomenological model with only two free parameters: the energy of the triplet at $B = 0$, E_0, and the splitting between the $F = 1, 3$ and the $F = 2$ manifold at $B = 0$.

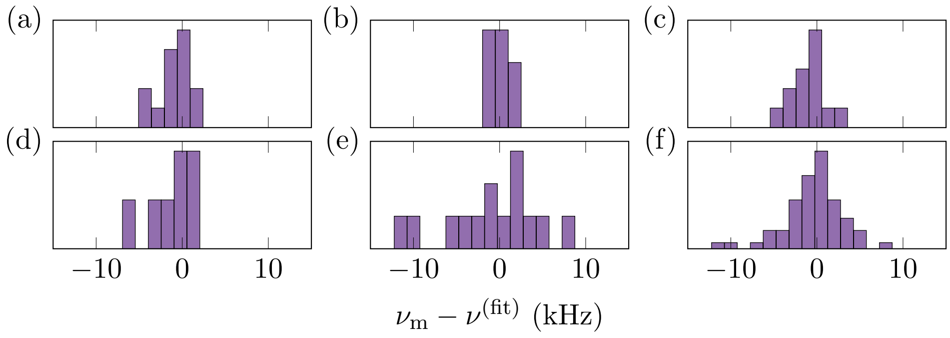

Figure 3.10: (a)-(e) Histograms of the distance between the experimental points and the fit for individual values of the magnetic field: 0.75 G, 1 G, 1.25 G, 1.5 G and 1.75 G. (f) Histograms of the distance between the experimental points and the fit for all the magnetic field values probed. The histograms are normalised and the bar width is fixed to 1.5 kHz.

3.3 Conclusion

In this chapter, we first introduced the interaction potential. We derived of the interaction potential for the simplest atom pair: H_2. We then briefly discussed its extension to alkali atoms. The calculation of these potentials shows the existence of two channels: a singlet potential and a triplet potential. In the case of ultracold gases, the relevant eigenstates are described by a few numbers: the scattering length a, which fully describes the collisions, and the range R_{vdW} of the van der Waals potential, dominant at large interatomic distance, which defines the weakly bound dimers relative energies. This allows us to simplify the expression of the interaction potential. Remarkably, the so-called van der Waals universality emphasises that these numbers, i.e the scattering length and the positions of the weakly bound states, define an ensemble which can be known from the measurement of one of its elements. This property motivates the study of the energy positions of the least-bound states of the atomic species, as they provide information on their interaction potentials and scattering properties. We described therefore an experimental method to study the spectroscopy of bound states: the photoassociation. Originally introduced with optical excitations to photoassociate atoms with excited or ground state molecules, radio-frequency- and microwave-induced photoassociation is also used to study ground state molecules. We also briefly discussed the role of the least-bound states in scattering resonances, such as Fano-Feshbach resonances.

We performed high-resolution mw-induced photoassociation in the electronic ground state of ^{87}Rb. We photoassociate pairs of atoms initially in the hyperfine level $f = 1$ to dimers with one atom in $f = 1$ and the other in $f = 2$ and with zero orbital angular momentum. We measured the complete Zeeman diagram of the least-bound rovibrational state and one Zeeman sub-level of the second-least-bound rovibrational state. We introduced a phenomenological model to describe a rovibrational state and its hyperfine and Zeeman diagram. This model is then fitted to our data with two free parameters: an energy offset and a coupling between the singlet and triplet potentials. It reproduces well our measurement and can be used to predict the positions of the Zeeman sub-levels, based on the knowledge of some of them.

4

High-precision photoassociation and measurement of the atom-dimer interaction

In a sample hosting isolated atoms and dimers at very low temperature, binary interactions between atoms and dimers are described as s-wave interactions and are associated with an atom-dimer scattering length a_{ad}. The existence of a universal relation between atom-atom and atom-dimer scattering lengths in bosonic systems remains an open question. For fermionic systems close to the unitary regime, however, the scattering length a is sufficient to calculate the atom-dimer scattering length a_{ad}. The three-body fermionic system has been studied for homo- and heteronuclear Fermi-Fermi mixtures [160–164] or Bose-Fermi mixtures [165–167] and the atom-dimer scattering length has been shown to depend on a and the mass balance. Effects of confinement on a_{ad} were also studied [168, 169]. Furthermore, the dimer-dimer scattering length a_{dd} is also determined by the scattering length a [170, 171].

In the case of bosonic systems, many works have focused on the vicinity of a scattering resonance $|a| \to +\infty$. This regime is of particular interest to study the Efimov effect [24] which predicts the presence of an infinite number of three-body bound states, or trimers, whose energy levels follow a geometric scaling determined by a *three-body parameter*. The atom-dimer scattering length a_{ad} is indeed of particular interest to look for Efimov trimers and parameters, as an atom-dimer scattering resonance is expected when a trimer merges into the two-body continuum. First studied in the case of ^{4}He [172, 173] and subsequently generalised to other species [174–176], a_{ad} depends on a and the three-body parameter in this regime and for low-energy collisions.

The existence of a van der Waals universal relation between a and a_{ad}, i.e. a relation that does not require knowledge of the core potential, was discussed by Giannakeas & Greene [177]. They computed the atom-dimer scattering length for two separable potentials: a pure van der Waals potential, with then an infinity of bound states, and a van der Waals potential with a soft-core and of tunable number of bound states b. The authors showed that the atom-dimer scattering length computed with the soft-core potential converges to the one computed with the van der Waals potential for $b \gtrsim 5$. A similar work was performed by Mestrom et al. using adiabatic hyperspherical representation and binary collisions described by a Lennard-Jones potential ($V(r) = C_{12}/r^{12} - C_6/r^6$) [178].

Experimental characterisation of atom-dimer interactions are mostly performed by measuring the inelastic losses in atom-dimer mixtures [179–189]. Atom-exchange reactions $A_2 + B \to A + AB$ have also been observed [190–193]. Atom-dimer line shifts and broadening as a function of the scattering length a have also been observed with light-heavy fermion dimers in a bath of heavy fermions. The computation of the atom-dimer scattering amplitude in such systems showed the important role of p-waves in the scattering process [194]. More recently, elastic collisions have also been studied for sympathetic cooling of molecules [195].

In this chapter, we describe features of interactions between atoms and dimers created by mw-induced photoassociation and present a hight-precision measurement of the associated atom-dimer scattering length a_{ad}. The photoassociation spectroscopy of the two least-bound rovibrational states ($n = -1, -2$) of ^{87}Rb, pairing an atom in the hyperfine level $f = 1$ with another in $f = 2$, showed the existence of a Zeeman sub-level magnetic-insensitive at first order, labelled $|\Psi_0^{(n)}\rangle$. While working at near zero temperature already eliminates the broadening of the line due to the kinetic energy distribution, the magnetic field insensitivity of this state further reduces the width of this line by eliminating the broadening due to magnetic fluctuations. This state is then of particular interest to perform high-precision measurement of its energy displacement with respect to the atomic bath characteristics for instance.
In the first section, we characterise the magnetic-insensitive lines $\mathrm{M}_{|n|}$: $|f = 1, m_f = 0; f = 1, m_f = 0\rangle \to |\Psi_0^{(n)}\rangle$. We observe a density-dependence of these lines that we attribute to atom-dimer interactions and from which we deduce, in the second section, the atom-dimer scattering length a_{ad}. Finally, we briefly discuss the possibility of observing mw-induced Feshbach resonances.

4.1 High-precision photoassociation spectroscopy

We detail, in this section, the measurement of the frequency shift of the lines M_1 and M_2 with the density and their typical width. We deduce from these measurements the lifetime and creation rate of the molecules. Taking advantage of the narrow linewidths of these transitions, we also characterise the photoassociation signal and its scaling with the probed experimental parameters.

4.1.1 Creation rate of the dimers

As described in Sec. 3.2.2, we perform photoassociation and observe the creation of molecules through the atomic losses. In order to characterise the creation rate of the dimers, let us distinguish the different loss mechanisms at play.
First, considering an assembly of free atoms in the hyperfine level $f = 1$, there exist two loss mechanisms: three-body recombinations and one-body losses due to background collisions. These loss mechanisms are well-known and were studied by Burt et al. [196]. If we now consider an atomic cloud of free atoms in the hyperfine level $f = 2$, they undergo as well losses due to three-body recombinations [197] and background collisions but, in addition, they experience hyperfine-changing two-body collisions. These two-body collisions are induced by dipole-dipole interactions and involve hyperfine transitions $|f = 2\rangle \to |f = 1\rangle$. The collision partners are then lost due to the release of the kinetic energy $\sim h \cdot 6.8\,\text{GHz}$ in the process.
We now come back to the case where we create dimers by pairing one atom in $f = 1$ with another in $f = 2$ from an initial cloud of free atoms in $f = 1$. Once the dimer is created, the two paired atoms are not detected anymore by our imaging and the dimer can decay via inelastic collisions with free atoms or undergo hyperfine relaxation following the same process described for atoms in $f = 2$. Therefore, the loss of free atoms in the initial state due to the creation of dimers scale as two-body losses.

Here, we aim at characterising the losses due to the creation of dimers only. We then study the atom losses in the state $|1\rangle \equiv |f = 1, m_f = 0\rangle$ with and without photoassociation.
Atoms in $|1\rangle$ with low density n_{a} mostly experience background collisions scaling as one-body

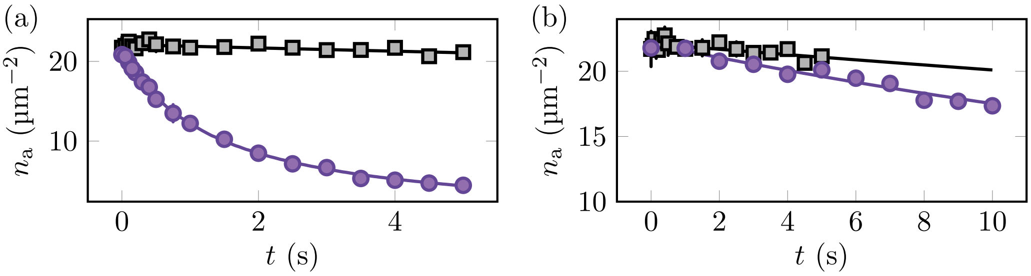

Figure 4.1: Atom losses in state $|1\rangle$ (black squares (a)-(b)) are well-described by one-body losses (solid black lines) at low densities. In the presence of a mw field resonant with the line to $n = -1$ (a) and $n = -2$ (b), the creation of dimers induces two-body losses (violet points) adjusted with Eq. (4.2) (solid violet lines).

losses. The evolution of the surface density in time is then written - excluding the creation of dimers:

$$\frac{\mathrm{d}n_\mathrm{a}}{\mathrm{d}t} = -\frac{1}{\tau}n_\mathrm{a}, \qquad n_\mathrm{a}(t) = n_\mathrm{a}(0)\exp(-t/\tau), \tag{4.1}$$

where τ is the characteristic lifetime of the atoms. Equivalently, the evolution of the surface density n_a when shining a mw field of frequency ν close to resonance with a bound state n, i.e including the losses due to creation of dimers, writes:

$$\left.\frac{\mathrm{d}n_\mathrm{a}}{\mathrm{d}t}\right|_\mathrm{mw} = -\beta_{(n)}n_\mathrm{a}^2 - \frac{1}{\tau}n_\mathrm{a}, \qquad n_\mathrm{a}(t) = \frac{n_\mathrm{a}(0)\exp(-t/\tau)}{1 + n_\mathrm{a}(0)\beta_{(n)}\tau[1-\exp(-t/\tau)]} \tag{4.2}$$

where $\beta_{(n)}$ is the time-independent loss coefficient of the bound state n and characterises the actual two-body losses due to the creation of dimers.
We prepare a sample of atoms in the state $|1\rangle$ with an initial surface density $n_\mathrm{a}(t=0) \sim 20\,\mu\mathrm{m}^{-2}$ and measure its surface density evolution while shining a resonant mw field and no mw field. The results are shown in Fig. 4.1 with fits to the data. We first extract the lifetime τ from a fit to the data without mw field using Eq. (4.1) and inject it in Eq. (4.2) to fit the data obtained with resonant mw. The evolution of n_a, in the presence of a mw field whose frequency ν is resonant to the transitions $\mathrm{M}_{|n|}$, is well-described by two-body losses. We find $\tau = 105\,\mathrm{s}$, $\beta_{(n=-1)} = 3.5\cdot10^{-2}\,\mu\mathrm{m}^2.\mathrm{s}^{-1}$ and $\beta_{(n=-2)} = 4/3\cdot7\cdot10^{-4}\,\mu\mathrm{m}^2.\mathrm{s}^{-1}$, where the factor 4/3 corrects for the reduced power of the amplifier used for addressing the level $n=-2$ (see previous chapter). We confirm that the coupling between the free state $|1;1\rangle$ and the bound state $n=-1$ is much larger than the one with the state $n=-2$ as the loss coefficient $\beta_{(n=-1)}$ is ~ 40 times larger than $\beta_{(n=-2)}$.

The lifetime measurement of atoms in $|1\rangle$, shown in Fig. 4.1, is valid for low densities. For higher densities, as mentioned above, atoms in $|1\rangle$ undergo three-body losses, so the losses are faster than predicted with $\tau = 105\,\mathrm{s}$. However, for short probing times $\lesssim 300\,\mathrm{ms}$, the effect of three-body losses at high densities remains negligible.

4.1.2 Density dependence of the bound state energies

The least-bound state $n=-1$ When starting with free atoms in state $|1\rangle$, the coupling with the bound state $|\Psi_0^{(n=-1)}\rangle$ is the largest achievable with our mw antennas[1] and allows

---

[1] The relative coupling strengths are given in appendix A for all the lines.

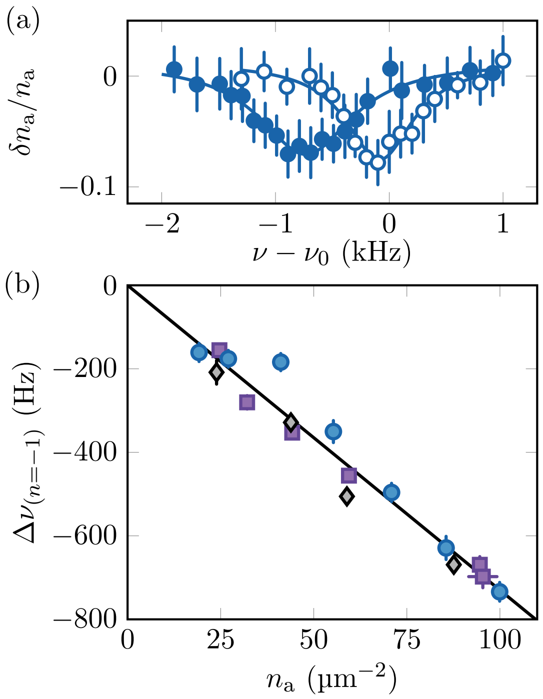

Figure 4.2: Density dependence of the line M_1. (a) Photoassociation signals for an initial density $n_\mathrm{a} = 27\,\mu\mathrm{m}^{-2}$ (empty points) and for an initial density $n_\mathrm{a} = 100\,\mu\mathrm{m}^{-2}$ (filled points). The depletion is fixed to $8\,\%$. (b) Variation of the resonant frequency $\Delta\nu_{(n=-1)}$ with the initial density n_a. The probing time is adjusted to keep a depletion constant to $8\,\%$ (blue points), $14\,\%$ (black diamonds) and $20\,\%$ (violet squares). The data collapse onto a single curve, adjusted by a linear function (black solid line).

us to observe photoassociation lines with depletions $\delta n_\mathrm{a}/n_\mathrm{a} \sim 10\,\%$ with mw excitations of duration $\delta t \lesssim 250\,\mathrm{ms}$. Because the probing times are short, we work in a perturbative regime. Moreover, as shown in the previous section, there are almost no one-body losses of atoms in $|1\rangle$ within this duration. As the depletion is exclusively due to the creation of dimers and remains small, it ensures that the modification of the density during the mw excitation is negligible. These experimental conditions, added to the fact that we work with a uniform in-plane density n_a, allows us to measure, with high precision, the effect of the density on the linewidth and the line frequency. More precisely:

(i) the in-plane density is uniform so there is no additional broadening.

(ii) the one-body losses during the excitation duration δt are close to zero, so the depletion we observe is only due to dimer creation. The density measured after shining an off-resonance mw field is then equal to the initial density $n_\mathrm{a}(t = 0) = n_\mathrm{a}(t = \delta t)$.

(iii) we work with small depletions so that the density of the sample does not change significantly during the mw excitation, even when the frequency ν is close to resonance.

We vary the surface density n_a from $20\,\mu\mathrm{m}^{-2}$ to $100\,\mu\mathrm{m}^{-2}$ and measure the resonant frequency of the transition M_1. We adjust the excitation duration δt to fix the depletion $\delta n_\mathrm{a}/n_\mathrm{a}$ at resonance. The loss signal is fitted with the Lorentzian function Eq. (3.28) and we extract the centre of the line ν_m for which the depletion is maximum and its full width at half maximum Γ. We measure the variation of the peak frequency $\Delta\nu_{(n=-1)} = \nu_\mathrm{m} - \nu_0$ with the surface

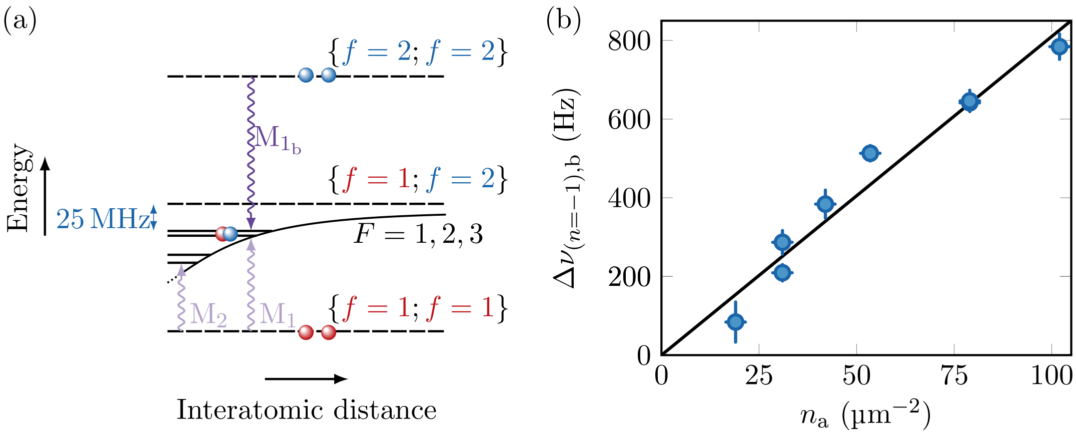

Figure 4.3: Density dependence of the line $|2;2\rangle \to |\Psi_0^{(n=-1)}\rangle$ which is represented in (a) with the transition M_{1_b}. The variation of the resonance frequency $\Delta\nu_{(n=-1),b}$ with the initial density of atoms in $|2\rangle$ is shown in (b). The depletion is fixed to 8 %. The solid black curve is a linear fit to the data.

density n_a and introduce the resonant frequency in the zero density limit $\nu_0 = \nu_m(n_a = 0)$. Fixing the depletion to $\delta n_a/n_a \sim 8\,\%$, we observe a linear shift of $\Delta\nu$ with the surface density n_a of the atomic sample, which goes up to $\Delta\nu_{(n=-1)} \sim 800\,\text{Hz}$ for $n_a = 100\,\mu\text{m}^{-2}$. We performed the same measurement for two other depletion values: $\delta n_a/n_a \sim 14\,\%, 20\,\%$. The three curves are shown in Fig. 4.2. The duration of the excitation lies within the range 50-255 ms depending on the density n_a and the depletion $\delta n_a/n_a$. All the data collapse on a same curve, which confirms that the chosen depletions are small enough to stay in the perturbative regime. We fit a linear function to all the data and find $\nu_0 = -24.984\,23(2)\,\text{MHz}$, from the hyperfine level $|f=1; f=2\rangle$ at zero magnetic field, and $\Delta\nu_{(n=-1)}/n_a = -7.3(3)\,\text{Hz}\cdot\mu\text{m}^2$.

We perform a similar measurement by addressing the state $|\Psi_0^{(n=-1)}\rangle$ from a cold sample of atoms in $|2\rangle \equiv |f=2, m_f=0\rangle$, as represented by the transition M_{1_b} in Fig. 4.3.a . In Chapter 3, this possibility had been eliminated because of the short lifetime of the atoms in the hyperfine level $f=2$. Indeed, the atomic gas in $|2\rangle$ experiences two- and one-body losses and their characteristic lifetime is $\sim 100\,\text{ms}$. Therefore, if we use mw excitations of similar durations on atoms in $|2\rangle$, the atomic density would be strongly reduced by hyperfine relaxation and the condition (ii) is no longer valid. However, it appears that the coupling strength of the line M_{1_b} is stronger than the M_1 one: shining the mw field during 4-9 ms is long enough to observe the transition $|2;2\rangle \to |\Psi_0^{(n=-1)}\rangle$ with a depletion $\delta n_a/n_a \sim 8\,\%$. Within this range of excitation durations, the atom losses without mw are negligible and we can measure the variation $\Delta\nu_{(n=-1),b}$ of the peak frequency with the surface density. The experimental data are shown in Fig. 4.3.b and we find a linear shift of slope $\Delta\nu_{(n=-1),b}/n_a = 8.1(9)\,\text{Hz}\cdot\mu\text{m}^2$ with $\nu_{0,b} = -24.984\,59(5)\,\text{MHz}$. The change of sign in the frequency variation comes from the fact that the frequency of the transition M_{1_b} is larger than the atom-atom transition frequency, whereas the transition M_1 has a smaller frequency than the atom-atom transition (see Fig. 4.3.a).

The second least-bound state $n = -2$ We reported in Sec. 3.2.2 the measurement of the magnetic-insensitive level of the second least-bound state, labelled $n=-2$. The coupling strength of the line $M_2 \equiv |1;1\rangle \to |\Psi_0^{(n=-2)}\rangle$ was, however, much smaller. We remind

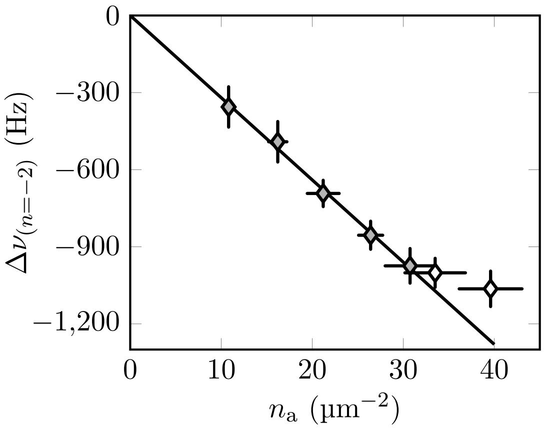

Figure 4.4: Variation of the resonance frequency of the line M_2 with the density. The horizontal error bars indicate the density range scanned during the excitation because of one-body background collisions of free atoms. For initial densities higher than $n_\mathrm{a} \gtrsim 30\,\mathrm{µm}^{-2}$ (empty diamonds), the off-resonance losses reaches $\gtrsim 15\,\%$ for a probing time of $\delta t = 10\,\mathrm{s}$ and the variation stops being linear. We measure the frequency shift for small densities (black full diamonds) by adjusting a linear function to the data (solid line).

that the probing time was 10 s and that we set the amplifier to three quarters of its maximum value, to prevent heating of the amplifier. Since we need much longer probing time ($\delta t = 10\,\mathrm{s}$) to observe the transition M_2, the presence of off-resonance three-body losses in $|1\rangle$ invalidates the condition (ii) for large densities. Indeed, for an initial surface density larger than $n_\mathrm{a} \gtrsim 30\,\mathrm{µm}^{-2}$ the atoms losses without mw for $\delta t = 10\,\mathrm{s}$ are larger than $\gtrsim 15\,\%$. We therefore restrict ourselves to the density range 10-30 µm^{-2} to study the shift of the resonance frequency $\Delta\nu_{(n=-2)}$ with the density. We fix the excitation time to $\delta t = 10\,\mathrm{s}$ as the depletion at resonance is always $\sim 15\,\%$ for the densities that we probe and the results are shown in Fig. 4.4. We observe again a linear shift with the density and a fit with a linear function gives $\Delta\nu_{(n=-2)}/n_\mathrm{a} = 32(1)\,\mathrm{Hz{\cdot}µm}^2$ and $\nu_0 = -642.219\,27(2)\,\mathrm{MHz}$. We also probed atomic samples with larger densities: as the density increases, the range of density explored during the excitation broadens. We observe a "saturation" of the peak frequency shift and the variation with density stops being linear. The interpretation of these data is complex and we do not take them into account in our study.

As for the least-bound state ($n = -1$), we expect the transition $|2;2\rangle \to |\Psi_0^{(n=-2)}\rangle$ to have a stronger coupling. However, even considering dimer creation ten times faster, the probing duration would be too long ($\delta t = 1\,\mathrm{s}$) to avoid large two-body atomic losses in $|2\rangle$ and thus we did not try (yet) to observe this transition.

A similar shift of the resonance with the density was observed by the group of D.J. Heinzen [152, 153] for the $n = -2$ bound state of the multiplicity $\{f = 1; f = 1\}$. We interpret, as they did, this density-dependence within a mean-field approach, although in our case, working with mw-induced photoassociation and homogeneous clouds simplifies greatly the problem and allows to a better precision. In the next paragraph, we complete the description of our photoassociation signal and the characterization of the state $|\Psi_0^{(n=-1)}\rangle$, whose position was measured precisely and deep in the perturbative regime. The mean-field interpretation of the density-shift described above is detailed further below, in Sec. 4.2.

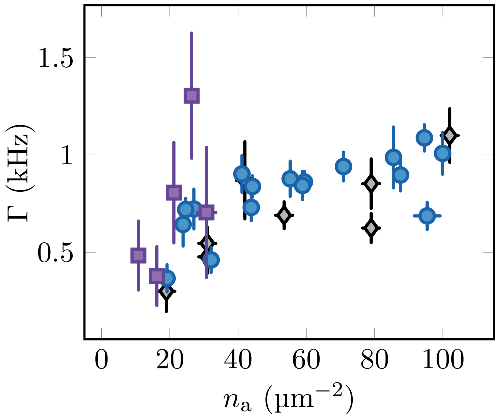

Figure 4.5: Variation of the line width Γ with the initial density n_a of the transitions M_1 (blues points), M_{1_b} (black diamonds) and M_2 (violet squares).

4.1.3 Characterisation of the photoassociation signal and lifetime of the dimer

We described in Sec. 3.2.2 and Sec. 4.1.1 the photoassociation signal with a Fermi golden rule considering two-body losses:

$$\delta n_a/n_a \propto n_a \delta t, \tag{4.3}$$

when neglecting the effect of the other loss mechanisms than photoassociation.We expect therefore the ratio

$$\mathcal{S}_1 = \frac{\delta n_a/n_a}{n_a \delta t} \tag{4.4}$$

to be constant for a given transition. In practice, however, we observed that the width of the transitions is also density-dependent. We show in Fig. 4.5 the evolution of the linewidth of the three transitions to the two magnetic-insensitive bound states: M_1, M_{1_b} and M_2. We observe line widths always smaller than $\lesssim 1$ kHz for the probed densities. This finite width can be attributed to the lifetime of the dimers. They can decay through two channels: via two-body inelastic collisions with free atoms or undergoing dipolar relaxation, the two atoms then separate by releasing the hyperfine energy. The width Γ of the three free-bound transitions collapse onto a single curve, however with a significant noise level. The lowest width we measure is $\Gamma = 300(104)$ Hz for a density of $n_a \sim 20$ µm^{-2}.

The coupling between a stable state and an unstable state, here the molecular state of finite lifetime $\propto 1/\Gamma$, affects the stability of the stable state (here the atomic state) and thus its loss rate [198]. The linewidth of the molecular state therefore contributes to $\delta n_a/n_a$ and, at resonance $\delta n_a/n_a \propto 1/\Gamma$ (see [198] for a complete demonstration). This dependence, hidden in Eq. (4.3), must be taken into account explicitly since the linewidth Γ varies with the density. The scaling of the losses is then described by:

$$\delta n_a/n_a \propto n_a \delta t/\Gamma, \qquad \mathcal{S}_2 = \frac{\delta n_a/n_a \Gamma}{n_a \delta t}, \tag{4.5}$$

where $\Gamma = \Gamma(n_a)$ and the ratio $\mathcal{S}_2$ should be constant for all the probed densities and depletions. We calculate $\mathcal{S}_1$ and $\mathcal{S}_2$ for each individual point and show them, for the three transitions of interest, in Fig. 4.6. We observe as expected a variation of $\mathcal{S}_1$ with the density, which vanishes when taking into account the variation of the linewidth with the density in $\mathcal{S}_2$. The constant $\mathcal{S}_2$ takes different values for the three transitions as they undergo different

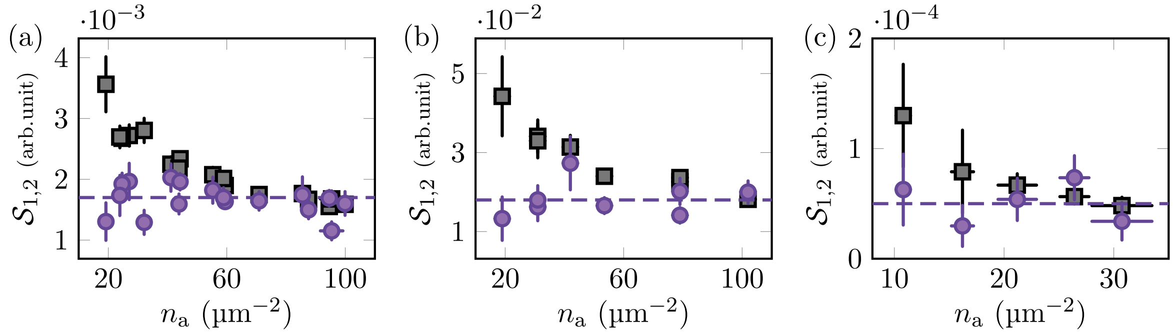

Figure 4.6: Variation of $\mathcal{S}_1$ (black squares) and $\mathcal{S}_2$ (violet points) with the initial density n_a for the transitions M_1 (a), $\mathrm{M}_{1_\mathrm{b}}$ (b) and M_2 (c). The quantities are calculated with the individual parameters of each points.

coupling strengths. We find $\mathcal{S}_{2_{(n=-1),b}}/\mathcal{S}_{2_{(n=-1)}} \sim 11$ and[2] $\mathcal{S}_{2_{(n=-1)}}/\mathcal{S}_{2_{(n=-2)}} \sim 3/4 \cdot 33$ and validate our Fermi gold rule approach.

4.2 Atom-dimer interaction and scattering length

We observed in Sec. 4.1.2 a clear dependence of the resonance frequency of the atom-dimer transition on the density n_a of the atomic bath. We interpret it as a feature of atom-dimer interactions with a mean-field approach and measure the associated atom-dimer scattering length a_ad.

Atoms and dimer density distributions We consider an initial sample of ultracold atoms in $|1\rangle$ or $|2\rangle$. The surface density n_a is uniform and we recall that the atoms are vertically confined in a harmonic potential of frequency $\omega_z/2\pi$ of which they occupy the ground state, labelled $n_z = 0$. The vertical density profile is then a Gaussian, which yields the 3D density profile:

$$\rho_\mathrm{a}(z) = \frac{n_\mathrm{a}}{\ell_z\sqrt{\pi}}\exp(-z^2/\ell_z^2), \qquad \int \rho_\mathrm{a}(z)\,\mathrm{d}z = n_\mathrm{a}, \tag{4.6}$$

with $\ell_z = \sqrt{\hbar/m\omega_z}$. We photoassociate pairs of these atoms to produce dimers. We decompose the initial and final states to their centre of mass (com) and relative (rel) motion states, $|\mathrm{com}\rangle \otimes |\mathrm{rel}\rangle$:

$$|\mathrm{initial}\rangle = |\boldsymbol{K}, n_z = 0\rangle \otimes |\phi_{\boldsymbol{k}}\rangle, \tag{4.7}$$

$$|\mathrm{final}\rangle = |\boldsymbol{K}, n_z' = 0\rangle \otimes |\phi_\mathrm{d}\rangle, \tag{4.8}$$

where $\boldsymbol{K}$ and $\boldsymbol{k}$ are wave vectors in the horizontal plane, $\phi_{\boldsymbol{k}}$ is the scattering state of the quasi-2D problem [65], and n_z' is the vibrational number associated with the level of the vertical harmonic potential occupied by the dimer. We assume that the oscillation angular frequency of the dimer in the vertical trap ω_z' is equal to the atoms one, $\omega_z = \hbar/(m\ell_z^2)$, which corresponds to a doubled spring constant if the dimer mass writes $m_\mathrm{d} = 2m$. If this were not the case and $\omega_z' \neq \omega_z$, we would expect to observe a comb of photoassociation lines, resulting from the projection of $|n_z\rangle$ into the dimer eigenbasis $|n_z'\rangle$. As we observe single lines with no

---

[2] $\mathcal{S}_{2_{(n=-2)}}$ is weighted by 3/4 to take into account that the amplifier power is $\sim 3/4$ the power used to address the other transitions.

side-bands, the centre of mass is not affected by the mw field and we write $n'_z = n_z = 0$. The centre of mass motion states writes the same whether the atoms are interacting or not, so we focus on the non-interacting system for simplicity. A non-interacting pair of atoms, labelled 1 and 2, is described by the following Hamiltonian and wave function:

$$\hat{H} = \sum_{j=1,2} \left[\frac{\hat{p}_j^2}{2m} + \frac{1}{2} m \omega_z^2 z_j^2 \right], \qquad \Psi(z_1, z_2) = \frac{1}{\ell_z \sqrt{\pi}} \exp[-(z_1^2 + z_2^2)/(2\ell_z^2)], \tag{4.9}$$

where the first term of the Hamiltonian is the kinetic energy and the second one the potential energy. We define the centre of mass and reduced variables:

$$Z = \frac{1}{2}(z_1 + z_2), \qquad z = z_1 - z_2, \qquad P = p_1 + p_2, \qquad p = \frac{1}{2}(p_1 - p_2), \tag{4.10}$$

in order to decompose the Hamiltonian and the wave function into two contributions, the centre of mass and the relative motions:

$$\hat{H} = \hat{H}_{\mathrm{com}} + \hat{H}_{\mathrm{rel}}, \qquad \hat{H}_{\mathrm{com}} = \frac{P^2}{2M} + \frac{1}{2} M \omega_z^2 Z^2, \qquad \hat{H}_{\mathrm{rel}} = \frac{\hat{p}^2}{2m_{\mathrm{r}}} + \frac{1}{2} m_{\mathrm{r}} \omega_z^2 z^2, \tag{4.11}$$

$$\Psi(Z, z) = \frac{1}{\ell_z \sqrt{\pi}} \exp[-Z^2/\ell_z^2] \exp[-z^2/(4\ell_z^2)]. \tag{4.12}$$

We find then the probability distribution of the centre of mass of two particles, narrower by a factor $\sqrt{2}$ than the single atom distribution Eq. (4.6):

$$f_{\mathrm{d}}(Z) = \frac{\sqrt{2}}{\ell_z \sqrt{\pi}} \exp(-2Z^2/\ell_z^2), \qquad \int f_{\mathrm{d}}(Z)\, \mathrm{d}Z = 1, \tag{4.13}$$

and write the dimer 3D density in the sample of area S: $\rho_{\mathrm{d}}(Z) = f_{\mathrm{d}}(Z)/S$.

Resonance frequency of the photoassociation The photoassociation rate is described by the Fermi golden rule Eq. (4.5). This process: (i) brings the energy coupling the free and bound state in the zero-density limit to the sample, couples two free atoms to a dimer and therefore (ii) removes two free atoms of the initial state to create a dimer, (iii) which interacts with the atom bath. We assume that the density of molecules is small enough to neglect dimer-dimer interactions. We write the energies provided by the photoassociation:

(i) $h\nu_0$: the zero-density limit energy coupling the free and bound state,

(ii) $-2\mu_{\mathrm{a}}$: since it removes two atoms of the bath, with the atomic chemical potential $\mu_{\mathrm{a}} = g_{\mathrm{aa}} n_{\mathrm{a}}$,

(iii) $E_{\mathrm{ad}} = g_{\mathrm{ad}} \int \rho_{\mathrm{a}}(z) f_{\mathrm{d}}(z)\, \mathrm{d}z$: the atom-dimer interaction energy.

The atomic interaction parameter g_{aa} writes

$$g_{\mathrm{aa}} = \frac{\hbar^2}{m} \frac{\sqrt{8\pi}}{\ell_z} a_{f_1 f_2}, \tag{4.14}$$

with $a_{f_1 f_2}$ the scattering length describing the collision between an atom in the hyperfine level f_1 and an atom in the hyperfine level f_2. We also introduced the atom-dimer interaction parameter g_{ad} which we write, assuming s-wave interactions because of the low temperature:

$$g_{\mathrm{ad}} = \frac{2\pi\hbar^2}{M_{\mathrm{r}}} a_{\mathrm{ad}}, \qquad M_{\mathrm{r}} = \frac{m \cdot m_{\mathrm{d}}}{m + m_{\mathrm{d}}} = \frac{2m}{3}, \tag{4.15}$$

with M_r the reduced mass of the system {atom + dimer} and a_ad the s-wave atom-dimer scattering length. We calculate the atom-dimer interaction energy using Eqs. (4.6) and (4.13) and find:

$$E_\mathrm{ad} = g_\mathrm{ad}\sqrt{\frac{2}{3}}\frac{n_\mathrm{a}}{\ell_z\sqrt{\pi}} = \mu_\mathrm{a}\frac{\sqrt{3}}{2}\frac{a_\mathrm{ad}}{a_{f_1f_2}}. \tag{4.16}$$

The variation of the resonance frequency $\Delta\nu = \nu_\mathrm{m}(n_\mathrm{a}) - \nu_0$ then reads:

$$h\Delta\nu = E_\mathrm{ad} - 2\mu_\mathrm{a} = \mu_\mathrm{a}\left(\frac{\sqrt{3}}{2}\frac{a_\mathrm{ad}}{a_{f_1f_2}} - 2\right). \tag{4.17}$$

This derivation leads to a linear density-dependence of the photoassociation resonance frequency from which we can calculate the atom-dimer scattering length:

$$a_\mathrm{ad} = \frac{2}{\sqrt{3}}a_{f_1f_2}\left(2 + \frac{h\Delta\nu}{\mu_\mathrm{a}}\right), \qquad \mu_\mathrm{a} = g_\mathrm{aa}n_\mathrm{a}. \tag{4.18}$$

We calibrate the chemical potential μ_a with an independent experiment, using Ramsey interferometry as described in Sec. 2.2.9. We measure the mean-field shift $\Delta\nu_\mathrm{a}$ of the magnetic-insensitive atomic transition $|1\rangle \to |2\rangle$:

$$h\Delta\nu_\mathrm{a} = \mu_\mathrm{a}\frac{a_{22} - a_{11}}{a_{f_1f_2}}, \tag{4.19}$$

and the values of the scattering lengths are estimated from [98] to $a_{11} = 100.9\,a_0$, $a_{22} - a_{11} = -6\,a_0$, and $a_{12} - a_{11} = -2\,a_0$. We insert this result into Eq. (4.18) and obtain an expression independent of any systematic error on the density calibration:

$$a_\mathrm{ad} = \frac{4}{\sqrt{3}}a_{f_1f_2} + \frac{2}{\sqrt{3}}\frac{\Delta\nu}{\Delta\nu_\mathrm{a}}(a_{22} - a_{11}) \tag{4.20}$$

Results We performed Ramsey interferometry in the same experimental conditions as for photoassociation, and found $\Delta\nu_\mathrm{a}/n_\mathrm{a} = -0.52(1)\,\mathrm{Hz{\cdot}\mu m^2}$. Combining this result with the three measured atom-dimer frequency shifts given in Sec. 4.1.2, we find:

$$\mathrm{M}_1: \quad a_\mathrm{ad}^{(n=-1)} = 184(2)\,a_0, \tag{4.21}$$

$$\mathrm{M}_{1_\mathrm{b}}: \quad a_\mathrm{ad}^{(n=-1),\mathrm{b}} = 165(7)\,a_0, \tag{4.22}$$

$$\mathrm{M}_2: \quad a_\mathrm{ad}^{(n=-2)} = 21(7)\,a_0. \tag{4.23}$$

These three atom-dimer scattering lengths are remarkably different from the impulse scattering length $a_\mathrm{ad}^\mathrm{impulse}$, calculated by summing independently the scattering amplitudes of each atom of the dimer with an atom of the bath. Considering an atomic bath in the hyperfine level f_1, the dimers created by the photoassociation are composed of two atoms in the hyperfine level f_1 and f_2 respectively and the impulse scattering length yields:

$$a_\mathrm{ad}^\mathrm{impulse} = \frac{M_\mathrm{r}}{m_\mathrm{r}}(a_{f_1f_1} + a_{f_1f_2}), \tag{4.24}$$

$$a_\mathrm{ad}^\mathrm{impulse}[\mathrm{M}_1] = \frac{4}{3}(a_{11} + a_{12}), \tag{4.25}$$

$$a_\mathrm{ad}^\mathrm{impulse}[\mathrm{M}_{1_\mathrm{b}}] = \frac{4}{3}(a_{22} + a_{12}), \tag{4.26}$$

First introduced for nucleon physics [199], it predicts $a_{\mathrm{ad}}^{\mathrm{impulse}}[\mathrm{M}_1] = 266\,a_0$ and $a_{\mathrm{ad}}^{\mathrm{impulse}}[\mathrm{M}_{1_\mathrm{b}}] = 258\,a_0$ while addressing the bound state $|\Psi_0^{(n=-1)}\rangle$ from $|1\rangle$ and $|2\rangle$ respectively. Studies on Fermi-Fermi and Bose-Fermi mixtures have also led to results differing from $a_{\mathrm{ad}}^{\mathrm{impulse}}$. Zhang et al. proposed an explanation for this discrepancy for Fermi dimers colliding with Bosons [167]: by noting that the Born approximation at first order gives the same result, they suggest that the discrepancy may come from higher orders. For instance, the Fermi dimer could survive many collisions with the bosonic bath, or could break into the scattering state after a first collision and then recombine after a second collision.

The scattering lengths describing the interaction of $|\Psi_0^{(n=-1)}\rangle$ and a bath of atoms in $|1\rangle$ and $|2\rangle$ are close to each other, like the atom-atom scattering length describing these baths, a_1 and a_2. These similarities, combined, could be consistent with the existence of a "van der Waals universal relation" linking the atom-dimer scattering length a_{ad} to the atomic scattering length a_f, for the least-bound states. However, the large difference between the atom-dimer scattering length of the states $|\Psi_0^{(n=-1)}\rangle$ and $|\Psi_0^{(n=-2)}\rangle$ interacting with a bath of atoms in state $|1\rangle$ reveals the importance of the radial wave function of the dimer in the scattering process.

We have previously mentioned a similar measurement performed by the group of D.J. Heinzen, in the second-to-least bound state ($n = -2$) of the multiplicity $\mathcal{A}\left(\{f = 1; f = 1\}\right)$ [152]. They deduced the scattering length $a_{\mathrm{ad}} = -180(150)a_0$ from the density shift they observed, but the inhomogeneity of the atomic sample makes the analysis more involved.

4.3 Microwave-induced Feshbach resonances

The existence of a magnetic-insensitive shallow bound state with a strong mw coupling to the atomic state $|1\rangle$ (which is also magnetic-insensitive) encourages the search for a mw-induced Feshbach resonance, introduced by Papoular et al. [146]. Since we have in hand a high-resolution spectroscopic tool composed of our two mw antennas, we indeed tried to observe such resonance.

We performed Ramsey interferometry on the magnetic-insensitive transition $|1\rangle \to |2\rangle$ with the mw antenna RS1, as described in Sec. 2.2.9, while dressing the atoms in $|1\rangle$ with a second mw field, provided by the antenna labelled RS2, with frequency ν_{d}. We remind that in the presence of interactions in the quantum gas, the transition frequency of $|1\rangle \to |2\rangle$ is shifted from its Bohr frequency. The frequency shift of the atomic transition, using mw $\pi/2$-pulses, follows Eq. (4.19) which writes here:

$$h\Delta\nu_{\mathrm{a}} = \mu_{\mathrm{a}}\frac{a_2 - a_1}{a_1}. \tag{4.27}$$

We start with an ultracold sample of atoms in $|1\rangle$ of fixed surface density n_{a} and perform Ramsey interferometry. We send two mw $\pi/2$-pulses separated by a probing time fixed to 10 ms to avoid phase separation of the two species $|1\rangle$ and $|2\rangle$. During the Ramsey spectroscopy, we dress the atoms with a mw field of frequency ν_{d}, and measure the atomic frequency shift $\Delta\nu_{\mathrm{a}}$. We scan the frequency ν_{d} around the resonance frequency of the transition M_1 and, from the measurement of $\Delta\nu_{\mathrm{a}}$, calculate the scattering length of atoms in $|1\rangle$, a_1.

The probing time must be short enough to keep low enough the atomic losses due to the production of dimers. In this case, the variation of the atomic density is negligible and does not affect the measurement of a_1. As we already show in Eq. (4.5), the losses depend on the density and the probing duration so that, for a given excitation time, the lower the density the lower the losses. However, the Ramsey signal is also proportional to the density, so that a balance must be found between these two criteria.

Unfortunately, we were not able to observe a resonance of the scattering length a_1 by following this protocol. We can confidently set an upper bound of the possible signal to $\Delta a_1 \lesssim 0.1\, a_0$. However, our study of the least-bound states paves the way to the observation of mw-induced FRs on more suitable atomic species, whose triplet and singlet scattering lengths have more distant values (as caesium, sodium or potassium), or on atom chips experimental setups to benefit from stronger mw field [200].

4.4 Conclusion

We have taken advantage of the presence of a magnetic-insensitive state $|\Psi_0^{(n)}\rangle$ in rovibrational bound states of ^{87}Rb to perform high-precision measurement of the photoassociation signals. We calibrated the dimer creation rate for the two least-bound states $n = -1, -2$. We validated the Fermi golden rule, used to characterise the photoassociation losses, and ensured that we perform all the measurements in a perturbative regime. Remarkably, our measurement is precise enough to observe a clear dependence of the resonance frequency and the linewidth of the transitions with the density of the atomic sample. We interpreted this density-dependence as a consequence of the interaction between the dimers and the atomic bath. We derived a mean-field model and measured the atom-dimer scattering lengths a_{ad} associated with the three transitions M_1, $\mathrm{M}_{1_\mathrm{b}}$ and M_2. Our measurement of the interaction of atoms in states $|1\rangle$ or $|2\rangle$ with the least-bound state $|\Psi_0^{(n=-1)}\rangle$ motivates the existence of a universal relation between the atom-dimer scattering length a_{ad} and the scattering length a, in the limit of shallow bound states. The combination with the measurement on the second-to-least bound state $|\Psi_0^{(n=-2)}\rangle$ shows the influence of the radial wave function. Finally, we proposed an experimental protocol for the observation of microwave-induced Feshbach resonances. Despite the precision of our measurements and our large mw couplings, we were not able to observe such a resonance.

Part III

Zero-temperature superfluid fraction in a density-modulated 2D Bose gas

5

Superfluidity in spatially modulated systems at zero temperature

Fundamental properties of superfluid states of matter, discovered in 1938, are subtle and diverse. They are usually characterised by a reduction of the moment of inertia and a frictionless flow. These latter conditions describing the emergence of a superfluid state are so general that, in the 1970's, the question of superfluidity was raised for solids, i.e. spatially ordered systems whose density $n(\boldsymbol{r})$ shows strong variations over distances of the order of the atomic spacing. The possibility of Bose-Einstein condensation in a crystalline solid at low temperature had already been studied by Chester, and the author had demonstrated that a crystalline solid can exhibit a Bose-Einstein condensate if it has a finite fraction of vacancies [201]. Later in 1970, Leggett went further and emphasised that an insulating solid could show a so-called *non-classical rotational inertia*[1] and that the associated superfluid fraction f_s would be bounded from above to a low value [36]. Considering N atoms in dimension D in a system of size L^D which undergoes a breaking of translational invariance in the direction x_1, i.e for instance a density modulation along x_1, Leggett estimated the superfluid fraction by evaluating the change of energy of the system as an answer to twisted boundary conditions (TBC) along x_1: $\phi(x_1+L, x_2, ..., x_D) = \exp(\mathrm{i}\theta)\phi(x_1, x_2, ..., x_D)$, and finds the following upper bound for the superfluid fraction:

$$f_\mathrm{s} \leq \frac{L^{D+1}}{N \int \frac{\mathrm{d}x_1}{n(x_1)}}. \tag{5.1}$$

In the case of an atomic cloud of homogeneous density, this relation simplifies to $f_\mathrm{s} \leq 1$. These discussions introduced the notion of a *supersolid* state of matter which describes a quantum state where particles form a spatially ordered structure, implying a *spontaneous* breaking of translational symmetry, but also show superfluid properties as they flow with zero viscosity for instance [202–204]. First predicted for solid helium, the observation of such state and/or properties has been an experimental challenge and has remained elusive for a long time [205–208]. Recently, observations of supersolid properties were reported in ultracold quantum gases experiments. First, two experimental groups observed simultaneously the emergence of supersolid properties by "crystallising" an ultracold gas while maintaining the inherent superfluidity of the Bose-Einstein condensate (BEC). The group from ETH Zurich coupled a BEC to the modes of two optical cavities, enhancing the atomic interactions such that the atoms spontaneously crystallised [209]. After atomic BECs were predicted to present a stripe phase with supersolid properties in the presence of spin-orbit coupling [210–214], researchers at MIT created an effective spin-orbit coupling on a two-component BEC which

---

[1] This refers to the decrease of the moment of inertia compared to a classical fluid, mentioned above.

produced the predicted density modulation of this stripe phase [215]. Supersolid phases have been observed later in dipolar Bose gases for which supersolidity arises from the competition of dipole-dipole and contact interactions without external enhancement [216–218]. While the first observations of such supersolid phase were one-dimensional, robust 2D supersolids were produced recently, also in dipolar gases [219, 220].

Although this area of research has received a lot of attention and despite recent observations, the historical result of Leggett Eq. (5.1) has never been tested experimentally. However, this result stands for density modulated quantum gases without necessarily imposing to work with supersolid phases and should then give an estimate of the superfluid fraction in systems where the breaking of the translational symmetry is not spontaneous but externally imposed. In this chapter, we propose an experimental protocol to measure the superfluid fraction in a 2D density-modulated ultracold Bose gas and compare it to the upper bound found by Leggett Eq. (5.1). This work was performed in collaboration with theoreticians at the University of Trento, S. Stringari and S. Roccuzzo.

In a first section, we derive the result of Leggett for a weakly-interacting 2D Bose gas at zero temperature and with a density modulation imposed by an external potential. Leggett's result is a static estimate of superfluidity, whereas superfluidity is intrinsically linked to the notion of transport. For this reason, we compare Leggett's integral with a measure of transport in the same system system. At finite temperature, the superfluid fraction and, by extension, the superfluid transition can be probed by measuring the propagation of sound in a system, i.e. phonon excitations. In the second section, we briefly summarise the results on sound propagation gathered for quantum gases. Afterwards, we write the expected zero-temperature sound velocities in a 2D density-modulated system from a thermodynamic model. Finally, gathering our results, we propose an experimental protocol, well-adapted to our experimental setup, to probe the superfluid fraction upper bound derived by Leggett. The implementation of this protocol and the results obtained will be the subject of the next chapter.

5.1 Superfluid fraction in a 2D modulated planar Bose gas

We consider a 2D Bose gas of N weakly-interacting atoms of mass m and at zero temperature $T = 0$. The interactions are described by the dimensionless parameter $\tilde{g}$. The gas is confined in a potential $V(\boldsymbol{r})$ that we consider here periodic along the direction y with a period λ, but homogeneous in the direction x. We describe the atomic cloud with a classical field $\psi(\boldsymbol{r})$ normalised as

$$\int |\psi(\boldsymbol{r})|^2 \,\mathrm{d}^2 r = N, \tag{5.2}$$

and whose energy functional reads:

$$E[\psi] = \int \left[\frac{\hbar^2}{2m} |\boldsymbol{\nabla}\psi|^2 + \frac{\hbar^2}{2m} \tilde{g} |\psi(\boldsymbol{r})|^4 + V(\boldsymbol{r}) |\psi(\boldsymbol{r})|^2 \right] \mathrm{d}^2 r. \tag{5.3}$$

The classical field approach was introduced in Chapter 1 and, at zero temperature, the ground state ψ_0 of the system satisfies the Gross-Pitaevskii (GP) equation introduced in Eq. (1.22)

$$-\frac{\hbar^2}{2m} \boldsymbol{\nabla}^2 \psi_0 + \frac{\hbar^2}{m} \tilde{g} |\psi_0|^2 \psi_0(\boldsymbol{r}) + V(\boldsymbol{r}) \psi_0(\boldsymbol{r}) = \mu_0 \psi_0(\boldsymbol{r}), \tag{5.4}$$

where μ_0 is the chemical potential.

In this section, we are interested in the estimate of the Leggett integral in the presence of the periodic potential. As mentioned in Chapter 1, superfluidity can be established either by imposing a constraint on the momentum of the system, i.e. placing ourselves in the moving frame, or by using twisted boundary conditions (TBC). Both methods are equivalent within a gauge transformation. In the first instance, we derive Leggett's analysis and therefore use the TBC as he originally did. Anticipating on the next section, we use the gauge transformation to write the relation between the superfluid fraction f_s of the system in the presence of a density modulation and the associated effective mass m^*.

5.1.1 Leggett's integral for a zero-temperature weakly-interacting Bose gas

We study the effect of the modulation along the y-axis on the superfluid character of the sample by imposing TBC. We determine the energy variation created by imposing an infinitesimal phase twist θ on the field ψ along the direction y, such that:

$$\psi(x+L,y)=\psi(x,y), \qquad\qquad \psi(x,y+L)=\exp(\mathrm{i}\theta)\psi(x,y), \tag{5.5}$$

where $L\times L$ is the area of the cloud and L is a multiple of the potential period λ. This energy difference between the "twisted" ground state and the "untwisted" ground state ψ_0 of the system defines the superfluid fraction f_s as [85]:

$$E(\theta)=E(0)+\frac{\hbar^2\theta^2 N}{2mL^2}f_{s,y}+\mathcal{O}(\theta^4). \tag{5.6}$$

Note that following this definition, the superfluid fraction f_s is a *tensor*. We work on the proper basis of this tensor, given by the axes x and y here, so its off-diagonal terms are zero. More precisely, considering twisted boundary conditions along y gives access to the component $f_{s,y}$ while twisting the boundary conditions along x yields the superfluid component $f_{s,x}$. In this section, we consider a zero-temperature anisotropic system where the potential $V(\boldsymbol{r})$ is spatially-modulated along y and homogeneous along x. As the density is kept homogeneous along the x-axis, the superfluid fraction component along x is equal to[2] $f_{s,x}=1$. We then study the component of the superfluid fraction tensor $f_{s,y}$ along the spatial modulation and look for the increase of energy $E(\theta)$ when twisting the field ψ along y.

In a density-phase approach, we look for the ground state ψ_θ, satisfying the TBC, written as:

$$\psi_\theta(\boldsymbol{r})=a_\theta(\boldsymbol{r})\exp[\mathrm{i}S_\theta(\boldsymbol{r})], \tag{5.7}$$

where $a_\theta(\boldsymbol{r})$ is a real function satisfying periodic boundary conditions with $a_0^2(\boldsymbol{r})=\psi_0^2(\boldsymbol{r})=n_0(\boldsymbol{r})$ and $S_\theta(\boldsymbol{r})$ is a phase profile. We define the associated velocity field as

$$\boldsymbol{v}_\theta(\boldsymbol{r})=\frac{\hbar}{m}\boldsymbol{\nabla}S_\theta. \tag{5.8}$$

Using Eq. (5.3) and Eq. (5.7), the energy functional Eq. (5.6) writes for such a twisted wave function:

$$E(\theta)=\int\left[\frac{\hbar^2}{2m}|\boldsymbol{\nabla}a_\theta|^2+\frac{\hbar^2}{2m}\tilde{g}|a_\theta|^4+V(r)|a_\theta|^2+\frac{m}{2}\boldsymbol{v}_\theta^2(\boldsymbol{r})a_\theta^2(\boldsymbol{r})\right]\mathrm{d}^2r. \tag{5.9}$$

---

[2] This is a result of Landau two-fluids model but the analysis we perform on the modulated axis in this chapter also applies to the x-axis, along which the potential V is homogeneous, and leads to the same result $f_{s,x}=1$.

In order to find the expression of the superfluid fraction, we minimize the energy functional $E(\theta)$. We introduce two Lagrangian variables μ and β to take into account the two constraints imposed by the normalisation Eq. (5.2) and the definition of the velocity field Eq. (5.8):

$$\int a_\theta^2(\boldsymbol{r})\,\mathrm{d}^2r = N, \tag{5.10}$$

$$\int_0^L \boldsymbol{v}_\theta(\boldsymbol{r})\cdot\boldsymbol{e}_y\,\mathrm{d}y = \frac{\hbar}{m}\theta, \tag{5.11}$$

and we keep only the twisted direction y, since the other one is invariant by translation. We minimize then the energy functional

$$E[a_\theta] + L\left[\frac{m}{2}\int_0^L v_\theta^2(y)a_\theta^2(y)\,\mathrm{d}y - \mu\int_0^L a_\theta^2(y)\,\mathrm{d}y - \beta\int_0^L v_\theta(y)\,\mathrm{d}y\right], \tag{5.12}$$

where $E[a_\theta]$ embeds the terms where only a_θ contributes. The minimization of the latter energy functional with respect to v_θ yields the velocity field

$$v_\theta(y) = \frac{\beta}{m a_\theta^2(y)} = \frac{\beta}{m n_0(y)} \qquad \xrightarrow{\text{Eq. (5.11)}} \qquad v_\theta(y) = \frac{\hbar\theta}{m n_0(y)}\frac{1}{\int\frac{\mathrm{d}y}{n_0(y)}}, \tag{5.13}$$

where we wrote $a_\theta(y)$ at the zero-th order in θ. By re-introducing the other axis, we find the contribution of the velocity field to $E(\theta)$ (Eq. (5.9)):

$$\frac{m}{2}\int \boldsymbol{v}_\theta^2(\boldsymbol{r})a_\theta^2(\boldsymbol{r})\,\mathrm{d}^2r = \frac{\hbar^2\theta^2}{2m}\frac{L}{\int\frac{dy}{n_0(y)}}. \tag{5.14}$$

The minimization of Eq. (5.12) with respect to a_θ leads to the following equation:

$$-\frac{\hbar^2}{2m}\frac{\mathrm{d}^2a_\theta}{\mathrm{d}y^2} + \frac{\hbar^2}{m}\tilde{g}a_\theta^3 + \left(V + \frac{m}{2}v_\theta^2\right)a_\theta - \mu a_\theta = 0. \tag{5.15}$$

This equation can be understood as the GP equation Eq. (5.4) with a source term $mv_\theta^2/2$. We remind that the GP equation is minimised for $\psi_0 = a_0$, i.e. when the boundary condition along y is not twisted $\theta = 0$. We look then for a solution of Eq. (5.15) in powers of θ with the form

$$a_\theta = a_0 + \delta a_\theta, \tag{5.16}$$

where δa_θ accounts for the corrections due to the source term. The latter is of order two in θ (see Eq. (5.13)) and thus the correction δa_θ will be of order θ^2 at least. The change $a_0 \to a_0 + \delta a_\theta$ has then no contribution of order θ^2 to $E[\psi]$ Eq. (5.3), since the contributions will be of order θ^4 at least.

Finally, there is no additional contribution of order two or less in θ coming from the minimization with respect to a_θ and $E(\theta) - E(0)$ then writes

$$E(\theta) - E(0) = \frac{\hbar^2\theta^2}{2m}\frac{L}{\int\frac{\mathrm{d}y}{n_0(y)}}. \tag{5.17}$$

The superfluid fraction component $f_{s,y}$ is then given by

$$f_{s,y} = \frac{L^3}{N\int\frac{\mathrm{d}y}{n_0(y)}} = \frac{1}{\langle n_0\rangle\langle 1/n_0\rangle}, \tag{5.18}$$

with

$$\langle n_0\rangle = \frac{N}{L^2} = \frac{1}{L}\int n_0(y)\,\mathrm{d}y, \qquad\qquad \langle 1/n_0\rangle = \frac{1}{L}\int \frac{\mathrm{d}y}{n_0(y)}. \tag{5.19}$$

We find that the superfluid fraction $f_{s,y}$ in a weakly-interacting 2D Bose gas of modulated density at $T=0$, and therefore described by the Gross-Pitaevskii equation, is given by the integral that Leggett found as an upper limit on the superfluid fraction studying solids.

5.1.2 Effective mass

We discussed the derivation of the superfluid fraction in the general case of an anisotropic system, with a potential inhomogeneous in y but homogeneous in the other direction (x). We now take into account the *periodicity* of the potential along y, characterised by a spatial period λ. In this context, one can write the solution of the GP equation with the so-called Bloch form:

$$\psi_q(\boldsymbol{r}) = \exp(\mathrm{i}\boldsymbol{q}\cdot\boldsymbol{r})u_q(\boldsymbol{r}), \qquad\qquad \boldsymbol{q} = q\boldsymbol{e}_y, \tag{5.20}$$

with q the quasi-momentum defined over the first Brillouin zone $|q| \leq \pi/\lambda$ and where $u_q(x)$ is a periodic function, of same periodicity than the potential, and solution of

$$\frac{(\hat{\boldsymbol{p}}+\hbar\boldsymbol{q})^2}{2m}u_q(\boldsymbol{r}) + \frac{\hbar^2}{m}|u_q(\boldsymbol{r})|^2u_q(\boldsymbol{r}) + V(\boldsymbol{r})u_q(\boldsymbol{r}) = \mu(q)u_q(\boldsymbol{r}). \tag{5.21}$$

In this case, the transport in the system is given by the Bloch band structure. We consider here the zone around $q\sim 0$, where the band curvature is fully characterised by the effective mass m_y^*, defined from a variation in the energy Eq. (5.21) due to a small change in q around $q=0$:

$$E(q) = E(0) + \frac{\hbar^2q^2N}{2m_y^*} + \mathcal{O}(q^3). \tag{5.22}$$

In order to link this formalism to the result previously obtained with TBC, we perform a well-known gauge transform to write solutions of the GPE $\tilde{\psi}$ from the solutions respecting TBC ψ:

$$\tilde{\psi}(\boldsymbol{r}) = \exp(\mathrm{i}\boldsymbol{A}\cdot\boldsymbol{r}/\hbar)\psi(\boldsymbol{r}), \qquad\qquad \boldsymbol{A} = -\frac{\hbar\theta}{L}\boldsymbol{e}_y, \tag{5.23}$$

such that $\tilde{\psi}$ satisfies periodic boundary conditions:

$$\tilde{\psi}(x+L,y) = \tilde{\psi}(x,y), \qquad\qquad \tilde{\psi}(x,y+L) = \tilde{\psi}(x,y). \tag{5.24}$$

The GP equation satisfied by $\tilde{\psi}_\theta = \exp(\mathrm{i}\boldsymbol{A}\cdot\boldsymbol{r}/\hbar)\psi_\theta(\boldsymbol{r})$ then writes

$$\frac{(\hat{\boldsymbol{p}}-\boldsymbol{A})^2}{2m}\tilde{\psi}_\theta(\boldsymbol{r}) + \frac{\hbar^2}{m}|\tilde{\psi}_\theta(\boldsymbol{r})|^2\tilde{\psi}_\theta(\boldsymbol{r}) + V(\boldsymbol{r})\tilde{\psi}_\theta(\boldsymbol{r}) = \mu_\theta\tilde{\psi}_\theta(\boldsymbol{r}), \tag{5.25}$$

with $\hat{\boldsymbol{p}} = -\mathrm{i}\hbar\boldsymbol{\nabla}$.

The functions $\tilde{\psi}_\theta$ and u_q satisfy now the same periodic boundary conditions and normalization condition. Moreover, the equations Eq. (5.21) and Eq. (5.25) are similar within the substitution

$$\hbar q\,\boldsymbol{e}_y \quad \longleftrightarrow \quad -\boldsymbol{A} = \frac{\hbar\theta}{L}\boldsymbol{e}_y. \tag{5.26}$$

The general relation Eq. (5.6) used in the previous section can be written with this substitution:

$$\frac{\theta}{L} \;\longleftrightarrow\; q, \qquad E(\theta) - E(0) = \frac{\hbar^2\theta^2 N}{2mL^2} f_{s,y} \;\longleftrightarrow\; E(q) - E(0) = \frac{\hbar^2 q^2 N}{2m} f_{s,y}, \tag{5.27}$$

and we obtain by identification with Eq. (5.22):

$$f_{s,y} = \frac{m}{m_y^*}. \tag{5.28}$$

Finally, we find that in the case of a periodic density-modulation the Leggett integral Eq. (5.18) is equal to the ratio of the mass m and effective mass m_y^* along the spatially-modulated direction.

5.2 Sound propagation in quantum gases

We introduced in Chapter 1 the notion of sound in quantum gases at zero temperature from the Bogoliubov excitation spectrum

$$\hbar\omega_k = \frac{\hbar^2}{2m}\sqrt{k^2(k^2 + 4\tilde{g}n)}. \tag{5.29}$$

The frequencies ω_k of the excitation modes associated with plane waves of wave vector k describe, in the low-k regime $k \ll k_\mathrm{c} \sim 1/\xi$, the propagation of phonons and simplify to the linear relation $\omega_k \sim c_0 k$ where $c_0 = \hbar\sqrt{\tilde{g}n}/m$ is the so-called Bogoliubov speed of sound. In the case of finite temperature, the superfluid dynamics can be described by the two-fluid model, introduced in 1938 by Tisza [221] and later studied by Landau in 1941 [84]. Superfluids are treated as the superposition of a superfluid and a normal component and the model assumes a local thermodynamic equilibrium ensured by collisions. First introduced for helium, this hydrodynamic model predicts the existence of two sounds: a *first sound* describing a density wave for which the superfluid and normal component oscillate in phase and a *second sound* describing a temperature wave for which the superfluid and normal component oscillate out of phase. The velocity of these sounds depends on the equation of state of the system and on the superfluid fraction f_s.

Such sound waves were predicted in ultracold strongly interacting Fermi gases [222] and were experimentally observed [69, 223, 224]. These systems exhibit sound waves similar to those encountered in liquid helium. The existence of the first and second sound was also predicted for 3D weakly-interacting Bose gases [225] although their nature is strongly modified due to the compressibility of the system. Indeed, the second sound is mainly an oscillation of the superfluid component alone and can be understood as a continuation of Bogoliubov sound. In the limit of dilute Bose gases, this second sound can be related to the superfluid fraction [225, 226]. In the case of 2D weakly-interacting Bose gases, the first and second sound are expected to show a discontinuity at the critical point of the BKT phase transition [227, 228]. The thermodynamic functions of a 2D Bose gas are continuous across the phase transition which makes the measurement of the sound velocity a nice way to determine its critical point. Sound propagation has been observed in Bose gases [68, 229–231], and a

recent experiment in a 2D geometry probed the first and the second sound across the BKT transition [47]. The authors used then the equation of state of the weakly-interacting 2D Bose gas to deduce the superfluid fraction of the atomic cloud. It consists in the first indirect measurement of the superfluid fraction over the transition in 2D Bose gases[3].
In a different context, experiments have been performed with density-modulated superfluid quantum gases to measure the critical velocity for which the frictionless flow vanishes [232]. Superfluids were loaded in moving optical lattices and experiments showed clear signals of the existence of a critical velocity [233–235]. First interpreted as a *classical* superfluid-insulator transition, they revealed the existence of dynamical instabilities [236–242], which have subsequently been a subject of research [243–246]. The existence of Josephson currents were also probed [247, 248]. Other works have highlighted the effect of interactions and/or disorder [249]. In the following, we study the dynamics of a 2D Bose gas loaded in a one-dimensional lattice. However, the experiments described in the following chapter are in a different regime than the cases mentioned above, being far from the tight-binding limit and considering relative atoms-lattice velocities much lower than the Laudau critical velocity $v_\mathrm{L} \sim 2\,\mathrm{mm/s}$.

We aim at writing here the relation between the sound velocity and the superfluid fraction in a 2D Bose gas of modulated density along one direction and at zero temperature $T = 0$. We write in the following a simple model of thermodynamics describing the system in the presence of a sound wave.
We take into account the small but finite thickness d_z of the system along the z-axis and describe it as a cloud of N atoms of mass m in a rectangular box of volume $\mathcal{V} = L \times L \times d_z$ with $d_z \ll L$. The potential $V(\boldsymbol{r})$ is periodic in y with a period λ and homogeneous in the other directions. The average particle density is written $n = N/\mathcal{V}$. We first remind some thermodynamics relations for a fluid at $T = 0$ which link the pressure P, the chemical potential μ, the free energy F and the entropy S:

$$P = \mathcal{F}(n), \qquad \mu = \mathcal{G}(n), \qquad \mathrm{d}F = -S\mathrm{d}T - P\mathrm{d}\mathcal{V} + \mu\mathrm{d}N. \tag{5.30}$$

We now consider a slice of area A in the plane (x, z) and of thickness δy along the y-axis. This atomic slab is of mesoscopic scale and contains $N_\mathrm{slab} = n(y, t)A\delta y$ atoms with $1 \ll N_\mathrm{slab} \ll N$. In order to study the propagation of a sound wave of wave vector $\boldsymbol{q} = q\boldsymbol{e}_y$, we choose the thickness of the slice as $\lambda \ll \delta_y \ll 2\pi/q$ and apply the Newton's equation on the modulated axis y. We describe then the pressure forces on the two faces (x, z) of the atomic slab, placed at $\pm\delta y/2$, and the displacement of these faces which creates a deformation of the slab without losses of atoms. The atomic slab in the modulated direction has a velocity $v(y, t)$ and a kinetic energy per particle of $m_y^* v^2/2$, where the use of the effective mass m_y^* comes from the presence of the modulation. The total effective mass of the slab is written $m^*_\mathrm{slab} = m_y^* N_\mathrm{slab}$. The equations of motion yield:

$$m^*_\mathrm{slab}\frac{\partial v}{\partial t} = A\left[P(y - \frac{\delta y}{2}, t) - P(y + \frac{\delta y}{2}, t)\right], \tag{5.31}$$

$$\delta\mathcal{V}(t + \mathrm{d}t) - \delta\mathcal{V}(t) = A\left[v(y - \frac{\delta y}{2}, t) - v(y - \frac{\delta y}{2}, t)\right]\mathrm{d}t, \tag{5.32}$$

---

[3] Note that there exists no direct measurement of the superfluid fraction yet.

and they simplify to

$$m_y^* n(y,t)\frac{\partial v}{\partial t} = -\frac{\partial P}{\partial y}, \tag{5.33}$$

$$\frac{\delta\mathcal{V}(t+\mathrm{d}t)-\delta\mathcal{V}(t)}{\mathrm{d}t} = A\delta y\frac{\partial v}{\partial y}. \tag{5.34}$$

The deformation of the atomic slab is associated to a change of pressure following Eq. (5.30) so the equation of motion Eq. (5.34) can be written as:

$$\mathrm{d}P = -n\mathcal{F}'(n)\frac{\mathrm{d}\mathcal{V}}{\mathcal{V}}, \qquad \frac{\partial P}{\partial t} = -n\mathcal{F}'(n)\frac{\partial v}{\partial y}. \tag{5.35}$$

Finally, by combining the equations of motion Eq. (5.33) and Eq. (5.35) we obtain the wave equation

$$\frac{m_y^*}{\mathcal{F}'(n)}\frac{\partial^2 v}{\partial t^2} = \frac{\partial^2 v}{\partial x^2}, \tag{5.36}$$

describing the propagation of sound along the y-axis with a velocity

$$c_y^2 = \frac{\mathcal{F}'(n)}{m_y^*}. \tag{5.37}$$

This leads us to a relation linking the sound velocity and the superfluid fraction along y Eq. (5.28):

$$c_y^2 = f_{s,y}\frac{\mathcal{F}'(n)}{m}. \tag{5.38}$$

The same analysis is performed along the x-axis. The only difference is that the potential is homogeneous in this direction, so the equation of motion Eq. (5.33) is written with $m_x^* = m$. The sound velocity along the x-axis c_x reads then $c_x^2 = \mathcal{F}'(n)/m$.
Therefore, the ratio of the speed of sound along and perpendicular to the periodic modulation is independent of $\mathcal{F}'(n)$, i.e. independent of the equation of state and writes

$$\frac{c_y^2}{c_x^2} = \frac{m}{m_y^*}. \tag{5.39}$$

Rigorously, the ratio Eq. (5.39) is equal to the ratio of the superfluid fraction components

$$\frac{c_y^2}{c_x^2} = \frac{m_x^*}{m_y^*} = \frac{f_{s,y}}{f_{s,x}}. \tag{5.40}$$

In our particular case, the potential is modulated along y only and homogeneous along the x-axis, hence we have $m_x^* = m$ and $f_{s,x} = 1$, so that the ratio of the sound velocities actually gives the superfluid fraction along y:

$$\frac{c_y^2}{c_x^2} = f_{s,y}. \tag{5.41}$$

In the following, we write the superfluid fraction along y: $f_\mathrm{s} \equiv f_{s,y}$ as we always have $f_{s,x} = 1$.

5.3 Discussion

In this chapter, we applied the analysis performed by Leggett in 1970 in the context of supersolidity [36] to the case of a weakly-interacting 2D Bose gas at zero temperature and whose density profile n is modulated along y. We found that the superfluid fraction f_s in this system is given by the upper bound found by Leggett for the superfluid fraction in solids:

$$f_\mathrm{s} = \frac{L}{N \int \frac{\mathrm{d}y}{n(y)}}. \tag{5.42}$$

The superfluid density depends on the density profile n_0 of the atomic cloud and more precisely on the density profile along the modulation $n_0(y)$. We also showed that this superfluid fraction is given by the ratio of the effective mass m_y^* along the modulated direction and the mass m:

$$f_\mathrm{s} = \frac{m}{m_y^*}. \tag{5.43}$$

In a second section, we briefly discussed the sound propagation in quantum gases and derived a simple model to describe the sound propagation in the density-modulated weakly-interacting 2D Bose gas at $T = 0$. This simple model led us to a relation between the sound velocity along the two axes of the cloud and the ratio of the effective masses:

$$\left(\frac{c_y}{c_x}\right)^2 = \frac{m}{m_y^*}. \tag{5.44}$$

The experimental setup, described in Chapter 2, allows us to produce a density-modulated gas at $T \sim 0$. This provides an experimental method to test the equality deduced from Eq. (5.43) and Eq. (5.44):

$$\frac{L}{N \int \frac{\mathrm{d}y}{n(y)}} \overset{?}{=} \left(\frac{c_y}{c_x}\right)^2, \tag{5.45}$$

which links Leggett's integral to a transport quantity.

On the one hand, the Leggett integral Eq. (5.42) can be calculated from in-situ measurement of the density profile n of the atomic sample. On the other hand, we propose to measure the sound velocities c_y and c_x along the modulation and perpendicular to the modulation respectively. The description of the experimental method and the analysis we have performed, together with the experimental results, is the subject of the next chapter.

6

Measurement of the superfluid fraction in a density-modulated ultracold Bose gas at zero temperature

The uniform 3D or 2D weakly-interacting Bose gas at zero temperature exhibits Bose-Einstein condensation and superfluid properties. In the two-fluid model, the superfluid density n_s is predicted to be equal to the total density, i.e. the superfluid fraction is $f_\mathrm{s} = 1$. We demonstrated in the previous chapter, by applying the same analysis as Leggett in 1970 [36], that in the presence of a breaking of translational invariance due to a periodic density modulation, the superfluid density is not equal to the total density and the superfluid fraction depends on the amplitude of the modulation. Leggett's results have never been proved experimentally and we describe in this chapter the first comparison of this result to a transport measurement.

In the first section, we describe the experimental protocol to measure the speed of sound in our planar Bose gas. Afterwards, we explain how we impose a density modulation to the atoms and calibrate their response. Finally, Leggett's integral is measured in the density-modulated atomic cloud from the speed of sound and from the in-situ density profiles.

6.1 Sound velocity measurement

Before getting to the heart of the matter, we describe in this section our experimental protocol to measure the sound velocity in a planar ultracold gas. This protocol is independent of the in-plane density profile.

The speed of sound in quantum gases has been the centre of interest of many experimental groups and we already mentioned in the previous chapter some remarkable experiments. Usually, the measurement of the sound velocity is performed by creating an excitation in the system and by monitoring its evolution. The excitation is created with a local deformation on the potential, which can be dynamically driven in time and space or adiabatically imposed and then removed abruptly[1] [47, 68, 69, 224]. The properties of the sound modes are determined from the time evolution of the density distribution, for instance by monitoring the position of the centre of mass.

---

[1] The results of these two protocols were recently numerically compared for a 2D Bose gas across the BKT transition [250].

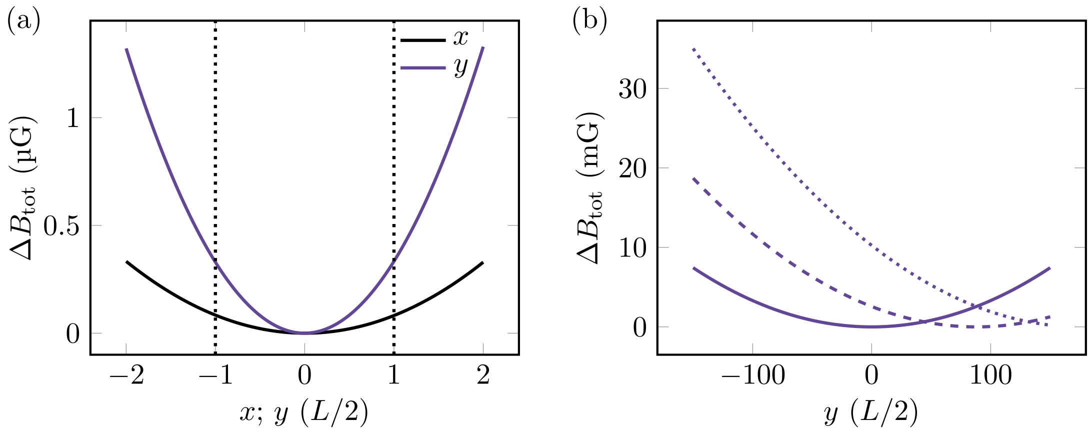

Figure 6.1: Magnitude of the total magnetic field $B_{\rm tot}$ after subtracting the magnetic field at the centre of the cloud $\Delta B_{\rm tot} = B_{\rm tot}(x, y, z) - B_{\rm tot}(0, 0, 0)$ (a) along both axes of the cloud, when the quadrupolar field $\boldsymbol{B_1}$ is centred of the atoms and (b) when we apply a bias field of 0 G (solid curve), 125 mG (dashed curve) and 250 mG (dotted curve) to shift the quadrupolar field centre along y. In (a) the difference between the x and y axes comes from the fact that the MOT coils, used to create the quadrupolar field, are oriented along the y-axis, and thus generate a stronger gradient in this direction.

6.1.1 Excitation of the atomic cloud

Sound propagation in a uniform 2D Bose gas has been studied in 2018 in our group [68]. This measurement was performed by modifying locally the bottom of the 2D box potential. The deformation (shaped as a potential step) was optically imprinted onto the atoms with an intensity modulator (see Chapter 2 for details). Two experimental protocols were explored: a driven regime protocol for which a time-dependent modulation is imposed to the system, or a quench protocol for which the free evolution of the system after a rapid perturbation of the density is monitored.
The protocol we present here will be implemented on atomic clouds whose in-plane density is modulated. We use a quench protocol with a different profile from the ones of 2018, as we imprint here a linear perturbation so that it is uniform across the atomic cloud[2]. We prepare the atoms in a magnetic-sensitive state and we adiabatically raise a magnetic field gradient which creates a linear perturbation. The abrupt extinction of the magnetic field gradient creates an excitation of the atomic cloud. This method has been implemented in other groups [47, 251] and is detailed in the following.

Magnetic-induced excitation We prepare the atoms in the magnetic-sensitive state $|f = 1, m_f = -1\rangle$ and cool them down to the minimal temperature accessible $T \lesssim 20\,\mathrm{nK}$. The atoms are confined in the horizontal plane (xy) in a box shaped as a square of side $L = 40\,\mu\mathrm{m}$. A vertical magnetic field $B = 3\,\mathrm{G}$ is applied and defines the quantization axis.

---

[2] Note that the ideal case would be to imprint the fundamental mode of the box potential, i.e. a sine perturbation. This could be performed by using the independent DMD with grey levels for instance. However, this DMD will be used to create a spatially-modulated potential onto the atoms (see Sec. 6.2) and it would be experimentally too challenging to imprint both the spatial modulation and the excitation from a single DMD. A third DMD could be installed on our setup, but this possibility was ruled out for practical reasons. Moreover, as we work in the perturbative regime, it does not matter that we do not imprint the fundamental mode.

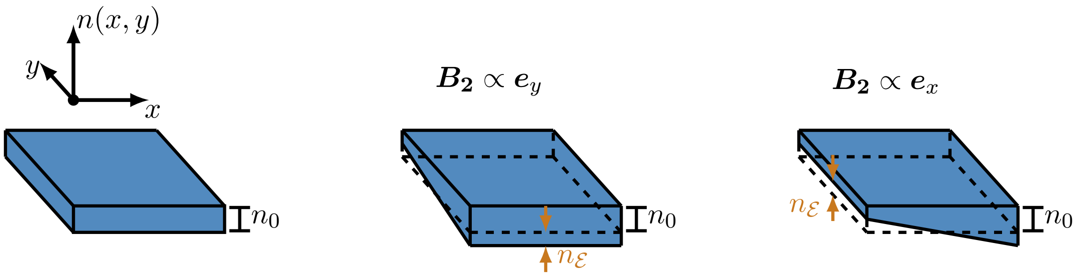

(a) (b) (c)

Figure 6.2: Magnetic excitation. (a) Density of the cloud in the 2D box potential at rest. The density is homogeneous $n(x, y) = n_0$ over the whole sample. (b)-(c) Density of the cloud when the box potential is tilted along the y (resp. x) axis. The density is linear along y with $\partial n(x, y)/\partial x = 0$ and $\partial n(x, y)/\partial y = 2n_\mathcal{E}/L$ (resp. x).

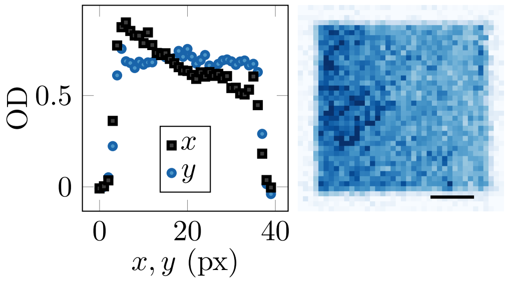

Figure 6.3: In-situ image (right) and profiles of the atomic cloud (left) in the presence of a gradient along the x-axis with $\bar{B}_{2_x} \sim 200\,\text{mG}$. Scale bar length: $10\,\mu\text{m}$.

In addition, we generate a quadrupolar magnetic field on the atoms, using the MOT coils[3] (see Chapter 2). We define a coordinate system $(\boldsymbol{e}_x, \boldsymbol{e}_y, \boldsymbol{e}_z)$ centred on the atomic cloud and the quadrupolar field, centred in $C_\text{grad} \equiv (x_0, y_0, z_0)$, writes:

$$\boldsymbol{B_1}(x, y, z) = b'_0 \left(-\frac{x - x_0}{2} \boldsymbol{e}_x + (y - y_0) \boldsymbol{e}_y - \frac{z - z_0}{2} \boldsymbol{e}_z \right), \tag{6.1}$$

where b'_0 is a static magnetic field gradient. The total magnetic field on the atoms is thus the sum of the quadrupolar field and the vertical field $\boldsymbol{B_\text{tot}}(x, y, z) = B\boldsymbol{e}_z + \boldsymbol{B_1}(x, y, z)$. The potential felt by the atoms depends on the norm of the total magnetic field $B_\text{tot} = |\boldsymbol{B_\text{tot}}|$ and reads:

$$V_\text{mag} = -g_f \mu_B B_\text{tot}. \tag{6.2}$$

The magnitude of the magnetic field close to the atoms when the quadrupolar field is centred on the cloud is shown in Fig. 6.1.a and is not linear but quadratic. However, the value of the gradient b'_0 is chosen small enough so that, in this configuration, the effective curvature of the potential across the cloud is small compared to its height. Indeed, we fix b'_0 so that the in-plane frequencies of the harmonic trap are $\omega_x/2\pi, \omega_y/2\pi < 1\,\text{Hz}$, which corresponds to a modification of the potential of $0.2\,\%$. In order to create a non-negligible magnetic field tilt over the atomic cloud, we adiabatically move the centre C_grad of the quadrupolar field. We use bias coils placed near the glass-cell to create additional small static magnetic fields on

---

[3] Note that we could have directly generated the magnetic field B in the horizontal plane with anti-Helmholtz coils but we need to keep a strong vertical field for technical reasons.

the axes x and y. This additional magnetic field writes:

$$\boldsymbol{B_2} = \bar{B}_{2x}\boldsymbol{e}_x + \bar{B}_{2y}\boldsymbol{e}_y, \tag{6.3}$$

where $\bar{B}_{2x}$ and $\bar{B}_{2y}$ are algebraic values. In order to have a proper control on the amplitude and direction of the displacement of the quadrupole field, we use bipolar power supply (High-Finesse BCS 2/10) to control the magnetic field generated by the bias coils.
As the distance between the centre of the atomic cloud and the centre of the quadrupolar field increases, the tilt of the potential increases along the direction of the displacement. In Fig. 6.1.b, we show the magnetic field felt by the atoms when we generate a bias field of 0, 125, and 250 mG along the y-axis. The magnetic field at the centre of the cloud and the amplitude of the gradient on the atoms increases. In Fig. 6.1.b, we display the magnitude of the magnetic field over a range of $150 \cdot L$ to highlight the shift of the quadrupolar field centre. In practice, the curvature of the magnetic field over the atomic cloud is negligible and the variation of the magnetic field is mostly linear. A scheme of the density profiles Fig. 6.2 displays the cloud at rest and in the presence of magnetic field gradient. We also show in figure Fig. 6.3 an image of the atoms in the presence of the magnetic field gradient.

We excite the atoms as follows: we adiabatically ramp up the current in the MOT and bias coils during 50 ms and generate a magnetic gradient on the atoms. We hold the atoms in the tilted potential during 100 ms and then instantaneously switch off the current in the bias coils. The magnetic gradient is subsequently switched off in ~ 1 ms as we shift back abruptly the quadrupolar field to the centre of the atomic cloud.
We characterise the strength of the excitation by comparing the tilt of the box potential to its height. In practice, we compute the height of the magnetic potential V_{mag} at half the side box, using Eq. (6.2), and compare it to the chemical potential μ_0 of the unperturbed atomic cloud. The excitation is then characterised by the quantity $\mathcal{E}$ defined as

$$\mathcal{E} = \frac{|\delta V_{\text{mag}}|/2}{\mu_0}, \qquad \delta V_{\text{mag}} = -g_f \mu_B \delta B_{\text{tot}}, \qquad \delta B_{\text{tot}} = b'_\alpha L, \tag{6.4}$$

where b'_α is the gradient along the axis $\alpha \in \{x, y\}$ and the total magnetic field is $\boldsymbol{B_{\text{tot}}} = B\boldsymbol{e}_z + \boldsymbol{B_1} + \boldsymbol{B_2}$.

Calibration of the magnetic field gradient The characterisation of the excitation strength requires the measurement of the magnetic field gradient across the cloud. We measure this gradient by performing Ramsey interferometry. Let us assume that the strongest gradient axis is $\alpha \in \{x, y\}$. We start from an atomic cloud in $|f = 1, m_f = -1\rangle$ in the presence of the quadrupolar field B_1 and we perform Ramsey interferometry on the magnetic-field-sensitive transition $|f = 1, m_f = -1\rangle \to |f = 2, m_f = 0\rangle$. More precisely, we send two microwave pulses of duration $\delta t = 10\,\mu\text{s}$ separated by a duration $\tau \gg \delta t$, and we assume that the atoms do not move during τ. The atoms do not feel the same magnetic field along the axis α, so the shift δ to the resonance $|f = 1, m_f = -1\rangle \to |f = 2, m_f = 0\rangle$ is spatially dependent. The transfer probability depends on δ and thus on space. After the second mw pulse, we observe interference fringes of spatial period i and angle $\theta = \pi/2$ with respect to the strongest direction of the gradient and resulting force. The probability to transfer the atoms into $|f = 2, m_f = 0\rangle$ writes:

$$\mathcal{P}(\alpha) = \cos^2\left(\frac{V_{\text{mag}}(\alpha)\tau}{\hbar}\right), \tag{6.5}$$

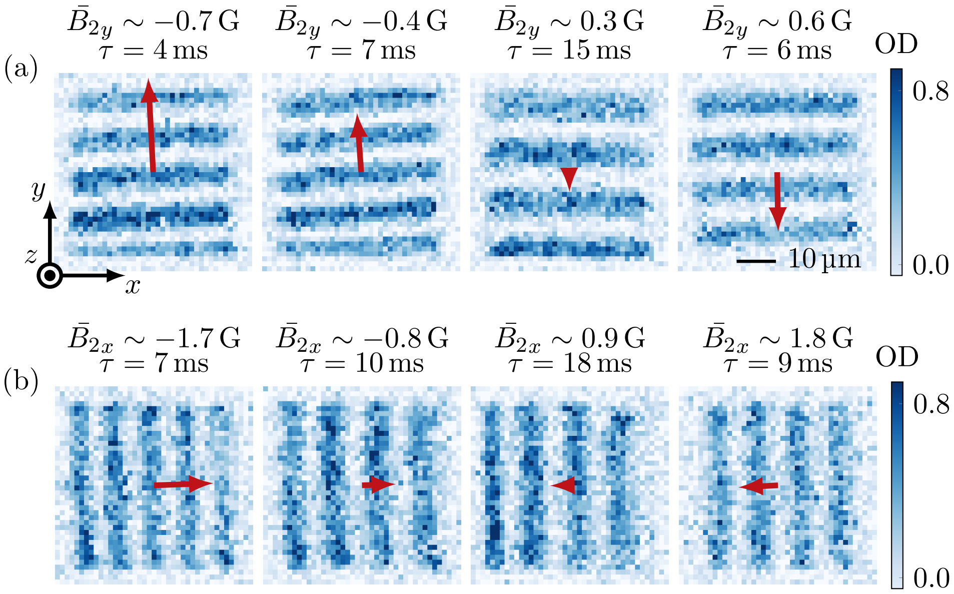

Figure 6.4: Measured OD after Ramsey interferometry on the transition $|f=1, m_f=-1\rangle \rightarrow |f=2, m_f=0\rangle$. (a) The quadrupolar field is shifted along the y-axis by varying $\bar{B}_{2y}$ and fixing $\bar{B}_{2x} \sim 0.3\,\mathrm{G}$. (b) The quadrupolar is shifted along the x-axis by varying $\bar{B}_{2x}$ and fixing $\bar{B}_{2y} \sim 0.1\,\mathrm{G}$. The components of the bias field $\bar{B}_{2x}$ and $\bar{B}_{2y}$ are indicated for each image together with the duration τ between the Ramsey pulses. The magnitude and orientation of the resulting force is indicated with a red arrow. The longest arrow corresponds to a gradient $b'_y = 19\,\mu\mathrm{G}/\mu\mathrm{m}$.

where, considering a linear magnetic field, the potential is written as follows:

$$V_{\mathrm{mag}}(\alpha) = -g_f \mu_B b'_\alpha \alpha. \tag{6.6}$$

We measure the fringe spacing i of the Ramsey interferometry pattern and deduce the magnetic field gradient b'_α from the periodicity of Eq. (6.5):

$$b'_\alpha = \frac{\hbar\pi}{g_f \mu_B} \frac{1}{i\tau}. \tag{6.7}$$

In practice, we adjust the duration separating the mw pulses τ, from a few to a tens of milliseconds, to have four or five fringes on the cloud for each gradient we probe. We show in Fig. 6.4 the typical Ramsey signals[4] obtained when we vary the components of the magnetic field $\boldsymbol{B_2}$ individually. This method allows us also to measure the direction of the resulting force $\boldsymbol{F}_{\mathrm{mag}} = -\boldsymbol{\nabla} V_{\mathrm{mag}}$, as we obtain the direction of the wave vector of the Ramsey fringes by performing Fourier transform. While we shift the quadrupolar field along the axis α, the resulting force $\boldsymbol{F}_{\mathrm{mag}}$ may not be aligned along α because of the presence of residual magnetic fields. In this case, the fringes are not perpendicular to the axis α. We correct these imperfections with the bias coils perpendicular to the α-axis.

6.1.2 Sound propagation

As already mentioned, the atoms are prepared in the state $|f=1, m_f=-1\rangle$ at the lowest temperature achievable with our cooling steps $T \lesssim 20\,\mathrm{nK}$. The surface density in the flat-

---

[4] As the in-situ images can be misleading, we emphasise that there is no periodic density modulation yet and those are interference patterns only.

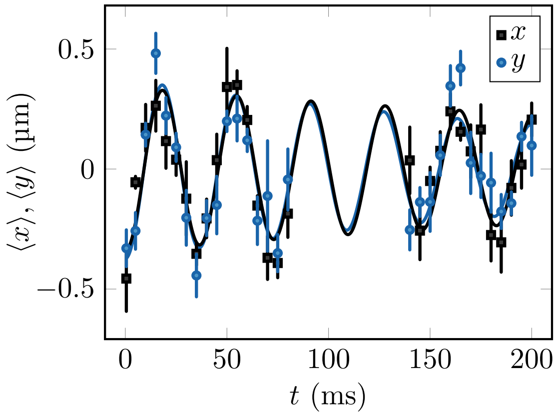

Figure 6.5: Oscillations of the centre of mass along the x-axis (resp y-axis), $\langle x \rangle$ (resp $\langle y \rangle$), when the excitation propagates along x (resp. y) (black points) (resp (blue squares)). The solid lines are fit to the data, adjusted using the function Eq. (6.8). The centre of mass oscillates at a frequency $\nu_x = 27.4(2)\,\text{Hz}$ when we excite the atoms along the x direction and at a frequency $\nu_y = 27.6(2)\,\text{Hz}$ when we excite them along the y direction. These frequencies correspond to a sound velocity $c = 2.2(2)\,\text{mm/s}$. Vertical errorbars are standard errors of the mean.

bottom box is fixed to $n_0 = 60(1)\,\mu\text{m}^{-2}$. We adiabatically ramp up the quadrupolar field $\boldsymbol{B_1}$ and the bias field $\boldsymbol{B_2}$ oriented along an axis $\alpha \in \{x, y\}$. We choose the magnetic field B_2 so that the gradient felt by the atoms is $b'_\alpha = 3.4\,\mu\text{G}/\mu\text{m}$, which corresponds to an excitation (see Eq. (6.4)) $\mathcal{E} \sim 4\,\%$. We hold the atoms in this configuration for 100 ms and then we abruptly switch off $\boldsymbol{B_2}$, exciting the atoms along α. The extinction of the bias field set the time origin $t = 0$. We let the atomic cloud oscillate for a duration t and then partially transfer the atoms to $|f = 2, m_f = 0\rangle$ where we measure the optical density (OD). We obtain the surface density profile in $|f = 1, m_f = -1\rangle$ from this OD.

The density profiles are integrated along the direction perpendicular to the excitation. We obtain a 1D density profile $n(\alpha)$ from which we calculate the position of the centre of mass. The centre of mass $\langle \alpha \rangle$ oscillates in time as the excitation propagates back and forth. The frequency of the oscillations ν is then proportional to the sound velocity $c = 2L\nu$. A typical evolution of the centre of mass is shown in Fig. 6.5 for an excitation along the x-axis and an excitation along the y-axis. We fit a damped oscillation $\langle \alpha \rangle(t)$ to the data with:

$$\langle \alpha \rangle(t) = A \exp\left(-\frac{\Gamma t}{2}\right)\left[\frac{\Gamma}{2\omega}\sin(\omega t) + \cos(\omega t)\right], \tag{6.8}$$

with an amplitude A, a damping parameter Γ and a frequency $\nu = \omega/2\pi$. In Fig. 6.5, we find that the centre of mass oscillates at a frequency $\nu_x = 27.4(2)\,\text{Hz}$ and $\nu_y = 27.6(2)\,\text{Hz}$ when we excite the atoms in the x and y direction respectively. These almost equal frequencies correspond to a sound velocity of $c = 2.20(1)\,\text{mm/s}$. As we work at near zero temperature and in a *homogeneous* cloud here, this sound velocity is expected to match Bogoliubov sound velocity $c_\text{B} = \hbar\sqrt{\tilde{g} n_0}/m$. In this particular case, we assume $c = c_\text{B}$ to calibrate our mean density[5] and find $n_0 = 60.0(3)\,\mu\text{m}^{-2}$.

---

[5] We also performed a Ramsey spectroscopy on the clock transition, as described in Chapter 2, to calibrate independently the density. This calibration gives a similar result but appears to be less robust: Indeed, we generate a stronger vertical magnetic field than usual ($B = 3\,\text{G}$) and thus we have a larger uncertainty on the Ramsey interferometry result.

In practice, one can argue that the excitation imposed to the atoms may excite many spatial modes. The oscillations of the density defect along the excited axis α can be decomposed into Fourier series:

$$n(\alpha) - \bar{n}(\alpha) = \sum_{j=1}^{+\infty} A_j(t) \cos(j\frac{\pi}{L}\alpha), \tag{6.9}$$

where $A_j(t)$ is the amplitude of the j-th mode[6]. The resulting oscillations of the centre of mass thus includes the contributions of many excited modes, whereas we are interested in the fundamental mode only, whose amplitude is given by:

$$A_1(t) = \frac{2}{L} \int_0^L [n(\alpha) - \bar{n}(\alpha)] \cos(\frac{\pi}{L}\alpha)\, \mathrm{d}\alpha. \tag{6.10}$$

As a safety check, we also measured the coefficient $A_1(t)$. We verified that, for the range of excitation magnitudes we use, the oscillation frequencies of $A_1(t)$ and $\langle\alpha\rangle(t)$ are always similar within errorbars.

6.2 Density-modulated 2D Bose gases

Our main goal in this chapter is to probe the superfluid fraction in a density-modulated gas at zero temperature. In this section, we describe how we break translational invariance in the bulk by imprinting a periodic potential:

$$V(y) = V_0 \sin\left(\frac{2\pi}{\lambda} y\right), \qquad V_0 \geq 0, \tag{6.11}$$

of spatial period λ, onto a cold uniform atomic cloud. Afterwards, we calibrate the response of the atoms to this modulated potential.

6.2.1 Imprinting a modulated density profile

Atoms are initially trapped in a 2D flat-bottom potential and we use an independent DMD to shine onto the atoms a repulsive light of wavelength 532 nm and whose intensity profile is shaped as a sine[7]. The effective waist of the light beam on the atomic plane $w = 85\,\mu\text{m}$ is large compared to the atomic cloud, so that the intensity profile over the atoms is almost uniform for a uniform DMD pattern.

In practice, the DMD behaviour depends on the working regime. Here we will work deep in the grey-level regime as we will imprint a continuous modulation. We therefore need a large density of mirrors turned "off" in order to locally imprint grey values. In this context, one can show that the DMD plays the role of an *amplitude modulator* [102]. More specifically, the light intensity sent onto the atoms scales quadratically with the reflectance of the DMD. Therefore, we shape the intensity profile of the light as a sine by dithering the following pattern on the DMD:

$$\mathcal{I}(x, y) = \sqrt{\beta + \gamma \sin\left(\frac{2\pi}{\lambda} y\right)}, \tag{6.12}$$

where the axes x and y are the atomic image plane coordinates. The profile $\mathcal{I}$ is dithered using the error diffusion algorithm. We choose $\beta = 0.5$ and $\gamma = 0.4$ in order to avoid defects

---

[6] We choose the cosine basis to ensure that the velocity field cancels on the edges of the box.

[7] We do not use the atomic response to the potential for correcting its profile, i.e. we do not perform any feedback loop between the atomic and potential profiles as discussed in Ref. [51].

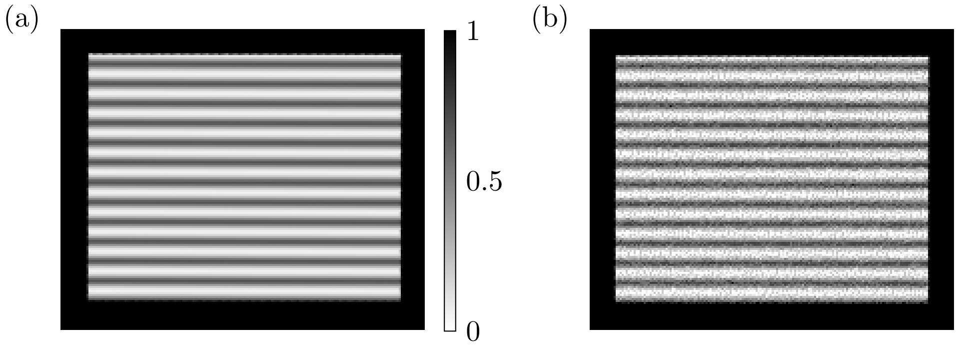

Figure 6.6: DMD pattern to imprint a sine on the atoms. (a) Continuous pattern $\mathcal{I}$ (see Eq. (6.12)) with $\beta = 0.5$ and $\gamma = 0.4$. (b) Dithered pattern $\mathcal{I}_{\text{dithered}}$ actually displayed on the DMD.

at the minima and maxima of the signal and so that $0 < \mathcal{I}(x, y) < 1$. There is then a small light offset onto the atoms at the minima, but the subsequent scattering rate remains low. We show in Fig. 6.6 the pattern $\mathcal{I}$ we generate, and the dithered pattern $\mathcal{I}_{\text{dithered}}$ displayed on the DMD.

There are two imaging systems on the setup allowing us to characterise the intensity profile that we send onto the atoms and the resulting potential. First, the green light beam at 532 nm used to create the modulated potential is collected on a control camera (see Fig. 6.7). This camera (A) is placed on the conjugate plane of the atoms so that we image the light intensity profile imprinted on the atoms. This imaging system has a resolution $\lesssim 1\,\mu\text{m}$ and a magnification 3.2. Second, our usual vertical absorption imaging of wavelength 780 nm is used to image the atomic density profiles (see Fig. 6.7). This imaging system (B) has a similar resolution $\lesssim 1\,\mu\text{m}$ and a magnification 11. We first use the control camera (A) to image the light intensity profile on the atomic plane and verify that we design well the potential.

We vary the light intensity and show in Fig. 6.8 the intensity profiles imaged on the control camera with a lattice of period $\lambda = 4\,\mu\text{m}$. As expected, we observe a sinusoidal modulation of the intensity along y. When we increase the light intensity on the DMD, the contrast $\mathcal{C} = (I_{\text{max}} - I_{\text{min}})/(I_{\text{max}} + I_{\text{min}})$ of the fringes increases linearly, $I_{\text{max,min}}$ being the intensity maxima and minima. We verified that we imprint a sine for all the range of intensities used. Moreover, we checked that we observed a sinusoidal modulation of the intensity for different lattice spacings. As the lattice period increases, the number of periods over the cloud decreases and the measurement of the contrast may be less robust. We therefore probed two lattice spatial phases ϕ and $\phi + \pi$, for lattice spacings $\lambda \geq 8\,\mu\text{m}$, and we verified that the measured contrast is phase independent. For each of those patterns, we varied the intensity of the light shined on the DMD and measured the contrast of the fringes on the camera control. We show in Fig. 6.9 the contrast on the control camera for a given intensity with respect to the different lattice spacings we probed. For lattices with period $\lambda \geq 4\,\mu\text{m}$, we find a mean contrast $\bar{\mathcal{C}} = 0.75(1)$ close to the expected value $\mathcal{C} = \gamma/\beta = 0.8$. For a lattice spacing of $2\,\mu\text{m}$, the contrast is attenuated. The pattern on the control camera starts indeed to blur, as a result of the finite optical resolution of our imaging.
As a conclusion, we observe the expected sine profile for a large range of intensities and lattice spacings λ. The results we will present in this chapter were obtained with a lattice spacing of $4\,\mu\text{m}$, for which we do not observe any loss of contrast on the control camera.

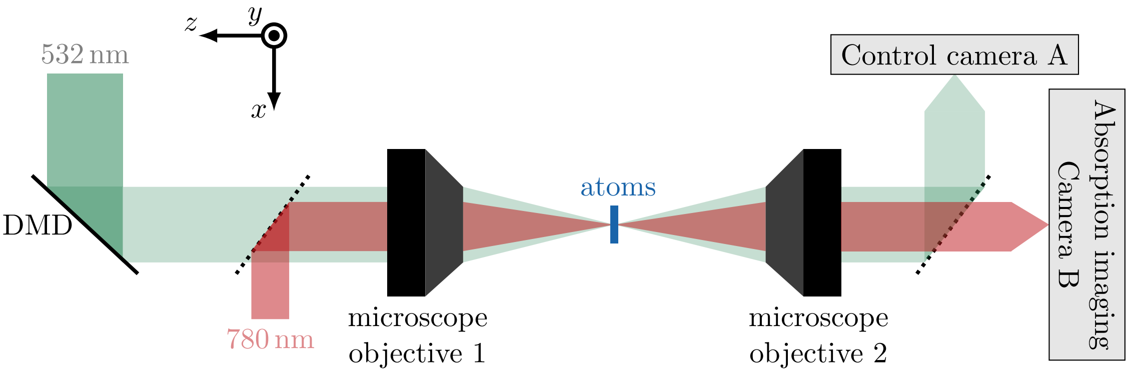

Figure 6.7: Representation of the optical system used to create and image the sinusoidal potential. We shine a DMD with a light beam of intensity I and wavelength 532 nm (green). The green light reflected towards the atoms has a spatially modulated intensity profile. The light passes through a first microscope objective of numerical aperture (NA) 0.4 before it reaches the atoms. Afterwards, the green light goes through a second microscope objective of same NA and is finally collected on a control camera. This camera (A) is placed on the image plane of the microscope so that we image the light intensity profile seen by the atoms. This imaging has a resolution $\lesssim 1\,\mu\text{m}$ and a magnification of 3.2. The green light is mixed with a red light beam of wavelength 780 nm used to perform absorption imaging of the atoms. This red light beam passes through the two microscope objectives before being collected on a second camera (B). This imaging system has a similar resolution $\lesssim 1\,\mu\text{m}$ and a magnification of 11.

Finally, we have to calibrate the potential depth V_0. A first method would be to estimate V_0 from the intensity I and the waist w of the light beam, however, it would lead to large systematic errors. Indeed, the light passes through a DMD and a microscope objective before reaching the atoms (see Fig. 6.7), which makes difficult to estimate the real light intensity on the atomic plane. We then prefer to calibrate the potential depth from the atomic response. This calibration is performed with the usual absorption imaging (see Fig. 6.7) and detailed in the following section. The atomic density profiles are however imaged with a different camera and light beam so the imaged profiles are affected differently by the finite spatial resolution.

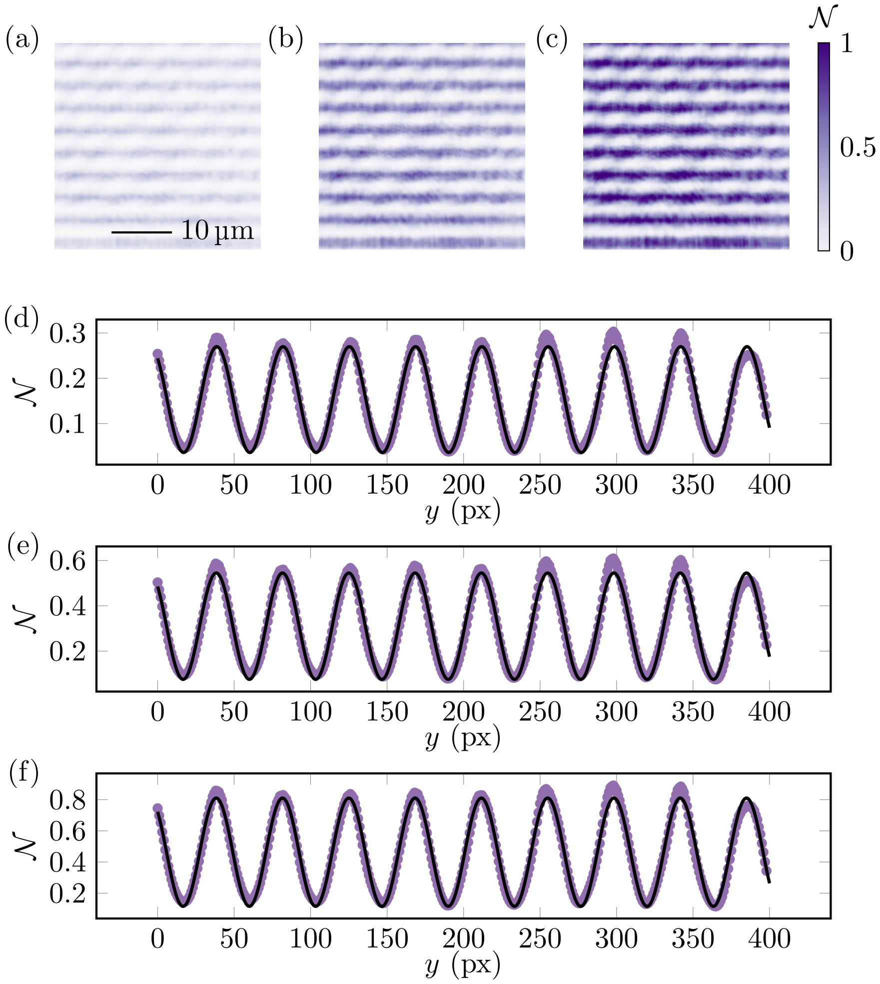

Figure 6.8: (a)-(c) Images of the intensity profiles on the control camera for a light intensity ratio of 1, 2 and 3 respectively (scale bar: 10 µm on the atomic plane). The colorbar indicates the normalised number of counts by pixel $\mathcal{N}$. (d)-(e) Averaged one-dimensional profiles along the modulation for a light intensity ratio 1, 2 and 3 respectively. The black solid lines are sine functions adjusted to the data.

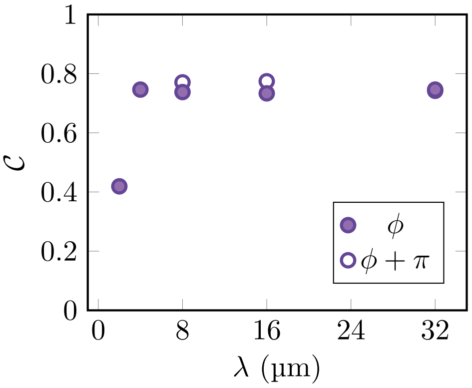

Figure 6.9: Contrast of the fringes $\mathcal{C}$ on the control camera for a given intensity I as a function of the lattice periods λ (filled points). For large lattice spacings, we also imprinted lattices with a π-phase shift (empty points) and we confirm that the contrast is phase-independent.

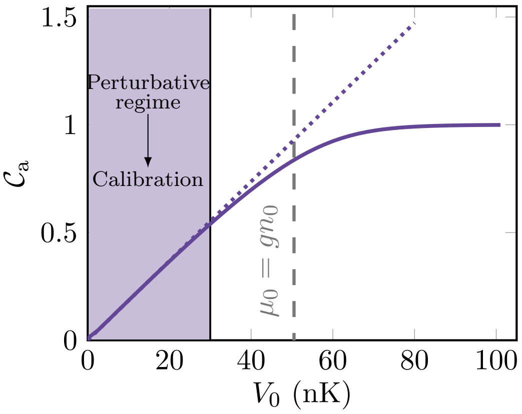

Figure 6.10: Atomic contrast $\mathcal{C}_\mathrm{a}$ of the density profile for $\lambda = 4\,\mu\mathrm{m}$ as a function of the potential depth V_0, obtained from GP simulations (solid line) performed in the group and the perturbative model (dotted line) described by Eq. (6.14). The shaded area represents the perturbative regime used to perform the calibration. The dashed vertical line indicates the value of μ_0.

6.2.2 Atomic response

In order to calibrate the potential depth, we image the density profile n at zero temperature and deep in the Thomas-Fermi regime. In a regime where the spatial scale of the perturbation is much larger than the healing length $\xi \sim 0.2\,\mu\mathrm{m}$, i.e with lattices of large period and low light intensities, one can usually apply the local density approximation (LDA), which yields:

$$n(y) = \frac{\mu_0 - V(y)}{g} = \frac{\mu_0}{g} + \frac{V_0}{g}\sin\left(\frac{2\pi}{\lambda}\right), \tag{6.13}$$

where $\mu_0 = gn_0$ is the unperturbed chemical potential. Therefore, the density profiles obtained within LDA match the potential. For instance, here we would have expected to image density profiles with sinusoidal modulations. For the modulated potentials we consider, however, the spatial scale of the perturbation is too large and we must add some correcting terms to this simple model. We distinguish two regimes:

- the regime of small amplitudes of modulation with lattice spacings λ large compared to the camera pixelsize $1.15\,\mu\mathrm{m}$, where the deviations from the LDA are small.
- the rest of the parameter diagram, where LDA fails.

Protocol The idea is the following: we calibrate the potential depth in the first regime, i.e. in the regime of shallow potentials. There, the Gross-Pitaevskii (GP) result (obtained from numerical simulations performed in the group) is well-approximated by static perturbation theory [87]. This perturbative derivation (see appendix B) yields a potential depth V_0 linearly dependent on the contrast $\mathcal{C}_\mathrm{a}$ of the density profile but dependent also on the wave vector of the lattice $k = 2\pi/\lambda$:

$$V_0 = \left(\mu_0 + \frac{\hbar^2 k^2}{4m}\right)\mathcal{C}_\mathrm{a}. \tag{6.14}$$

We show in Fig. 6.10 the contrast $\mathcal{C}_\mathrm{a}$, obtained from this perturbative relation and from the GP simulations for a lattice of period $\lambda = 4\,\mu\mathrm{m}$. Fixing the mean density to $n_0 = 60\,\mu\mathrm{m}^{-2}$, we find that the two curves are superimposed up to $V_0 \sim 0.6\,\mu_0$.

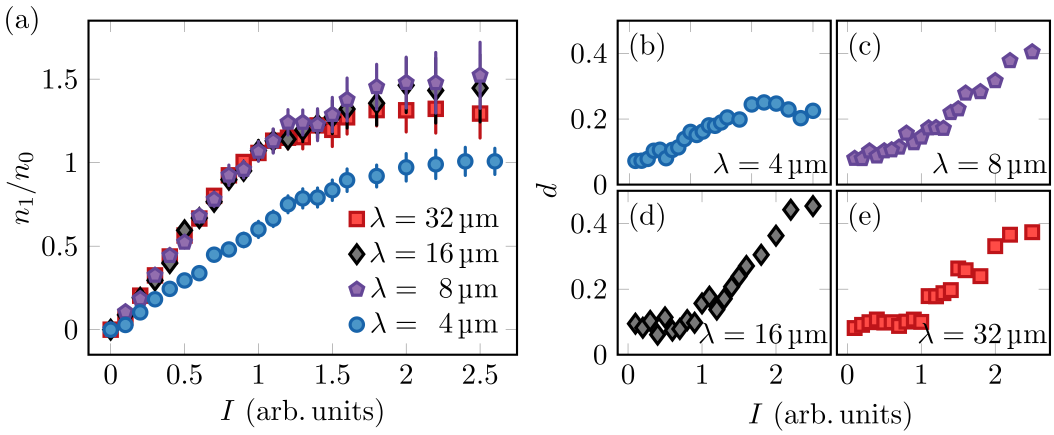

Figure 6.11: (a) Contrast $\mathcal{C}_a = n_1/n_0$ for a lattice spacing of $\lambda = 4\,\mu$m (blue points), $\lambda = 8\,\mu$m (violet pentagons), $\lambda = 16\,\mu$m (black diamonds) and $\lambda = 32\,\mu$m (red squares), as a function of the light intensity[8] I. (a)-(c) Distance (rms) d from the adjusted sine function Eq. (6.15) and the measured density profiles $n(y)$ with respect with the intensity I for a lattice spacing of $\lambda = 4$, 8, 16, 32 µm respectively. *Data extracted from a preliminary analysis.*

Experimentally, one can then calibrate the potential depth by measuring the contrast of density profiles from which we calculate V_0 with Eq. (6.14) up to $V_0 \sim 0.6\,\mu_0$ (i.e. $V_0 \sim 30\,$nK in Fig. 6.10), where the perturbative regime ends.

Measurement on density profiles We image the atoms in spatially modulated potentials created with various lattice spacings and light intensities. In practice, we prepare the atoms in the state $|f = 1, m_f = -1\rangle$ at a temperature $T \lesssim 20\,$nK. We imprint the sine potential with a given light intensity I and spacing λ. After a waiting time of 100 ms, we partially transfer the atoms in the state $|f = 2, m_f = 0\rangle$. We measure the OD in $|f = 2, m_f = 0\rangle$ and calculate the density profile $n(x, y)$ from this measurement. The profiles are then integrated along the x direction, along which the density is uniform.

In order to extract the amplitude of modulation, we assume that the density profile is well-described by a sine and we adjust the following function to the modulated profile $n(y)$:

$$n_0 + n_1 \sin\left(\frac{2\pi}{\lambda} y\right), \tag{6.15}$$

where n_1 is the amplitude of the modulation and n_0 the mean density. This function is expected to fit the profiles $n(y)$ for $V_0 \ll \mu_0$, and thus this approximation is suitable for the regime used for the calibration. We show in Fig. 6.13 a catalogue of density profiles observed for lattice spacings $\lambda = 4$, 8, 16, 32 µm and two different light intensities. In every case, we observe a modulation of the surface density $n(x, y)$ with the period λ.

The atomic contrast $\mathcal{C}_a = n_1/n_0$ measured using Eq. (6.15) is displayed in Fig. 6.11 for four different lattice spacings. The depletion increases linearly in the regime of low intensities and then saturates. We remind that the fit function Eq. (6.15) is suitable for the low amplitude regime only and we show in Fig. 6.11.b-c-d-e the rms distance d between the sinusoidal fit to the data and the density profiles. We observe that d increases strongly when the atomic contrast saturates. For higher light intensities, the sine function does not capture the whole density profile and this is why we obtain depletions $n_1/n_0 > 1$.

---

[8] The intensity I of the light beam is collected by a photodiode and hence proportional to a voltage.

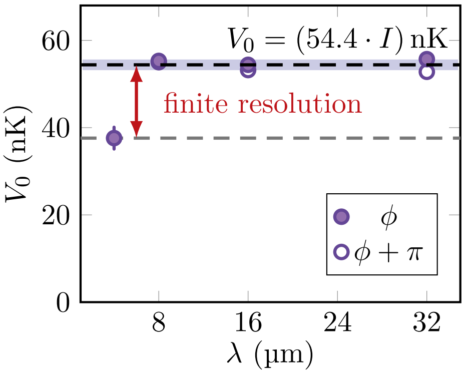

Figure 6.12: Potential depth V_0 for a given intensity I, extracted in the linear regime $V_0 < 0.6\,\mu_0$, as a function of the lattice period and for two different lattice phases ϕ. The potential measured for $\lambda = 4\,\mu\mathrm{m}$ is $\sim 30\,\%$ smaller than the potential measured with lattices of period $\lambda \geq 8\,\mu\mathrm{m}$. Indeed, the amplitude of the modulation n_1 measured with a lattice of period $\lambda = 4\,\mu\mathrm{m}$ is attenuated by our finite imaging resolution and gives an artificially smaller potential. Thus, the potential depth is calibrated from the lattices of large periods ($\lambda \geq 8\,\mu\mathrm{m}$) and its value is represented with the horizontal black dashed line together with its standard deviation (violet shade). We also verified that this value is independent of the lattice phase ϕ. *Data extracted from a preliminary analysis.*

Calculation of the potential depth We calculate the potential depth V_0 in the linear regime, i.e up to $V_0 < 0.6\,\mu_0$, using the perturbative model and the measured values of n_1/n_0:

$$V_0 = \left(\mu_0 + \frac{\hbar^2 k^2}{4m}\right) \frac{n_1}{n_0}, \tag{6.16}$$

and we extrapolate it for large depletions. The potential depth for a given intensity I is shown in Fig. 6.12 as a function of the lattice spacing. As we apply the correction to the LDA, depending on the wave vector k, we expect to correct the large difference between the depletion for a lattice of spacing $\lambda = 4\,\mu\mathrm{m}$ and lattices of larger spacing, observed in Fig. 6.11. The potential measured with the perturbative model for lattice spacings $\lambda \geq 8\,\mu\mathrm{m}$ are similar. However, the discrepancy with the lattice of period $\lambda = 4\,\mu\mathrm{m}$ remains, as the measured value is $\sim 30\,\%$ smaller. We confirmed previously by using our first imaging system (control camera A) that the light intensity profile I reaching the atoms has the same mean and contrast for lattices of period $\lambda \geq 4\,\mu\mathrm{m}$. We thus interpret this deviation as a limitation of the finite spatial resolution *of the second imaging system (B), at 780 nm,* which artificially reduces the amplitude n_1 measured for lattices of small period and hence decreases the potential depth. Finally, we assume that the atoms feel the same potential depth for all lattices of period $\lambda \geq 4\,\mu\mathrm{m}$ and thus calibrate V_0 using the atomic response to lattice potentials of large spacing $\lambda \geq 8\,\mu\mathrm{m}$. We therefore find a linear relation between the potential depth V_0 and the light intensity I yielding $V_0 = (54.4 \cdot I)\,\mathrm{nK}$.

Attenuation of the density modulation by our imaging system The attenuation of the density signal can be understood by considering that the two imaging systems are well-described by a Gaussian point spread function (PSF) written:

$$\mathcal{P} = \frac{1}{2\pi\sigma^2} \exp\left(-\boldsymbol{r}^2/2\sigma^2\right), \qquad \boldsymbol{r} = (x, y). \tag{6.17}$$

In this case, a sine profile written as Eq. (6.15) would undergo the following attenuation:

$$\mathcal{P} \otimes n(y) \qquad \longrightarrow \qquad n_{\mathrm{PSF}}(y) = n_0 + n_1 \exp\left(-\frac{k^2\sigma^2}{2}\right) \sin\left(\frac{2\pi}{\lambda} y\right). \tag{6.18}$$

We adjusted the depletion n_1/n_0 measured with the absorption imaging (B) with the function Eq. (6.18) and we find $\sigma_{780} = 0.53(6)\,\mu\mathrm{m}$. This value is close to the ones usually measured on the experiment. The difference between the two imaging systems can be explained first by the light wavelength difference as there is less diffraction with a 532 nm light than a 780 nm light. Moreover, the modelling of absorption imaging of atoms is always challenging, as we do not completely control the dynamics of the atoms during the imaging light pulse.

To summarize, we verified that we imprint the good potential, i.e. a sinusoidal modulation, on the light intensity profiles. We also used the atoms in the regime of shallow lattice potentials to calibrate the potential depth they feel. We can finally move to the heart of the chapter and measure the superfluid fraction in a density-modulated weakly-interacting 2D Bose gas at zero temperature.

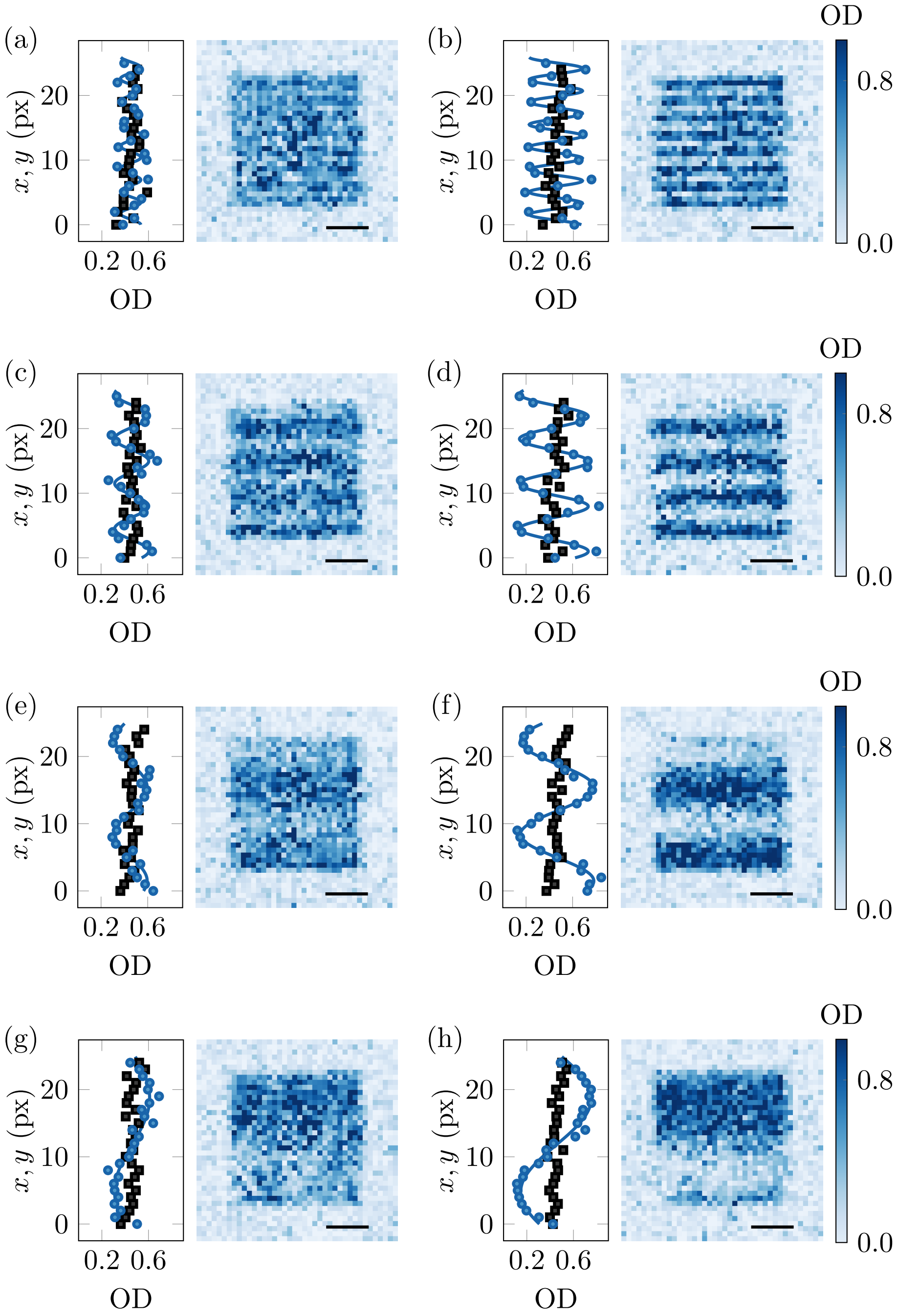

Figure 6.13: Images of the atomic cloud in a periodic potential of period $\lambda = 4\,\mu\text{m}$ (a)-(b), $\lambda = 8\,\mu\text{m}$ (c)-(d), $\lambda = 16\,\mu\text{m}$ (e)-(f) and $\lambda = 32\,\mu\text{m}$ (g)-(h) (scale bar: $10\,\mu\text{m}$). The average profiles in the direction x (black squares) and y (blue points) are shown on the left. The blue solid lines are fit to the data in the y-axis, using a sine function. The light intensity is doubled between the left and the right columns. Here, the in-plane confinement is a square box of side $L = 32\,\mu\text{m}$.

6.3 Breaking translational invariance in a superfluid

We probe the zero-temperature superfluid fraction in a density-modulated planar Bose gas with two experimental protocols. In the first part of this section, we describe the measurement of the sound propagation along the two axes of an atomic cloud modulated by a one-dimensional sinusoidal potential. We vary the potential depth V_0 of the lattice and deduce Leggett's integral (as defined in Ref. [36] and derived for our system in the previous chapter) from the sound velocities along and perpendicular to the modulation:

$$f_s = \left(\frac{c_y}{c_x}\right)^2 . \tag{6.19}$$

Afterwards, we describe the measurement of Leggett's integral from the density profiles n:

$$f_s = \frac{L}{N \int \frac{\mathrm{d}y}{n(y)}} . \tag{6.20}$$

This measurement requires to work with in-situ images of the density-modulated cloud. As mentioned in the previous section, measured density profiles are affected by our finite spatial resolution and therefore we cannot directly compute Leggett's integral. We describe an analysis method which allows us to restore the signal and extract a partial measurement of Leggett's integral.

Experimentally, we take two data sets for a given potential depth: we measure the equilibrium density profile and then perform a measurement of the sound velocity in the same conditions using the protocol described in Sec. 6.1. The preparation of the atomic sample is therefore the same for both experiments. The atoms are cooled down to $T \lesssim 20\,\mathrm{nK}$ in the magnetic-sensitive state $|f = 1, m_f = -1\rangle$. After letting the atoms thermalize, we adiabatically switch on the lattice potential

$$V(y) = V_0 \sin\left(\frac{2\pi}{\lambda} y\right) , \tag{6.21}$$

with a given potential depth V_0 and a lattice period $\lambda = 4\,\mu\mathrm{m}$. The mean density is fixed to $n_0 = 60(1)\,\mu\mathrm{m}^{-2}$ for all potential depths probed.

6.3.1 Sound propagation in a gas of modulated density

We study sound propagation in a density-modulated atomic sample by following the experimental protocol described in Sec. 6.1. After having prepared the atoms in the modulated potential Eq. (6.21) of potential depth V_0, we adiabatically switch on a linear magnetic field along the density modulation (y-axis) which tilts the potential felt by the atoms. At a time $t = 0$ we abruptly switch off the magnetic field gradient and we monitor the atomic response to this excitation for a duration $t \sim 200\,\mathrm{ms}$. We perform the same experiment by generating a magnetic excitation along the x-axis, i.e perpendicular to the density modulation.
The evolution of the position of the centre of mass is measured along each axis and we report in Fig. 6.14.a an example of measured signals. The position of the centre of mass oscillates and we obtain the sound velocity c in both directions by measuring its oscillation frequency $\nu = c/2L$. We show in Fig. 6.14.b the sound velocities along the modulation c_y and perpendicular to the modulation c_x as a function of the potential depth V_0. As expected, the sound velocity along the density modulation decreases when the potential depth increases, as the depletion of the atomic cloud and the effective mass m^* becomes larger. We observe a slight

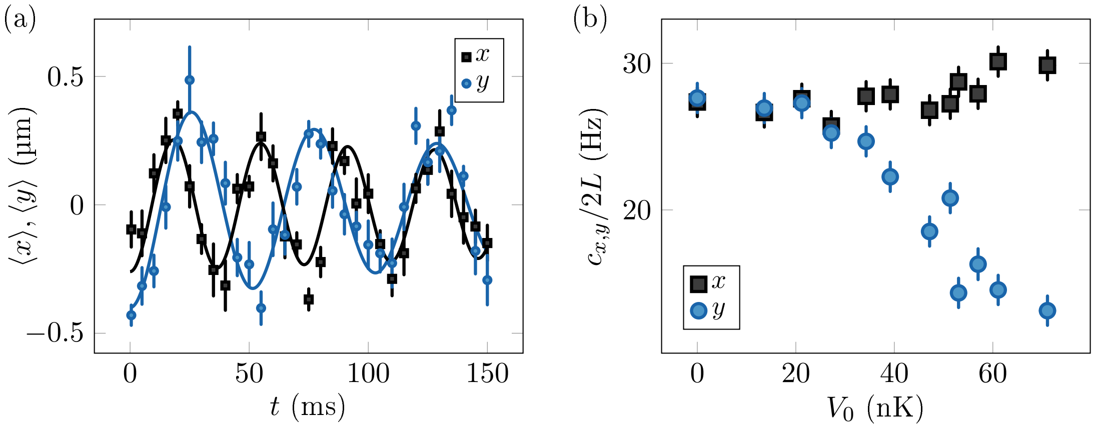

Figure 6.14: Sound propagation. (a) Oscillations of the centre of mass along the x (black squares) and y directions (blue points) after a magnetic excitation of the cloud. Vertical errorbars are standard errors of the mean. (b) Sound velocities along the density modulation (blue points) and perpendicular to the modulation (black squares) as a function of the amplitude V_0 of the sine potential. Horizontal errorbars are standard deviations smaller than the size points. Vertical errorbars of 1 Hz are estimated from a statistical error. *Data extracted from a preliminary analysis.*

increase of the sound velocity along the axis perpendicular to the modulation because of the modification of the density distribution[9].

Finally, we report in Fig. 6.16 the superfluid fraction obtained from the measurement of the sound velocity as a function of the potential depth V_0 normalised to the chemical potential μ_0 and discuss our measurement in section Sec. 6.3.3.

6.3.2 Leggett's integral from density profiles

The measurement of the superfluid fraction following Leggett's integral Eq. (6.20) requires to measure the density profile $n(y)$ at equilibrium. After the preparation of the atoms in $|f = 1, m_f = -1\rangle$ in the presence of the periodic potential $V(y)$ of potential depth V_0, we take ten images of the atomic cloud by partially transferring it in the state $|f = 2, m_f = 0\rangle$. The density profiles are calculated from the OD measured in $|f = 2, m_f = 0\rangle$, as usual.

As mentioned in the section Sec. 6.2, our absorption imaging is limited by the finite spatial resolution for a lattice period of $\lambda = 4\,\mu\text{m}$ and we are not able to properly measure the amplitude of the modulation on the atoms. This prohibits a direct numerical integration of the raw density profiles. We propose here a method to correct the effect of the finite spatial resolution. This method relies on the relation established in Sec. 6.2 between the potential depth V_0 and the *real* amplitude of the modulation n_1^{c} in the limit of low potential depth:

$$V_0 = \left(g + \frac{\hbar^2 k^2}{4 m n_0}\right) n_1^{\mathrm{c}}. \tag{6.22}$$

In Sec. 6.2.2, we calibrated the potential depth V_0 for a given light intensity I. Therefore we use this calibrated value to compute a correction factor $r = n_1^{\mathrm{c}}/n_1$ to the measured amplitude

---

[9] In the previous chapter, we showed that the speed of sound depends on the density via the pressure $P = \mathcal{F}(n)$. Indeed, in the homogeneous direction, the speed of sound writes $c_x = \mathcal{F}'(n)/m$ and thus depends on the density distribution.

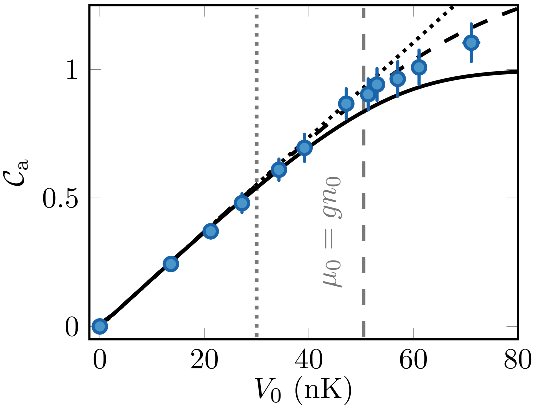

Figure 6.15: Corrected contrast $\mathcal{C}_\mathrm{a} = n_1^\mathrm{c}/n_0$ induced by a periodic potential of period $\lambda = 4\,\mu\mathrm{m}$ as a function of the potential depth V_0 (blue points). We obtain depletions larger than 1 for large potential depths because the contribution of higher harmonics on the density profiles are filtered out by the absorption imaging system. The solid black line is the result of Gross-Pitaevskii simulations without spatial filtering of the density profiles. As expected, the depletion saturates to one. The dashed black line is the result of Gross-Pitaevskii simulations where the density profile is filtered and we extract the contribution of the fundamental mode only, as for the experimental data. The dotted black lines is the perturbative model Eq. (6.16) used to calibrate the potential V_0 and the correction factor r. This calibration was performed on potential values up to $V_0 < 0.6\,\mu_0$ with the same mean density n_0. The limit of the calibration regime is represented by the vertical grey dotted line. The grey vertical dashed line indicates the value of the chemical potential μ_0 of the atoms without modulation and with the same mean density n_0. Errorbars are standard deviations and horizontal errorbars are smaller than the point size. *Data extracted from a preliminary analysis.*

n_1 following:

$$V_0 = \left(g + \frac{\hbar^2 k^2}{4mn_0}\right) r n_1. \tag{6.23}$$

The correction factor r, defined for a $4\,\mu\mathrm{m}$-period lattice, is then calculated in the perturbative regime and extrapolated for all probed potential depths. We find $r = 1.45(9)$.
As emphasised earlier, we fit the density profiles $n(y)$ with a sine function in the perturbative regime. For deeper lattices, this approximation breaks and the density profiles can be decomposed in Fourier series. There are therefore two important points to consider:

- The correction of the atomic signal amplitude allows us to correct the amplitude of the *fundamental spatial mode* only, i.e. the sine contribution of period λ. Indeed, the calibration of the correction factor is performed in the perturbative regime where the contribution of the higher harmonics is negligible and is not taken into account.

- Moreover, experimental access to the higher harmonic amplitudes is in all cases compromised by the fact that our optical resolution $\sim 1\,\mu\mathrm{m}$ is not small compared to the period of the first harmonic $\lambda/2 = 2\,\mu\mathrm{m}$. In conclusion, the absorption imaging system acts as a low pass filter and our measurement of Leggett's integral is therefore limited to the effect of the spatial density modulation with the period λ.

We show in Fig. 6.15 the *corrected* contrast $\mathcal{C}_\mathrm{a} = n_1^\mathrm{c}/n_0$ as a function of the potential depth V_0, for the complete experimental data set. The data are compared to numerical GP simulations performed in the group, for which the depletion saturates at one. We also show numerical GP simulations where the depletion n_1/n_0 is obtained by keeping the fundamental mode only of the density profile, as for the experimental data. We also display the result of the perturbative expansion Eq. (6.16). By construction, the data taken with $V_0 < 0.6\,\mu_0$ lies on the perturbative result (superimposed with the GP simulation in this regime). When the potential depth V_0 increases, the corrected depletion follows the result obtained from the fundamental mode of the GP simulations. For potential depths larger than μ_0, we obtain depletions larger than one $n_1^{\mathrm{c}}/n_0 > 1$ because the effect of the higher harmonics in the density response are filtered out.

In summary, we are able to restore the signal of the fundamental spatial mode. For each potential depth probed, we fit the density profiles $n(y)$ with the sine function:

$$n_0 + n_1 \sin\left(\frac{2\pi}{\lambda} y\right). \tag{6.24}$$

We obtain the mean density (experimentally fixed to $n_0 = 60(1)\,\mu\mathrm{m}^{-2}$) and the measured amplitude n_1, from which we calculate the corrected amplitude $n_1^{\mathrm{c}} = r n_1$. Assuming that we have a sinusoidal density modulation of period λ, mean n_0 and amplitude n_1^{c}, the computation of Leggett's integral Eq. (6.20) is analytic and yields:

$$f_{\mathrm{s}} = \sqrt{1 - \left(\frac{n_1^{\mathrm{c}}}{n_0}\right)^2}. \tag{6.25}$$

In the next section, we show in Fig. 6.16 the superfluid fraction computed with Eq. (6.25) and compare it to the result obtained from the sound measurement.

6.3.3 Final result and discussion

The superfluid fraction, given by Leggett's integral in our system, is probed for different potential depths and with two methods: by measuring the sound velocities along the modulated and homogeneous density profiles, and by measuring the density profiles. The results of these two measurements are shown in Fig. 6.16 as a function of the normalised potential depth V_0/μ_0. While the superfluid fraction is predicted to be $f_{\mathrm{s}} = 1$ in a zero-temperature homogeneous superfluid, we observe a superfluid fraction decreasing when the potential depth increases. The results from the two measurements are in good agreement up to $V_0/\mu_0 \sim 1.15$. The discrepancy for larger depths can be explained by the fact that the superfluid fraction extracted from the in-situ analysis is performed on a signal spatially filtered by the absorption imaging, where only the fundamental spatial mode of the density profile is taken into account. The experimental data are compared to GP simulations with the full density profile and GP simulations with a filtered signal, keeping the fundamental modulation only. On the one hand, Leggett's integral measured from the speed of sound agrees well with the GP simulations calculated with the complete density signal. On the other hand, results from density profiles are closer to the GP simulations obtained with the filtered density, as expected. For potential depth $V_0/\mu_0 \gtrsim 1.15$, the depletion of the atomic cloud is $n_1^{\mathrm{c}}/n_0 \geq 1$, as shown in Fig. 6.15. Therefore, Leggett's integral is not defined, and the superfluid fraction obtained from in-situ profiles is *manually* set to zero. Finally, even with a partial measurement of in-situ density profiles, we observe Leggett's integral decreasing when the translational invariance is broken.

These two protocols provide a robust measurement of the reduction of the superfluid fraction down to $f_{\mathrm{s}} \sim 0.3$ in the presence of a density-modulation and at zero temperature, and could be improved with minor experimental modifications.

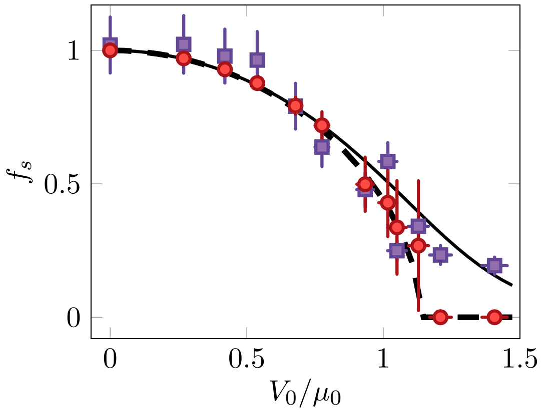

Figure 6.16: Superfluid fraction f_s in a density-modulated 2D Bose gas at zero temperature as a function of the potential depth V_0 normalised to the chemical potential μ_0. The superfluid fraction is extracted from sound propagation (violet squares) and from the estimate of Leggett's integral on in-situ images (red points). The measurement on in-situ images is partial as we extract only the fundamental mode of the spatial modulation. The superfluid fraction measured from in-situ images is set to zero at large lattice amplitudes $V_0/\mu_0 \gtrsim 1.15$. Indeed, for large values the spatially filtered contrast goes beyond one and Leggett's integral is not defined anymore. The sound measurement gives finite superfluid fraction for all the lattice amplitudes probed. The superfluid fraction is also displayed for the GP simulations on filtered density profiles (dashed line) and for GP simulations with the complete density signal (solid line). *Data extracted from a preliminary analysis.*

6.4 Conclusion

In this chapter we have probed the superfluid fraction in a zero-temperature weakly-interacting 2D Bose gas experiencing a breaking of translational invariance.

Superfluidity is intrinsically linked to the notion of transport and we started by describing an experimental protocol to measure the sound velocity in our atomic sample. We excite the atoms at rest with a linear perturbation of their potential, uniform over the atomic cloud. This perturbation is created with a magnetic field gradient. When switching off abruptly the magnetic field gradient, the position of the centre of mass of the atomic cloud oscillates in time with a frequency yielding the sound velocity.

In a second section, we detailed how, starting from a homogeneous planar Bose gas, we impose a density modulation by optically imprinting a sinusoidal lattice of period $\lambda = 4\,\mu\text{m}$. We characterised the light intensity profiles sent onto the atoms and we calibrated the potential depth of the lattice using the atomic response to this potential.

In the last section, we described the measurement of the sound velocity along and perpendicular to the density modulation. We observe that the speed of sound along the perturbation decreases when the potential depth increases. This behaviour is expected as the speed of sound is inversely proportional to the effective mass, which increases with the potential depth. We also detailed the estimate of Leggett's integral, derived in the previous chapter for our system, from the density profiles. This calculation requires to work on the in-situ images of the density profiles. These profiles are spatially filtered out by our absorption imaging, and thus the estimation of the density profiles is partial.

However, we could compare the superfluid fraction obtained from the speed of sound ratio to Leggett's integral over a large range of potential depths. We confirmed that, in the presence of a spatially-modulated potential breaking translational invariance, the zero-temperature superfluid fraction decreases when the amplitude of the modulation increases. These results were also compared to Gross-Pitaevskii simulations performed in the team, with which they are in good agreement.

Conclusion

In this thesis, I emphasised the diversity of physics approachable through cold atom experimental platforms by describing two results obtained in different contexts.

The first part of the thesis is dedicated to the general features of the 2D weakly-interacting Bose gas. In Chapter 1, the theoretical framework of the two-dimensional weakly-interacting Bose gas is described through a classical field approach. The weak interactions at play in our quasi-2D Bose gas are taken into account in a contact potential describing 3D collisions. The emergence of the superfluid phase and the restoration of a quasi-long-range order thanks to repulsive interactions is also described. The experimental setup that we use to produce planar Bose gases of repulsive weak interactions is detailed in Chapter 2. I gave a description of the large toolbox that we use to fully control the geometry of the atomic cloud, its density and temperature and finally I introduced our microwave chains allowing for high-precision spectroscopy measurements.

In the second part of this manuscript, I described our recent measurement on the least-bound dimers of rubidium 87. In Chapter 3, I first introduced the interatomic potential for hydrogen and alkali atoms. In the context of ultracold gases, these potentials are described by a few numbers as the s-wave scattering length a and the range of the van der Waals potential R_{vdW}. We highlighted the relation between the scattering states, fully described by a, and the positions of the least-bound states, given by R_{vdW} when van der Waals interactions are dominant at large interatomic distance. This so-called van der Waals universality allows a simpler characterisation of the interatomic potential. Finally, we focused on the least-bound states or rubidium 87. These states are of large physical interest in ultracold physics as they allow to tune the atomic interaction strength via Fano-Feshbach resonances. We presented a simple model to describe the hyperfine and Zeeman levels of a given least-bound rovibrational state. We then described the detection via mw-induced photoassociation of the whole Zeeman diagram of the least-bound state of ^{87}Rb, composed of one atom in the hyperfine level $f = 1$ and one atom in the hyperfine level $f = 2$. Adjusting our simple model to these data, we could estimate the coupling strength between the triplet potential and the singlet potential.

In Chapter 4, we focused on one particular state of the Zeeman diagram which has the specificity to be magnetic-field-insensitive. The energy dependence of this state on the density of the atomic bath is highlighted thanks to a high-precision spectroscopy. We used a mean-field approach to interpret these results as the effect of atom-dimer interactions and measured the associated atom-dimer scattering length a_{ad}. Finally, we measured this atom-dimer scattering length for two atomic baths and for the second-to-least bound state with one atomic bath. The perturbative model we derived can be used for any atomic species as long as their hyperfine coupling is large compared to the depth of the least-bound states. It allows to detect precisely bound states after the measurement of only a few bound states of the same multiplicity. We measured the atom-dimer scattering lengths far from the universal regime, yet, we obtain two close values when probing it with two different atomic baths of close atom-atom scattering lengths. This result is consistent with the existence of a van der Waals universality for atom-dimer interactions with bosons. Finally, we were not able to observe mw-induced Fano-Feshbach with our setup and atomic species, but these measurements pave the way for investigation with more suitable atomic species as sodium, potassium or caesium or for atom chips experimental setups which benefit from stronger mw fields.

The third part of this manuscript is dedicated to the zero-temperature superfluid fraction in a weakly-interacting 2D Bose gas when we impose a breaking of translational invariance. In Chapter 5, I introduced the original analysis performed by Leggett in 1970 in the context of supersolids. We applied the same analysis for our atomic systems, i.e. we studied the superfluid fraction defined within the framework of twisted boundary conditions for a 2D Bose gas in the presence of a potential spatially-modulated along one direction. We demonstrated that in the context of systems described by the Gross-Piteavskii equation, the integral found by Leggett as an upper-bound on the superfluid fraction in solids gives the actual superfluid fraction. By further constraining the modulation to be periodic, we linked this superfluid fraction to sound velocity along and perpendicular to the periodic spatial-modulation.

In Chapter 6, we described the experimental testing of Leggett's integral. We imposed a sinusoidal density-modulation to our atomic sample and used two experimental protocols: we excited the atoms and measured the sound velocity along both axis and, starting from a similar system, we measured Leggett's integral from the in-situ profile of the sample. We observed the superfluid fraction decreasing when increasing the amplitude of the density modulation. The two experimental protocols gave results in good agreement, although the measurement of Leggett's integral from density profiles is limited by our imaging system.

A first improvement would be to work on the experimental setup to have a better resolution. Furthermore, the comparison of Leggett's superfluid fraction definition with a transport measurement now done, one might want to get rid of the periodicity constraint on the density-modulation to study Leggett's integral with more exotic potentials. This possibility should be carefully considered, as new constraints may arise. The comparison of Leggett's integral and sound velocities with more complex potentials as superlattice have been numerically studied in the group and led to encouraging results, although the experimental implementation of such systems is not trivial. Finally, this measurement can also reopen the discussion of the validity of Leggett's result in actual supersolids.

Appendices

A

Zeeman diagram: parameters and data set

A.1 Model

We derived in Chapter 3 a simple model to describe the hyperfine and the Zeeman diagram of a rovibrational state loosely bound. The Hamiltonian acting on free pairs of atoms $|f_1, m_{f_1}; f_2, m_{f_2}\rangle$ is a sum of three contributions:

$$\hat{H} = \hat{H}_{\text{hfs}} + \hat{H}_{\text{Z}} + \hat{H}_{\text{st}}, \tag{A.1}$$

the hyperfine splitting $\hat{H}_{\text{hfs}}$, the Zeeman term $\hat{H}_{\text{Z}}$ and a singlet-triplet coupling $\hat{H}_{\text{st}}$. In order to diagonalise the Hamiltonian Eq. (A.1), one writes the atom pairs states in the decoupled basis:

$$|f_1, m_{f_1}; f_2, m_{f_2}\rangle \quad \to |\sigma_1,\, \iota_1;\, \sigma_2,\, \iota_2\rangle \equiv |s_1 = 1/2,\, \sigma_1,\, i_1 = 3/2,\, \iota_1;\, s_2 = 1/2,\, \sigma_2,\, i_2 = 3/2,\, \iota_2\rangle, \tag{A.2}$$

where the projections on the quantization axis z of the electronic spin angular momentum $s = 1/2$ and the nucleic spin angular momentum $i = 3/2$ are written $\sigma = \pm 1/2$ and $\iota = \pm 1/2,\, \pm 3/2$. We give therefore the hyperfine levels $|f, m_f\rangle$ of an atom of ^{87}Rb in its electronic ground state in the decoupled basis in Tab. A.1.

$\|f, m_f\rangle$	$\|\sigma,\, \iota\rangle$
$\|1, +1\rangle$	$-\sqrt{3}/2\|-1/2,\, 3/2\rangle + 1/2\|1/2,\, 1/2\rangle$
$\|1,\ \ 0\rangle$	$1/\sqrt{2}\big[\|1/2,\, -1/2\rangle + \|-1/2,\, 1/2\rangle\big]$
$\|1, -1\rangle$	$\sqrt{3}/2\|1/2,\, -3/2\rangle - 1/2\|-1/2,\, -1/2\rangle$
$\|2, +2\rangle$	$\|1/2,\, 3/2\rangle$
$\|2, +1\rangle$	$1/2\|-1/2,\, 3/2\rangle + \sqrt{3}/2\|1/2,\, 1/2\rangle$
$\|2,\ \ 0\rangle$	$1/\sqrt{2}\big[\|1/2,\, -1/2\rangle - \|-1/2,\, 1/2\rangle\big]$
$\|2, -1\rangle$	$1/2\|1/2,\, -3/2\rangle + \sqrt{3}/2\|-1/2,\, -1/2\rangle$
$\|2, -2\rangle$	$\|-1/2,\, -3/2\rangle$

Table A.1: Table of the hyperfine levels of an atom of ^{87}Rb in its electronic ground state in the coupled basis (first column) and in the decoupled basis (second column).

A.2 Coupling to a microwave field

We performed mw-induced photoassociation to measure the Zeeman diagram of the least-bound state $n = -1$ of the branch $\{f = 1; f = 2\}$ of ^{87}Rb. The magnetic field created by the microwave of frequency $\nu = \omega/2\pi$ is written in a basis $(\boldsymbol{e}_x, \boldsymbol{e}_y, \boldsymbol{e}_z)$:

$$\boldsymbol{B}_\omega(t) = \frac{1}{2}\left[B_{\omega,x}\exp(i\phi_x)\boldsymbol{e}_x + B_{\omega,y}\exp(i\phi_y)\boldsymbol{e}_y + B_{\omega,z}\exp(i\phi_z)\boldsymbol{e}_z\right]\exp(-i\omega t) + \text{c.c.}, \quad \text{(A.3)}$$

where the variables $B_{\omega,j}$ and ϕ_j are amplitudes and phases respectively. The real amplitude writes $B_\omega^2 = B_{\omega,x}^2 + B_{\omega,y}^2 + B_{\omega,z}^2$ and we introduce the complex unit vector $\boldsymbol{\varepsilon} = (\varepsilon_x, \varepsilon_y, \varepsilon_z)$ whose component along the axis α writes $\varepsilon_\alpha = |\varepsilon_\alpha|\exp(i\phi_\alpha)$. Using these notations, the field equivalently reads:

$$\boldsymbol{B}_\omega(t) = \frac{B_\omega}{2}\boldsymbol{\varepsilon}\exp(-i\omega t) + \text{c.c.} \quad \text{(A.4)}$$

The coupling of such field to the electronic degree of freedom of atoms of ^{87}Rb in their electronic ground state writes:

$$\hat{W} = \frac{\mu_B g_s}{\hbar}\hat{\boldsymbol{s}}\cdot\boldsymbol{B}_\omega(t), \quad \text{(A.5)}$$

with $\hat{\boldsymbol{s}}$ the electronic spin of the atoms.

We compute the matrix elements of $\hat{W}$ for atomic transitions between the two hyperfine levels $f = 1 \to f = 2$ of the ground state. The comparison of these matrix elements with the measured Rabi frequency of the corresponding transitions will then give the value of $B_\omega\boldsymbol{\varepsilon}$ in Eq. (A.4) and thus the mw field tomography.
We write the field $\boldsymbol{B}_\omega(t)$ in the spherical basis $(\boldsymbol{e}_+, \boldsymbol{e}_-, \boldsymbol{e}_0)$, for convenience. The basis change $(\boldsymbol{e}_x, \boldsymbol{e}_y, \boldsymbol{e}_z) \leftrightarrow (\boldsymbol{e}_+, \boldsymbol{e}_-, \boldsymbol{e}_0)$ is written:

$$\boldsymbol{e}_+ = -\frac{\boldsymbol{e}_x + i\boldsymbol{e}_y}{\sqrt{2}}, \quad \boldsymbol{e}_- = \frac{\boldsymbol{e}_x - i\boldsymbol{e}_y}{\sqrt{2}}, \quad \boldsymbol{e}_0 = \boldsymbol{e}_z, \quad \boldsymbol{e}_x = \frac{\boldsymbol{e}_- - \boldsymbol{e}_+}{\sqrt{2}}, \quad \boldsymbol{e}_y = i\frac{\boldsymbol{e}_+ + \boldsymbol{e}_-}{\sqrt{2}}. \quad \text{(A.6)}$$

The unit vector $\boldsymbol{\varepsilon}$ writes $\boldsymbol{\varepsilon} = (\varepsilon_+, \varepsilon_-, \varepsilon_0)$ in the spherical basis an its components are transposed from one basis to another following:

$$\varepsilon_+ = \frac{-\varepsilon_x + i\varepsilon_y}{\sqrt{2}}, \quad \varepsilon_- = \frac{\varepsilon_x + i\varepsilon_y}{\sqrt{2}} \quad \varepsilon_0 = \varepsilon_z, \quad \varepsilon_x = \frac{\varepsilon_- - \varepsilon_+}{\sqrt{2}}, \quad \varepsilon_y = -i\frac{\varepsilon_+ + \varepsilon_-}{\sqrt{2}}. \quad \text{(A.7)}$$

The coupling Hamiltonian Eq. (A.5) reads in the spherical basis:

$$\hat{W} = \frac{\mu_B g_s}{\hbar}\frac{B_\omega}{2}\left(\frac{1}{\sqrt{2}}(S_-\varepsilon_- - S_+\varepsilon_+) + S_z\varepsilon_0\right)\exp(-i\omega t) + \text{c.c.}, \quad \text{(A.8)}$$

with the rising and lowering operators $s_\pm = s_x \pm i s_y$. We decompose the coupling Hamiltonian in three contributions: $\hat{W}_+$, $\hat{W}_-$ and $\hat{W}_0$ corresponding to σ_+ $(\Delta m_f = +1)$, σ_- $(\Delta m_f = -1)$ and π $(\Delta m_f = 0)$ transitions respectively. They are written in the frame rotating with the mw:

$$\hat{W}_+ = -\frac{\mu_B g_s}{\hbar}\frac{B_\omega}{2}\frac{1}{\sqrt{2}}\left[S_+\varepsilon_+\exp(-i\omega t) + \text{c.c.}\right], \quad \text{(A.9)}$$

$$\hat{W}_- = -\frac{\mu_B g_s}{\hbar}\frac{B_\omega}{2}\frac{1}{\sqrt{2}}\left[S_-\varepsilon_-\exp(-i\omega t) + \text{c.c.}\right], \quad \text{(A.10)}$$

$$\hat{W}_0 = -\frac{\mu_B g_s}{\hbar}\frac{B_\omega}{2}\left[S_z\varepsilon_z\exp(-i\omega t) + \text{c.c.}\right]. \quad \text{(A.11)}$$

mw chain	B_ω (mG)	$\lvert\varepsilon_x\rvert$	$\lvert\varepsilon_y\rvert$	$\lvert\varepsilon_z\rvert$	$\phi_x-\phi_z$	$\phi_y-\phi_z$
RS1	15	0.58	0.60	0.55	0.04π	0.42π
RS2	32	0.25	0.10	0.96	0.43π	0.09π

Table A.2: Tomography of the mw fields Eq. (A.4) produced by the two antennas installed on our experimental setup.

We consider the transitions between the hyperfine levels $|f=1,m_f=0\rangle \rightarrow |f=2,m_f=0,\pm1\rangle$ and, using their expression in the decoupled basis (see Tab. A.1), we compute their associated Rabi frequencies:

$$\Omega_{\sigma_+} = \frac{\mu_B g_s}{\hbar^2}\frac{B_\omega|\varepsilon_+|}{\sqrt{2}}|\langle 2,1|\,S_+|1,0\rangle| = \frac{\mu_B g_s}{\hbar}B_\omega\frac{\sqrt{3}|\varepsilon_+|}{4}, \tag{A.12}$$

$$\Omega_{\sigma_-} = \frac{\mu_B g_s}{\hbar^2}\frac{B_\omega|\varepsilon_-|}{\sqrt{2}}|\langle 2,-1|\,S_-|1,0\rangle| = \frac{\mu_B g_s}{\hbar}B_\omega\frac{\sqrt{3}|\varepsilon_-|}{4}, \tag{A.13}$$

$$\Omega_{\pi} = \frac{\mu_B g_s}{\hbar^2}B_\omega|\varepsilon_+||\langle 2,0|\,S_z|1,0\rangle| = \frac{\mu_B g_s}{\hbar}B_\omega\frac{|\varepsilon_0|}{2}. \tag{A.14}$$

$$\tag{A.15}$$

We measure these three Rabi frequencies while applying a static external field B along the space directions $\alpha \equiv x,\,y,\,z$. We obtain then nine Rabi frequencies and, as the global phase of the mw field is not accessible, we only need five parameters to know the field tomography : $(B_\omega,\,|\varepsilon_x|,\,|\varepsilon_y|,\,|\varepsilon_z|,\,(\phi_x-\phi_z),\,(\phi_y-\phi_z))$. These parameters are calculated using the following equations:

$$\eta \equiv \frac{\mu_B g_s}{\hbar}B_\omega = 2\sqrt{\sum_\alpha(\Omega_\pi^\alpha)^2}, \tag{A.16}$$

$$|\varepsilon_{\alpha_j}| = \frac{2}{\eta}\Omega_\pi^{\alpha_j}, \tag{A.17}$$

$$\phi_{\alpha_j}-\phi_{\alpha_k} = \arcsin\left(\frac{8}{3}\frac{(\Omega_{\sigma_+}^{\alpha_l})^2-(\Omega_{\sigma_-}^{\alpha_l})^2}{|\varepsilon_j||\varepsilon_k|\eta^2}\right). \tag{A.18}$$

We defined $\Omega_\mathcal{P}^\alpha$ as the Rabi frequency of a transition of polarisation $\mathcal{P}$ with an external static magnetic field along the axis α.

We performed this field tomography calibration for the two antennas installed in our experimental setup and we give in Tab. A.2 the results we obtained.

A.3 Experimental parameters

The atoms are initially prepared in the hyperfine level $f=1$, in pure states or binary mixtures of the sub-levels. The atomic sample has a homogeneous in-plane profile when prepared in pure states. In the case of binary mixtures, we prepare the sample is an array of microtraps of size $\sim 5\,\mu$m in order to prevent spatial separation of the two components due to residual magnetic field gradients. We give in Tab. A.3 the experimental parameters we used to observe the fifteen levels of the $n=-1$ rovibrational state. We precise for each: its total angular momentum projection m_F, the initial state from which we photoassociate the atoms, the

m_F	N	Initial state	Cloud	$\mathcal{P}$	$B_\omega^{\mathcal{P}}$ (mG)	Ω/Ω_0	δt (s)	$\delta n_\mathrm{a}/n_\mathrm{a}$ (%)	Γ (kHz)
3	12	$\|+1;+1\rangle$	Bulk	σ^+	12	0.48	5	33	3.2
2	7	$\|+1;+1\rangle$	Bulk	π	31	0.85	1	20	3.6
	13	$\|+1;0\rangle$	Patches	σ^+	12	0.39	10	17	2.9
1	4	$\|+1;+1\rangle$	Bulk	σ^-	23	0.37	5	24	3.1
	11	$\|0;0\rangle$	Bulk	σ^+	12	0.34	0.5	9	1.8
	15	$\|-1;+1\rangle$	Patches	σ^+	12	0.35	5	22	2.7
0	3	$\|-1;+1\rangle$	Patches	π	31	0.55	5	21	2.7
	9	$\|0;0\rangle$	Bulk	π	31	1	0.115	14	0.8
	14	$\|-1;+1\rangle$	Patches	π	31	0.66	2.5	25	6
-1	1	$\|-1;+1\rangle$	Patches	σ^-	8	0.18	10	23	3.7
	5	$\|0;0\rangle$	Bulk	σ^-	8	0.21	1	11	1.5
	10	$\|-1;-1\rangle$	Bulk	σ^+	12	0.19	10	21	1.8
-2	2	$\|-1;0\rangle$	Patches	σ^-	8	0.19	10	13	6
	8	$\|-1;-1\rangle$	Bulk	π	31	0.85	0.5	14	2.3
-3	6	$\|-1;-1\rangle$	Bulk	σ^-	8	0.21	5	17	3.5

Table A.3: Experimental parameters used to determine the Zeeman diagram of the least-bounded rovibrational state. Sub-levels are sorted by projection of the total angular momentum m_F. We attribute to each level a number (N) standing for its position in the energy scale at large magnetic field, N= 1 being the lowest in energy. Atoms are originally in the $|f=1, m_f\rangle$ hyperfine state of the electronic ground state and the different pairs of initial states are labelled with the notation $|m_{f_1}; m_{f_2}\rangle$. When starting from pure states $|m_{f_1}; m_{f_2}=m_{f_1}\rangle$, loss spectroscopy is performed on a uniform planar gas while the measurement is done in small patches array for mixtures. The polarisation of the microwave field which drives a given atom pair to dimer transition is labelled $\mathcal{P}$. We send microwave pulses during a fixed time δt for a given Zeeman level. Their amplitude in the polarisation $\mathcal{P}$ is given by $B_\omega^{\mathcal{P}}$. The orientation of the external magnetic is perpendicular to the plane for all levels but N= 4, for which we rotate it into the plane to obtain a larger coupling strength. Two different antennas and microwave sources are used in this work and for each transition we chose the one giving the largest excitation strength Ω/Ω_0. The two last columns give the measured average depletion $\delta n_\mathrm{a}/n_\mathrm{a}$ and full width at half maximum Γ.

cloud shape, the polarisation of the transition $\mathcal{P}$ and the corresponding mw field amplitude $B_\omega^{\mathcal{P}} = |B_\omega \varepsilon_{\mathcal{P}}|$. The matrix elements $\hbar\Omega = \langle \text{final}|\hat{W}|\text{initail}\rangle$, extracted from our model, do not give a complete information on the overlap between the bound and free states. Indeed, we consider only the angular part of the wave functions and do not have any information on their radial part. We give however the relative elements Ω/Ω_0, normalized with respect to the coupling Ω_0 of the strongest line: M_1. Finally, we give the duration of the excitation t and the typical measured depletion and line width.

A.4 Data set

We measured the fifteen sub-levels of the Zeeman diagram of the least-bound state $n=-1$ of the multiplicity $\{f=1; f=2\}$ over $\sim 2\,\mathrm{G}$. We give in Tab. A.4 the initial state and the measured position of the dimers from the energy of a free pair in $|f=1; f=2\rangle$ at zero-magnetic field. We also give for each experimental point the distance between the dimer energy measured and the dimer energy predicted by our simple model using our best fit to the data.

N	Initial state	$B = 0.75$ G	$B = 1$ G	$B = 1.25$ G	$B = 1.5$ G	$B = 1.75$ G
12	$\vert +1;+1\rangle$	-24.462	-24.587	-24.118	-23.947	-23.778
		-2	1	-2	-7	-10
7	$\vert +1;+1\rangle$	-25.616	-25.553	-25.516	-25.485	-25.468
		-3	0	-2	2	-1
13	$\vert +1;0\rangle$	-24.380		-23.790		-23.146
		2		5		8
4	$\vert +1;+1\rangle$	-26.214	-26.354	-26.505	-26.664	-26.827
		1	1	0	4	3
11	$\vert 0;0\rangle$	-24.595	-24.431	-24.267	-24.097	-23.928
		1	3	-1	3	2
15	$\vert -1;+1\rangle$	-23.640		-22.642		-21.624
		-5		-3		-12
3	$\vert -1;+1\rangle$	-26.712		-27.356		-28.027
		-0		4		5
9	$\vert 0;0\rangle$	-24.985	-24.985	-24.985	-24.985	-24.985
		0	0	0	0	0
14	$\vert -1;+1\rangle$	-24.338		-23.694		-23.020
		-1		-5		-3
1	$\vert -1;+1\rangle$	-27.097		-28.068		-29.078
		0		0		11
5	$\vert 0;0\rangle$	-25.698	-25.876	-26.049	-26.223	-26.394
		0	-2	1	-2	2
10	$\vert -1;-1\rangle$	-24.822	-24.685	-24.538	-24.381	-24.221
		-1	-2	-2	-4	-4
2	$\vert -1;0\rangle$	-26.926		-27.569		-28.235
		-5		-3		-6
8	$\vert -1;-1\rangle$	-25.180	-25.208	-25.225	-25.240	-25.251
		-1	-2	0	-1	-1
6	$\vert -1;-1\rangle$	-25.511	-25.686	-25.856	-26.031	-26.202
		3	2	3	1	3

Table A.4: Zeeman diagram measurement. The atomic sample is prepared in the hyperfine level $f = 1$ manifold. The initial state from which we performed photoassociation can be either a pure state or a binary mixture of the $f = 1$ sub-levels and is given for each bound level, labelled N from the lowest energy. We write it as $|m_{f_1}, m_{f_2}\rangle \equiv |f_1 = 1, m_{f_1}; f_2 = 1, m_{f_2}\rangle$ for convenience. We give the position of the dimers in MHz with respect with the free pair $|f_1 = 1; f_2 = 2\rangle$ at zero-magnetic field (first sub-row) and its deviation in kHz from the fit (second sub-row). All errorbars are estimated at 1 kHz.

B

Linear response to a periodic potential

In the second part of this manuscript, we imposed a breaking of translational invariance in our atomic sample by imprinting a periodic potential of period λ:

$$V(y) = V_0 \cos\left(\frac{2\pi}{\lambda} y\right). \tag{B.1}$$

We calibrate the potential depth V_0 using the response from the atomic density profile to lattices with large periods and small depths. We relate the density perturbation to the potential depth using linear response theory, see Ref. [87].

For a system of N particles with coordinates $\boldsymbol{r}_i$, the perturbation to the many-body Hamiltonian write:

$$\begin{aligned} W &= \sum_{i=1}^{N} V_0 \cos(k y_i) && \text{(B.2)} \\ &= \frac{V_0}{2} \left[\sum_{i=1}^{N} \exp[-\mathrm{i} k y_i] + \text{c.c.}\right] && \text{(B.3)} \\ &= \frac{V_0}{2} \left[\rho_{\boldsymbol{k}} + \rho_{\boldsymbol{k}}^{\dagger}\right] && \text{(B.4)} \end{aligned}$$

where $\boldsymbol{k} = 2\pi/\lambda\, \boldsymbol{e}_y$ is the wave vector or the lattice potential and ρ_k is the Fourier component of the density operator

$$\rho_{\boldsymbol{k}} = \sum_{i=1}^{N} \exp[-\mathrm{i} \boldsymbol{k} \cdot \boldsymbol{r}_i]. \tag{B.5}$$

In the context of linear response theory, this Hamiltonian corresponds to a perturbation $G = \rho_{\boldsymbol{k}}$ of strength $\lambda = -V_0/2$, where we used the notations of [87] (Eq. (7.1)). The perturbed density profile is expected to be of the form

$$n(x, y) = n_0 + n_1 \cos(k y), \tag{B.6}$$

and our goal is the relate the contrast n_1/n_0 with V_0.
Linear theory gives us access to the $\delta\langle\rho_{\boldsymbol{k}}\rangle$, so that it is natural to consider

$$\langle\cos(k y)\rangle = \langle\frac{1}{N} \sum_{i=1}^{N} \cos(k y_i)\rangle = \frac{1}{2N} \left(\delta\langle\rho_{\boldsymbol{k}}\rangle + \delta\langle\rho_{\boldsymbol{k}}^{\dagger}\rangle\right). \tag{B.7}$$

On the one hand we have:

$$\langle\cos(ky)\rangle = \frac{\int_0^L \cos(ky) n(x,y)\,\mathrm{d}y}{\int_0^L n(x,y)\,\mathrm{d}y} = \frac{n_1}{2n_0}, \tag{B.8}$$

where L is the size of the system and is a multiple of the period λ.

On the other hand, $\delta\langle\rho_{\boldsymbol{k}}\rangle$ is the fluctuation of the system induced by the periodic perturbation and is determined by the dynamic polarizability χ defined in [87] (Eq. (7.2)) as:

$$\delta\langle\rho_{\boldsymbol{k}}^\dagger\rangle = \lambda\chi_{\rho_{\boldsymbol{k}}^\dagger,\rho_{\boldsymbol{k}}}(0) + \lambda^*\chi_{\rho_{\boldsymbol{k}}^\dagger,\rho_{\boldsymbol{k}}^\dagger}(0), \tag{B.9}$$

where we recall that $\lambda = -V_0/2$. Using this definition we find

$$\langle\cos(ky)\rangle = -\frac{V_0}{4N}\left[\chi_{\rho_{\boldsymbol{k}},\rho_{\boldsymbol{k}}}(0) + \chi_{\rho_{\boldsymbol{k}},\rho_{\boldsymbol{k}}^\dagger}(0) + \chi_{\rho_{\boldsymbol{k}}^\dagger,\rho_{\boldsymbol{k}}}(0) + \chi_{\rho_{\boldsymbol{k}}^\dagger,\rho_{\boldsymbol{k}}^\dagger}(0)\right] \tag{B.10}$$

$$= -\frac{V_0}{4N}\left[\chi_{\rho_{\boldsymbol{k}}^\dagger}(0) + \chi_{\rho_{\boldsymbol{k}}}(0)\right], \tag{B.11}$$

where we used the relation $\chi_{\rho_{\boldsymbol{k}},\rho_{\boldsymbol{k}}}(0) = \chi_{\rho_{\boldsymbol{k}}^\dagger,\rho_{\boldsymbol{k}}^\dagger}(0) = 0$ given in [87] (Eq. (7.3)) and the notation $\chi_F \equiv \chi_{F^\dagger,F}$.

The linear density response function has been studied in the context of the weakly-interacting gas of bosons and in this case, one can show that (see Eqs. (7.24) and (7.90) of Ref. [87]):

$$\chi_{\rho_{\boldsymbol{k}}^\dagger}(0) = \chi_{\rho_{\boldsymbol{k}}}(0) = \frac{N\hbar^2k^2}{m\varepsilon^2(k)} \tag{B.12}$$

where $\varepsilon(k)$ is the Bogoliubov excitation spectrum, suitable for zero-temperature gases:

$$\varepsilon^2(k) = \frac{\hbar^2k^2}{2m}\left(\frac{\hbar^2k^2}{2m} + 2gn_0\right). \tag{B.13}$$

Finally, using our previous result Eq. (B.8), we find that in the perturbative regime the contrast of the density profile in the presence of a periodic potential writes

$$\frac{n_1}{n_0} = -\frac{V_0}{\frac{\hbar^2k^2}{4m} + gn_0}. \tag{B.14}$$

Publications

LIST OF PUBLICATIONS:

- *Magnetic dipolar interaction between hyperfine clock states in a planar alkali Bose gas*, Y. -Q. Zou, B. Bakkali-Hassani, C. Maury, É. Le Cerf, S. Nascimbene, J. Dalibard and J. Beugnon, Physical Review Letters **125**, 233604, (December 2020).
- *Tan's two-body contact across the superfluid transition of a planar Bose gas*, Y.-Q. Zou, B. Bakkali-Hassani, C. Maury, É. Le Cerf, S. Nascimbene, J. Dalibard and J. Beugnon, Nature communications **12**, 760, (February 2021).
- *Optical control of the density and spin spatial profiles of a planar Bose gas*, Y.-Q. Zou, É. Le Cerf, B. Bakkali-Hassani, C. Maury, G. Chauveau, P. C. M. Castilho, R. Saint-Jalm, S. Nascimbene, J. Dalibard and J. Beugnon, Journal of Physics B: Atomic, Molecular, and Optical Physics **54**, 08LT01, (April 2021).
- *Realization of a Townes soliton in a two-component planar Bose gas*, B. Bakkali-Hassani, C. Maury, Y.-Q. Zou, É. Le Cerf, R. Saint-Jalm, P. C. M. Castilho, S. Nascimbene, J. Dalibard and J. Beugnon, Physical Review Letters **127**, 023603, (July 2021).
- *The cross-over from Townes solitons to droplets in a 2D Bose mixture*, B. Bakkali-Hassani, C. Maury, S. Stringari, S. Nascimbene, J. Dalibard and J. Beugnon, New Journal of Physics **25**, (January 2023).
- *Precision measurement of atom-dimer interaction in a uniform planar Bose gas*, C. Maury, B. Bakkali-Hassani, G. Chauveau, F. Rabec, S. Nascimbene, J. Dalibard and J. Beugnon, Physical Review Research **5**, L012020, (February. 2023).
- *Superfluid fraction in an interacting spatially modulated Bose-Einstein condensate*, G. Chauveau, C. Maury, F. Rabec, C. Heintze, G. Brochier, S. Nascimbene, J. Dalibard and J. Beugnon, ArXiv:2302.01776, (February 2023).

References

[1] A. Einstein; "Quantentheorie des einatomigen idealen Gases"; in "Sitzungsberichte der Preussischen Akademie der Wissenschaften," . 2 citations on pages 7 and 13

[2] M. H. Anderson, J. R. Ensher, M. R. Matthews, C. E. Wieman & E. A. Cornell; "Observation of Bose-Einstein Condensation in a Dilute Atomic Vapor"; Science **269**, pp. 198–201 (1995). 2 citations on pages 7 and 14

[3] C. C. Bradley, C. A. Sackett, J. J. Tollett & R. G. Hulet; "Evidence of Bose-Einstein Condensation in an Atomic Gas with Attractive Interactions"; Phys. Rev. Lett. **75**, pp. 1687–1690 (1995). 2 citations on pages 7 and 14

[4] K. B. Davis, M. O. Mewes, M. R. Andrews, N. J. van Druten, D. S. Durfee, D. M. Kurn & W. Ketterle; "Bose-Einstein Condensation in a Gas of Sodium Atoms"; Phys. Rev. Lett. **75**, pp. 3969–3973 (1995). 2 citations on pages 7 and 14

[5] P. Kapitza; "Viscosity of Liquid Helium below the λ-Point"; Nature **141** (1938). 2 citations on pages 7 and 23

[6] J. F. Allen & A. D. Misener; "Flow of Liquid Helium II"; Nature **141** (1938). 2 citations on pages 7 and 23

[7] V. F. Sears & E. C. Svensson; "Pair Correlations and the Condensate Fraction in Superfluid ^{4}He"; Phys. Rev. Lett. **43**, pp. 2009–2012 (1979). Cited on page 7

[8] I. Bloch, J. Dalibard & W. Zwerger; "Many-body physics with ultracold gases"; Rev. Mod. Phys. **80**, pp. 885–964 (2008). 2 citations on pages 7 and 24

[9] M. R. Andrews, C. G. Townsend, H. Miesner, D. S. Durfee, D. M. Kurn & W. Ketterle; "Observation of Interference Between Two Bose Condensates"; Science **275(5300)**, pp. 637—641 (1997). Cited on page 7

[10] I. Bloch, T. W. I, Hansch & T. Esslinger; "Measurement of the spatial coherence of a trapped Bose gas at the phase transition"; Nature **403**, pp. 166—170 (2000). Cited on page 7

[11] B. DeMarco & D. S. Jin; "Onset of Fermi Degeneracy in a Trapped Atomic Gas"; Science **285**, pp. 1703–1706 (1999). Cited on page 7

[12] A. G. Truscott, K. E. Strecker, W. I. McAlexander, G. B. Partridge & R. G. Hulet; "Observation of Fermi Pressure in a Gas of Trapped Atoms"; Science **291**, pp. 2570–2572 (2001). Cited on page 7

[13] F. Schreck, L. Khaykovich, K. L. Corwin, G. Ferrari, T. Bourdel, J. Cubizolles & C. Salomon; "Quasipure Bose-Einstein Condensate Immersed in a Fermi Sea"; Phys. Rev. Lett. **87**, p. 080403 (2001). Cited on page 7

[14] A. Griesmaier, J. Werner, S. Hensler, J. Stuhler & T. Pfau; "Bose-Einstein Condensation of Chromium"; Phys. Rev. Lett. **94**, p. 160401 (2005). Cited on page 7

[15] M. Lu, N. Q. Burdick, S. H. Youn & B. L. Lev; "Strongly Dipolar Bose-Einstein Condensate of Dysprosium"; Phys. Rev. Lett. **107**, p. 190401 (2011). Cited on page 7

[16] J. Lim, H. Lee & J. Ahn; "Review of cold Rydberg atoms and their applications"; Journal of the Korean Physical Society **63**, pp. 867–876 (2013). Cited on page 7

[17] H. Ritsch, P. Domokos, F. Brennecke & T. Esslinger; "Cold atoms in cavity-generated dynamical optical potentials"; Rev. Mod. Phys. **85**, pp. 553–601 (2013). Cited on page 7

[18] S. Inouye, M. R. Andrews, J. B. Stenger, H. J. Miesner, D. M. Stamper-Kurn & W. Ketterle; "Observation of Feshbach resonances in a Bose–Einstein condensate"; Nature **392**, pp. 151–154 (1998). 2 citations on pages 7 and 54

[19] P. Courteille, R. S. Freeland, D. J. Heinzen, F. A. van Abeelen & B. J. Verhaar; "Observation of a Feshbach Resonance in Cold Atom Scattering"; Phys. Rev. Lett. **81**, pp. 69–72 (1998). 2 citations on pages 7 and 54

[20] S. L. Cornish, N. R. Claussen, J. L. Roberts, E. A. Cornell & C. E. Wieman; "Stable ^{85}Rb Bose-Einstein Condensates with Widely Tunable Interactions"; Phys. Rev. Lett. **85**, pp. 1795–1798 (2000). Cited on page 7

[21] K. M. O'Hara, S. L. Hemmer, M. E. Gehm, S. R. Granade & J. E. Thomas; "Observation of a Strongly Interacting Degenerate Fermi Gas of Atoms"; Science **298**, pp. 2179–2182 (2002). Cited on page 7

[22] T. Bourdel, L. Khaykovich, J. Cubizolles, J. Zhang, F. Chevy, M. Teichmann, L. Tarruell, S. J. J. M. F. Kokkelmans & C. Salomon; "Experimental Study of the BEC-BCS Crossover Region in Lithium 6"; Phys. Rev. Lett. **93**, p. 050401 (2004). Cited on page 8

[23] M. Bartenstein, A. Altmeyer, S. Riedl, S. Jochim, C. Chin, J. H. Denschlag & R. Grimm; "Crossover from a Molecular Bose-Einstein Condensate to a Degenerate Fermi Gas"; Phys. Rev. Lett. **92**, p. 120401 (2004). Cited on page 8

[24] P. Naidon & S. Endo; "Efimov physics: a review"; Reports on Progress in Physics **80**, p. 056001 (2017). 2 citations on pages 8 and 69

[25] V. L. Berezinsky; "Destruction of Long-range Order in One-dimensional and Two-dimensional Systems Possessing a Continuous Symmetry Group. II. Quantum Systems." Sov. Phys. JETP **34**, p. 610 (1972). 2 citations on pages 8 and 23

[26] J. M. Kosterlitz & D. J. Thouless; "Ordering, metastability and phase transitions in two-dimensional systems"; Journal of Physics C: Solid State Physics **6**, pp. 1181–1203 (1973). 2 citations on pages 8 and 23

[27] J. V. José; *40 Years of Berezinskii-Kosterlitz-Thouless Theory* (World Scientific). (2013). Cited on page 8

[28] B. Paredes, A. Widera, V. Murg, O. Mandel, S. Fölling, I. Cirac, G. Shlyapnikov, T. Hänsch & I. Bloch; "Tonks–Girardeau gas of ultracold atoms in an optical lattice"; Nature **429**, pp. 277–281 (2004). Cited on page 8

[29] T. Kinoshita, T. Wenger & D. S. Weiss; "Observation of a One-Dimensional Tonks-Girardeau Gas"; Science **305**, pp. 1125–1128 (2004). Cited on page 8

[30] J. Hubbard; "Electron correlations in narrow energy bands"; Proc. R. Soc. Lond. A **276**, pp. 238–257 (1963). Cited on page 8

[31] M. Greiner, O. Mandel, T. Esslinger, T. W. Hänsch & I. Bloch; "Quantum phase transition from a superfluid to a Mott insulator in a gas of ultracold atoms"; Nature **415**, pp. 39–44 (2002). Cited on page 8

[32] T. Stöferle, H. Moritz, C. Schori, M. Köhl & T. Esslinger; "Transition from a Strongly Interacting 1D Superfluid to a Mott Insulator"; Phys. Rev. Lett. **92**, p. 130403 (2004). Cited on page 8

[33] I. B. Spielman, W. D. Phillips & J. V. Porto; "Mott-Insulator Transition in a Two-Dimensional Atomic Bose Gas"; Phys. Rev. Lett. **98**, p. 080404 (2007). Cited on page 8

[34] M. Köhl, H. Moritz, T. Stöferle, C. Schori & T. Esslinger; "Superfluid to Mott insulator transition in one, two, and three dimensions"; Journal of Low Temperature Physics **138**, pp. 635–644 (2005). Cited on page 8

[35] N. Navon, R. P. Smith & Z. Hadzibabic; "Quantum gases in optical boxes"; Nature Physics **17**, pp. 1334–1341 (2021). Cited on page 8

[36] A. J. Leggett; "Can a Solid Be "Superfluid"?" Phys. Rev. Lett. **25**, pp. 1543–1546 (1970). 5 citations on pages 9, 83, 91, 93, and 108

[37] Z. Hadzibabi, P. Krüger, M. Cheneau, B. Battelier & J. Dalibard; "Berezinskii-Kosterlitz-Thouless crossover in a trapped atomis gas"; Nature **441**, pp. 1118–1121 (2006). 2 citations on pages 9 and 25

[38] P. Cladé, C. Ryu, A. Ramanathan, K. Helmerson & W. D. Phillips; "Observation of a 2D Bose Gas: From Thermal to Quasicondensate to Superfluid"; Phys. Rev. Lett. **102**, p. 170401 (2009). 2 citations on pages 9 and 22

[39] G. Roumpos, M. Lohse, W. H. Nitsche, J. Keeling, M. H. Szymańska, P. B. Littlewood, A. Löffler, S. Höfling, L. Worschech, A. Forchel & Y. Yamamoto; "Power-law decay of the spatial correlation function in exciton-polariton condensates"; Proceedings of the National Academy of Sciences **109**, pp. 6467–6472 (2012). Cited on page 9

[40] W. H. Nitsche, N. Y. Kim, G. Roumpos, C. Schneider, M. Kamp, S. Höfling, A. Forchel & Y. Yamamoto; "Algebraic order and the Berezinskii-Kosterlitz-Thouless transition in an exciton-polariton gas"; Phys. Rev. B **90**, p. 205430 (2014). Cited on page 9

[41] P. A. Murthy, I. Boettcher, L. Bayha, M. Holzmann, D. Kedar, M. Neidig, M. G. Ries, A. N. Wenz, G. Zürn & S. Jochim; "Observation of the Berezinskii-Kosterlitz-Thouless Phase Transition in an Ultracold Fermi Gas"; Phys. Rev. Lett. **115**, p. 010401 (2015). Cited on page 9

[42] D. Caputo, D. Ballarini, G. Dagvadorj, C. Sanchez Muñoz, M. De Giorgi, L. Dominici, K. West, L. Pfeiffer, G. Gigli, F. Laussy, M. Szymanska & D. Sanvitto; "Topological order and thermal equilibrium in polariton condensates"; Nature Materials **17**, pp. 145–151 (2018). Cited on page 9

[43] R. Saint-Jalm; *Exploration de la physique à deux dimensions avec des gaz de Bose dans des potentiels à fond plat : ordre en phase et symétrie dynamique*; Theses; Université Paris sciences et lettres (2019); HAL:tel-03116129. 4 citations on pages 9, 26, 29, and 34

[44] S. Dang, M. Zamorano, S. Suffit, K. West, K. Baldwin, L. Pfeiffer, M. Holzmann & F. m. c. Dubin; "Observation of algebraic time order for two-dimensional dipolar excitons"; Phys. Rev. Res. **2**, p. 032013 (2020). Cited on page 9

[45] S. Sunami, V. P. Singh, D. Garrick, A. Beregi, A. J. Barker, K. Luksch, E. Bentine, L. Mathey & C. J. Foot; "Observation of the Berezinskii-Kosterlitz-Thouless Transition in a Two-Dimensional Bose Gas via Matter-Wave Interferometry"; Phys. Rev. Lett. **128**, p. 250402 (2022). 2 citations on pages 9 and 26

[46] D. J. Bishop & J. D. Reppy; "Study of the Superfluid Transition in Two-Dimensional ^{4}He Films"; Phys. Rev. Lett. **40**, pp. 1727–1730 (1978). Cited on page 9

[47] P. Christodoulou, M. Gałka, N. Dogra, R. Lopes, J. Schmitt & Z. Hadzibabic; "Observation of first and second sound in a BKT superfluid"; Nature **594**, pp. 191–194 (2021). 6 citations on pages 9, 20, 25, 89, 93, and 94

[48] T. Yefsah, R. Desbuquois, L. Chomaz, K. J. Günter & J. Dalibard; "Exploring the Thermodynamics of a Two-Dimensional Bose Gas"; Physical Review Letters **107** (2011). 2 citations on pages 9 and 27

[49] C.-L. Hung, X. Zhang, N. Gemelke & C. Chin; "Observation of scale invariance and universality in two-dimensional Bose gases"; Nature **470**, pp. 236–239 (2011). 3 citations on pages 9, 22, and 27

[50] R. Desbuquois, T. Yefsah, L. Chomaz, C. Weitenberg, L. Corman, S. Nascimbène & J. Dalibard; "Determination of Scale-Invariant Equations of State without Fitting Parameters: Application to the Two-Dimensional Bose Gas Across the Berezinskii-Kosterlitz-Thouless Transition"; Phys. Rev. Lett. **113**, p. 020404 (2014). Cited on page 9

[51] Y.-Q. Zou, É. L. Cerf, B. Bakkali-Hassani, C. Maury, G. Chauveau, P. C. M. Castilho, R. Saint-Jalm, S. Nascimbene, J. Dalibard & J. Beugnon; "Optical control of the density and spin spatial profiles of a planar Bose gas"; Journal of Physics B: Atomic, Molecular and Optical Physics **54**, p. 08LT01 (2021). 3 citations on pages 9, 35, and 99

[52] B. Bakkali-Hassani, C. Maury, Y.-Q. Zou, É. L. Cerf, R. Saint-Jalm, P. Castilho, S. Nascimbene, J. Dalibard & J. Beugnon; "Realization of a Townes Soliton in a Two-Component Planar Bose Gas"; Physical Review Letters **127** (2021). 3 citations on pages 9, 21, and 36

[53] B. Bakkali-Hassani, C. Maury, S. Stringari, S. Nascimbene, J. Dalibard & J. Beugnon; "The cross-over from Townes solitons to droplets in a 2D Bose mixture"; New Journal of Physics **25**, p. 013007 (2023). 2 citations on pages 9 and 21

[54] Y.-Q. Zou, B. Bakkali-Hassani, C. Maury, É. L. Cerf, S. Nascimbene, J. Dalibard & J. Beugnon; “Magnetic Dipolar Interaction between Hyperfine Clock States in a Planar Alkali Bose Gas”; Physical Review Letters **125** (2020). 2 citations on pages 9 and 18

[55] Y.-Q. Zou, B. Bakkali-Hassani, C. Maury, É. L. Cerf, S. Nascimbene, J. Dalibard & J. Beugnon; “Tan’s two-body contact across the superfluid transition of a planar Bose gas”; Nature Communications **12** (2021). 3 citations on pages 9, 22, and 40

[56] Z. Hadzibabic & J. Dalibard; “Two-dimensional Bose fluids: An atomic physics perspective”; La Rivista del Nuovo Cimento **34**, p. 389–434 (2011). 3 citations on pages 13, 18, and 23

[57] J. Dalibard; “Fluides quantiques de basse dimension et transition Kosterlitz-Thouless”; (2017); Collège de France lectures. 2 citations on pages 13 and 21

[58] O. Penrose & L. Onsager; “Bose-Einstein Condensation and Liquid Helium”; Phys. Rev. **104**, pp. 576–584 (1956). Cited on page 14

[59] D. Petrov, D. Gangardt & G. Shlyapnikov; “Low-dimensional trapped gases”; J. Phys. IV France **116**, pp. 5–44 (2004). 2 citations on pages 15 and 17

[60] N. D. Mermin & H. Wagner; “Absence of Ferromagnetism or Antiferromagnetism in One- or Two-Dimensional Isotropic Heisenberg Models”; Phys. Rev. Lett. **17**, pp. 1133–1136 (1966). Cited on page 15

[61] P. C. Hohenberg; “Existence of Long-Range Order in One and Two Dimensions”; Phys. Rev. **158**, pp. 383–386 (1967). Cited on page 15

[62] J. Mitroy & M. W. J. Bromley; “Semiempirical calculation of van der Waals coefficients for alkali-metal and alkaline-earth-metal atoms”; Phys. Rev. A **68**, p. 052714 (2003). 3 citations on pages 15, 46, and 56

[63] J. Dalibard; “Les interactions entre atomes dans les gaz quantiques: De l’universalité de van der Waals aux résonances de Fano-Feshbach”; (2021); Collège de France lectures. 3 citations on pages 16, 49, and 55

[64] D. S. Petrov, M. Holzmann & G. V. Shlyapnikov; “Bose-Einstein Condensation in Quasi-2D Trapped Gases”; Physical Review Letters **84**, pp. 2551–2555 (2000). 2 citations on pages 18 and 22

[65] D. S. Petrov & G. V. Shlyapnikov; “Interatomic collisions in a tightly confined Bose gas”; Physical Review A **64** (2001). 2 citations on pages 18 and 76

[66] T. Yefsah; *Thermodynamique du gaz de Bose à deux dimensions*; Theses; Université Pierre et Marie Curie - Paris VI (2011); HAL:tel-00737502. Cited on page 18

[67] N. N. Bogoliubov; “On the theory of superfluidity”; J. Phys. (USSR) **11**, pp. 23–32 (1947). Cited on page 19

[68] J. Ville, R. Saint-Jalm, É. L. Cerf, M. Aidelsburger, S. Nascimbène, J. Dalibard & J. Beugnon; “Sound Propagation in a Uniform Superfluid Two-Dimensional Bose Gas”; Physical Review Letters **121** (2018). 4 citations on pages 20, 88, 93, and 94

[69] M. Bohlen, L. Sobirey, N. Luick, H. Biss, T. Enss, T. Lompe & H. Moritz; "Sound Propagation and Quantum-Limited Damping in a Two-Dimensional Fermi Gas"; Physical Review Letters **124** (2020). 3 citations on pages 20, 88, and 93

[70] R. Saint-Jalm, P. Castilho, É. L. Cerf, B. Bakkali-Hassani, J.-L. Ville, S. Nascimbene, J. Beugnon & J. Dalibard; "Dynamical Symmetry and Breathers in a Two-Dimensional Bose Gas"; Physical Review X **9** (2019). Cited on page 21

[71] C.-A. Chen & C.-L. Hung; "Observation of Universal Quench Dynamics and Townes Soliton Formation from Modulational Instability in Two-Dimensional Bose Gases"; Phys. Rev. Lett. **125**, p. 250401 (2020). Cited on page 21

[72] C.-A. Chen & C.-L. Hung; "Observation of Scale Invariance in Two-Dimensional Matter-Wave Townes Solitons"; Phys. Rev. Lett. **127**, p. 023604 (2021). Cited on page 21

[73] B. Bakkali-Hassani; *Testing scale invariance in a two-dimensional Bose gas : preparation and characterization of solitary waves*; Theses; Sorbonne Université (2021); HAL:tel-03591031. 3 citations on pages 22, 36, and 40

[74] Y. Kagan, B. V. Svistunov & G. V. Shlyapnikov; "Influence on inelastic processes of the phase transition in a weakly collisional two-dimensional Bose gas"; Journal of Experimental and Theoretical Physics **66**, p. 552 (1987). Cited on page 22

[75] Y. Kagan, V. A. Kashurnikov, A. V. Krasavin, N. V. Prokof'ev & B. Svistunov; "Quasicondensation in a two-dimensional interacting Bose gas"; Phys. Rev. A **61**, p. 043608 (2000). Cited on page 22

[76] S. Tung, G. Lamporesi, D. Lobser, L. Xia & E. A. Cornell; "Observation of the Presuperfluid Regime in a Two-Dimensional Bose Gas"; Phys. Rev. Lett. **105**, p. 230408 (2010). Cited on page 22

[77] S. Tan; "Energetics of a strongly correlated Fermi gas"; Annals of Physics **323**, pp. 2952–2970 (2008). Cited on page 22

[78] S. Tan; "Generalized virial theorem and pressure relation for a strongly correlated Fermi gas"; Annals of Physics **323**, pp. 2987–2990 (2008). Cited on page 22

[79] S. Tan; "Large momentum part of a strongly correlated Fermi gas"; Annals of Physics **323**, pp. 2971–2986 (2008). Cited on page 22

[80] A. Rançon & N. Dupuis; "Tan's two-body contact in a planar Bose gas: experiment vs theory"; (2022); ArXiv:2212.06857. Cited on page 22

[81] C. Mora & Y. Castin; "Extension of Bogoliubov theory to quasicondensates"; Phys. Rev. A **67**, p. 053615 (2003). Cited on page 23

[82] Y. Castin; "Simple theoretical tools for low dimension Bose gases"; J. Phys. IV France **116**, pp. 89–132 (2004). Cited on page 23

[83] J. M. Kosterlitz; "The critical properties of the two-dimensional xy model"; Journal of Physics C Solid State Physics **7**, pp. 1046–1060 (1974). Cited on page 23

[84] L. Landau; "Theory of the Superfluidity of Helium II"; Phys. Rev. **60**, pp. 356–358 (1941). 2 citations on pages 23 and 88

[85] J. Dalibard; “Cohérence et superfluidité dans les gaz atomiques”; (2015); Collège de France lectures. 3 citations on pages 23, 24, and 85

[86] B. V. Svistunov, E. S. Babaev & N. V. Prokof’ev; *Superfluid States of Matter* (CRC Press). (2015). Cited on page 23

[87] L. Pitaevskii & S. Stringari; *Bose-Einstein Condensation and Superfluidity* (Oxford University Press) (2016). 4 citations on pages 23, 103, 125, and 126

[88] S. K. Ma; *Statistical mechanics* (World Scientific). (1985). Cited on page 23

[89] A. J. Leggett; *Quantum fluids* (Oxford Univerity Press). (2006). Cited on page 23

[90] G. B. Hess & W. M. Fairbank; “Measurements of Angular Momentum in Superfluid Helium”; Phys. Rev. Lett. **19**, pp. 216–218 (1967). Cited on page 24

[91] N. Prokof’ev & B. Svistunov; “Two-dimensional weakly interacting Bose gas in the fluctuation region”; Phys. Rev. A **66**, p. 043608 (2002). Cited on page 25

[92] N. Prokof’ev, O. Ruebenacker & B. Svistunov; “Critical Point of a Weakly Interacting Two-Dimensional Bose Gas”; Phys. Rev. Lett. **87**, p. 270402 (2001). Cited on page 25

[93] D. S. Fisher & P. C. Hohenberg; “Dilute Bose gas in two dimensions”; Phys. Rev. B **37**, pp. 4936–4943 (1988). Cited on page 25

[94] R. J. Fletcher, M. Robert-de Saint-Vincent, J. Man, N. Navon, R. P. Smith, K. G. H. Viebahn & Z. Hadzibabic; “Connecting Berezinskii-Kosterlitz-Thouless and BEC Phase Transitions by Tuning Interactions in a Trapped Gas”; Phys. Rev. Lett. **114**, p. 255302 (2015). Cited on page 25

[95] L. Corman; *The two-dimensional Bose Gas in box potentials*; Theses; Université Paris sciences et lettres (2016); HAL:tel-01449982. Cited on page 29

[96] J.-L. Ville; *Quantum gases in box potentials : sound and light in bosonic Flatland*; Theses; Université Paris sciences et lettres (2018); HAL:tel-01925194. 2 citations on pages 29 and 37

[97] É. Le Cerf; *Demixing phenomena in 2D Bose gases*; Theses; Sorbonne Université (2020); HAL:tel-03019926. 3 citations on pages 29, 35, and 36

[98] P. A. Altin, G. McDonald, D. Döring, J. E. Debs, T. H. Barter, J. D. Close, N. P. Robins, S. A. Haine, T. M. Hanna & R. P. Anderson; “Optically trapped atom interferometry using the clock transition of large Rb-87 Bose-Einstein condensates”; New Journal of Physics **13**, p. 065020 (2011). 4 citations on pages 30, 34, 41, and 78

[99] D. Steck; “Rubidium 87 D Line Data”; (2003). Cited on page 30

[100] T. C. Li, H. Kelkar, D. Medellin & M. G. Raizen; “Real-time control of the periodicity of a standing wave: an optical accordion”; Optics Express **16**, p. 5465 (2008). Cited on page 34

[101] J. L. Ville, T. Bienaimé, R. Saint-Jalm, L. Corman, M. Aidelsburger, L. Chomaz, K. Kleinlein, D. Perconte, S. Nascimbène, J. Dalibard & J. Beugnon; “Loading and compression of a single two-dimensional Bose gas in an optical accordion”; Physical Review A **95** (2017). Cited on page 34

[102] C. Dorrer & J. D. Zuegel; "Design and analysis of binary beam shapers using error diffusion"; J. Opt. Soc. Am. B **24**, pp. 1268–1275 (2007). 2 citations on pages 35 and 99

[103] K. Hueck, N. Luick, L. Sobirey, J. Siegl, T. Lompe & H. Moritz; "Two-Dimensional Homogeneous Fermi Gases"; Physical Review Letters **120** (2018). Cited on page 39

[104] F. London; "Zur Theorie und Systematik der Molekularkräfte"; Zeitschrift für Physik **63**, pp. 245–279. Cited on page 46

[105] W. Heitler & F. London; "Wechselwirkung neutraler Atome und homöopolare Bindung nach der Quantenmechanik"; Z. Physik **44**, p. 455 (1927). Cited on page 47

[106] L. D. Landau & E. M. Lifshitz; *Mécanique quantique.* (1975). Cited on page 49

[107] W. Schöllkopf & J. P. Toennies; "Nondestructive Mass Selection of Small van der Waals Clusters"; Science **266**, pp. 1345–1348 (1994). Cited on page 50

[108] R. J. LeRoy & R. B. Bernstein; "Dissociation Energy and Long-Range Potential of Diatomic Molecules from Vibrational Spacings of Higher Levels"; The Journal of Chemical Physics **52**, pp. 3869–3879 (1970). Cited on page 50

[109] L. I. Schiff; *Quantum mechanics.* (1968). Cited on page 50

[110] G. F. Gribakin & V. V. Flambaum; "Calculation of the scattering length in atomic collisions using the semiclassical approximation"; Phys. Rev. A **48**, pp. 546–553 (1993). Cited on page 50

[111] J. D. Weinstein, R. deCarvalho, T. Guillet, B. Friedrich & J. M. Doyle; "Magnetic trapping of Calcium monohydride molecules at millikelvin temperatures"; Nature **395**, pp. 148–150 (1998). Cited on page 50

[112] H. L. Bethlem, G. Berden, F. M. H. Crompvoets, R. T. Jongma, A. J. A. van Roij & G. Meijer; "Electrostatic trapping of Ammonia molecules"; Nature **406**, pp. 491–494 (2000). Cited on page 51

[113] W. C. Stwalley & H. Wang; "Photoassociation of Ultracold Atoms: A New Spectroscopic Technique"; Journal of Molecular Spectroscopy **195**, pp. 194–228 (1999). Cited on page 51

[114] N. Vanhaecke, D. Comparat, A. Crubellier & P. Pillet; "Photoassociation spectroscopy of ultra-cold long-range molecules"; Comptes Rendus Physique **5**, pp. 161–169 (2004). Cited on page 51

[115] K. M. Jones, E. Tiesinga, P. D. Lett & P. S. Julienne; "Ultracold photoassociation spectroscopy: Long-range molecules and atomic scattering"; Rev. Mod. Phys. **78**, pp. 483–535 (2006). Cited on page 51

[116] J. Ulmanis, J. Deiglmayr, M. Repp, R. Wester & M. Weidemüller; "Ultracold Molecules Formed by Photoassociation: Heteronuclear Dimers, Inelastic Collisions, and Interactions with Ultrashort Laser Pulses"; Chemical Reviews **112**, pp. 4890–4927 (2012). Cited on page 51

[117] H. R. Thorsheim, J. Weiner & P. S. Julienne; "Laser-induced photoassociation of ultracold sodium atoms"; Phys. Rev. Lett. **58**, pp. 2420–2423 (1987). Cited on page 51

[118] A. Fioretti, D. Comparat, A. Crubellier, O. Dulieu, F. Masnou-Seeuws & P. Pillet; "Formation of Cold Cs_2 Molecules through Photoassociation"; Phys. Rev. Lett. **80**, pp. 4402–4405 (1998). Cited on page 51

[119] J. D. Miller, R. A. Cline & D. J. Heinzen; "Photoassociation spectrum of ultracold Rb atoms"; Phys. Rev. Lett. **71**, pp. 2204–2207 (1993). Cited on page 52

[120] V. Bagnato, L. Marcassa, C. Tsao, Y. Wang & J. Weiner; "Two-color spectroscopy of colliding ultracold atoms"; Phys. Rev. Lett. **70**, pp. 3225–3228 (1993). Cited on page 52

[121] P. D. Lett, K. Helmerson, W. D. Phillips, L. P. Ratliff, S. L. Rolston & M. E. Wagshul; "Spectroscopy of Na_2 by photoassociation of laser-cooled Na"; Phys. Rev. Lett. **71**, pp. 2200–2203 (1993). Cited on page 52

[122] R. A. Cline, J. D. Miller & D. J. Heinzen; "Study of Rb_2 Long-Range States by High-Resolution Photoassociation Spectroscopy"; Phys. Rev. Lett. **73**, pp. 632–635 (1994). Cited on page 52

[123] L. P. Ratliff, M. E. Wagshul, P. D. Lett, S. L. Rolston & W. D. Phillips; "Photoassociative spectroscopy of 1g, 0+u, and 0−g states of Na2"; The Journal of Chemical Physics **101**, pp. 2638–2641 (1994). Cited on page 52

[124] W. I. McAlexander, E. R. I. Abraham, N. W. M. Ritchie, C. J. Williams, H. T. C. Stoof & R. G. Hulet; "Precise atomic radiative lifetime via photoassociative spectroscopy of ultracold lithium"; Phys. Rev. A **51**, pp. R871–R874 (1995). Cited on page 52

[125] C. C. Tsai, R. S. Freeland, J. M. Vogels, H. M. J. M. Boesten, B. J. Verhaar & D. J. Heinzen; "Two-Color Photoassociation Spectroscopy of Ground State Rb_2"; Phys. Rev. Lett. **79**, pp. 1245–1248 (1997). Cited on page 52

[126] D. Comparat, C. Drag, A. Fioretti, O. Dulieu & P. Pillet; "Photoassociative Spectroscopy and Formation of Cold Molecules in Cold Cesium Vapor: Trap–Loss Spectrum versus Ion Spectrum"; Journal of Molecular Spectroscopy **195**, pp. 229–235 (1999). Cited on page 52

[127] C. Drag, B. Laburthe Tolra, B. T'Jampens, D. Comparat, M. Allegrini, A. Crubellier & P. Pillet; "Photoassociative Spectroscopy as a Self-Sufficient Tool for the Determination of the Cs Triplet Scattering Length"; Phys. Rev. Lett. **85**, pp. 1408–1411 (2000). Cited on page 52

[128] A. N. Nikolov, J. R. Ensher, E. E. Eyler, H. Wang, W. C. Stwalley & P. L. Gould; "Efficient Production of Ground-State Potassium Molecules at Sub-mK Temperatures by Two-Step Photoassociation"; Phys. Rev. Lett. **84**, pp. 246–249 (2000). Cited on page 52

[129] E. R. I. Abraham, W. I. McAlexander, C. A. Sackett & R. G. Hulet; "Spectroscopic Determination of the s-Wave Scattering Length of Lithium"; Phys. Rev. Lett. **74**, pp. 1315–1318 (1995). Cited on page 52

[130] E. Tiesinga, C. Williams, P. Julienne, K. Jones, P. Lett & W. Phillips; "A spectroscopic determination of scattering lengths for sodium atom collisions"; Journal of Research of the National Institute of Standards and Technology **101**, p. 505 (1996). Cited on page 52

[131] J. L. Bohn, J. P. Burke, C. H. Greene, H. Wang, P. L. Gould & W. C. Stwalley; "Collisional properties of ultracold potassium: Consequences for degenerate Bose and Fermi gases"; Phys. Rev. A **59**, pp. 3660–3664 (1999). Cited on page 52

[132] M. Borkowski, A. A. Buchachenko, R. Ciuryło, P. S. Julienne, H. Yamada, Y. Kikuchi, K. Takahashi, Y. Takasu & Y. Takahashi; "Beyond-Born-Oppenheimer effects in sub-kHz-precision photoassociation spectroscopy of Ytterbium atoms"; Phys. Rev. A **96**, p. 063405 (2017). Cited on page 52

[133] A. J. Kerman, C. Chin, V. Vuletić, S. Chu, P. J. Leo, C. J. Williams & P. S. Julienne; "Determination of Cs–Cs interaction parameters using Feshbach spectroscopy"; Comptes Rendus de l'Académie des Sciences - Series IV - Physics **2**, pp. 633–639 (2001). Cited on page 52

[134] H. Feshbach; "Unified theory of nuclear reactions"; Annals of Physics **5**, pp. 357–390 (1958). Cited on page 52

[135] H. Feshbach; "A unified theory of nuclear reactions. II"; Annals of Physics **19**, pp. 287–313 (1962). Cited on page 52

[136] U. Fano; "Effects of Configuration Interaction on Intensities and Phase Shifts"; Phys. Rev. **124**, pp. 1866–1878 (1961). Cited on page 52

[137] W. C. Stwalley; "Stability of Spin-Aligned Hydrogen at Low Temperatures and High Magnetic Fields: New Field-Dependent Scattering Resonances and Predissociations"; Phys. Rev. Lett. **37**, pp. 1628–1631 (1976). Cited on page 52

[138] M. W. Reynolds, I. Shinkoda, R. W. Cline & W. N. Hardy; "Observation of inverse predissociation of spin-polarized atomic Hydrogen at low temperatures"; Phys. Rev. B **34**, pp. 4912–4915 (1986). Cited on page 52

[139] E. Tiesinga, B. J. Verhaar & H. T. C. Stoof; "Threshold and resonance phenomena in ultracold ground-state collisions"; Phys. Rev. A **47**, pp. 4114–4122 (1993). Cited on page 52

[140] A. J. Moerdijk, B. J. Verhaar & A. Axelsson; "Resonances in ultracold collisions of ^{6}Li, ^{7}Li, and ^{23}Na"; Phys. Rev. A **51**, pp. 4852–4861 (1995). Cited on page 52

[141] T. Köhler, K. Góral & P. S. Julienne; "Production of cold molecules via magnetically tunable Feshbach resonances"; Rev. Mod. Phys. **78**, pp. 1311–1361 (2006). Cited on page 53

[142] C. Chin, R. Grimm, P. Julienne & E. Tiesinga; "Feshbach resonances in ultracold gases"; Rev. Mod. Phys. **82**, pp. 1225–1286 (2010). Cited on page 53

[143] P. O. Fedichev, Y. Kagan, G. V. Shlyapnikov & J. T. M. Walraven; "Influence of Nearly Resonant Light on the Scattering Length in Low-Temperature Atomic Gases"; Phys. Rev. Lett. **77**, pp. 2913–2916 (1996). Cited on page 54

[144] M. Theis, G. Thalhammer, K. Winkler, M. Hellwig, G. Ruff, R. Grimm & J. H. Denschlag; "Tuning the Scattering Length with an Optically Induced Feshbach Resonance"; Phys. Rev. Lett. **93**, p. 123001 (2004). Cited on page 54

[145] G. Thalhammer, M. Theis, K. Winkler, R. Grimm & J. H. Denschlag; "Inducing an optical Feshbach resonance via stimulated Raman coupling"; Phys. Rev. A **71**, p. 033403 (2005). Cited on page 54

[146] D. J. Papoular, G. V. Shlyapnikov & J. Dalibard; "Microwave-induced Fano-Feshbach resonances"; Phys. Rev. A **81**, p. 041603 (2010). 2 citations on pages 55 and 79

[147] A. M. Kaufman, R. P. Anderson, T. M. Hanna, E. Tiesinga, P. S. Julienne & D. S. Hall; "Radio-frequency dressing of multiple Feshbach resonances"; Phys. Rev. A **80**, p. 050701 (2009). 2 citations on pages 55 and 57

[148] T. V. Tscherbul, T. Calarco, I. Lesanovsky, R. V. Krems, A. Dalgarno & J. Schmiedmayer; "rf-field-induced Feshbach resonances"; Phys. Rev. A **81**, p. 050701 (2010). 2 citations on pages 55 and 57

[149] J. Weiner, V. S. Bagnato, S. Zilio & P. S. Julienne; "Experiments and theory in cold and ultracold collisions"; Rev. Mod. Phys. **71**, pp. 1–85 (1999). Cited on page 55

[150] M. Deiss, B. Drews, J. H. Denschlag, N. Bouloufa-Maafa, R. Vexiau & O. Dulieu; "Polarizability of ultracold Rb_2 molecules in the rovibrational ground state of $a^3\Sigma_u^+$"; New Journal of Physics **17**, p. 065019 (2015). Cited on page 56

[151] E. G. M. van Kempen, S. J. J. M. F. Kokkelmans, D. J. Heinzen & B. J. Verhaar; "Interisotope Determination of Ultracold Rubidium Interactions from Three High-Precision Experiments"; Phys. Rev. Lett. **88**, p. 093201 (2002). Cited on page 56

[152] R. Wynar, R. S. Freeland, D. J. Han, C. Ryu & D. J. Heinzen; "Molecules in a Bose-Einstein Condensate"; Science **287**, pp. 1016–1019 (2000). 4 citations on pages 56, 65, 74, and 79

[153] R. H. Wynar; *Ultra-cold molecules in an atomic Bose-Einstein condensate*; Ph.D. thesis; University of Texas, Austin (2000). 3 citations on pages 56, 60, and 74

[154] R. Freeland; *Photoassociation spectroscopy of ultracold and Bose-condensed atomic gasses*; Ph.D. thesis; University of Texas, Austin (2001). Cited on page 56

[155] I. Mordovin; *Radio-frequency induced association of molecules in* ^{87}Rb; Ph.D. thesis; Swinburne University of Technology (2015); Swinburne Theses Collection. 3 citations on pages 56, 59, and 65

[156] T. M. Hanna, E. Tiesinga & P. S. Julienne; "Prediction of Feshbach resonances from three input parameters"; Phys. Rev. A **79**, p. 040701 (2009). Cited on page 57

[157] T. M. Hanna, E. Tiesinga & P. S. Julienne; "Creation and manipulation of Feshbach resonances with radiofrequency radiation"; New Journal of Physics **12**, p. 083031 (2010). Cited on page 57

[158] P. Naidon, E. Tiesinga & P. S. Julienne; "Two-Body Transients in Coupled Atomic-Molecular Bose-Einstein Condensates"; Phys. Rev. Lett. **100**, p. 093001 (2008). Cited on page 62

[159] M. Yan, B. J. DeSalvo, Y. Huang, P. Naidon & T. C. Killian; "Rabi Oscillations between Atomic and Molecular Condensates Driven with Coherent One-Color Photoassociation"; Phys. Rev. Lett. **111**, p. 150402 (2013). Cited on page 62

[160] G. V. Skorniakov & K. A. Ter-Martirosian; "Tree body problem for short range forces. I. Scattering of low energy neutrons by deuterons"; Soviet Phys. JETP **4** (1957). Cited on page 69

[161] D. S. Petrov; "Three-body problem in Fermi gases with short-range interparticle interaction"; Phys. Rev. A **67**, p. 010703 (2003). Cited on page 69

[162] M. Iskin & C. A. R. Sá de Melo; "Fermi-Fermi mixtures in the strong-attraction limit"; Phys. Rev. A **77**, p. 013625 (2008). Cited on page 69

[163] F. Alzetto, R. Combescot & X. Leyronas; "Atom-dimer scattering length for fermions with different masses: Analytical study of limiting cases"; Phys. Rev. A **82**, p. 062706 (2010). Cited on page 69

[164] F. Alzetto, R. Combescot & X. Leyronas; "Atom-dimer scattering amplitude for fermionic mixtures with different masses: s-wave and p-wave contributions"; Phys. Rev. A **86**, p. 062708 (2012). Cited on page 69

[165] M. Iskin; "Dimer-atom scattering between two identical fermions and a third particle"; Phys. Rev. A **81**, p. 043634 (2010). Cited on page 69

[166] X. Cui; "Atom-dimer scattering and stability of Bose and Fermi mixtures"; Phys. Rev. A **90**, p. 041603 (2014). Cited on page 69

[167] R. Zhang, W. Zhang, H. Zhai & P. Zhang; "Calibration of the interaction energy between Bose and Fermi superfluids"; Phys. Rev. A **90**, p. 063614 (2014). 2 citations on pages 69 and 79

[168] C. Mora, R. Egger, A. O. Gogolin & A. Komnik; "Atom-Dimer Scattering for Confined Ultracold Fermion Gases"; Phys. Rev. Lett. **93**, p. 170403 (2004). Cited on page 69

[169] J. Levinsen, T. G. Tiecke, J. T. M. Walraven & D. S. Petrov; "Atom-Dimer Scattering and Long-Lived Trimers in Fermionic Mixtures"; Phys. Rev. Lett. **103**, p. 153202 (2009). Cited on page 69

[170] D. S. Petrov, C. Salomon & G. V. Shlyapnikov; "Weakly Bound Dimers of Fermionic Atoms"; Phys. Rev. Lett. **93**, p. 090404 (2004). Cited on page 69

[171] J. Levinsen & D. S. Petrov; "Atom-dimer and dimer-dimer scattering in fermionic mixtures near a narrow Feshbach resonance"; The European Physical Journal D **65**, pp. 67–82 (2011). Cited on page 69

[172] P. Bedaque, H.-W. Hammer & U. van Kolck; "The three-boson system with short-range interactions"; Nuclear Physics A **646**, pp. 444–466 (1999). Cited on page 69

[173] E. Braaten & H.-W. Hammer; "Universality in the three-body problem for ^{4}He atoms"; Phys. Rev. A **67**, p. 042706 (2003). Cited on page 69

[174] D. S. Petrov; "Three-Boson Problem near a Narrow Feshbach Resonance"; Phys. Rev. Lett. **93**, p. 143201 (2004). Cited on page 69

[175] E. Braaten & H.-W. Hammer; "Universality in few-body systems with large scattering length"; Physics Reports **428**, pp. 259–390 (2006). Cited on page 69

[176] C. Gao & P. Zhang; "Atom-dimer scattering in a heteronuclear mixture with a finite intraspecies scattering length"; Phys. Rev. A **97**, p. 042701 (2018). Cited on page 69

[177] P. Giannakeas & C. H. Greene; "Van der Waals Universality in Homonuclear Atom-Dimer Elastic Collisions"; Few-Body Systems **58** (2016). Cited on page 69

[178] P. M. A. Mestrom, J. Wang, C. H. Greene & J. P. D'Incao; "Efimov–van der Waals universality for ultracold atoms with positive scattering lengths"; Phys. Rev. A **95**, p. 032707 (2017). Cited on page 69

[179] P. Staanum, S. D. Kraft, J. Lange, R. Wester & M. Weidemüller; "Experimental Investigation of Ultracold Atom-Molecule Collisions"; Phys. Rev. Lett. **96**, p. 023201 (2006). Cited on page 69

[180] N. Zahzam, T. Vogt, M. Mudrich, D. Comparat & P. Pillet; "Atom-Molecule Collisions in an Optically Trapped Gas"; Phys. Rev. Lett. **96**, p. 023202 (2006). Cited on page 69

[181] T. Lompe, T. B. Ottenstein, F. Serwane, K. Viering, A. N. Wenz, G. Zürn & S. Jochim; "Atom-Dimer Scattering in a Three-Component Fermi Gas"; Phys. Rev. Lett. **105**, p. 103201 (2010). Cited on page 69

[182] S. Nakajima, M. Horikoshi, T. Mukaiyama, P. Naidon & M. Ueda; "Nonuniversal Efimov Atom-Dimer Resonances in a Three-Component Mixture of ^{6}Li"; Phys. Rev. Lett. **105**, p. 023201 (2010). Cited on page 69

[183] M. T. Hummon, T. V. Tscherbul, J. Kłos, H.-I. Lu, E. Tsikata, W. C. Campbell, A. Dalgarno & J. M. Doyle; "Cold **N**+NH Collisions in a Magnetic Trap"; Phys. Rev. Lett. **106**, p. 053201 (2011). Cited on page 69

[184] R. S. Bloom, M.-G. Hu, T. D. Cumby & D. S. Jin; "Tests of Universal Three-Body Physics in an Ultracold Bose-Fermi Mixture"; Phys. Rev. Lett. **111**, p. 105301 (2013). Cited on page 69

[185] A. Zenesini, B. Huang, M. Berninger, H.-C. Nägerl, F. Ferlaino & R. Grimm; "Resonant atom-dimer collisions in cesium: Testing universality at positive scattering lengths"; Phys. Rev. A **90**, p. 022704 (2014). Cited on page 69

[186] K. Kato, Y. Wang, J. Kobayashi, P. S. Julienne & S. Inouye; "Isotopic Shift of Atom-Dimer Efimov Resonances in K-Rb Mixtures: Critical Effect of Multichannel Feshbach Physics"; Phys. Rev. Lett. **118**, p. 163401 (2017). Cited on page 69

[187] H. Yang, D.-C. Zhang, L. Liu, Y.-X. Liu, J. Nan, B. Zhao & J.-W. Pan; "Observation of magnetically tunable Feshbach resonances in ultracold ¡sup¿23¡/sup¿Na¡sup¿40¡/sup¿K + ¡sup¿40¡/sup¿K collisions"; Science **363**, pp. 261–264 (2019). Cited on page 69

[188] P. D. Gregory, J. A. Blackmore, F. M. D, L. M. Fernley, S. L. Bromley, J. M. Hutson & S. L. Cornish; "Molecule–molecule and atom–molecule collisions with ultracold RbCs molecules"; New Journal of Physics **23**, p. 125004 (2021). Cited on page 69

[189] S. Jurgilas, A. Chakraborty, C. J. H. Rich, L. Caldwell, H. J. Williams, N. J. Fitch, B. E. Sauer, M. D. Frye, J. M. Hutson & M. R. Tarbutt; "Collisions between Ultracold Molecules and Atoms in a Magnetic Trap"; Phys. Rev. Lett. **126**, p. 153401 (2021). Cited on page 69

[190] S. Knoop, F. Ferlaino, M. Berninger, M. Mark, H.-C. Nägerl, R. Grimm, J. P. D'Incao & B. D. Esry; "Magnetically Controlled Exchange Process in an Ultracold Atom-Dimer Mixture"; Phys. Rev. Lett. **104**, p. 053201 (2010). Cited on page 69

[191] J. Rui, H. Yang, L. Liu, D.-C. Zhang, Y.-X. Liu, J. Nan, Y.-A. Chen, B. Zhao & J.-W. Pan; "Controlled state-to-state atom-exchange reaction in an ultracold atom–dimer mixture"; Nature Physics **13**, pp. 699–703 (2017). Cited on page 69

[192] Y.-X. Liu, J. Nan, D.-C. Zhang, L. Liu, H. Yang, J. Rui, B. Zhao & J.-W. Pan; "Observation of a threshold behavior in an ultracold endothermic atom-exchange process involving Feshbach molecules"; Phys. Rev. A **100**, p. 032706 (2019). Cited on page 69

[193] J. Nan, Y.-X. Liu, D.-C. Zhang, L. Liu, H. Yang, B. Zhao & J.-W. Pan; "Universality in the atom-exchange reaction involving Feshbach molecules"; Phys. Rev. A **100**, p. 062704 (2019). Cited on page 69

[194] M. Jag, M. Zaccanti, M. Cetina, R. S. Lous, F. Schreck, R. Grimm, D. S. Petrov & J. Levinsen; "Observation of a Strong Atom-Dimer Attraction in a Mass-Imbalanced Fermi-Fermi Mixture"; Phys. Rev. Lett. **112**, p. 075302 (2014). Cited on page 69

[195] H. Son, J. J. Park, W. Ketterle & A. O. Jamison; "Collisional cooling of ultracold molecules"; Nature **580**, pp. 197–200 (2020). Cited on page 70

[196] E. A. Burt, R. W. Ghrist, C. J. Myatt, M. J. Holland, E. A. Cornell & C. E. Wieman; "Coherence, Correlations, and Collisions: What One Learns about Bose-Einstein Condensates from Their Decay"; Phys. Rev. Lett. **79**, pp. 337–340 (1997). Cited on page 70

[197] J. Söding, D. Guéry-Odelin, F. Chevy, H. Inamori & J. Dalibard; "Three-body decay of a rubidium Bose–Einstein condensate"; Applied Physics B **69**, pp. 257–261 (1999). Cited on page 70

[198] C. Cohen-Tannoudji, B. Diu & F. Laloë; "Quantum Mechanics I"; chapter IV - H (Willey VCH). Cited on page 75

[199] G. F. Chew & G. C. Wick; "The Impulse Approximation"; Phys. Rev. **85**, pp. 636–642 (1952). Cited on page 79

[200] P. Böhi, M. F. Riedel, J. Hoffrogge, J. Reichel, T. W. Hänsch & P. Treutlein; "Coherent manipulation of Bose–Einstein condensates with state-dependent microwave potentials on an atom chip"; Nature Physics **5**, pp. 592–597 (2019). Cited on page 80

[201] G. V. Chester; "Speculations on Bose-Einstein Condensation and Quantum Crystals"; Phys. Rev. A **2**, pp. 256–258 (1970). Cited on page 83

[202] S. Balibar; "The enigma of supersolidity"; Nature **464**, pp. 176–182 (2010). Cited on page 83

[203] M. Boninsegni & N. V. Prokof'ev; "Colloquium: Supersolids: What and where are they?" Rev. Mod. Phys. **84**, pp. 759–776 (2012). Cited on page 83

[204] W. Zwerger; "Basic Concepts and some current Directions in Ultracold Gases"; (2021); Collège de France lectures. Cited on page 83

[205] E. Kim & M. H. W. Chan; "Probable observation of a supersolid helium phase"; Nature **427**, pp. 225–227 (2004). Cited on page 83

[206] E. Kim & M. H. W. Chan; "Observation of Superflow in Solid Helium"; Science **305**, pp. 1941–1944 (2004). Cited on page 83

[207] S. Balibar & F. Caupin; "Supersolidity and disorder"; Journal of Physics: Condensed Matter **20**, p. 173201 (2008). Cited on page 83

[208] D. Y. Kim & M. H. W. Chan; "Absence of Supersolidity in Solid Helium in Porous Vycor Glass"; Phys. Rev. Lett. **109**, p. 155301 (2012). Cited on page 83

[209] J. Léonard, A. Morales, P. Zupancic, T. Esslinger & T. Donner; "Supersolid formation in a quantum gas breaking a continuous translational symmetry"; Nature **543**, pp. 87–90 (2017). Cited on page 83

[210] C. Wang, C. Gao, C.-M. Jian & H. Zhai; "Spin-Orbit Coupled Spinor Bose-Einstein Condensates"; Phys. Rev. Lett. **105**, p. 160403 (2010). Cited on page 83

[211] T.-L. Ho & S. Zhang; "Bose-Einstein Condensates with Spin-Orbit Interaction"; Phys. Rev. Lett. **107**, p. 150403 (2011). Cited on page 83

[212] Y. Li, L. P. Pitaevskii & S. Stringari; "Quantum Tricriticality and Phase Transitions in Spin-Orbit Coupled Bose-Einstein Condensates"; Phys. Rev. Lett. **108**, p. 225301 (2012). Cited on page 83

[213] Y. Li, G. I. Martone, L. P. Pitaevskii & S. Stringari; "Superstripes and the Excitation Spectrum of a Spin-Orbit-Coupled Bose-Einstein Condensate"; Phys. Rev. Lett. **110**, p. 235302 (2013). Cited on page 83

[214] W. Han, G. Juzeliūnas, W. Zhang & W.-M. Liu; "Supersolid with nontrivial topological spin textures in spin-orbit-coupled Bose gases"; Phys. Rev. A **91**, p. 013607 (2015). Cited on page 83

[215] J. R. Li, J. Lee, W. Huang, S. Burchesky, B. Shteynas, F. C. Top, A. O. Jamison & W. Ketterle; "A stripe phase with supersolid properties in spin–orbit-coupled Bose–Einstein condensates"; Nature **543**, pp. 91–94 (2017). Cited on page 84

[216] F. Böttcher, J.-N. Schmidt, M. Wenzel, J. Hertkorn, M. Guo, T. Langen & T. Pfau; "Transient Supersolid Properties in an Array of Dipolar Quantum Droplets"; Phys. Rev. X **9**, p. 011051 (2019). Cited on page 84

[217] L. Tanzi, E. Lucioni, F. Famà, J. Catani, A. Fioretti, C. Gabbanini, R. N. Bisset, L. Santos & G. Modugno; "Observation of a Dipolar Quantum Gas with Metastable Supersolid Properties"; Phys. Rev. Lett. **122**, p. 130405 (2019). Cited on page 84

[218] L. Chomaz, D. Petter, P. Ilzhöfer, G. Natale, A. Trautmann, C. Politi, G. Durastante, R. M. W. van Bijnen, A. Patscheider, M. Sohmen, M. J. Mark & F. Ferlaino; "Long-Lived and Transient Supersolid Behaviors in Dipolar Quantum Gases"; Phys. Rev. X **9**, p. 021012 (2019). Cited on page 84

[219] M. A. Norcia, C. Politi, L. Klaus, E. Poli, M. Sohmen, M. J. Mark, R. N. Bisset, L. Santos & F. Ferlaino; "Two-dimensional supersolidity in a dipolar quantum gas"; Nature **596**, pp. 357–361 (2021). Cited on page 84

[220] T. Bland, E. Poli, C. Politi, L. Klaus, M. A. Norcia, F. Ferlaino, L. Santos & R. N. Bisset; "Two-Dimensional Supersolid Formation in Dipolar Condensates"; Phys. Rev. Lett. **128**, p. 195302 (2022). Cited on page 84

[221] L. Tisza; "Transport Phenomena in Helium II"; Nature **141**, p. 913 (1938). Cited on page 88

[222] E. Taylor, H. Hu, X.-J. Liu, L. P. Pitaevskii, A. Griffin & S. Stringari; "First and second sound in a strongly interacting Fermi gas"; Phys. Rev. A **80**, p. 053601 (2009). Cited on page 88

[223] L. A. Sidorenkov, M. K. Tey, R. Grimm, Y. H. Hou, L. Pitaevskii & S. Stringari; "Second sound and the superfluid fraction in a Fermi gas with resonant interactions"; Nature **498**, pp. 78–81 (2013). Cited on page 88

[224] P. B. Patel, Z. Yan, B. Mukherjee, R. J. Fletcher, J. Struck & M. W. Zwierlein; "Universal sound diffusion in a strongly interacting Fermi gas"; Science **370**, pp. 1222–1226 (2020). 2 citations on pages 88 and 93

[225] A. Griffin & E. Zaremba; "First and second sound in a uniform Bose gas"; Phys. Rev. A **56**, pp. 4839–4844 (1997). Cited on page 88

[226] A. Griffin, T. Nikuni & E. Zaremba; *Bose-Condensed Gases at Finite Temperatures* (Cambridge University Press) (2009). Cited on page 88

[227] T. Ozawa & S. Stringari; "Discontinuities in the First and Second Sound Velocities at the Berezinskii-Kosterlitz-Thouless Transition"; Phys. Rev. Lett. **112**, p. 025302 (2014). Cited on page 88

[228] M. Ota & S. Stringari; "Second sound in a two-dimensional Bose gas: From the weakly to the strongly interacting regime"; Phys. Rev. A **97**, p. 033604 (2018). Cited on page 88

[229] M. R. Andrews, D. M. Kurn, H.-J. Miesner, D. S. Durfee, C. G. Townsend, S. Inouye & W. Ketterle; "Propagation of Sound in a Bose-Einstein Condensate"; Phys. Rev. Lett. **79**, pp. 553–556 (1997). Cited on page 88

[230] R. Meppelink, S. B. Koller & P. van der Straten; "Sound propagation in a Bose-Einstein condensate at finite temperatures"; Phys. Rev. A **80**, p. 043605 (2009). Cited on page 88

[231] B. Yang, Y.-Y. Chen, Y.-G. Zheng, H. Sun, H.-N. Dai, X.-W. Guan, Z.-S. Yuan & J.-W. Pan; "Quantum criticality and the Tomonaga-Luttinger liquid in one-dimensional Bose gases"; Phys. Rev. Lett. **119**, p. 165701 (2017). Cited on page 88

[232] O. Morsch & M. Oberthaler; "Dynamics of Bose-Einstein condensates in optical lattices"; Rev. Mod. Phys. **78**, pp. 179–215 (2006). Cited on page 89

[233] S. Burger, F. S. Cataliotti, C. Fort, F. Minardi, M. Inguscio, M. L. Chiofalo & M. P. Tosi; "Superfluid and Dissipative Dynamics of a Bose-Einstein Condensate in a Periodic Optical Potential"; Phys. Rev. Lett. **86**, pp. 4447–4450 (2001). Cited on page 89

[234] D. E. Miller, J. K. Chin, C. A. Stan, Y. Liu, W. Setiawan, C. Sanner & W. Ketterle; "Critical Velocity for Superfluid Flow across the BEC-BCS Crossover"; Phys. Rev. Lett. **99**, p. 070402 (2007). Cited on page 89

[235] L. Sobirey, N. Luick, M. Bohlen, H. Biss, H. Moritz & T. Lompe; "Observation of superfluidity in a strongly correlated two-dimensional Fermi gas"; Science **372**, pp. 844–846 (2021). Cited on page 89

[236] B. Wu & Q. Niu; "Superfluidity of Bose–Einstein condensate in an optical lattice: Landau–Zener tunnelling and dynamical instability"; New Journal of Physics **5**, p. 104 (2003). Cited on page 89

[237] B. Wu & Q. Niu; "Landau and dynamical instabilities of the superflow of Bose-Einstein condensates in optical lattices"; Phys. Rev. A **64**, p. 061603 (2001). Cited on page 89

[238] A. Smerzi, A. Trombettoni, P. G. Kevrekidis & A. R. Bishop; "Dynamical Superfluid-Insulator Transition in a Chain of Weakly Coupled Bose-Einstein Condensates"; Phys. Rev. Lett. **89**, p. 170402 (2002). Cited on page 89

[239] C. Menotti, A. Smerzi & A. Trombettoni; "Superfluid dynamics of a Bose–Einstein condensate in a periodic potential"; New Journal of Physics **5**, p. 112 (2003). Cited on page 89

[240] E. Taylor & E. Zaremba; "Bogoliubov sound speed in periodically modulated Bose-Einstein condensates"; Phys. Rev. A **68**, p. 053611 (2003). Cited on page 89

[241] M. Modugno, C. Tozzo & F. Dalfovo; "Role of transverse excitations in the instability of Bose-Einstein condensates moving in optical lattices"; Phys. Rev. A **70**, p. 043625 (2004). Cited on page 89

[242] K. Iigaya, S. Konabe, I. Danshita & T. Nikuni; "Landau damping: Instability mechanism of superfluid Bose gases moving in optical lattices"; Phys. Rev. A **74**, p. 053611 (2006). Cited on page 89

[243] F. S. Cataliotti, L. Fallani, F. Ferlaino, C. Fort, P. Maddaloni & M. Inguscio; "Superfluid current disruption in a chain of weakly coupled Bose–Einstein condensates"; New Journal of Physics **5**, p. 71 (2003). Cited on page 89

[244] L. Fallani, L. De Sarlo, J. E. Lye, M. Modugno, R. Saers, C. Fort & M. Inguscio; "Observation of Dynamical Instability for a Bose-Einstein Condensate in a Moving 1D Optical Lattice"; Phys. Rev. Lett. **93**, p. 140406 (2004). Cited on page 89

[245] L. De Sarlo, L. Fallani, J. E. Lye, M. Modugno, R. Saers, C. Fort & M. Inguscio; "Unstable regimes for a Bose-Einstein condensate in an optical lattice"; Phys. Rev. A **72**, p. 013603 (2005). Cited on page 89

[246] J. Mun, P. Medley, G. K. Campbell, L. G. Marcassa, D. E. Pritchard & W. Ketterle; "Phase Diagram for a Bose-Einstein Condensate Moving in an Optical Lattice"; Phys. Rev. Lett. **99**, p. 150604 (2007). Cited on page 89

[247] F. S. Cataliotti, S. Burger, C. Fort, P. Maddaloni, F. Minardi, A. Trombettoni, A. Smerzi & M. Inguscio; "Josephson Junction Arrays with Bose-Einstein Condensates"; Science **293**, pp. 843–846 (2001). Cited on page 89

[248] M. Krämer, L. Pitaevskii & S. Stringari; "Macroscopic Dynamics of a Trapped Bose-Einstein Condensate in the Presence of 1D and 2D Optical Lattices"; Phys. Rev. Lett. **88**, p. 180404 (2002). Cited on page 89

[249] L. Tanzi, E. Lucioni, S. Chaudhuri, L. Gori, A. Kumar, C. D'Errico, M. Inguscio & G. Modugno; "Transport of a Bose Gas in 1D Disordered Lattices at the Fluid-Insulator Transition"; Phys. Rev. Lett. **111**, p. 115301 (2013). Cited on page 89

[250] V. P. Singh & L. Mathey; "First and second sound in a dilute Bose gas across the BKT transition"; New Journal of Physics **24**, p. 073024 (2022). Cited on page 93

[251] M. Gałka, P. Christodoulou, M. Gazo, A. Karailiev, N. Dogra, J. Schmitt & Z. Hadzibabic; "Emergence of Isotropy and Dynamic Scaling in 2D Wave Turbulence in a Homogeneous Bose Gas"; Phys. Rev. Lett. **129**, p. 190402 (2022). Cited on page 94